The University of Nottingham

Division of Materials, Mechanics and Structures

MULTI-SCALE MODELLING OF POLYMER COMPOSITE MATERIALS AT HIGH RATES OF STRAIN

by

Mark Jonathan Lidgett

MEng (Hons)

Thesis submitted to the University of Nottingham
for the degree of Doctor of Philosophy

August 2012

Contents

Abstract

The overall objective of this thesis was to develop a methodology for predicting the high strain rate properties of macro scale polymer composite materials through micro and meso scale finite element modelling.

The focus in this study was on multi-layered multi-material polymer composite laminates consisting of 0/90 and ± 45 layers of either; S2 Glass/Epoxy or Carbon/Epoxy non crimp fabric.

A multi-scale finite element modelling methodology was developed at the micro and meso scale for predicting the elastic response, damage initiation, damage evolution and strain rate dependence of macro scale polymer composite materials. The methodology was implemented in the Abaqus finite element package utilising Python scripting for simulation definition and Fortran code for user defined explicit material subroutines.

Micro scale unit cells were tested in longitudinal, transverse and shear loading directions over a range of strain rates. The results of the micro scale testing were converted into material properties of the meso scale yarns / tows. Meso scale unit cells were tested in in-plane, through thickness and shear loading directions over of a range of strain rates. The results of the meso scale testing were converted into material properties of macro scale polymer composite materials.

The modelling methodology was validated against experimental testing conducted on meso scale samples over a range of strain rates using an electromechanical universal static test machine and an instrumented falling weight drop tower.

The contribution to knowledge from this study is the development of a validated modelling methodology for predicting the elastic, damage and strain rate dependent response of polymer composite materials at a micro and meso scale.

Acknowledgements

The author would like to thank Dr Richard Brooks and Prof Nicholas Warrior for their supervision throughout the entirety of this project.

This study was financially supported by the UK Engineering and Physical Sciences Research Council (EPSRC) through the Nottingham Innovative Manufacturing Research Centre (NIMRC) and the Technology Strategy Board (TSB) through contract reference TP/8/MAT/6/I/Q1576E.

Partners in the TSB funded Lightweight Materials and Structures for Blast and Ballistic Survivability (LiMBS) project are thanked for their support: Aigis Blast Protection, BAE Systems, BAE Systems Surface Ships, MIRA, Permali, QinetiQ, Sigmatex and TPS.

Thank you to all the members of the Polymer Composites Research Group at The University of Nottingham.

Finally, thanks to my girlfriend, family and friends for their continued support and encouragement throughout my work.

Abbreviations and Notations

2D	Two Dimensional
3D	Three Dimensional
ACAVP	Advanced Composite Armoured Vehicle Platform
AFV	Armoured Fighting Vehicle
AISI	American Iron and Steel Institute
ASI	Abaqus Scripting Interface
CAE	Computer Aided Engineering
CAFV	Carbon Fibre for Armoured Fighting Vehicles
DS	Dassault Systémes
EPSRC	Engineering and Physical Sciences Research Council
FE	Finite Element
FEA	Finite Element Analysis
FEM	Finite Element Method
FSP	Fragment Simulating Projectile
GIM	Group Interaction Modelling
GUI	Graphical User Interface
HPC	High Performance Computer
IED	Improvised Explosive Device
JIEDDO	Joint Improvised Explosive Device Defeat Organization
LiMBS	Lightweight Materials and Structures for Blast and Ballistic Survivability
MoD	Ministry of Defence
NCF	Non Crimp Fabric
NIMRC	Nottingham Innovative Manufacturing Research Centre
PE4	Plastic Explosive
ROM	Rule of Mixtures
RUC	Representative Unit Cell
RVE	Representative Volume Element
S2	A grade of glass fibre that offers increased stiffness, strength, toughness and impact performance [1].
SEM	Scanning Electron Microscope
TSB	Technology Strategy Board
UD	Unidirectional
UHMWPE	Ultra High Molecular Weight Poly-Ethylene

$\dot{\varepsilon}_o$	Quasi Static Reference Strain Rate
$\dot{\varepsilon}$	Strain Rate
A_o	Quasi Static Parameter
A_{RT}	Rate Adjusted Parameter
C_{XX}	Stiffness Constant for XX direction
C_A	Strain Rate Scaling Constant for Parameter A
E	Stiffness
e_{max}	Largest Value of Maximum Stress Criteria
f	Fibre Volume Fraction
G	Shear Stiffness
h	Separation of Fibres at Micro Scale
ln	Natural Log
m	Strain Softening Parameter
p	Row of Matrix
q	Column of Matrix
R	Closest Centre to Centre Spacing of Fibres at Micro Scale (when multiplied by 2)
r	Radius
v	Poisson's Ratio
Vf	Volume Fraction
wt%	Weight Percent
ε	Strain
σ	Stress
ω	Damage Variable
x, y, z	Coordinate Axes
u, v, w	Displacement in x, y, z Coordinate Axes
i, j ,k	Periods in x, y, z Coordinate Axes

1 Introduction

1.1 Background

In a 2010 annual report by the Joint Improvised Explosive Device Defeat Organization (JIEDDO) [2] it is stated that improvised explosive devices (IED) continue to pose the main threat to coalition forces in both Afghanistan and Iraq. From October 2009 to October 2010 there were 19393 civilian, security force and coalition force IED casualties (wounded and killed in action) in Afghanistan and Iraq combined [2]. The alarming effectiveness of this weapon is due to the insurgents understanding of the coalition forces need to use convoys of vehicles to supplement troops fighting on the front line. The placement of IEDs by the roadside to disrupt these convoys has become a common tactic indicated by the 15218 effective and ineffective IED attacks that occurred from January 2010 to September 2010 in Afghanistan and Iraq [2]. Many vehicles that travel in these convoys do not offer adequate protection from IED explosions, such as the controversial Snatch Land Rover [3], and if they do it is often at the expense of reducing mobility in action, fuel efficiency and engine service life due to heavy conventional steel, aluminium or hard metal armour. To address these issues there has been an increased interest in fibre reinforced polymer composite materials for military vehicle armour due to their key advantages:

- High stiffness
- High strength
- Low density
- High strength to weight ratio
- Good corrosion resistance
- Easy to transport, handle and install
- Good opportunities for optimised performance by varying reinforcements and matrices
- Good retrofitting opportunities

There have been several examples of composite materials being used as armour in military vehicles. The majority of Armoured Fighting Vehicles

(AFV) in current military service have spall liners made from composite materials. Spall is small fragments of material that have detached from a larger body in the vehicle due to rapid deformation, usually from a blast or ballistic event. Spall can travel at high speeds effectively creating dangerous ballistic projectiles. Spall liners are used to line the interior of the vehicle to protect against occupant injury. The Force Protection Ocelot, which is known as the Foxhound in British military service, is a light protected patrol vehicle with specialised protection again IEDs. This specialised protection comes in the form a V shaped hull, to focus blasts away from the vehicle, and advanced composite materials. The confidence in this composite material military vehicle is demonstrated by the Ministry of Defence (MoD) who have signed a £180m contract for 200 new patrol vehicles to replace the Snatch Land Rover [4]. French and Wright [5] detailed the use of glass fibre composites materials for the hull of an AFV called the Advanced Composite Armoured Vehicle Platform (ACAVP). In this programme the composite hull acted as both a structural and blast / ballistic protective material. The structural requirements were to carry the loads from the suspension and associated equipment and the blast / ballistic requirements were to provide the adequate level of occupant protection. The major conclusion from this study was that to make significant weight savings the use of carbon fibre composites should be considered in place of glass fibre composites in multi-layered multi-material structures.

The inclusion of composite materials in military vehicles is clearly on the increase which brings about new challenges for engineers. The composite materials need to go through rigorous, time consuming and expensive experimental blast and ballistic trials to ensure an adequate level of protection is offered to military personnel. This has brought forward the development of computational simulations of the response of composite materials to blast and ballistic loading to reduce the amount of experimental trails required and aid in the design process. These simulations, however, are not straightforward and often require a multitude of composite material properties which would normally be obtained from an experimental material characterisation programme, such as that conducted by Brown *et al* [6]. Multi-scale finite element (FE) modelling has the capability to provide these material properties computationally which would

reduce, and in some circumstances completely remove, the need for an experimental material characterisation programme.

Hierarchical multi-scale finite element modelling, where there is an information transfer from the smaller length scale to the larger length scale, is prevalent in composite material modelling. This thesis focuses on modelling composite materials at the micro and meso scale where there is an information transfer, in the form of material properties, between the micro and meso scale. At the micro scale, fibres are embedded in a matrix material to form a yarn or tow i.e. a fibre bundle. At the meso scale, yarns are arranged in a desired architecture, e.g. non-crimped or plain weave, and embedded in a matrix material. The results of the meso scale modelling will provide macro scale material properties where the macro scale consists of several meso scale laminae, comprising a repeated yarn structure, which are stacked to form a composite laminate.

1.2 Objectives and Scope

The overall objective of this thesis is to develop a methodology for predicting the high strain rate properties of macro scale polymer composite materials through micro and meso scale finite element modelling. The multi-scale modelling methodology to be presented will be applicable for many types of composite materials but the focus in this study will be on multi-layered multi-material polymer composite laminates consisting of 0/90 and ± 45 layers of either; S2 Glass/Epoxy or Carbon/Epoxy non crimp fabric.

1.3 Thesis Layout

This thesis is comprised of seven chapters. Following this introduction the chapter by chapter thesis layout is as follows:

Chapter 2 contains a review of the literature which has been split into three main areas. Firstly a brief review on the general characteristics of polymer composite materials is presented. Secondly the experimental characterisation of composite materials is detailed with reference to three types of testing; low, medium and high strain rate. Finally the state of the art in multi-scale finite element modelling of composite materials is

presented. Examples of modelling at the micro, meso and macro scale are given to envisage the modelling approach adopted in this thesis.

Chapter 3 details the modelling methodology for the micro and meso scale. Attention is paid to the definition and generation of unit cells, the derivation and application of periodic boundary conditions based on translational symmetry and the constituent material models.

Chapter 4 presents the micro scale modelling results in longitudinal, transverse and shear loading over a range of strain rates. The discussion of these results, as well as some parametric studies, is also included in this section.

Chapter 5 presents the meso scale modelling results in in-plane, through thickness and shear loading over a range of strain rates. The discussion of these results, as well as some parametric studies, is also included in this section.

Chapter 6 presents the experimental validation of the previous two chapters of modelling. The experimental testing is limited to in-plane tension, compression and shear testing over a range of strain rates on meso scale non-crimp fabric (NCF) cross-ply laminates. Details of the experimental methods in terms of material specification and test methods are also presented.

Chapter 7 presents a discussion of the work conducted and details the main conclusions. Recommendations for future work are also given in this chapter.

2 Literature Review

2.1 Introduction

This chapter presents and reviews the important aspects of this research. An overview of composite materials is presented which focuses on the types of materials under consideration in this study. The techniques for low, intermediate and high strain rate experimental characterisation of composite materials are detailed followed by the techniques for computational characterisation of composite materials through multi-scale finite element modelling.

Where possible review paper references are given to avoid excessive reporting of already well-established, and detailed, techniques. Should more information be desired it is suggested the reader consult the many references provided in the chapter.

2.2 Composite Materials

"Composite materials, also called composites, a solid material that results when two or more different substances, each with its own characteristics, are combined to create a new substance whose properties are superior to those of the original components in a specific application." [7]

These two substances are usually a reinforcement material and a matrix material. Reinforcements can come in the form of mono-filaments, multi-filaments, short fibres, whiskers and particulates. Matrices can come in the form of polymer resins (thermoset and thermoplastic), metals and ceramics. This thesis focuses on multi-filament reinforcements and thermoset polymer resin matrices and all further discussion in this literature review will be based around this subsection of composite materials.

2.2.1 Characteristics of Polymer Composite Materials

Multi-filament reinforcements are made up of thousands of fibres (commonly carbon, glass or aramid) i.e. a fibre bundle. These fibre bundles can be arranged into desired fibre bundle architectures. The simplest of fibre bundle architecture is that of a unidirectional (UD) composite material where all fibres are aligned parallel to each other. Weaving, braiding and knitting can also be used to create more complex fibre bundle architectures. Polymer composite materials are usually made up of layers or laminae; where laminae can be stacked to create a laminate. A typical laminate construction would involve orientating adjacent unidirectional laminae at 90° to each other creating a 0°/90° laminate, seen in Figure 2-1. The laminate is balanced about the mid-plane with one 90° and one 0° layer either side. The elliptical shaped fibre bundles can be seen in the 0° layers.

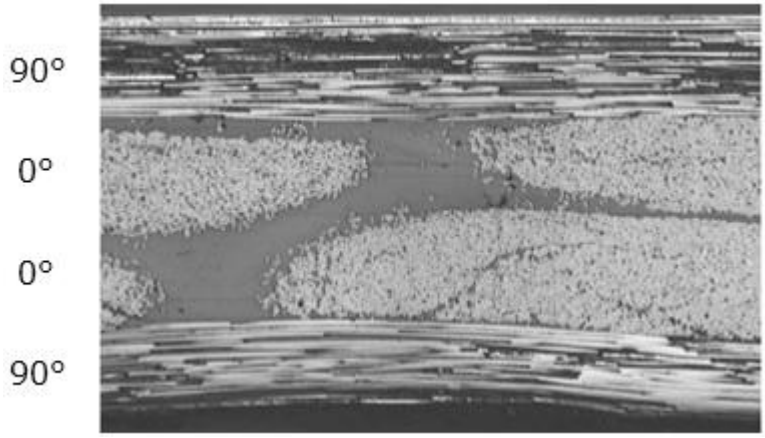

Figure 2-1. Micrograph of a balanced 0°/90° cross ply carbon vinyl-ester laminate [8]

Thermosetting resin matrices commonly come in the liquid form of epoxy, un-saturated polyester and vinyl ester and are converted to a solid during manufacture by a chemical cross linking process.

The two constituents, reinforcement and matrix, come together during manufacture or in an intermediate stage. There are many types of manufacturing routes of composite materials such as; impregnation (intermediate stage), injection moulding, compression moulding, pultrusion, filament winding and resin injection. As fabrication of composite materials is not a focus of this thesis please consult Hull and Clyne [9] for further information.

2.2.2 Elastic Deformation of Polymer Composite Materials

Unidirectional composite materials tend to exhibit a large axial stiffness and, in comparison, a low transverse stiffness. This is due to the high axial stiffness of the fibres bearing the load when stressed in the axial direction, whereas, in transverse loading a more matrix dominated response is observed. The initial response to loading of a unidirectional composite is in general a linear elastic one.

The initial elastic response of a cross ply laminate is commonly approximated as a bi linear curve. The point where the two linear sections intersect corresponds to failure of the plies perpendicular to the loading direction.

2.2.3 Damage and Failure of Polymer Composite Materials

This section discusses the damage and failure mechanisms of unidirectional and cross-ply laminates subjected to different loading conditions. For a more in depth review one should consult Hull and Clyne [9].

Unidirectional Laminates

Unidirectional composite lamina can fail by a variety of different mechanisms: axial tensile failure, axial compressive failure, transverse tensile failure, transverse compressive failure and shear failure.

Axial tensile failure occurs due to stress in the direction parallel to the fibres. If the matrix has a lower failure strain than the fibres then initial damage occurs in the matrix in the form of micro-cracking. This progressive cracking transfers load to the fibres. Final failure occurs in the form of fibre fracture at the failure strain of the fibres as seen in Figure 2-2. Fibre fracture can occur before matrix cracking if the failure strain of the matrix is greater than that of the fibres.

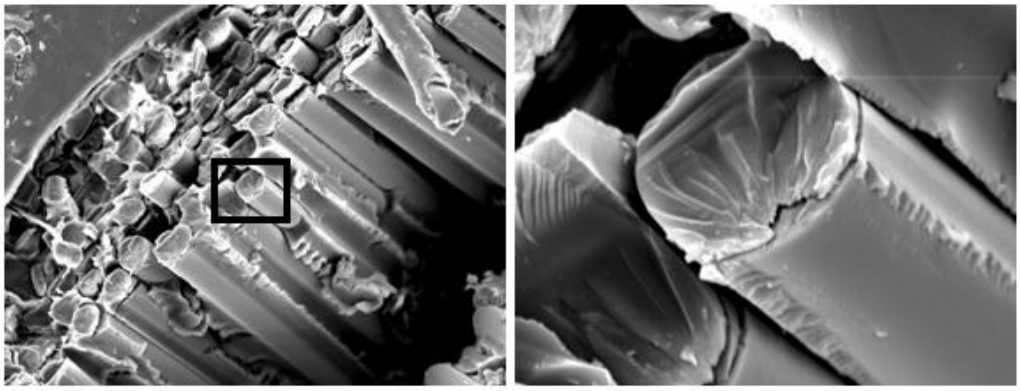

Figure 2-2. Fibre fracture in glass fibre composite. Right image is a magnified image of the rectangular area in the left image. [10]

Axial compressive stress can cause fibres to buckle which generates compressive and tensile stresses across different sections of the fibre enabling fracture or distortion. As the amount of buckling increases failure of the composite occurs. Buckling instability can also cause a kink band in the fibres leading to composite failure as seen in Figure 2-3. The axial compressive stress strain response usually has a lower initial stiffness and failure stress than the axial tensile loading stress strain response.

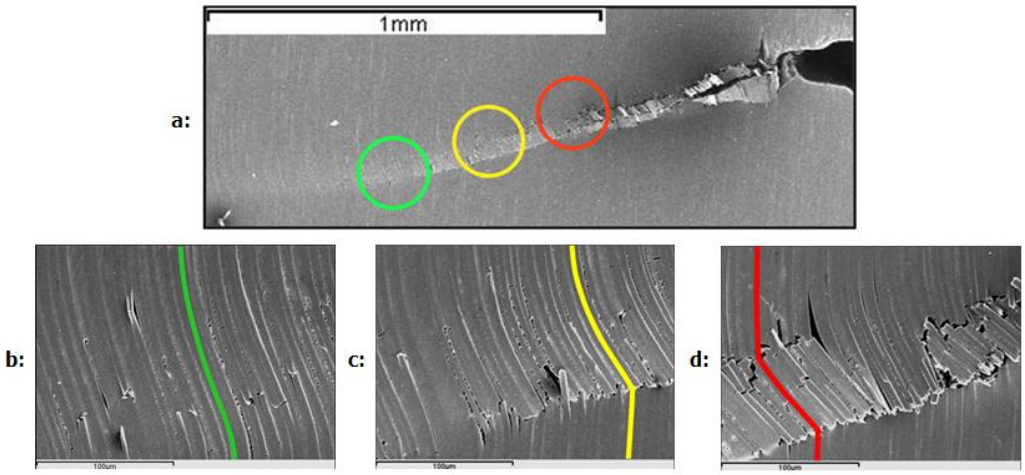

Figure 2-3. (a) Low magnification of a crack propagating from right to left, (b) Initial fibre buckling, (c) Initial cracking, (d) Fully developed kink-band. [10]

Transverse tensile failure is a complex failure mechanism that is affected by multiple factors such as the interfacial strength, fibre distribution and void content. The presence of fibres actually reduces the transverse tensile strength and failure strain of the matrix. If the interfacial strength is low then cracks will initiate at the interface between fibre and matrix, however, if the interfacial strength is high then the cracks will initiate in the matrix close to the interface. These cracks will then spread through the material

via the highly stressed matrix regions as seen in Figure 2-4. If the fibres have a layered structure, hence a low transverse strength, then it is possible for failure to occur within the fibres.

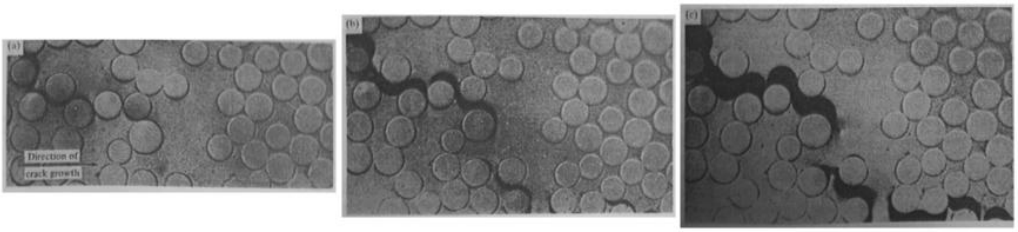

Figure 2-4. Scanning Electron Microscope (SEM) micrographs illustrating the propagation of a transverse tensile crack in a polyester/glass lamina. [9]

Transverse compressive failure occurs when the shear stress on planes parallel to the fibre axis reaches the shear strength of the matrix.

There are three different types of shear failure for unidirectional composite lamina. Type one causes sliding of fibres over each other axially, type two causes sliding of fibres over each other laterally and type three is through thickness shear which can cause fibre fracture.

Cross-Ply Laminates

A balanced cross ply (0°/90°) laminate can also damage through a variety of different mechanisms as with unidirectional composite materials. In in-plane tensile loading the following sequence of failure occurs; (a) through thickness cracking of transverse plies seen in Figure 2-5, (b) parallel to the fibres cracking of axial plies and finally (c) transverse to the fibre direction cracking of axial plies (i.e. final failure). This sequence of events is depicted in Figure 2-6.

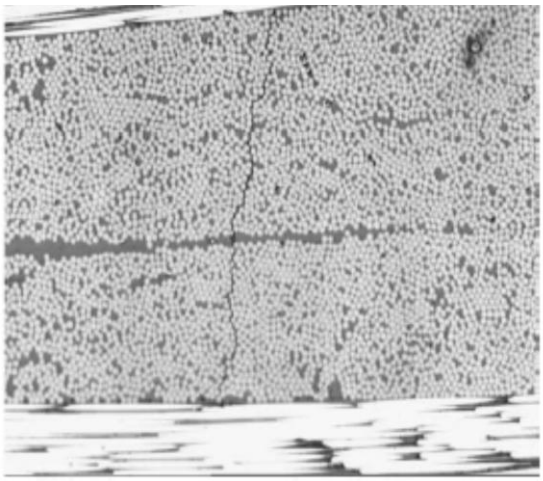

Figure 2-5. Micrograph of a though thickness crack in plies transverse to the loading direction in a 0°/90° carbon vinyl-ester cross ply laminate [8]

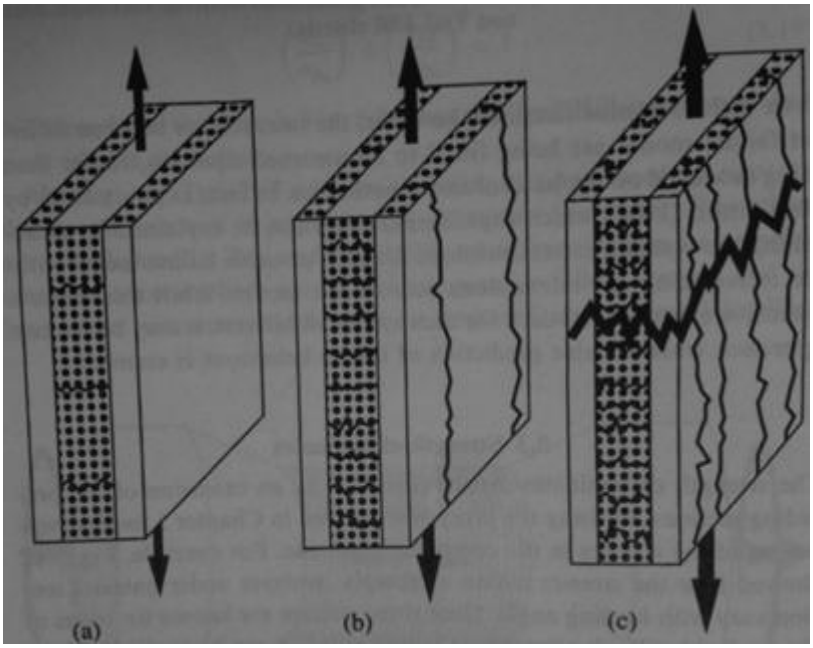

Figure 2-6. Loading of a cross-ply laminate parallel to one of the fibre directions. (a) Through thickness cracking of transverse plies, (b) Parallel to the fibres cracking of axial plies, (c) Transverse to the fibre direction cracking of axial plies. [9]

Initially the axial plies carry the majority of the load. Even though the transverse plies do not carry a significant amount of load they are still the first to fail due to the much lower strength of unidirectional laminates in the transverse direction when compared to the axial direction. The cracking of the transverse plies, therefore, does not transfer a large amount of load to the axial plies as they were already bearing the majority. This leads to the axial plies remaining undamaged for some time after the initial damage in the transverse plies. As the load increases the axial plies develop cracks parallel to the fibres. This occurs due to the axial plies

stretching in the loading direction and, therefore, contracting perpendicular to the loading direction. The transverse plies structure resists this contraction generating transverse tensile stress which causes the axial plies to crack parallel to the fibres. As the load further increases cracks perpendicular to the loading direction will develop across the axial plies causing ultimate final failure. This occurs when the stress reaches the tensile strength of the fibres and they fracture. Transverse cracks can then easily develop through the entirety of the laminate as there is little or no resistance to the applied stress.

Mattsson *et al* [11] conducted tensile tests on NCF cross ply composites and investigated the effect of layer stacking sequence. The paper shows, in the form of micrographs, the variety of damage mechanisms that can occur, such as, fibre bundle breaks and delamination. Delamination is a critical failure mode for layered composite materials. It occurs due to interlaminar stresses (generated through a mismatch in Poisson's ratios between various layers) and leads to separation of the plies.

2.2.4 Strain Rate Dependence of Polymer Composite Materials

Polymers behave in an elastic manner before the point of yield. This reversible elongation before yield is due to bending and stretching of covalent bonds in the polymer backbone and recoverable uncoiling of polymer chains. The point of yield occurs when there is irreversible slippage of polymer chains. As these mechanisms are time dependent, low stiffness / low strength polymers may resemble high stiffness / high strength polymers if the material is tested at a high rate of strain.

Polymers can be considered as viscoelastic materials where they exhibit characteristics of both elastic and viscous materials. Upon loading elastic materials they strain immediately, whereas, viscous materials strain linearly with time. Upon removal of loading elastic materials return to their original shape, whereas, viscous materials do not. In terms of a mathematical model an elastic material can be represented by springs, a viscous material by dashpots/dampeners and a viscoelastic material by a combination of both in series or parallel. Polymers can be modelled explicitly as viscoelastic materials or as elastic materials with the rate

dependence accounted for in other ways, such as scaling of material properties.

The polymer of interest in this study is epoxy resin and its strain rate dependence has been investigated by a number of researchers [12-17]. The general trend is that an increase in strain rate increases the stiffness and strength of the epoxy resin, as seen in Figure 2-7.

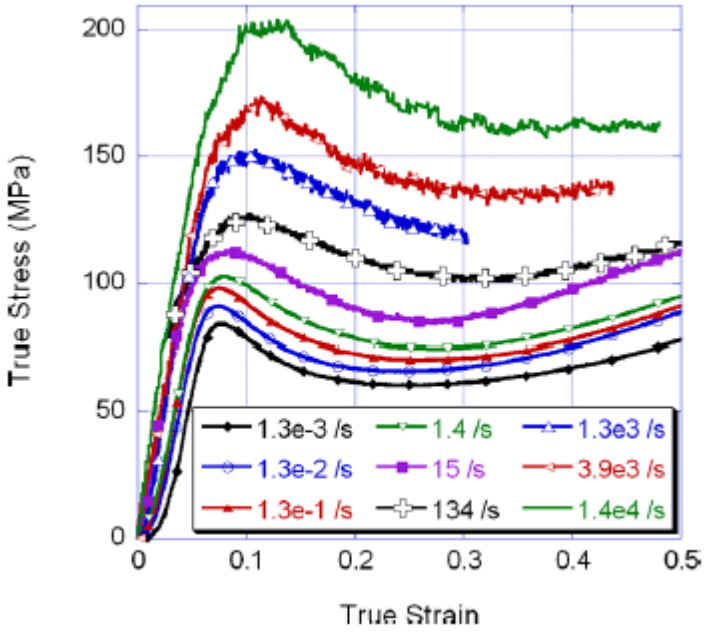

Figure 2-7. Epoxy resin true stress strain curves at different strain rates [14]

The fibres of interest in this study are carbon and S2 glass. S2 glass fibres (typical composition: SiO_2 65 wt%, Al_2O_3 25 wt% and MgO 10 wt%) have a higher strain to failure and modulus than E glass fibres (typical composition: SiO_2 54 wt%, Al_2O_3 14 wt%, CaO + MgO 22 wt% and B_2O_3 10 wt%) [18]. It is widely accepted that carbon fibres are strain rate insensitive in the sense that strain rate has a negligible effect on stiffness, ultimate strength and failure strain [19, 20]. Yazici [21] concluded that S2 glass fibres are rate sensitive, however, it is important to realise this conclusion was drawn from tests over a range of low strain rates, less than 1 /s. The ultimate strength and stiffness both increased to a maximum and then decreased with increasing strain rate.

The behaviour of the fibre / matrix interfacial layer can exhibit strain rate dependence. This was demonstrated by Tanoglu *et al* [22] who conducted dynamic interfacial loading on E-glass/epoxy-amine samples. The test

used a micro indentation method to debond the fibre from the matrix at the interface. The tests were performed up to displacement rates of 3000 μm/s generating high shear strain rates. The results demonstrated strain rate dependence showing an increase in average apparent shear strength with increasing displacement rate.

Fishpool *et al* [23] evaluated compatible, semi-compatible, incompatible and smart sized S2 glass fibre reinforced epoxy composites. The compatible / semi-compatible sizings were surface treatments used to strengthen the bond at the fibre / matrix interface. The incompatible sizing was starch oil system applied to the fibre which inhibited adhesion at the fibre / matrix interface. The smart sizing was developed to generate strong interfacial strengths under static load conditions and weak interfacial strengths under dynamic loading conditions. Double notch shear and double cantilever bream tests on unidirectional laminates were conducted at both quasi-static and dynamic rates of strain. All fibre sizing types exhibited strain rate dependence in the double notch shear and double cantilever beam tests. The amount of strain rate dependence varied depending on the type of sizing showing that the fibre / matrix interface can have a significant effect on the strain rate dependence of the composite.

Vural and Ravichandran [24] tested unidirectional S2 glass/epoxy composites at strain rates up to 10,000 /s in compression. From 0.001 /s to 10,000 /s test strain rates the compressive strength increased by 50% and the stiffness increased by more than 100%.

Hosur *et al* [25] conducted high strain rate (up to 817 /s) compression tests on unidirectional and cross ply carbon epoxy laminates. Unidirectional laminates were loaded in the longitudinal and transverse directions and the cross ply laminates were loaded in the in-plane and through thickness directions. In all samples and loading conditions the dynamic stiffness and strength values were larger than the static stiffness and strength values, except for the cross ply laminate loaded through the thickness where the static strength was greater than the dynamic strength. For cross ply in-plane loading, cross ply through thickness loading, UD 0° loading and UD 90° loading the peak stress changed by +0.7%, -19%, +26% and +25% respectively when comparing static loading to high rate

loading at 817/s. For cross ply in-plane, cross ply through thickness, UD 0° loading and UD 90° loading the stiffness changed by +57%, +11%, +87% and +50% respectively when comparing static loading to high rate loading at 817/s.

Okoli *et al* [26] investigated the effect of strain rate on the failure modes of woven glass epoxy composite laminates. This was conducted by testing samples in tension at $1.7x10^{-2}$ mm/s and 10 mm/s and studying the resulting fractured surfaces using a scanning electron microscope (SEM). The failure mode changed from brittle fibre failure with fibre pull out at low rate loading to brittle failure with a large amount of matrix damage before final fracture at high rate loading. The increased matrix damage at high rate loading lead to bunch fibre pull out, this implied that the fibre-matrix interfacial bond strength was exceeded before the tensile failure strength of the composite.

The effect of strain rate on composite materials has been reviewed by multiple authors [27, 28]. These reviews should be consulted for further information on the strain rate dependence on polymer composite materials.

This section demonstrates the importance of strain rate dependence when designing for dynamic loading conditions. It had been seen by multiple authors that material properties such as stiffness and strength can change by a staggering amount when the rate of loading is increased. Not only this but it has been shown that there can be a change in the mechanisms of failure as the rate of loading is increased, demonstrated by Okoli *et al* [26].

2.3 Experimental Characterisation of Composite Material Properties

This section gives a brief overview of the experimental techniques required to characterise polymer composite materials from quasi-static to high rates of strain. Figure 2-8 demonstrates that a variety of different experimental techniques are required not only for different loading condition tests (tension, compression and shear) but also for different strain rate tests (quasi-static, intermediate and high). Quasi static strain rates range from 10^{-4} to 10^{-3} /s, intermediate strain rates range from 10^{-1} /s to 10^{2} /s and

high strain rates are greater than 10^3 /s. When operating in the high strain rate region inertia and wave propagation effects begin to become important when analysing the experimental results and at rates higher than 10^5 /s one has to consider thermodynamic effects [29].

Mode	Applicable strain rate (s^{-1})	Testing techniques
Compression	<0.1	Conventional testing machine
	0.1–100	Servo-hydraulic machine
	0.1–500	Cam plastometer and drop test
	200–10^4	Hopkinson pressure bar
	10^4–10^5	Direct impact using air gun apparatus
Tension	<0.1	Convensional testing machine
	0.1–100	Servo-hydraulic machine
	100–10^4	Hopkinson pressure bar in tension
	10^4	Expanding ring
	$>10^5$	Flyer plate
Shear	<0.1	Convensional testing machine
	0.1–100	Servo-hydraulic machine
	10–10^3	Torsional impact
	100–10^4	Hopkinson pressure bar in torsion
	10^3–10^4	Double-notch shear and punch
	10^4–10^7	Pressure-shear plate impact

Figure 2-8. Experimental techniques for different loading modes and strain rates [30]

Information on high strain rate experimental techniques can be found in the following review papers and books by Zukas *et al* [29], Hamouda and Hashmi [30] and Field *et al* [31].

Experimental characterisation of composite materials can be time consuming, multifaceted, in terms of using numerous different strain rate test procedures and equipment, and often prohibitively expensive [32]. This has led to the increased interest in multi-scale modelling characterisation of composite materials which will be discussed in the subsequent section.

2.4 Multi-Scale Modelling Characterisation of Composite Material Properties

Multi-scale finite element modelling has the ability to handle the response of the composite material at larger scales whilst retaining the detailed response at the smaller scales. An interesting review paper on multi-scale modelling and virtual testing has been conducted by Cox and Yang [33] and should be consulted for a broader introduction to the topic. The multi-scale modelling approach adopted in this thesis is known as a hierarchical information transfer process where the information transferred between the scales is material properties. This thesis focuses on modelling composite materials at the micro and meso scale. At the micro scale, fibres are embedded in a matrix material to form a yarn or tow i.e. a fibre bundle. At the meso scale, yarns are arranged in a desired architecture, e.g. non-crimped, and embedded in a matrix material. The results of the micro scale finite element modelling will provide properties for the meso scale yarns. The results of the meso scale modelling will provide macro scale material properties where the macro scale consists of several meso scale laminae, comprising a repeated yarn structure, which are stacked to form a composite laminate.

This section now gives a general overview of unit cell modelling and the finite element method used in all scales of a multi-scale modelling process. The following sections detail how the finite element method has been utilised to model the response of polymer composite materials in terms of the material response, damage initiation, damage evolution and strain rate dependence. The section is concluded with examples from the literature of multi-scale modelling.

2.4.1 Unit Cell Modelling

The start of this section gave an explanation of the structure of the micro and meso scale. These structures are often represented by unit cells. It can be assumed that unit cells have an idealised structure that is repeatable and periodic.

The most common assumption at the micro scale is that the fibres are aligned parallel to each other and are arranged in a hexagonal or square lattice with each fibre having a circular cross section with the same

diameter, as described by Hull and Clyne [9]. From one of these arrangements many repeatable unit cells can be identified as demonstrated in Figure 2-9.

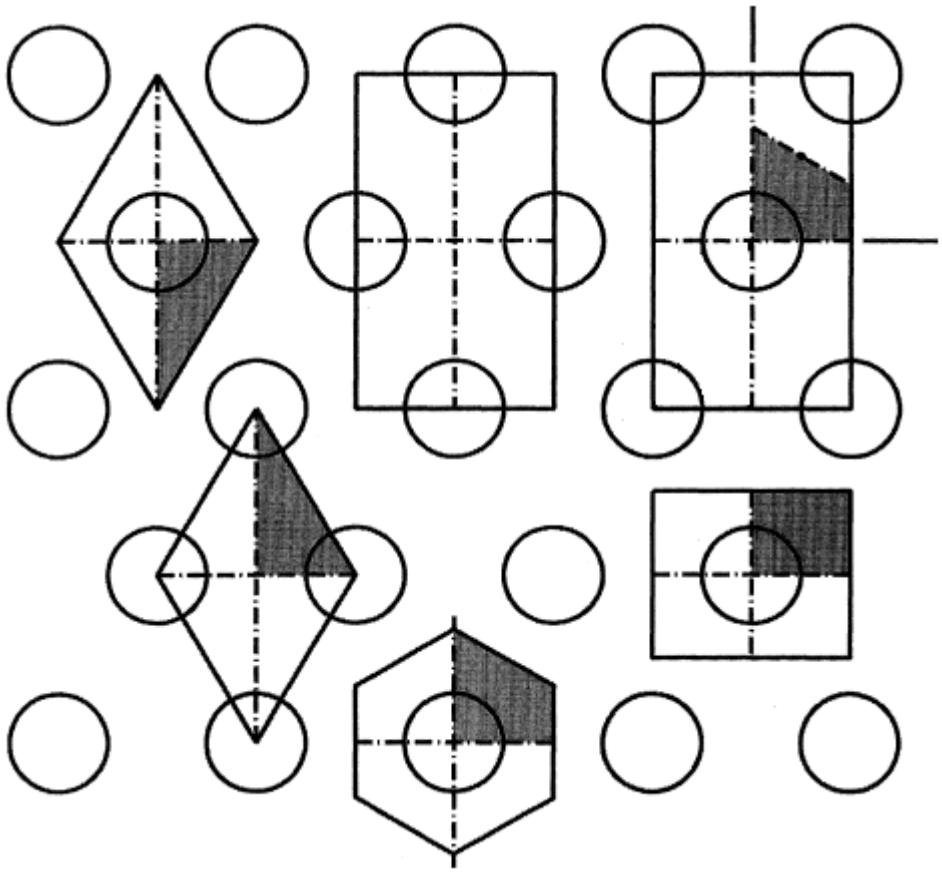

Figure 2-9. A hexagonal fibre matrix layout and various periodic elements and unit cells. Shaded areas show that with further symmetry consideration smaller unit cells can be identified [34]

Li [35] determined appropriate periodic boundary conditions for micro scale unit cells. Li warned how the application of incorrect boundary conditions leads to effectively different microstructures even though the unit cells may look geometrically identical. It was demonstrated how this can lead to a difference in effective properties calculated though micro scale unit cell finite element modelling of composite materials.

At the meso scale the unit cell is identified based on the fabric architecture. Small unit cells consisting of a few yarns can be identified for simple fabric architectures; such as non crimp fabrics. Whereas; for complex fabric architectures such as 3D woven structures, larger unit cells may be necessary.

2.4.2 Finite Element Method

The finite element method (FEM), also known as finite element analysis (FEA), is a numerical technique in continuum and structural mechanics. In the FEM the domain is divided up into small regions or elements. The behaviour of each individual element is defined by the elements' displacement and material law. Continuity and equilibrium equations are utilised to assembly all elements together. With the application of satisfactory boundary conditions a solution can be found for the overall system of linear algebraic equations.

The implicit and explicit methods are two types of approaches used in finite element analysis to obtain solutions to the overall system of linear algebraic equations. The implicit method calculates the state at time $t+\Delta t$ based on information at time $t+\Delta t$, whereas, the explicit method calculates the state at time $t+\Delta t$ based on information at time t. The implicit method tends to be used in low strain rate quasi-static analyses, whereas, the explicit method is more suited to high strain rate dynamic analyses. An explicit solution is more efficient than an implicit solution since no matrix inversion is required, however, the explicit solution is not unconditionally stable like the implicit solution so it requires a large number of small time steps, hence, making it unsuitable for lengthy quasi-static analyses. The efficiency of the explicit solution can be taken advantage of in short dynamic transient problems where the small time step size required for stability is not an issue.

The methods described above have for some time now been integrated into commercial FEA software packages such as ABAQUS™, ANSYS™, COMSOL™, LS-DYNA™, LUCAS™, MADYMO™, NASTRAN™, PAM-CRASH™ and RADIOSS™ to name but a few of the more popular packages. There are also numerous free / open source FEA software packages available.

The finite element modelling of polymer composite materials can broadly be divided into four sections; constitutive models, damage initiation modelling, damage evolution modelling and strain rate dependent modelling. The state of the art in the literature will be reviewed for each of these four sections which correspond to features of the stress strain curve in Figure 2-10. The constitutive model section details the response of the material which corresponds to the entirety of the stress strain curve. The

damage initiation modelling section details the initial failure of the material which corresponds to point B in the stress strain curve. The damage evolution section details the post elastic response of the material i.e. lines BC or BD depending on the type of degradation (sudden or gradual). The strain rate dependent modelling section details how the linear elastic region, initial failure point and damage evolution region can change with strain rate. Strain rate can change the gradient of line AB, the location of point B and the shape of the line BD.

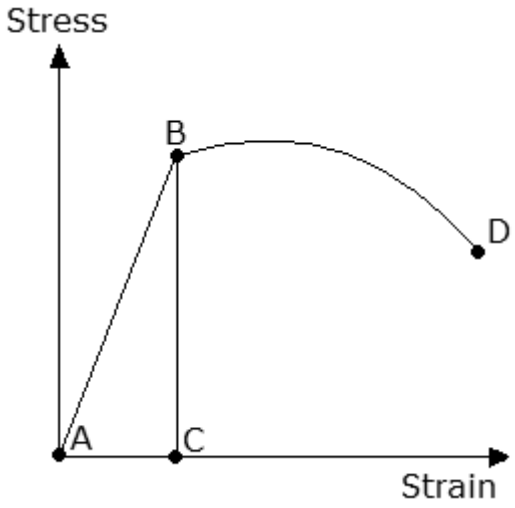

Figure 2-10. Features of a stress strain curve

2.4.3 Constitutive Models

Constitutive equations describe relationships between two physical quantities. In stress analysis, constitutive equations link the state of strain to the state of stress. For linear elastic materials the constitutive equation is commonly known as Hooke's Law seen mathematically in Equation 2-1, where σ is stress, E is stiffness and ε is strain. The relationship in Equation 2-1 is a one dimensional model. For three dimensional models matrix notation is used as in Equation 2-2 where σ is a 1x6 stress matrix, ε is a 1x6 strain matrix and C is a 6x6 stiffness matrix. The notation p and q denotes the row and column of the matrices respectively.

$$\sigma = E\varepsilon \qquad \textbf{2-1}$$

$$\sigma_p = C_{pq}\,\varepsilon_q \qquad \textbf{2-2}$$

Equation 2-2 can be expanded and written out as in Equation 2-3.

$$\begin{bmatrix}\sigma_{11}\\ \sigma_{22}\\ \sigma_{33}\\ \sigma_{23}\\ \sigma_{31}\\ \sigma_{12}\end{bmatrix} = \begin{bmatrix}C_{11} & C_{12} & C_{13} & C_{14} & C_{15} & C_{16}\\ C_{21} & C_{22} & C_{23} & C_{24} & C_{25} & C_{26}\\ C_{31} & C_{32} & C_{33} & C_{34} & C_{35} & C_{36}\\ C_{41} & C_{42} & C_{43} & C_{44} & C_{45} & C_{46}\\ C_{51} & C_{52} & C_{53} & C_{54} & C_{55} & C_{56}\\ C_{61} & C_{62} & C_{63} & C_{64} & C_{65} & C_{66}\end{bmatrix}\begin{bmatrix}\varepsilon_{11}\\ \varepsilon_{22}\\ \varepsilon_{33}\\ \varepsilon_{23}\\ \varepsilon_{31}\\ \varepsilon_{12}\end{bmatrix} \qquad \textbf{2-3}$$

It appears at first that for a three dimensional analysis there are 36 independent stiffness constants. However, this is not the case, as $C_{pq} = C_{qp}$ due to thermodynamic considerations relating to elastic strain energy [36]. This creates symmetry about the leading matrix diagonal leading to only 21 independent stiffness constants. This is the number of constants required for a completely anisotropic material. The number of independent stiffness constants is further reduced if the material exhibits a certain type of symmetry such as orthotropic (9 constants), transversely isotropic (5 constants) or isotropic (2 constants). This concept is clearly demonstrated in Figure 2-11. The matrix constituent in composite materials is often defined as an isotropic material; whereas, the fibrous constituent can be isotropic (glass fibres) or transversely isotropic (carbon fibres) i.e. carbon fibres are much stiffer in the longitudinal direction than the transverse direction. A single unidirectional lamina can be considered as an orthotropic material but is often treated as transversely isotropic.

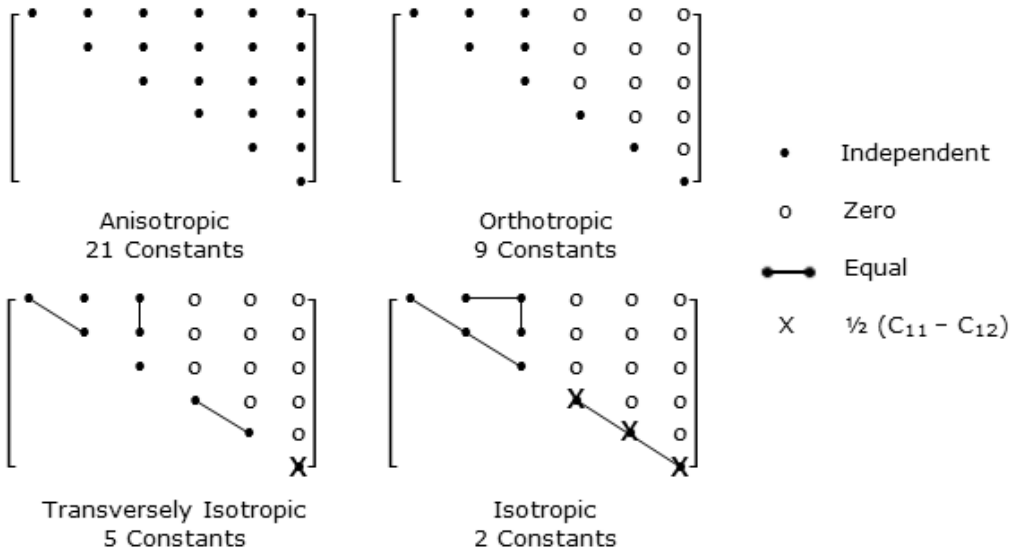

Figure 2-11. Examples of stiffness matrices of materials exhibiting different types of symmetry, reproduced from [36]

For further information on the constitutive models used to model the linear elastic response, and indeed the post elastic response, please consult the following literature documents [9, 36, 37].

2.4.4 Damage Initiation Modelling

The initiation of damage in finite element modelling is controlled by failure criteria. Failure criteria are mathematical equations that define the state of stress and strain at the point of damage initiation. Failure criteria can be divided into two groups; 'mode independent' and 'mode dependent' [37]. Mode independent failure criteria predict the occurrence of damage but do not identify the failure mode / type of damage, whereas, mode dependent failure criteria can do both as they usually consist of several equations with each one representing a particular type of failure mode. Failure criteria can be further categorised as 'non-interactive' and 'interactive' [37]. In non-interactive failure criteria the failure prediction in one loading mode is not affected by the failure in another loading mode, whereas, in interactive failure criteria the opposite is true due to the multiple components present in the mathematical equations. The most commonly used failure criteria are listed in Figure 2-12. For additional information on any of the failure criteria mentioned please consult the references given in the detailed review paper by Garnich and Akula [37].

Mode Independent	Mode Dependent
Maximum Stress Criterion	Hashin-Rotem Criterion
Maximum Strain Criterion	Hashin Criterion
Distortional Energy Criterion	Lee Criterion
Hill Criterion	Christensen Criterion
Tsai-Hill Criterion	Mayes and Hansen Criterion
Hoffman Criterion	
Chamis Criterion	
Tsai-Wu Criterion	
Sandhu Criterion	

Figure 2-12. Mode independent and mode dependent failure criteria

Zhao *et al* [38] analysed the progressive failure of NCF composite laminates using FEA. A representative volume element (RVE) of a 0°/90° balanced cross-ply laminate was loaded in in-plane tension. Combinations of different failure criteria were used for the tows and resin. The maximum

stress, Hoffman and Tsai-Wu failure criterion were considered for the tows, whereas, the maximum stress, von Mises and Drucker-Prager failure criterion were considered for the polymer resin. Full details of these failure criteria are given in the paper. The use of all these different failure criteria generated nine different tow/resin failure criteria combinations. The different combinations generated different load-strain curves and damage contours. The recommendations arising from the paper, following consideration of the load-strain curves and damage evolution patterns, were to use the maximum stress criterion for the tows and the maximum stress criterion or the Drucker Prager criterion for the polymer resin.

A comprehensive review of failure criteria for composite materials was performed by Orifici *et al* [39]. The authors have included the mathematical equations for the most common failure criteria for different constituents and loading modes.

2.4.5 Damage Evolution Modelling

Damage evolution occurs after damage initiation. The evolution of damage can be broadly classified into two categories; sudden degradation and gradual degradation. In sudden degradation, material properties are reduced instantaneously to a fraction of the original value. In gradual degradation, materials properties are functions of developing field variables. In Figure 2-10 line BC represents sudden degradation and line BD represents gradual degradation. For path BC the stiffness at point B has been instantaneously reduced to practically zero hence the sharp vertical drop off in stress. For path BD the stiffness has been gradually reduced starting at point B, the stiffness is a function of the strain developing field variable. Garnich and Akula [37] have extensively detailed the different sudden and gradual degradation models. Knight [40] also discusses the damage evolution strategies that provide material degradation after damage initiation. The author classified the different models into two broad categories, similar to Garnich and Akula [37], heuristic models based on ply discounting material degradation (sudden) and models based on continuum damage mechanics using internal state variables (gradual).

2.4.6 Strain Rate Dependent Modelling

As explained in 2.2.4, 'Strain Rate Dependence of Polymer Composite Materials', the material properties, such as stiffness and strength, of polymer composite materials can be strain rate dependent. The inclusion of this feature in modelling work has only recently been considered by researchers; hence, there is limited literature in the field and limited support for strain rate effects in commercially available finite element packages.

In the finite element package LS-DYNA there are eleven available composite materials models (MAT 22, 52, 55, 58, 59, 114, 116, 117, 118, 161 and 162). Schweizerhof *et al* [41] tested and critically reviewed some of these material models and the paper should be consulted for further information on the merits and limits of composite material models in LS-DYNA. Figure 2-13 gives an overview of these material models and indicates if the model contains failure criteria, the control of damage after failure and strain rate effects. Out of the eleven available composite models only three incorporate strain rate effects and, of these three, only two incorporate both damage effects and strain rate effects (MAT 161 and MAT 162). MAT 161 and 162 are progressive failure analysis models for composite materials which have incorporated Hashin failure criteria. The models can be used to simulate fibre failure, matrix damage and delamination. A damage mechanics approach, based on theory by Matzenmiller [42], is used which allows control of the softening behaviour after damage initiation. Strain rate dependence is available for stiffness and strength parameters. The issue with these models is that they are only available for solid elements, a version for shell elements has not yet been released, and an additional license from Materials Sciences Corporation is required as they developed and continue to support the models. Therefore, if one wants to simulate composite failure, damage and strain rate effects and your finite element software of choice is LS-DYNA and you are not prepared to spend a large amount of money for a MAT161/162 license or spend a large amount of time developing your own material model then you would have to compromise with simpler model such as MAT114 and miss out damage effects or MAT 54/55/58 and miss out strain rate effects.

	FAIL	DAM	SRATE
MAT 22	X		
MAT 54	X	X	
MAT 55	X	X	
MAT 58	X	X	
MAT 59	X		
MAT 114	X		X
MAT 116			
MAT 117			
MAT 118			
MAT 161	X	X	X
MAT 162	X	X	X

Figure 2-13. Summary of LS-DYNA composite material models where FAIL = failure criteria, DAM = damage effects and SRATE = strain rate effects

Abaqus has a rate dependent yield function that can be used when the yield strength depends on the rate of stain and when the anticipated strain rates are significant. This function can be used for the following material models: the isotropic hardening metal plasticity models (Mises and Johnson-Cook), the isotropic component of the nonlinear isotropic/kinematic plasticity models, the Drucker-Prager plasticity model and the crushable foam plasticity model. The rate dependent yield function is defined by providing tabular data, by defining overstress power law parameters or by providing yield stress ratios. The Abaqus documentation states that; 'Rate-dependent yield in dynamic analysis should be specified such that the yield stress increases with increasing strain rate' [43]. This is an obvious limitation to the built in rate dependent yield function as one would not be able to specify a decrease in yield stress with increasing strain rate.

Yen [44] presented a computational constitutive model to be utilised in the progressive failure of composites laminates under ballistic impacts. The model incorporated progressive failure as well as the strain rate dependence of the materials. The model was implemented in LS-DYNA as a regular material subroutine. The strain rate dependence of strength was controlled by multiplying the quasi-static values by a scale factor. This scale factor is unity plus strain rate constant multiplied by the natural log of the strain rate. Yen [44] went on to simulate the ballistic impact of S2-

Glass/Epoxy composite panels. The results indicated a good correlation between experimental and numerical ballistic fibre damage. It was concluded that the strain rate effect needs further investigation by experimentally characterising the strain rate dependence of various composite materials, for modelling input properties as well as modelling validation.

Zheng and Binienda [45] presented a rate-dependent shell element composite material model. The model was implemented in LS-DYNA as a user defined material. Rate dependence was incorporated in the elastic modulus of the matrix constituent through a logarithmic scaling law developed by Yen [44]. IM7/977-2 polymer composite materials were tested in longitudinal tension for three laminate arrangements (10°, 45° and 90°). The material was tested experimentally, by Goldberg et al [46], and computationally from low (1 /s) to high (400 /s) rates of strain. The numerical results in the form of a stress strain curves compared well with the experimental stress strain curves at the low strain rates. The experimental curves at the high strain rates often showed a larger initial stiffness than the numerical results. The researchers attributed this large initial stiffness to an artefact of the specimen geometry and the way the stress waves propagated through the specimen in the experimental testing. At the high strain rates some experimental curves flatten out and the numerical curves remain straight, Zheng and Binienda [45] explain that this could be due to early failure in the experimental specimens.

Daniel et al [47] conducted quasi-static, intermediate and high strain rate experimental testing on unidirectional carbon/epoxy composites. Off-axis specimens were tested to produce stress states combining transverse normal and in-plane shear stresses. The results showed that stiffness and strengths varied linearly with the logarithm of strain rate. The strength values obtained in experimental testing were then predicted with a range of classical failure criteria (maximum stress, Tsai-Hill, Tsai-Wu), partially interactive failure criteria (Hashin-Rotem and Sun) and the authors NU theory. The NU theory was primarily applicable to interfiber / interlaminar failure for transverse normal and in-plane shear stress states. The NU theory was expressed as three sub-criteria (compressive, shear and tensile dominated failure) presented in one common failure envelope with strain rate effects based on logarithmic scaling laws. With NU theory failure

envelopes compared well to experimental results at all strain rates and gave better predictions than all the other failure criteria. Figure 2-14 shows the experimental results and the NU theory predicted failure envelopes discussed above and demonstrates the importance of including strain rate effects in the failure prediction of composite materials, especially when simulating in the high strain rate regime.

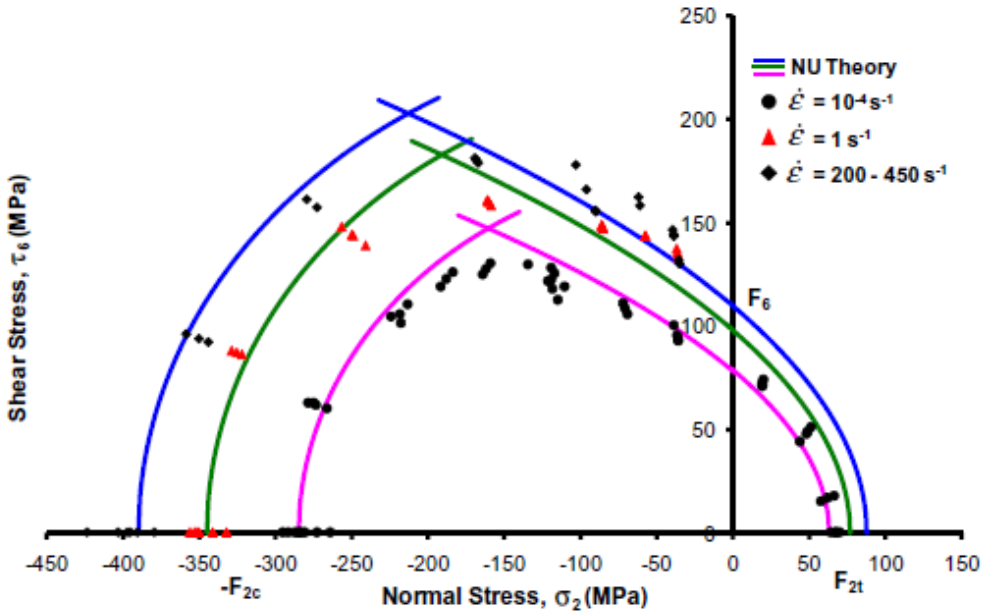

Figure 2-14. Comparison of experimental results and failure envelopes predicted by the NU theory for AS4/3501-6 carbon/epoxy composite at three strain rates by Daniel *et al* [47]

Meyer and Mayer [48] presented a strain rate dependent material and failure model for the static and dynamic material behaviour of fibre reinforced composites. A viscoelastic constitutive model and an improved version of the Failure Mode Concept of Cuntze [49] were implemented as a user defined material model in LS-DYNA. The improvement in Cuntze Failure Mode Concept was to incorporate strain rate dependent material strength behaviour. 0°/90° glass fibre reinforced composites were tested experimentally and numerically under different types of loading from 10^{-4} to 10^{3} /s. It was concluded that the new model developed by Meyer and Mayer allowed good prediction of strain rate dependent material behaviour and accurate prediction of the strain rate dependent onset of failure.

Heimbs *et al* [50] used LS-DYNA in conjunction with MAT 54 to simulate the crash behaviour of the nose cone of an F1 racing car front impact

structure. The sandwich structure was modelled using the layered shell element approach. A certain number of shell elements were defined through the thickness to represent the core and skin laminate layers. The core and skin were modelled as orthotropic linear elastic materials using MAT 54 which is based on the Chang/Chang failure criteria. In the skin the erosion of individual layers and total absorbed energy was controlled with MAT 54 failure strain parameters. The crash front algorithm of MAT 54 was also used in the skin to reduce the strength of elements close to failed elements to allow continuous crushing. In the core elastic-perfect plastic stress strain behaviour was modelled. The reason for detailing this literature document is that the researchers have clearly gone into a lot of detail in modelling the nose cone impact structure and yet have neglected to consider strain rate effects in an application that one would consider it to be of paramount importance.

2.4.7 Multi-Scale Modelling

This section gives examples from the literature of modelling at the micro, meso and macro scale; hence, details the multi-scale modelling approach.

A multi-scale finite element modelling approach with the aims of complementing and replacing experimental tests for material characterisation was described by Ernst *et al* [51]. Glass/epoxy composite materials were modelled at the micro (fibre and matrix), meso (tow architecture) and macro scale (homogeneous layer or textile layer) as seen in Figure 2-15.

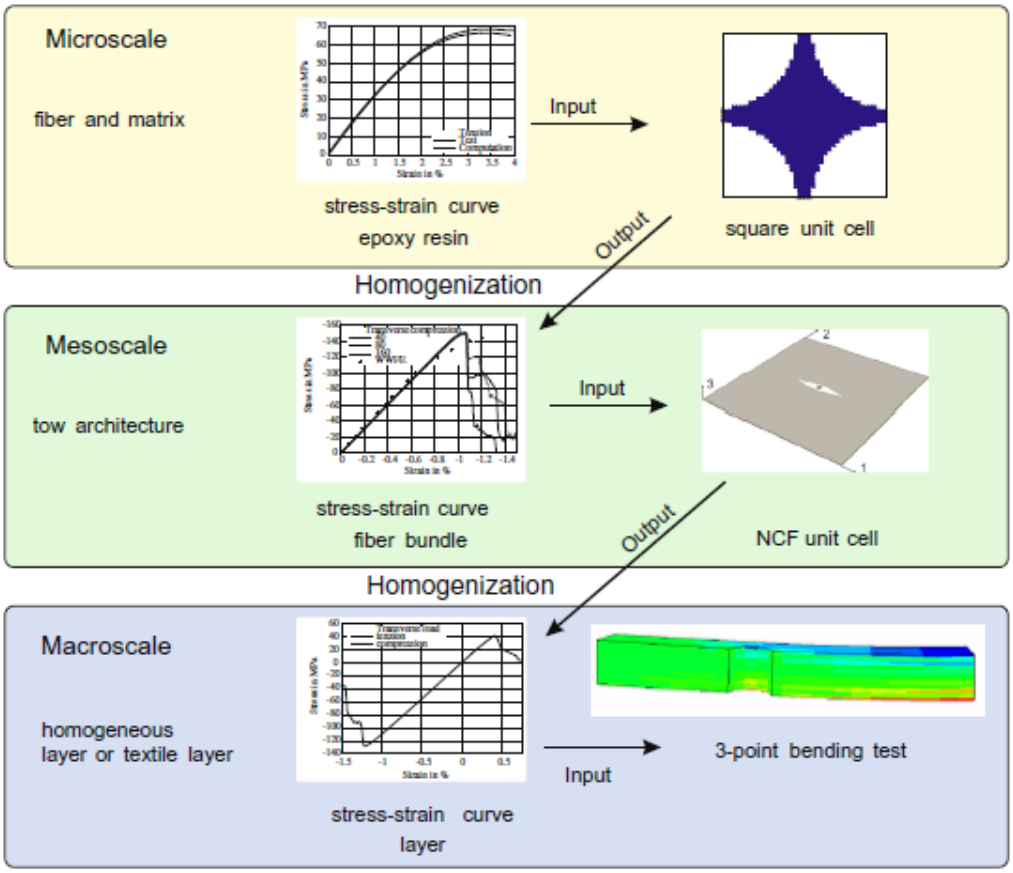

Figure 2-15. Multi-scale modelling approach conducted by Ernst *et al* [51]

The micro scale unit cell, square packing, was tested in tension and compression in the transverse direction and also in in-plane and transverse shear. Micro scale loading in the fibre direction was not considered in this study as it is stated in the paper that several rules of mixture approaches give good estimates for properties in this direction. The meso scale unit cell, NCF, was tested with normal loads in three directions and in three shear loadings. The macro scale validation test was a three point bend test of a thick NCF specimen. Simplified periodic boundary conditions were applied to both micro and meso scale unit cells as described by Sun and Vaidya [52]. The epoxy resin (micro and meso) was treated as an isotropic material, the fibres (micro) were modelled as linear elastic materials and the fibre bundles (meso) were modelled as transversely isotropic materials. The response of the epoxy resin was controlled with an elastic-plastic material model that took into account the pressure dependency of the material. A quadratic failure surface was used for the epoxy resin that was proposed by Fiedler *et al* [53] along with consideration of the material strength under pure shear. When the failure criterion was reached the stiffness of the epoxy resin was degraded by a damage evolution law

according to Lemaitre and Chaboche [54]. This involved using a scalar damage variable varying from zero to one which was subtracted from unity and multiplied by the effective stress. After damage was initiated the fracture energy proposal of Hillerborg *et al* [55]was used to reduce mesh-dependency by creating a stress-relative displacement response. The fibre bundles strength was predicted by the invariant-based quadratic criterion and the softening formulation presented by Vogler *et al* [56]. At the macro scale an orthotropic linear elastic material model up to failure was applied and failure was predicted with the criterion of Juhasz *et al* [57] which is based on the fracture hypothesis of Mohr. Damage evolution was controlled by Puck's formulation [58] where stiffness of damaged plies were degraded gradually with increasing load until ultimate failure of the laminate. The macro scale finite element results compared well with experimental results, especially in terms of the progressive failure. The final failure, however, was under predicted which was attributed to insufficient isotropic damage formulation. This paper clearly demonstrates the complexity of multi-scale modelling. With the addition of strain rate dependence, which this paper does not consider, the complexity is further increased.

Wang *et al* [59] presented micro scale yarn and meso scale woven composite finite element modelling to predict stiffness values of a 3D woven orthogonal interlock composite. A unit cell approach was taken where at both scales periodic boundary conditions were applied. At the micro scale the yarns were considered as unidirectional composites with fibres arranged in idealised hexagonal packing. The meso scale unit cell was constructed with weft and warp yarns in the desired architecture to form a 3D woven composite. The micro scale modelling predicted material constants for the yarns which were then used in the meso scale modelling to predict the material parameters of 3D woven composites. The FEA took place in NASTRAN and the stiffness predictions were in good agreement with available test data. The limitation of this paper is that it only considers the elastic response, it is however mentioned in future work that damage analysis is work that is currently being conducted.

Van Den Broucke *et al* [60] modelled the elastic and damage behaviour of NCF and UD braided composites. The Ladevèze continuum damage mechanics model for UD composites was utilised to predict damage at the

micro scale. The model distinguished between different loading modes and translated them into a deterioration scheme for the mechanical properties. These mechanical properties were used in the meso scale model which was generated using the WiseTex suite [61]. The elements in the yarns, generated using FETex (the finite element analysis section of the WiseTex suite), were assigned properties based on their location in the structure as fibre orientation and volume fraction can vary within the yarn. The meso scale RVE was tested in six loading conditions with periodic boundary conditions to obtain homogenised material properties. The predicted elastic and damage properties for all selected validation materials showed good agreement with experimental values apart from in bi-axial samples which was attributed to geometrical non-linearities not considered in the simulations. In-plane properties of quadri-axial samples could not be calculated due to simulation convergence problems. This paper further demonstrates the complexity involved in multi-scale modelling, to such an extent that special software packages, such as the WiseTex suite, are often used to ease geometry generation at each of the scales of analysis.

Okereke *et al* [62] presented a virtual testing procedure for the numerical homogenisation of elastic and damage behaviour of bi-directional composites. Analysis took place at the micro scale (individual fibres and matrix), meso scale I (matrix pockets and yarns of different orientation), meso scale II (unidirectional reinforced plies of single orientation) and macro scale (global structure of composite). Initial results gave reliable predictions of the elastic properties, damage initiation and damage evolution at the macro scale. This paper further demonstrates that multi-scale modelling can be a reliable route for establishing composite properties, in both the elastic and damage regions.

Zhang *et al* [63] conduced hierarchical multi-scale modelling of fibre reinforced composites. Information was transferred between the micro, meso and macro scale. At the micro scale a 3D column model was used to calculate the residual stresses, due to the difference in thermal expansion during manufacture, which were fed into the meso scale model as interfacial frictional stresses. At the meso scale five fibres were modelled with one centrally fractured fibre for stress transfer distribution analysis with a shear-lag model. Meso scale analysis also took into account the plasticity of the matrix. Macro scale modelling consisted of Monte Carlo

simulations on a regular square bundle array of fibres. The residual stress and stress transfer information was integrated into the macro scale progressive damage model through average stress concentration factors. The macro scale modelling was able to predict the stress strain behaviour of the composite material which compared well to experimental testing. This paper demonstrates that multi-scale modelling can be tailored to a particular area of interest i.e. in this paper the micro scale focused on residual stresses due to differences in thermal expansion.

Foreman *et al* [64] conducted multi-scale modelling at the molecular scale, using group interaction modelling (GIM), and at the micro scale, using FEA. GIM is used to predict the strain rate dependent stress-strain behaviour through yield of an amine cured epoxy resin matrix. This data is then used in FEA modelling of a unidirectional carbon/epoxy composites to determine strain concentration factors of fibres adjacent to a fibre break. Although this paper only bridges two scales of analysis, one of them, which is outside of the scope of this thesis, it is of interest due to the strain rate dependence included which appears in very few literature papers.

Grujicic *et al* [65] formulated and implemented, as a material subroutine suitable for commercial finite element packages, a multi-scale unit cell continuum damage material model for 0°/90° cross-ply unidirectional composites. The authors explained how the idea behind the modelling was to simulate the mechanical response of the meso scale unit cell and homogenise this into an equivalent response of a continuum material for use in macro scale modelling. The type of multi-scale modelling in this paper differs from those previously described as the process is a coupled meso scale / continuum level model. The researchers detailed how the coupling between the continuum material formulation and the unit-cell geometry and mechanical response was done in the following way:

"(a) the deformation state of a continuum material point (as quantified by the corresponding deformation gradient) is used to update the unit-cell geometry; (b) the updated unit-cell geometry and the state of the continuum material at the end of the previous time increment are used to update the extent of structural damage in the unit cell; and (c) the updated material state obtained in point (b) is then used to compute the stress state at the end of the current time increment."

This type of multi-scale modelling can be classed as a seamless integration of the scales rather than hierarchical multi-scale modelling. The Ultra High Molecular Weight Poly-Ethylene (UHMWPE) meso scale yarns were modelled as orthotropic linear elastic materials up to the point of failure, under axial tension or transverse shear. The polymer matrix was modelled as a linear isotropic material. The paper has paid a lot of attention to interfacial bonding failure between the yarns and the matrix. An extensive amount of time was taken to perform atomic simulations to gain information of interfacial bonding / de-bonding behaviour; this information was then subsequently used in the meso scale simulations. It was pointed out in the paper that reviewers of the work indicated that the response of composite materials is strain rate dependent. The authors' response to this was that the material model was intended to be used only in the high rate loading regime where the constituent materials tend to behave as linear elastic materials with weak rate dependency. This is a very broad statement and only holds for certain types of composite materials. For example, looking at Figure 2-7, the rate dependency of epoxy resin is prevalent across the full range of strain rates. Macro scale finite element validation testing was conducted through ballistic impacts on composite laminates. The results obtained were comparable with experimental testing reported in [66].

Lua *et al* [67] produced a hybrid damage model by combining discrete and continuum damage models. The continuum damage model degraded the stiffness of the woven E-glass / vinyl-ester composite based on stress strain behaviour and failure criteria. The discrete damage model captured delamination with a cohesive interface model. This hybrid model was implemented in LS-DYNA via a user defined material model and was used to perform multi-scale modelling at the constituent, ply and laminated composite scale. The scales were seamlessly integrated together through multilevel homogenisation and decomposition. The response at the meso scale (e.g. plain weave unit cell) was decomposed to give the response at the micro scale (e.g. sub cell of plain weave unit cell). This micro scale response was then used in a micromechanics model to enable progressive damage analysis using modified Hashin failure criteria and damage evolution theory based on work by Matzenmiller [42]. The homogenised damaged material properties at the meso scale were then based on the

damaged material properties at the micro scale. Macro scale laminate properties were calculated from individual ply properties and it was at this scale that the cohesive interface model for delamination and propagation was utilised. The authors simulated the dynamic shock loading of a circular laminated composite plate, the low velocity impact of the bottom base plate of a composite hat stiffener and the drop weight impact of a composite sandwich beam. This multi-scale modelling paper, along with others presented in this section, does not consider strain rate dependence. It is, therefore, surprising that numerical results correlate well with experimental data when the three events simulated (dynamic shock, low velocity impact and drop weight impact) are not in the quasi-static strain rate range. It has also been shown by other researchers that the effect of strain rate on the stress strain response of E-glass / vinyl ester composites, used in this work by Lua *et al* [67], can be significant [68].

Fujita *et al* [69] studied the transverse strength of unidirectional composites by performing 2D FE modelling of randomly dispersed fibres in a resin matrix, where interfacial elements connected fibres and resin. Damage was defined using Hoffman's criterion and Mises criterion for interfacial and resin regions respectively. Transverse tension simulations based on damage mechanics were conducted for 20 random fibre dispersions at 40% and 60% volume fraction. The results showed that an increase in volume fraction lead to a lower transverse tensile strength. This was due to the small distances between damaged interfaces at high volume fractions; hence, a lower amount of stress was required to bridge these gaps. A comparison was made between the transverse tensile stress strain response of an idealised hexagonally packed unit cell and a random model. In the idealised unit cell the interfacial elements all damaged at the same time which corresponded to a large drop in stress in the stress strain curve followed by a gradual increase in stress as the resin damaged. In the random model the stress grew gradually after initial interfacial damage of some fibre/resin interfaces. The future work stated in the paper explained how the authors would like to utilise the results from their work in a multi-scale analysis; continuing to the meso and macro scale. This would allow an estimation of strength at the larger scales using fibre bundle properties based on randomly dispersed fibre distributions at the micro scale. This paper has been included to show the exciting areas that multi-scale modelling is branching into and how the multi-scale approach

can be used to establish many different properties such as statistical strength distributions of composite laminates based on randomly dispersed fibres at the micro scale.

2.5 Conclusions

This chapter presented an overview of composite materials which focused on the types of materials under consideration in this study. The techniques for low, intermediate and high strain rate experimental characterisation of composite materials were detailed followed by the techniques for computational characterisation of composite materials through multi-scale finite element modelling.

It has been shown that the interest in simulating composite materials under high strain rate loading is intensifying due to the requirement of lightweight military vehicle armour, which is subjected to blast and ballistic events. Simulations may never fully replace experimental testing but it has been demonstrated that it has the opportunity to reduce the amount of experimental testing required, resulting in significant time and cost savings.

The review of composite materials showed that they consist of multiple constituents with different structures at different scales. This has led many researchers considering a multi-scale analysis to capture the detail of the materials' response at the micro, meso and macro scale. A purely elastic analysis at these multiple scales has been shown to be extremely involved and complex by multiple researchers. The addition of damage initiation has been considered by some but few have taken on the task of simulating how the damage evolves after initial failure. There is also a very apparent gap in the literature that few people consider the strain rate dependence of composite materials, especially in a multi-scale analysis, even in applications where one would consider it of paramount importance. These observations of the literature are backed up in concluding remarks in work by Aminjikarai and Tabiei [70]:

"Though numerous micro-mechanical models have been developed in the past for modelling the behavior of unidirectional polymer matrix composites, there are very few that consider their progressive post-failure and even fewer that account for their strain-rate dependent behaviour."

It is clear that there is a need for a multi-scale modelling methodology which can predict macro scale component behaviour with knowledge of micro and meso constituent behaviour and material structure. The methodology should allow prediction of not only elastic behaviour but also damage behaviour, initiation and evolution, and strain rate dependent behaviour.

3 Modelling Methodology

3.1 Introduction

The multi-scale modelling approach adopted in this thesis is depicted in Figure 3-1 where FEA at the micro scale provides input properties for the meso scale and FEA at the meso scale provides input properties for the macro scale.

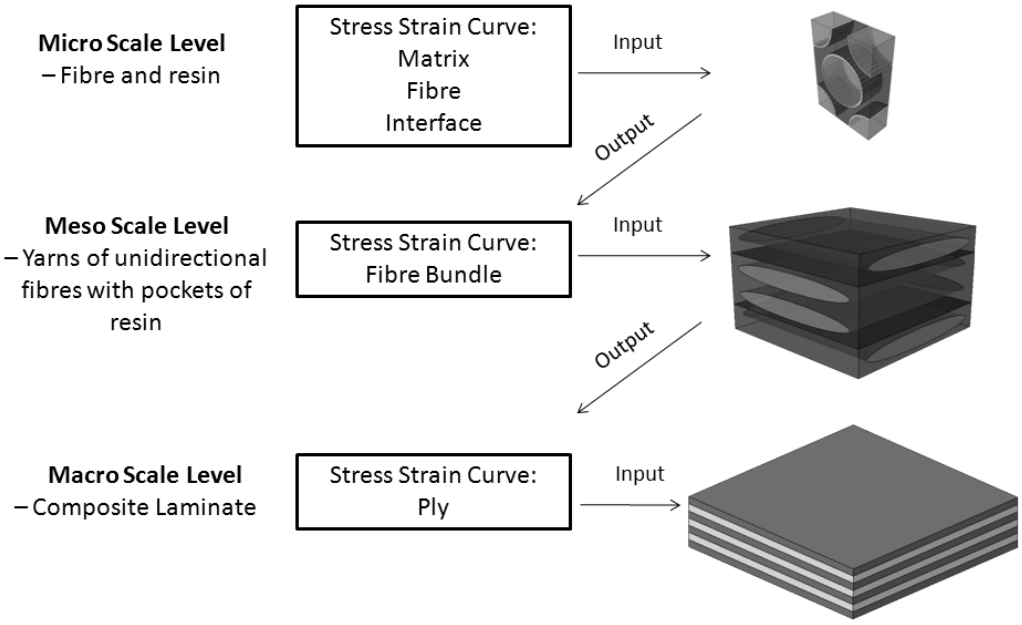

Figure 3-1. Multi-scale modelling approach

3.2 Unit Cell Definitions and Generation

Python scripting has been utilised to automate the geometry generation of the micro and meso scale unit cells shown in Figure 3-2. The micro scale geometry consists of fibres surrounded by an interface all embedded in a matrix material. The meso scale geometry consists of yarns arranged in a balanced, about the mid-plane, 0°/90° NCF fabric architecture all embedded in a matrix material.

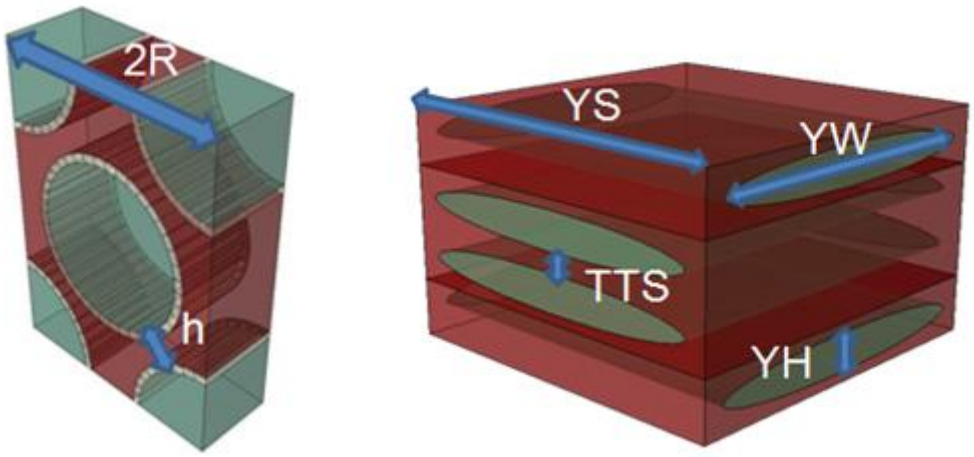

Figure 3-2. Micro and meso scale unit cell geometries. Micro parameters: 2R – closest centre to centre spacing of fibres, h – separation of the fibres. Meso parameters: YH – yarn height, YW – yarn width, YS – yarn spacing, TTS – through thickness spacing.

3.2.1 Micro Scale Unit Cell

Fibre Packing

The micro scale unit cell geometry, seen in Figure 3-2, is generated based on the fibre radius (r) and fibre volume fraction (f). Assumptions are made that all fibres are aligned parallel to one another and that they are arranged in an idealised hexagonal packing arrangement. The closest centre to centre spacing of the fibres (2R) is then calculated from Equation 3-1 and the separation of the fibres (h) from Equation 3-2. These equations are taken from Hull and Clyne [9].

$$R = \frac{r}{\sqrt{(2\sqrt{3}\,f)/\pi}} \qquad \textbf{3-1}$$

$$h = 2r\left[\left(\frac{\pi}{2f\sqrt{3}}\right)^{1/2} - 1\right] \qquad \textbf{3-2}$$

The idealised hexagonal packing was chosen over square packing due to the higher maximum volume fraction that can be obtained. Hexagonal packing has a theoretical maximum of 90.7%, whereas, for square packing it is 78.5%. The hexagonal packing also appeared to better represent reality from the micrographs taken on the materials under consideration in this project. High volume fraction randomly packed representative unit

cells (RUC) were considered to be outside the scope of this project due to the large amount of simulations already involved in testing at multiple scales and at multiple strain rates. The use of randomly packed unit cells would involve even more testing due to the statistical nature of RUC analysis.

The size of the hexagonal unit cell could be reduced by using symmetry e.g. vertical and horizontal symmetry for a quarter size unit cell. This would give the advantage of reduced simulation times due to a reduced number of elements. However, the unit cell has been kept as shown in Figure 3-2 to enable easier application of periodic boundary conditions based only on translational symmetry. Another way to reduce simulation time by reducing the number of elements would be to reduce the thickness of the unit cell in the longitudinal direction. The thickness was arbitrarily set as the same as the radius of the fibre. Depending on the type of loading it could even be possible to perform some 2D analyses; this would significantly reduce the simulation time. However, this would require more time spent on producing material models that work in both 2D and 3D.

Interfacial Layer

There is an interfacial layer around all fibres in the micro unit cell. Half of the interfacial volume takes up matrix volume and the other half of the interfacial volume takes up fibre volume. This obviously reduces the maximum possible fibre volume fraction; however, the interfacial layer is thin at one tenth of the fibre radius. Mishnaevsky and Brøndsted [71] also considered interface de-bonding as a 3D process rather than a 2D process involving the opening of two contacting plane surfaces. The thought behind this was that fibres can be rough and the interface regions in many composites contain interphases. Both of these factors influence the interface de-bonding process and they do not occur in a 2D space, rather in a 3D thin layer somewhere between the fibre and matrix. This point of view was also taken by Tursun *et al* [72] who conducted damage modelling on particle reinforced composites.

Fibre Diameter Measurements

Cross sectional micrographs through the thickness of laminates were taken so multiple fibres within a yarn could be viewed and analysed. Three micrographs were taken and 25 fibre diameters were measured in each

micrograph using a piece of image processing and analysis software, coded in Java, known as ImageJ [73]. The average of the 75 fibre diameters was taken to be the fibre diameter in the modelling work. This was performed for both S2 glass and carbon fibres.

Fibre Volume Fraction Measurements

Micro scale volume fractions were obtained from multiple high magnification cross sectional micrographs of fibre bundles and an automated image analysis procedure developed at The University of Nottingham [74]. The method involved identifying firstly, a point within the fibres cross sectional area as in Figure 3-3 (a), and, secondly, a window that was sufficiently large enough to capture the whole filament centred on this location. In this window, local colour gradients were calculated as in Figure 3-3 (b). As the light varied across the micrograph an absolute threshold value could not be used to identify pixels that were positioned on the fibre boundary. A relative threshold value was used which identified a boundary pixel in-between a fibre and matrix pixel. It was possible that the window used to capture the whole fibre could contain parts of other fibres; therefore, boundary pixels on other fibres would be identified. To identify the boundary pixels for only the current fibre of interest the centre point of the fibre was used and those boundary pixels at a defined radius away were identified. The fibre boundary was constructed by fitting an ellipse that passed through these boundary pixels. Radius and position were determined for each individual fibre in the yarn, Figure 3-3 (c). All this information was used to create the black and white image shown in Figure 3-3 (d). This process was repeated for all the high magnification cross sectional micrographs taken.

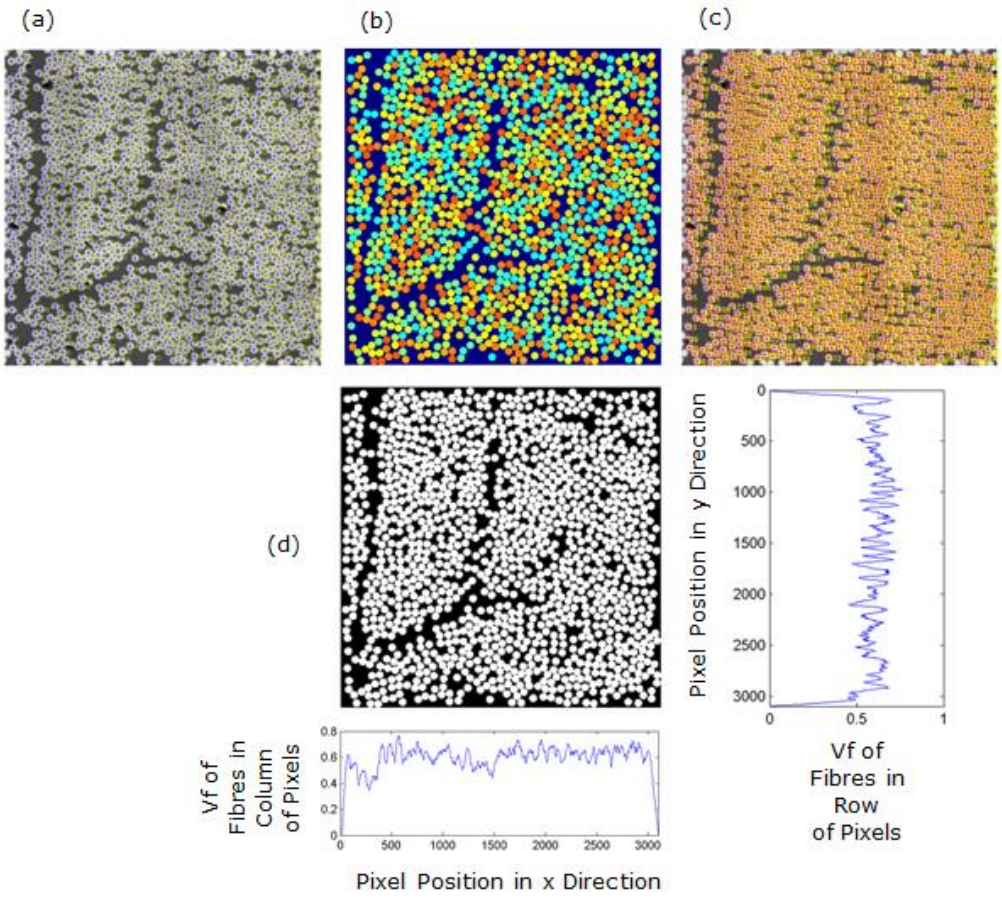

Figure 3-3. Fibre volume fraction analysis for a section of a carbon/epoxy yarn. (a)Identification of fibre location, (b) Colour map for overlap check, (c) Fibre centre and boundary identification and (d) Black and white image showing volume fraction on a pixel line by pixel line basis horizontally and vertically. Vf = Volume Fraction.

The black and white images, an example is Figure 3-3 (d), are then all assembled together to create one large image of the entire yarn demonstrated in Figure 3-4. The location of the example black and white image, Figure 3-3 (d), in the yarn cross section is indicated in Figure 3-4 in the bottom right of the figure. The fibre volume fraction within the yarn boundary is then calculated by segmenting the assembled image into a finite number of vertical slices. The yarn boundary is determined in such a way that an envelope is determined around the detected fibre cross sections, Figure 3-4. The number of pixels in the vertical slices between the top and bottom of the yarn boundary belonging to a fibre are counted. Any pixels not counted are assumed to be matrix or void regions. The volume fraction within the yarn boundary can then be calculated as the number of fibre pixels divided by the number of non-fibre pixels. Performing this on a slice by slice basis also allows extra information on how the volume fraction varies across the yarn.

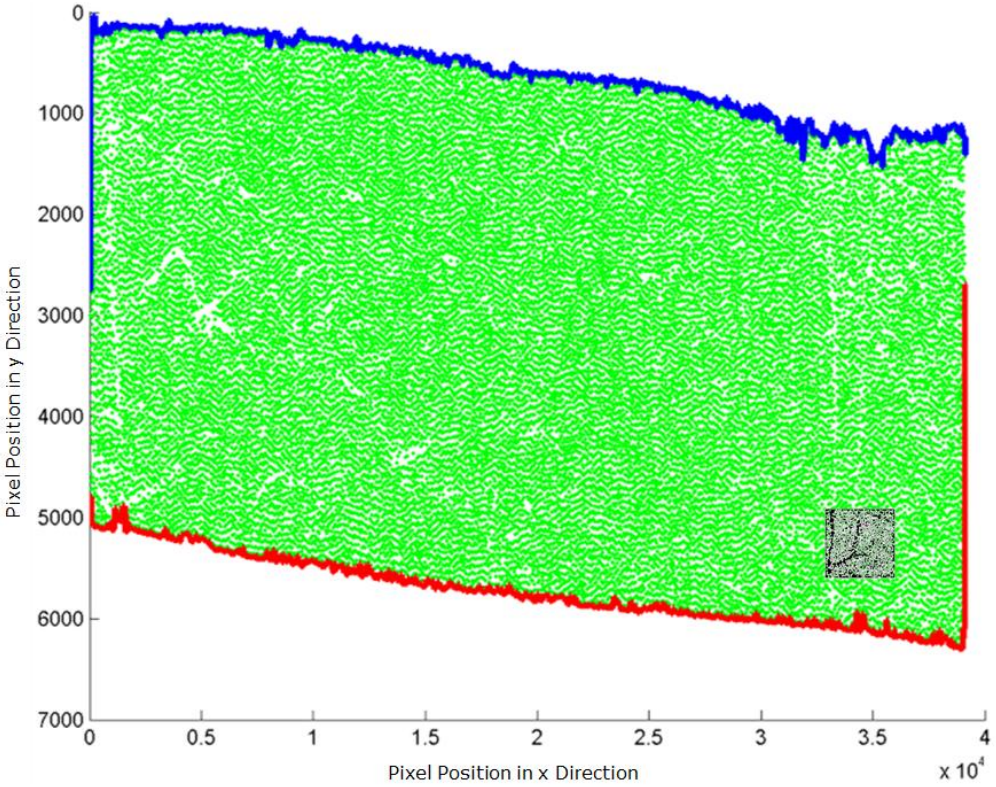

Figure 3-4. Carbon/epoxy yarn cross section showing fibres in green, the top boundary in blue and the bottom boundary in red.

3.2.2 Meso Scale Unit Cell

The meso scale unit cell consists of four unidirectional yarns / fibre bundles embedded in a matrix material. The yarns are arranged in a balanced, about the mid-plane, 0°/90° NCF fabric architecture as seen in Figure 3-2.

The reason for modelling a balanced about the mid-plane NCF rather than an unbalanced NCF is due to the shear deformation that occurs in an unbalanced layup when subjected to a uniaxial displacement as seen in Figure 3-5.

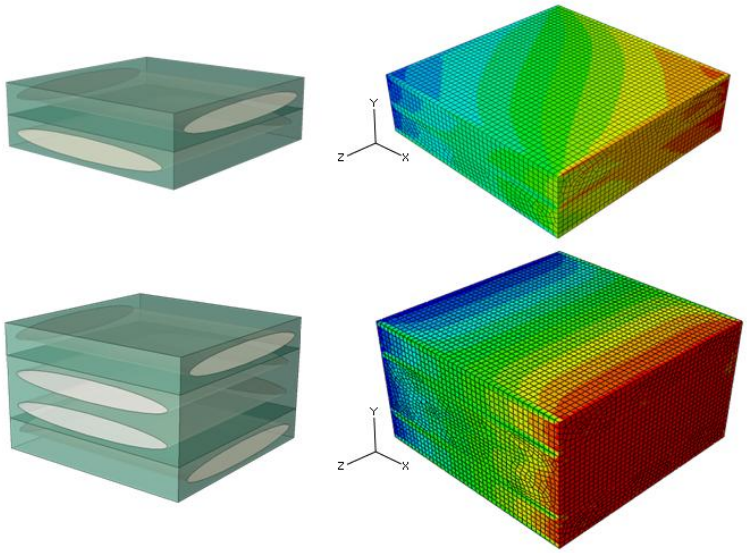

Figure 3-5. Unbalanced NCF (TOP) and balanced NCF (BOTTOM) subjected to in-plane tension in the x direction. Contours show displacement in the x direction where red indicates a large positive displacement and blue indicates a large negative displacement

The yarn width and yarn height are taken as an average of multiple measurements on micrographs of S2 glass and carbon laminates. In the analysis 24 carbon yarns and 13 S2 glass yarns were measured. The yarn spacing and through thickness spacing in the model are adjusted by a proportional amount to give the desired meso scale volume fraction.

The two yarns not aligned along the z direction have local material axes assigned. The material axes are set so the z direction is parallel to the yarn direction. This is important for the application of material properties, as longitudinal and transverse yarn properties can be different, and the correct functioning of the yarn user defined material model detailed in 3.4.4.

3.3 Boundary Conditions

Periodic boundary conditions have been applied to both micro and meso scale unit cells. These boundary conditions imply that each unit cell has the same deformation mode and there is no separation or overlap between adjacent unit cells. Figure 3-6 shows a single unit cell that has periodic boundary conditions and has been subjected to shear loading. If the unit cell is repeated horizontally and vertically it is clearly seen there is no separation or overlap between adjacent unit cells. If one now considers damage within a unit cell with periodic boundary conditions the implication

is that the damage is also periodic i.e. every unit cell has the same amount of damage, location of damage etc. In reality damage will most likely occur at various locations due to stress concentrations and the damage progression will be different for different locations of initial damage.

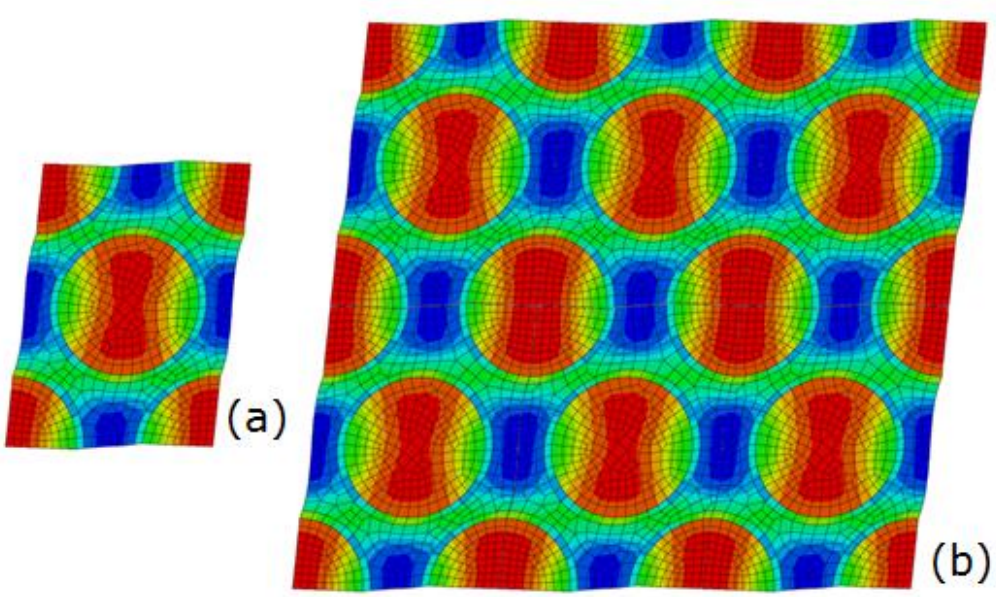

Figure 3-6. (a) Single unit cell with periodic boundary conditions in transverse shear loading and (b) six copies of the single unit cell in (a). Contours show von Mises stress where red is high stress and blue is low stress.

Boundary conditions have been derived and applied to unit cells based on translational symmetry following the method described in a paper by Li and Wongsto [75]. The derivation of these boundary conditions will now be detailed with reference to Figure 3-7. Although the unit cells in Figure 3-7 are micro scale unit cells the derivation and application of the boundary conditions applies in the same way to the meso scale unit cell.

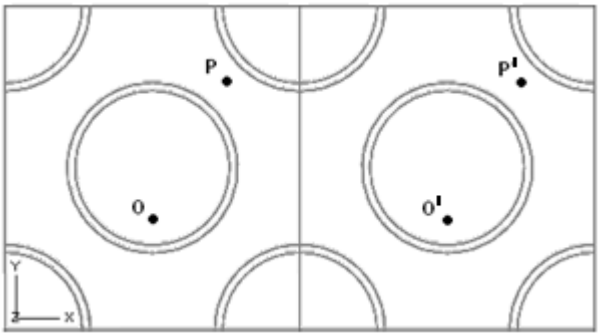

Figure 3-7. Periodic unit cells where point P'/ O' is the image point P/O in another unit cell.

The displacement of point P′ minus the displacement of point O′ in any one direction is equal to the displacement of P minus the displacement of O; Equation 3-3. The equations can be rearranged to show that the displacement of point P′ minus the displacement of point P is equal to the displacement of point O′ minus the displacement of point O; Equation 3-4. The terms u, v, w are displacements in the x, y and z direction respectively.

$$\begin{aligned} u_{p'} - u_{o'} &= u_p - u_o \\ v_{p'} - v_{o'} &= v_p - v_o \\ w_{p'} - w_{o'} &= w_p - w_o \end{aligned} \qquad \textbf{3-3}$$

$$\begin{aligned} u_{p'} - u_p &= u_{o'} - u_o \\ v_{p'} - v_p &= v_{o'} - v_o \\ w_{p'} - w_p &= w_{o'} - w_o \end{aligned} \qquad \textbf{3-4}$$

Equation 3-5 shows the relationship between the macroscopic strains ε_x, ε_y, ε_z, ε_{yz}, ε_{xz}, ε_{xy} and the relative displacements between a point P in the unit cell and a point P′ in another cell where x, y and z are coordinates of P and x′, y′ and z′ are coordinates of P′. One can now consider point P and P′ to exist anywhere in their unit cells as long as point P′ is an image of point P, hence the replacement of P and P′ with coordinates.

$$\begin{aligned} u'-u &= (x'-x)\varepsilon_x + (y'-y)\varepsilon_{xy} + (z'-z)\varepsilon_{xz} \\ v'-v &= (y'-y)\varepsilon_y + (z'-z)\varepsilon_{yz} \\ w'-w &= (z'-z)\varepsilon_z \end{aligned} \qquad \textbf{3-5}$$

Equation 3-5 can be written in terms of translational symmetry transformations A,B and C where i, j and k represent the number of unit cell periods in the x, y and z directions respectively. The width, height and depth of the unit cell are defined by 2a, 2b and 2c respectively.

$$(x'-x) = A(i, j, k) = 2ai$$
$$(y'-y) = B(i, j, k) = 2bj \qquad \textbf{3-6}$$
$$(z'-z) = C(i, j, k) = 2ck$$

$$u'-u = 2ai\varepsilon_x + 2bj\varepsilon_{xy} + 2ck\varepsilon_{xz}$$
$$v'-v = 2bj\varepsilon_y + 2ck\varepsilon_{yz} \qquad \textbf{3-7}$$
$$w'-w = 2ck\varepsilon_z$$

One can now use Equation 3-7 to derive the boundary conditions for the six faces, twelve edges and eight corners of the unit cell, defined in Figure 3-8, by substituting in values for i, j and k. The boundary conditions for the faces, edges and corners are given in Figure 3-9.

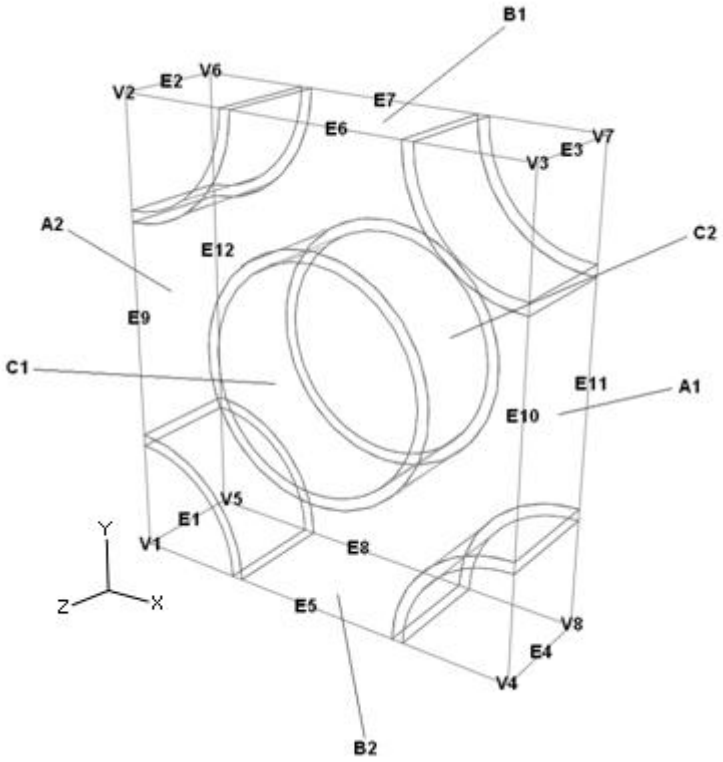

Figure 3-8. Definition of face, edge and corner labels for a micro unit cell

Faces	Edges 1–4	Edges 5–8	Edges 9–12
$i=1,\ j=0,\ k=0$	$i=0,\ j=1,\ k=0$	$i=0,\ j=1,\ k=0$	$i=1,\ j=0,\ k=0$
$u_{A2}-u_{A1}=2a\varepsilon_x$	$u_{E2}-u_{E1}=2b\varepsilon_{xy}$	$u_{E6}-u_{E5}=2b\varepsilon_{xy}$	$u_{E10}-u_{E9}=2a\varepsilon_x$
$v_{A2}-v_{A1}=0$	$v_{E2}-v_{E1}=2b\varepsilon_y$	$v_{E6}-v_{E5}=2b\varepsilon_y$	$v_{E10}-v_{E9}=0$
$w_{A2}-w_{A1}=0$	$w_{E2}-w_{E1}=0$	$w_{E6}-w_{E5}=0$	$w_{E10}-w_{E9}=0$
$i=0,\ j=1,\ k=0$	$i=1,\ j=1,\ k=0$	$i=0,\ j=1,\ k=1$	$i=1,\ j=0,\ k=1$
$u_{B2}-u_{B1}=2b\varepsilon_{xy}$	$u_{E3}-u_{E1}=2a\varepsilon_x+2b\varepsilon_{xy}$	$u_{E7}-u_{E5}=2b\varepsilon_{xy}+2c\varepsilon_{xz}$	$u_{E11}-u_{E9}=2a\varepsilon_x+2c\varepsilon_{xz}$
$v_{B2}-v_{B1}=2b\varepsilon_y$	$v_{E3}-v_{E1}=2b\varepsilon_y$	$v_{E7}-v_{E5}=2b\varepsilon_y+2c\varepsilon_{yz}$	$v_{E11}-v_{E9}=2c\varepsilon_{yz}$
$w_{B2}-w_{B1}=0$	$w_{E3}-w_{E1}=0$	$w_{E7}-w_{E5}=2c\varepsilon_z$	$w_{E11}-w_{E9}=2c\varepsilon_z$
$i=0,\ j=0,\ k=1$	$i=1,\ j=0,\ k=0$	$i=0,\ j=0,\ k=1$	$i=0,\ j=0,\ k=1$
$u_{C2}-u_{C1}=2c\varepsilon_{xz}$	$u_{E4}-u_{E1}=2a\varepsilon_x$	$u_{E8}-u_{E5}=2c\varepsilon_{xz}$	$u_{E12}-u_{E9}=2c\varepsilon_{xz}$
$v_{C2}-v_{C1}=2c\varepsilon_{yz}$	$v_{E4}-v_{E1}=0$	$v_{E8}-v_{E5}=2c\varepsilon_{yz}$	$v_{E12}-v_{E9}=2c\varepsilon_{yz}$
$w_{C2}-w_{C1}=2c\varepsilon_z$	$w_{E4}-w_{E1}=0$	$w_{E8}-w_{E5}=2c\varepsilon_z$	$w_{E12}-w_{E9}=2c\varepsilon_z$
Corners			
$i=0,\ j=1$ and $k=0$	$i=0,\ j=1$ and $k=1$		
$u_{V2}-u_{V1}=2b\varepsilon_{xy}$	$u_{V6}-u_{V1}=2b\varepsilon_{xy}+2c\varepsilon_{xz}$		
$v_{V2}-v_{V1}=2b\varepsilon_y$	$v_{V6}-v_{V1}=2b\varepsilon_y+2c\varepsilon_{yz}$		
$w_{V2}-w_{V1}=0$	$w_{V6}-w_{V1}=2c\varepsilon_z$		
$i=1,\ j=1$ and $k=0$	$i=1,\ j=1$ and $k=1$		
$u_{V3}-u_{V1}=2a\varepsilon_x+2b\varepsilon_{xy}$	$u_{V7}-u_{V1}=2a\varepsilon_x+2b\varepsilon_{xy}+2c\varepsilon_{xz}$		
$v_{V3}-v_{V1}=2b\varepsilon_y$	$v_{V7}-v_{V1}=2b\varepsilon_y+2c\varepsilon_{yz}$		
$w_{V3}-w_{V1}=0$	$w_{V7}-w_{V1}=2c\varepsilon_z$		
$i=1,\ j=0$ and $k=0$	$i=1,\ j=0$ and $k=1$		
$u_{V4}-u_{V1}=2a\varepsilon_x$	$u_{V8}-u_{V1}=2a\varepsilon_x+2c\varepsilon_{xz}$		
$v_{V4}-v_{V1}=0$	$v_{V8}-v_{V1}=2c\varepsilon_{yz}$		
$w_{V4}-w_{V1}=0$	$w_{V8}-w_{V1}=2c\varepsilon_z$		
$i=0,\ j=0$ and $k=1$			
$u_{V5}-u_{V1}=2c\varepsilon_{xz}$			
$v_{V5}-v_{V1}=2c\varepsilon_{yz}$			
$w_{V5}-w_{V1}=2c\varepsilon_z$			

Figure 3-9. Equations for boundary conditions at faces, edges and corners of the unit cell [76]

Python scripting has again been utilised here, with the knowledge of the size of the unit cell, to identify the node labels and nodal coordinates of the nodes on the faces, edges and corners of the unit cell. The nodes are then sorted according to their nodal coordinates in the x, y and then z direction so that the node labels for a particular face/edge/corner will now be listed in a node set systematically. Linear constraint equations can now be used to link a node on one face/edge/corner of the unit cell to the corresponding node on the other face/edge/corner. As meshes on opposite faces have been made identical this will create a linear constraint equation on nodes on A1 and A2 with the same y and z coordinates, B1 and B2 with the same x and z coordinates and C1 and C2 with the same x and y coordinates.

Dummy nodes are generated in Abaqus to represent the macroscopic strains in the linear constraint equations. By applying a displacement to these dummy nodes, which are linked to faces, edges and corners of the unit cell through the linear constraint equations; one can apply a direct strain to the unit cell. The applied strain is ramped over the entire simulation time to give a constant strain rate test, except in high rate meso scale loading due to the numerical instability discussed in section 5.3.3. Although the unit cell is subjected to a constant strain rate the individual

elements at various locations throughout the unit cell may be subjected to a strain rate differing from the desired unit cell strain rate. The average of the strain rate for all the elements, however, compares well to the desired unit cell strain rate.

It is important to note here that this work is capturing strain rate effects and is not a study of the stress wave propagation within the unit cells. The movement of stress waves, generated by impact loading, through composite materials is complex due to the materials underlying micro and meso structure. The stress waves do not propagate uniformly due to the orientation of fibres and different material properties in different directions, unlike isotropic materials where the material properties are the same in all directions. The area of stress wave propagation is considered outside the scope of this thesis.

Only one set of boundary conditions is needed for all loading conditions such as tension, compression and shear. To put the cell under different loading, a boundary displacement is applied to a different macroscopic strain dummy node. The stress is obtained by dividing the reaction force at the dummy node by the volume of the unit cell and the strain is obtained from the displacement at the dummy node.

3.4 Material Models

Two user defined subroutines have been written in Fortran; one which contains material models for all micro scale constituents (matrix, fibre and interface) and one which contains material models for all meso scale constituents (matrix and yarn), see Figure 3-10 for a summary. The material properties used in these material models are given in Appendix B.

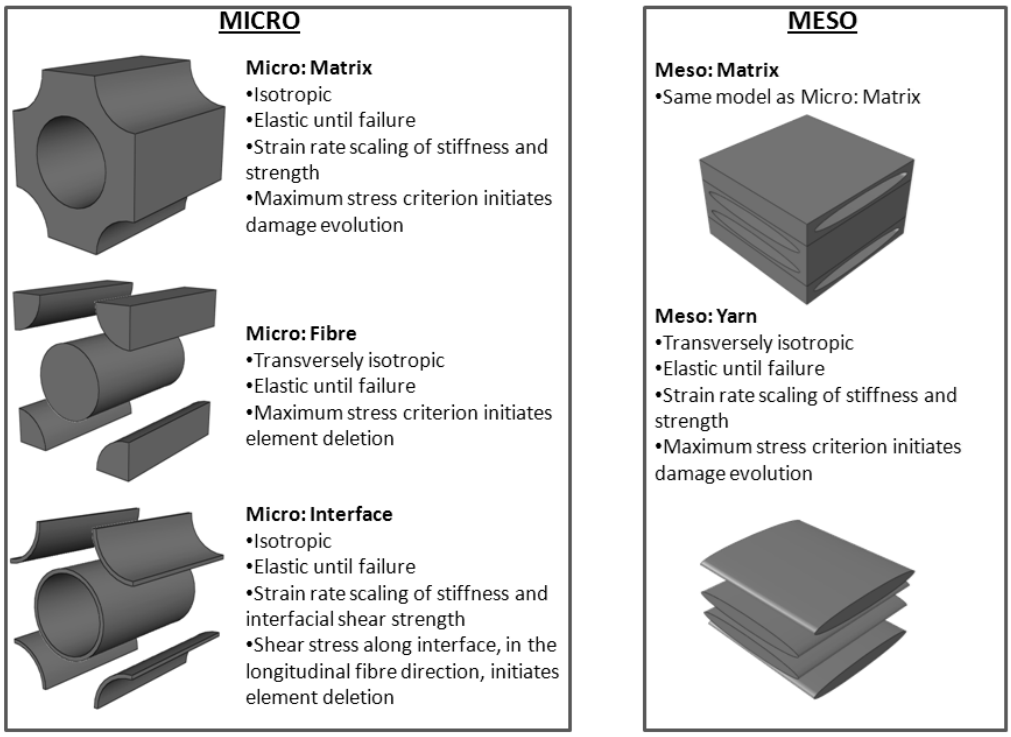

Figure 3-10. Summary of the features of the micro and meso scale constituent material models

The subroutines are called for all element integration points at all time increments in the analysis. The correct material model for the element integration point of interest is called by the subroutine based on the constituent names.

At the start of all material models multiple Abaqus variables are defined. Some are variables that are just passed in for information, some are variables that can be updated and some are variables that must be defined. User defined material properties are read into the material models and assigned variable names. All material models are contained within a loop which runs from one to the number of integration points which will be the same as the number of elements due to the use of reduced integration elements. In all material models all six components of the current strain are calculated with the strain increment variable that is passed in for information and the state variable that contains the level of strain from the previous time increment. State variables in user subroutines in Abaqus are values that can be defined at each increment in the analysis. The values from the previous increment are made available in the current increment. The state variables can be defined as functions of other variables.

3.4.1 Matrix Material Model

This section details the matrix material model in the order that operations would be performed after the common features to all material models detailed at the start of section 3.4. The matrix material model is called for all element integration points at all time increments in the analysis. The matrix material model is identical for the micro and meso scale analyses.

Using the current strain level and current simulation time all six components of strain rate (three direct and three shear) are calculated. From these values numerous maximum strain rate values are calculated.

The strain rate scaling of stiffness and strength then occurs and is based on the logarithmic equation shown in Equation 3-8 [44]. A_{RT} is the rate adjusted parameter, A_o is the quasi static value, $\dot{\varepsilon}$ is the effective strain rate, $\dot{\varepsilon_o}$ is a quasi static reference strain rate which is set to one and C_A is the strain rate scaling constant for the parameter.

$$A_{RT} = A_o\left(1 + C_A ln\left({\dot{\varepsilon}}/{\dot{\varepsilon}_o}\right)\right) \qquad \textbf{3-8}$$

The stiffness is scaled using the maximum strain rate. If the maximum strain rate is a direct strain rate then the Young's' modulus is scaled and the shear stiffness is calculated from this using the Poisson's' ratio. If the maximum strain rate is a shear strain rate then the shear stiffness is scaled and the Young's' modulus is calculated from this using the Poisson's' ratio. The matrix material of interest exhibits two distinct regions of strain rate dependency [14, 17]. The stiffness scales differently at low and high rates. This is implemented in the subroutine with a strain rate threshold where, if the strain rate is lower than this threshold, a low strain rate scaling constant is used and if the strain rate is higher than this threshold a high strain rate scaling constant is used. This effectively allows a bi-linear scaling relationship.

The tensile strength is scaled based on the maximum positive direct strain rate. The compressive strength is scaled based on the maximum negative direct strain rate. The shear strength is scaled based on the maximum shear strain rate, positive or negative. For all strength scaling a bi-linear scaling law is also used in the same manner as stiffness scaling. No strain

rate scaling of stiffness or strength occurs if the strain rate is less than one or if the element integration point has had damage initiated. Strain rate scaling of stiffness and strength is performed due to the differences in properties of matrix materials at low and high rates of testing, as discussed in section 2.2.4. If this scaling was not performed unit cells would be subjected to high rates of loading with stiffness and strength values that are only valid at low rates of loading.

The maximum stress failure criterion is applied by calculating multiple stress to strength ratios, using the scaled stiffness and strength values as well as the current strain values. Six stress to strength ratios are calculated, three direct and three shear. The stress to strength ratios are calculated by multiplying the stiffness by the current strain, giving stress, and then dividing the result by the strength. The stiffness can be direct or shear and then the strain and strength would correspond to this. The three direct stress to strength ratios use tensile or compressive stress depending on what loading the current element of interest is subject to. When any of the stress to strength ratios reach or surpass unity then damage is initiated. A summary of the maximum stress failure criterion taken from Knight Jr [40] is given is Figure 3-11.

$$e_1^t = \frac{\sigma_{11}}{X_T} \text{ for } \sigma_{11} \geq 0; \quad e_1^c = \frac{|\sigma_{11}|}{X_C} \text{ for } \sigma_{11} \leq 0$$

$$e_2^t = \frac{\sigma_{22}}{Y_T} \text{ for } \sigma_{22} \geq 0; \quad e_2^c = \frac{|\sigma_{22}|}{Y_C} \text{ for } \sigma_{22} \leq 0$$

$$e_3^t = \frac{\sigma_{33}}{Z_T} \text{ for } \sigma_{33} \geq 0; \quad e_3^c = \frac{|\sigma_{33}|}{Z_C} \text{ for } \sigma_{33} \leq 0$$

$$e_4 = \frac{|\tau_{12}|}{S_{12}}; \quad e_5 = \frac{|\tau_{23}|}{S_{23}}; \quad e_6 = \frac{|\tau_{13}|}{S_{13}}$$

Figure 3-11. Summary of the maximum stress failure criterion [40]

When damage is initiated strain rate scaling ceases to occur and damage evolution begins to occur. The damage evolution in this thesis is based on damage mechanics theory by Matzenmiller [42] who developed a constitutive model for damage in fibre reinforced composite materials. The researchers used a homogenised continuum for the model where internal variables were used to describe the damage evolution under loading as

degradation of material stiffness. The theory lends itself well to implementation in finite element codes due to it being a strain-controlled continuum model. However, the effect of reducing the stiffness of elements on boundary conditions should be given careful consideration, as discussed in section 3.3.

The damage evolution in this thesis can be thought of as stiffness degradation utilising Equations 3-9, 3-10 and 3-11. The variables in the equations are the damage variable, (ω), the largest value of all the maximum stress criteria (e_{max}), the strain softening parameter (m), the direct stiffness (E) and the shear stiffness (G). The direct stiffness and shear stiffness is always the strain rate scaled value when damage was initiated, not the quasi static value.

$$\omega = 1 - exp^{\frac{1}{m}(1-{e_{max}}^{m})} \quad \textbf{3-9}$$

$$E = (1-\omega)\,E \quad \textbf{3-10}$$

$$G = (1-\omega)\,G \quad \textbf{3-11}$$

The damage variable varies from zero, no damage, to one, maximum damage. This can be clearly seen in Equations 3-10 and 3-11 where a value of zero for the damage variable would give no change in stiffness, whereas, a value greater than one would reduce the stiffness. The rate of this stiffness reduction is controlled by the strain softening parameter, m, which can give post elastic responses ranging from sudden degradation through to gradual stiffness degradation as seen in Figure 3-12. A positive value of m gives a reduction in stiffness, a negative value of m gives an increase in stiffness and a value of zero gives a perfectly plastic response. The material model is coded in such a way that the damage variable can never decrease i.e. no healing of material can occur. Also the damage variable is limited to 0.99 to avoid any numerical errors when dividing by zero. At this value of 0.99 the stiffness of the element will be extremely low which can cause excessive distortion, hence, at this point the element is deleted from the analysis.

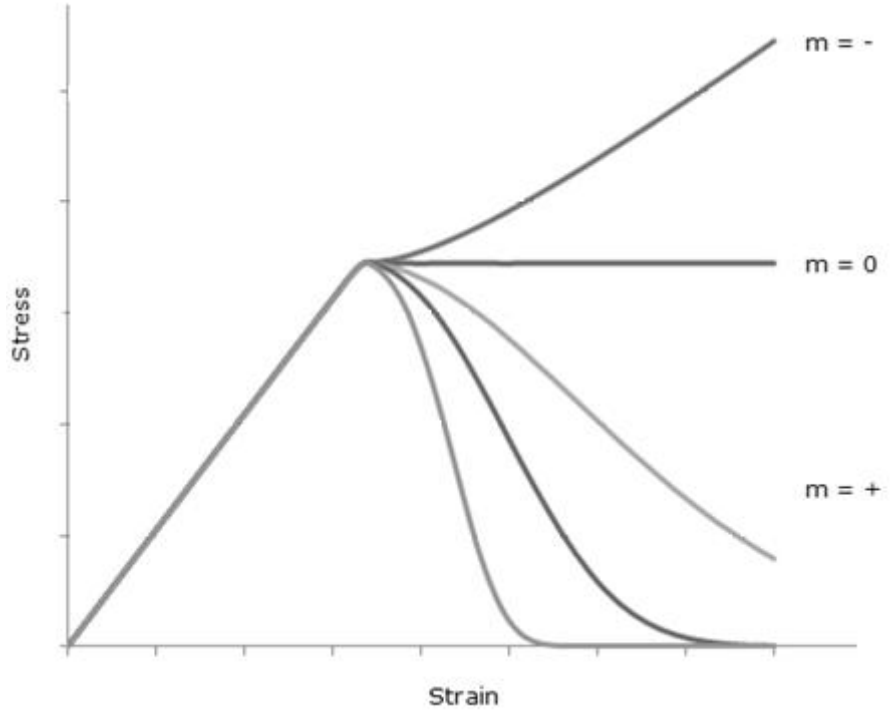

Figure 3-12. Control of post elastic response using strain softening parameter (m)

The penultimate step in the matrix constituent section of the VUMAT is to calculate the 6x6 isotropic compliance matrix and then perform matrix inversion to calculate the 6x6 stiffness matrix. The stiffness values at this stage may or may not have gone through strain rate scaling and damage evolution. The final step is to use the stiffness matrix and the current strain values in a column matrix (1x6) to calculate the new stress column matrix (1x6) through matrix multiplication.

3.4.2 Fibre Material Model

This section details the fibre material model in the order that operations would be performed after the common features to all material models detailed at the start of section 3.4. The fibre material model is called for all element integration points at all time increments in the analysis. The fibre material model is used at the micro scale of analysis.

The stress in the longitudinal fibre direction is compared to the tensile / compressive strength of the fibre depending on the type of loading. If the fibre strength is exceeded then the element deletion state variable is set to zero. A value of one indicates the integration point is still active in the analysis and a value of zero indicates the integration point has been

deleted from the analysis, giving a brittle failure. The initial value of the element deletion sate variable is one.

Assuming the element has not been deleted from the analysis the next step in the fibre constituent section of the VUMAT is to calculate the 6x6 stiffness matrix for a transversely isotropic material. The new stress state is then calculated through matrix multiplication of the stiffness matrix with the column strain matrix.

3.4.3 Interface Material Model

This section details the interface material model in the order that operations would be performed after the common features to all material models detailed at the start of section 3.4. The interface material model is called for all element integration points at all time increments in the analysis. The interface material model is used at the micro scale of analysis. The differences between the matrix and interface material models are that the interface fails based on longitudinal shear strength only, whereas the matrix considers failure in all loading, and the interface fails through element deletion not damage evolution.

Using the current strain level and current simulation time all six components of strain rate (three direct and three shear) are calculated. From these values numerous maximum strain rate values are calculated.

The strain rate scaling of the interface stiffness is performed in an identical manner to the matrix material model. The strain rate scaling of the interfacial shear strength is based on Equation 3-8, a single strain rate scaling constant (i.e. no bi-linear scaling) and the longitudinal shear strain rate in the fibre direction.

The shear stress in the longitudinal fibre direction is compared to the interfacial shear strength. If the interfacial shear strength is exceeded then the element deletion state variable is set to zero. A value of one indicates the integration point is still active in the analysis and a value of zero indicates the integration point has been deleted from the analysis, giving brittle shear failure at the interface.

The penultimate step in the interface constituent section of the VUMAT, assuming the element has not been deleted from the analysis, is to calculate the 6x6 isotropic compliance matrix and then perform matrix inversion to calculate the 6x6 stiffness matrix. The final step is to calculate the new stress state through matrix multiplication of the stiffness matrix with the column strain matrix.

3.4.4 Yarn Material Model

This section details the yarn material model in the order that operations would be performed after the common features to all material models detailed at the start of section 3.4. The yarn material model is called for all element integration points at all time increments in the analysis. The yarn material model is used at the meso scale of analysis. The material properties used in the yarn material model come from the modelling results at the micro scale.

Using the current strain level and current simulation time all six components of strain rate (three direct and three shear) are calculated. From these values numerous maximum strain rate values are calculated.

The strain rate scaling of all strength values (longitudinal tensile, longitudinal compressive, transverse tensile, transverse compressive and shear strengths) is based on Equation 3-8, the maximum strain rate and one strain rate scaling constant (i.e. no bi-linear scaling as with the matrix material model) which is the same value for all strengths. The strain rate scaling of stiffness (longitudinal, transverse and shear values) is based on Equation 3-8, the maximum strain rate and one strain rate scaling constant (i.e. no bi-linear scaling as with the matrix material model) which is different for longitudinal, transverse and shear stiffness scaling.

The damage initiation, damage evolution and final stress state calculations are then performed as described in section 3.4.1. The difference, due to the transversely isotropic nature of the yarns, is that (a) a strain softening parameter is selected based on the largest maximum stress criteria, (b) further Poisson's ratios are calculated and (c) the stiffness reduction in Equations 3-10 and 3-11 is applied to all stiffness values (longitudinal, transverse and shear).

3.5 Implementation in Abaqus

Finite element modelling can be split into three broad steps; pre-processing, solver and post-processing. Pre-processing is the stage where a simulation is fully defined in terms of part geometry, assembly definitions, material properties, analysis steps, interactions, loads, boundary conditions, mesh generation etc. All this information is utilised to create an input file that can be sent and analysed in a solver. The solver will generate an output file that contains all the desired results, e.g. stresses and strains, within a particular model. This output file can be analysed in the post-processing stage to obtain the desired information.

The finite element package utilised in this work is Abaqus, a DS SIMULIA product where SIMULIA is the DS (Dassault Systémes) brand that delivers the Abaqus product. Abaqus/CAE, in conjunction with Python scripting, is used in the pre and post-processing stage and Abaqus/Explicit, in conjunction with Fortran coded user defined material models, is used in simulations as the solver.

One can use the Abaqus/CAE graphical user interface (GUI) to perform various tasks to set up a simulation in the pre-processing stage. Upon performing these tasks one would execute numerous operations by interacting with the GUI e.g. selecting a surface on a model to apply a boundary condition. Each operation executed in the GUI internally generates commands in an object oriented programming language called Python. These commands are sent to the Abaqus/CAE kernel. The kernel, the brains of Abaqus/CAE, interprets the commands and performs the task you selected. The GUI can be thought of as the interface between the user and the kernel. Python scripting allows direct communication with the kernel, effectively bypassing the GUI. One can create a file containing Python commands to perform the same tasks as you would perform using the GUI. The key advantage of using Python scripting is the ability to automate repetitive tasks whether this is in the generation of a model or submission of multiple jobs. The integration of Python scripting into Abaqus is shown in diagrammatic form in Figure 3-13.

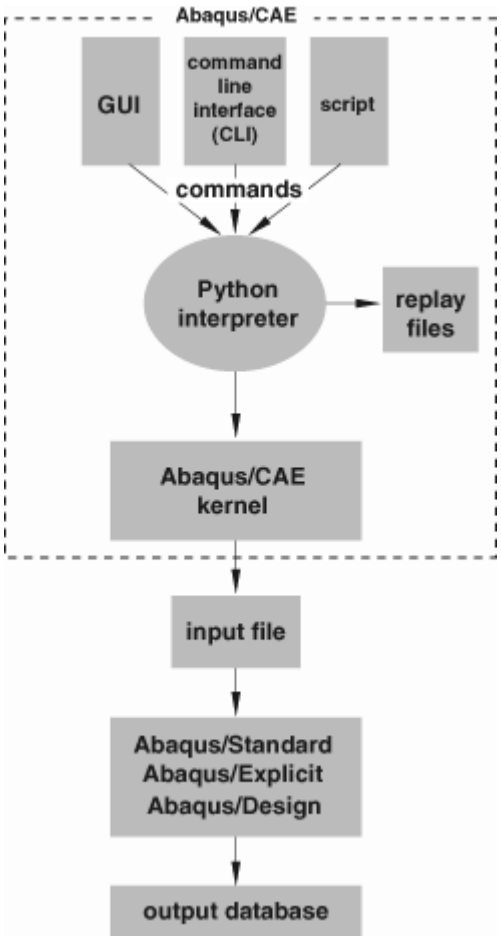

Figure 3-13. Abaqus pre-processing, solver and post-processing information transfer [43]

The Abaqus/Explicit solver works on an input file created in the pre-processing stage and generates an output file for the post-processing stage, seen in Figure 3-13. The Abaqus documentation [43] gives detailed information on explicit dynamic analyses as well as the following general overview:

"The explicit dynamics procedure performs a large number of small time increments efficiently. An explicit central-difference time integration rule is used; each increment is relatively inexpensive (compared to the direct-integration dynamic analysis procedure available in Abaqus/Standard) because there is no solution for a set of simultaneous equations. The explicit central-difference operator satisfies the dynamic equilibrium equations at the beginning of the increment, t; the accelerations calculated at time t are used to advance the velocity solution to time $t + \Delta t/2$ and the displacement solution to time $t + \Delta t$."

Gutkin and Pinho [77] focused on the modelling techniques for failure of carbon/epoxy composite materials. The authors implemented physically based failure criteria models in implicit and explicit user defined subroutines in Abaqus. An open hole tension laminate model with layup $[90/0/\pm45]_{3S}$ was subjected to a displacement rate of 10mm/s. The implicit model took three times as long to run as the explicit model.

The explicit procedure discussed earlier is implemented with a user defined subroutine which is executed at every step of the analysis and is written in the programming language Fortran. A user subroutine to define material behaviour in the Abaqus/Explicit product is called a VUMAT. A VUMAT can be used to define the mechanical constitutive behaviour of a material and is called for blocks of material calculation points at all time increments in the analysis. The VUMAT can use and update solution dependent state variables and use any field variables that are passed in for information. For example, a solution dependent state variable could be a damage variable that varies from zero to one where zero indicates no damage and one indicates maximum damage. This damage variable which is a solution dependent state variable could be based on a field variable that has been passed in for information, such as a particular component of strain. The state variables are of particular importance as this information will be carried forward to the following time increment in the analysis. In this thesis the VUMAT is used to define mechanical constitutive behaviour, initiate damage, evolve damage and include strain rate dependence.

In the post-processing stage the output files can be viewed in Abaqus/CAE and results in terms of stress strain curves produced manually within the GUI. Python scripting can again be utilised here to automate the repetitive task of generating stress strain curves for multiple simulations.

All simulations were run on either a powerful desktop computer (two quad core Intel Xeon CPU E5520 2.27GHz processors, 32 GB RAM and Microsoft Windows XP Professional x64 Edition operating system) or The University of Nottingham High Performance Computer (HPC).

4 Micro Scale Modelling

4.1 Introduction

This chapter involves the numerical simulation and prediction of high strain rate material properties of unidirectional composite fibre bundles. Specifically the modelling takes place at the micro scale where fibres surrounded by an interfacial layer are embedded in a matrix material. Finite element analysis of carbon/epoxy and S2 glass/epoxy micro scale unit cells provides the high strain rate properties of carbon/epoxy and S2 glass/epoxy meso scale yarns / fibre bundles.

The chapter first details some micrograph work followed by some modelling studies that have been conducted to obtain certain modelling parameters and to gain confidence in the user defined material models, as described in 3.4. Following this, micro scale modelling results are presented for both carbon/epoxy and S2 glass/epoxy unit cells. The unit cells have been tested in longitudinal tension, longitudinal compression, transverse tension, transverse compression, longitudinal shear and transverse shear loading. Each loading condition has been tested over a range of strain rates from 1 /s to 10000 /s. The analysis of the data is then presented which ultimately provides high strain rate material properties for use in meso scale modelling. The chapter is concluded with a detailed discussion of the results.

4.2 Micro Scale Micrograph Analyses

4.2.1 Fibre Diameter Study

This section presents the results of the fibre diameter measurement process described in section 3.2.1. The S2 glass and carbon fibre diameters, shown in Figure 4-1, were found to be 12.1μm (standard deviation of 1.1μm) and 8.94μm (standard deviation of 0.5μm) respectively. This compared to values of 11μm for E glass, different grade to S2, and 8μm carbon reported in Hull and Clyne [9].

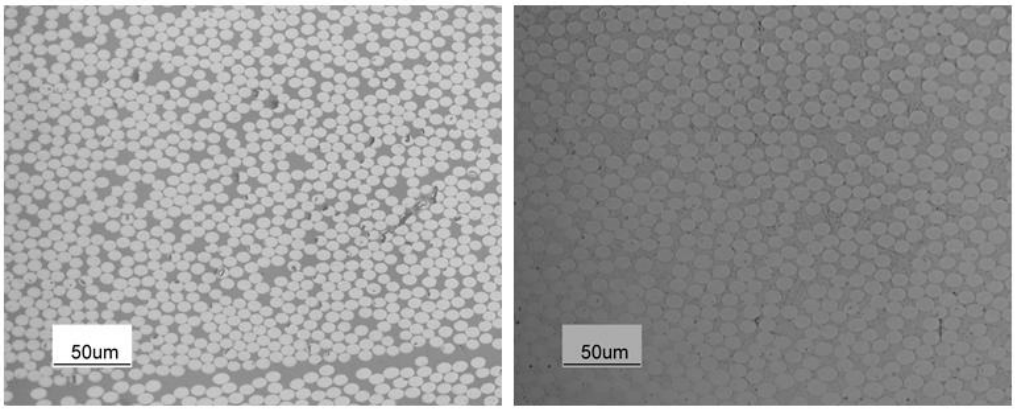

Figure 4-1. Optical micrographs of cross sections of unidirectional carbon/epoxy (left) and S2 glass/epoxy (right) yarns

The variability in fibre diameter is partly due to the human error inherently involved in the measurement process. In the image analysis software ImageJ [73] a line is drawn across the diameter of a fibre, the number of pixels along this line is then measured and using the scale of the micrograph an image a length in μm is calculated. This obviously relies on the user of the software to accurately draw the line in the correct position at the start and end of the fibre and directly across the diameter. The edge of the fibres can be blurred as seen in Figure 4-2, depending on the magnification of the micrograph, hence a difficulty is encountered with identifying the start and end of the fibre.

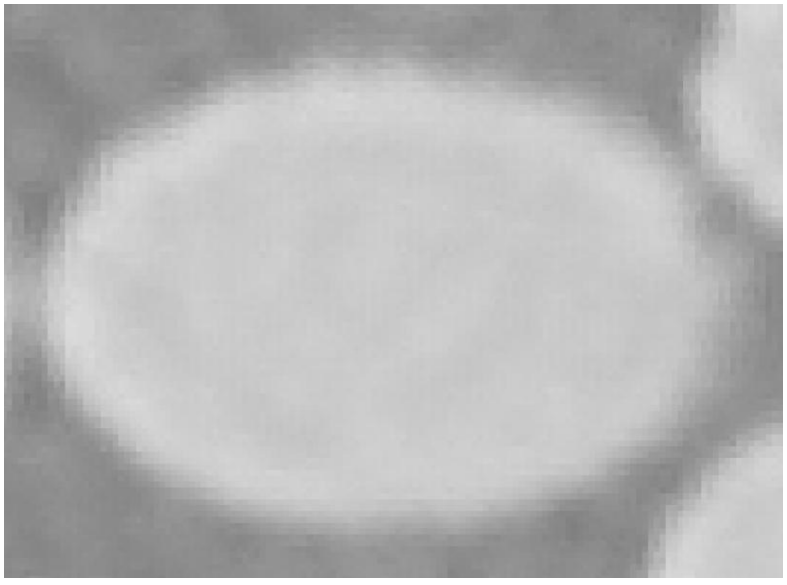

Figure 4-2. Zoomed micrograph image of the cross section of one individual carbon fibre approximately 1000 pixels in diameter

Also in a unidirectional material not all fibres will be perfectly aligned at zero degrees i.e. in a micrograph they will not be coming directly 'out of the image' as seen in Figure 4-3. This is due a combination of the inability to achieve 100% alignment of fibres in the manufacturing process and the inability to perfectly cut the laminate perpendicular to the fibre direction for microscope analysis samples. This leads to some fibres appearing slightly elliptical rather than circular. This is not an issue in measuring the fibre diameter as the shortest length of the ellipse will always be the fibre diameter and it is this length that has been measured for the results in this thesis.

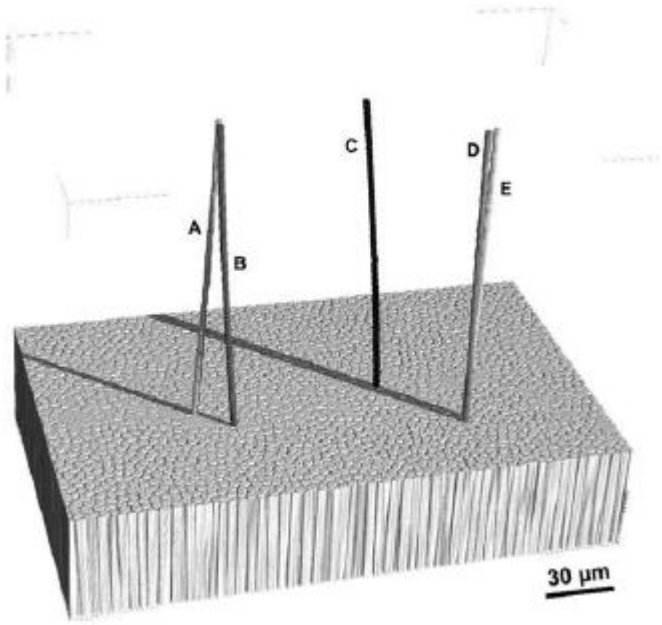

Figure 4-3. Typical features resulting from the angular variation in unidirectional continuous reinforced polymers. Five segmented fibres are shown where A, B and C are located within channels separating fibre bundles and D and E are located next to each other and within fibre bundles.

4.2.2 Fibre Volume Fraction Study

This section presents the results of the fibre volume fraction measurement process described in section 3.2.1. The fibre volume fractions within the yarn boundaries for the carbon/epoxy and S2 glass/epoxy yarns were found to be 66.28% and 54.32% respectively. As the volume fraction in the yarn was calculated for multiple thin vertical columns of area across the width of the yarn, explained in 3.2.1, a histogram can be created putting the volume fraction of each thin column in a certain numerical

range on the x axis, shown in Figure 4-4 for the carbon/epoxy yarn and Figure 4-5 for the S2 glass/epoxy yarn.

The two plots effectively show how much the volume fraction varies across the width of the yarn. The mean value of the volume fraction of the thin vertical columns is shown in the top left of the figures with a standard deviation. This standard deviation shows how much the volume fraction of the thin vertical columns varies from the mean value. A lower standard deviation in the carbon yarn than in the S2 glass yarn indicates less variation in the volume fraction across the width of the yarn, i.e. a more consistent packing of fibres. This is also intuitively seen from the shape of the graphs where the carbon plot has a narrow bell shape and the S2 glass plot has wider bell shape.

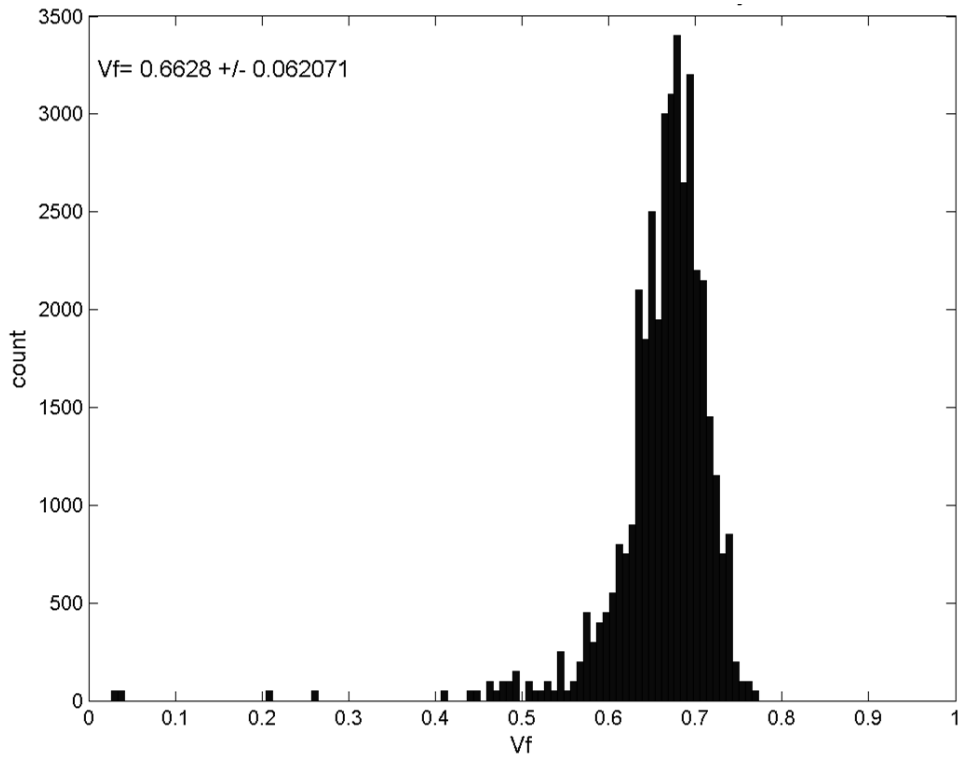

Figure 4-4. Histogram showing count against volume fraction for the carbon/epoxy yarn

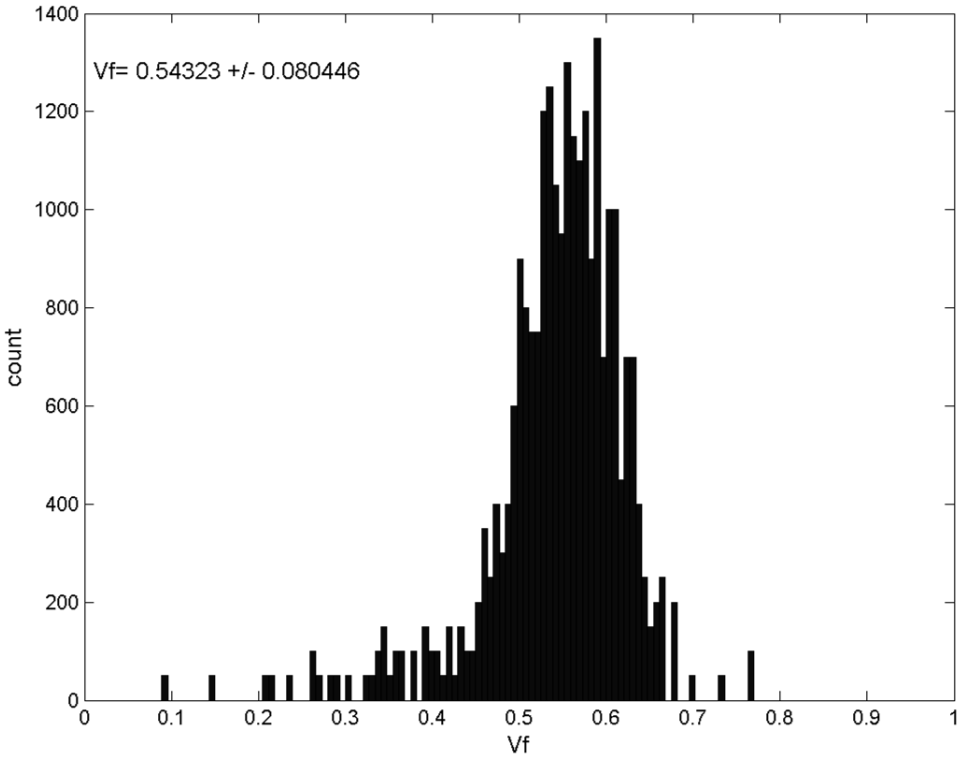

Figure 4-5. Histogram showing count against volume fraction for the S2 glass/epoxy yarn

4.3 Micro Scale Modelling Studies

4.3.1 Mesh Sensitivity Study

A mesh sensitivity study was conducted on a carbon/epoxy micro scale unit cell as described in 3.2.1 with the measured fibre diameter from the previous section and the fibre spacing defined by the measured fibre volume fraction. The mesh sensitivity study was performed on the carbon/epoxy unit cell as the fibre volume fraction is higher, hence, the fibre spacing is smaller which requires a denser mesh. A suitable mesh for the carbon/epoxy unit cell will be more than suitable for the S2 glass/epoxy unit cell. The unit cell was tested at six different mesh densities in transverse tension at 10000/s. Transverse tension was chosen so the effect of mesh density could be observed on not only the stiffness and strength but also the post elastic damage response. The unit cell was tested at a high strain rate of 10000 /s for speed of analysis. The effect of mesh density on the stress strain response is presented in Figure 4-6.

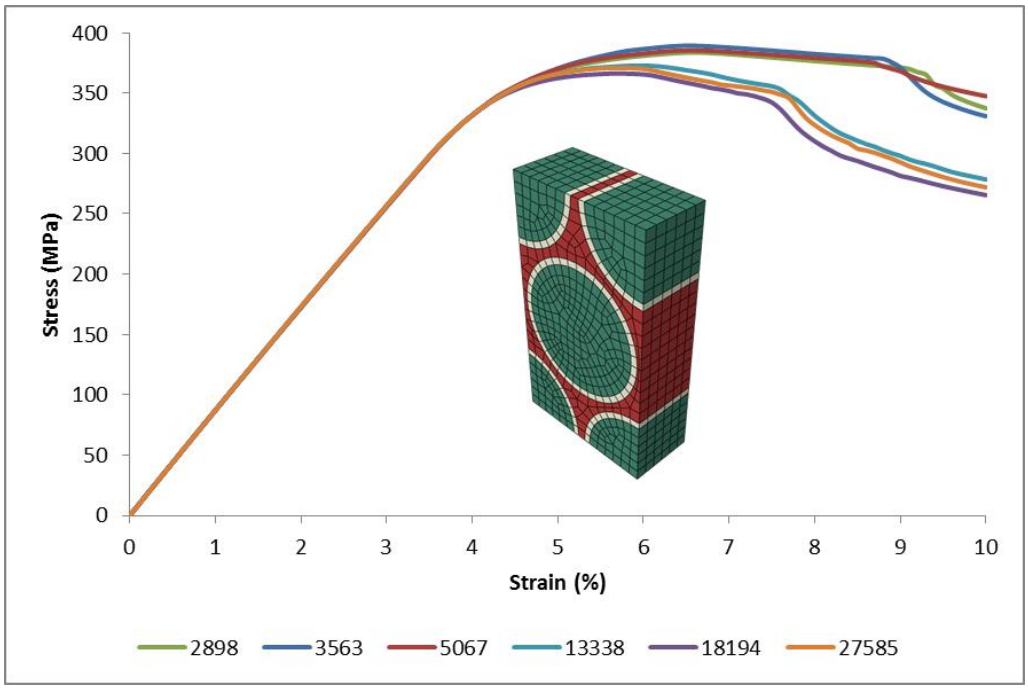

Figure 4-6. Stress strain response of a carbon epoxy micro unit cell with six different mesh densities, number of elements shown in legend, subjected to transverse tension at 10000 /s. The unit cell is shown with a mesh containing 2898 elements.

The stiffness of the unit cell and stress at which damage is initiated does not change significantly with increasing mesh density. The difference in the stress strain responses is seen in the post elastic region. The three coarsest and three finest meshes produce two types of post elastic response. The three finer meshes have a post elastic response where more stiffness degradation of elements has taken place. The difference in the post elastic response between the three coarsest and the three finest meshes would correspond to a different strain softening parameter, m, which controls the rate of stiffness degradation after damage initiation, see Figure 3-12. The difference in this m value would be very small, less than 1.0, and when parameters are averaged for use in larger scales of analysis this would most likely prove insignificant

The simulation run times for some of the finer meshes are too long when it is taken into consideration that there are multiple materials, scales of analysis, loading conditions and strain rates to be tested. The long run times can be attributed to two main factors; material models and boundary conditions. An increased number of elements means more integration points for the complex user defined subroutines. An increased number of elements also means more nodes on surfaces and edges which leads to

more linear constraint equations to implement periodic boundary conditions.

Taking the above discussion points into consideration it was decided to run with a coarser mesh density, 2898 elements for the carbon/epoxy micro scale unit cell.

4.3.2 Mass Scaling Study

Mass scaling involves adding nonphysical mass to the model in order to achieve a larger stable time step and, therefore, reduced simulation run times. The technique should only be used when the addition of the nonphysical mass does not significantly affect the overall results. A S2 glass/epoxy micro scale unit cell was tested in transverse tension with increasing density values from the original value. From the results the maximum mass scaling that could be used without affecting the results was when the density was multiplied by 1e9. This appropriate level of mass scaling was chosen to be used for the micro simulations at the lowest strain rate where long simulations run times were expected.

4.3.3 Fibre Strength Study

This study was conducted to gain confidence in the material models, described in 3.4. Changes were made in the fibre constituent material properties where the resulting unit cell response would be predictable, hence, it could be ascertained if the material models were capturing realistic material behaviour. A S2 glass/epoxy micro scale unit cell was tested in transverse tension, longitudinal tension and transverse shear. All tests were at a strain rate of 10000 /s for speed of analysis, the material models were not altered in any way so strain rate effects were still included. Each test was conducted with a low tensile/compressive fibre strength (-10% normal strength), the normal fibre tensile/compressive strength and a high fibre tensile/compressive strength (+10% normal strength). In terms of the stress strain response there was no change in transverse tension and transverse shear loading responses. In longitudinal tension the strength of the unit cell increased with increasing fibre strength as shown in Figure 4-7. This is what one would expect and is generally in line with changes in fibre strength.

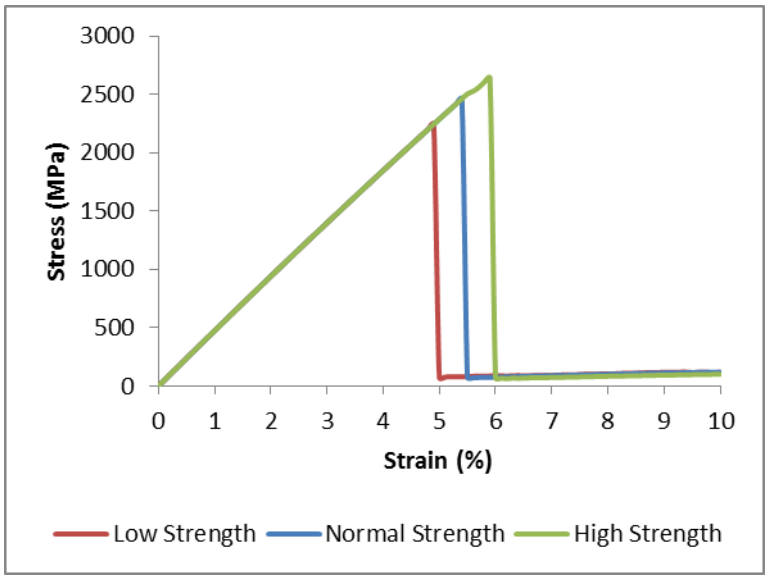

Figure 4-7. Stress strain curves of S2 glass epoxy micro unit cell in longitudinal tension at 10000 /s with low, normal and high tensile and compressive fibre strength

4.3.4 Interface Strength Study

This study was conducted to gain confidence in the material models, described in 3.4. Changes were made in the interface constituent material properties where the resulting unit cell response would be predictable, hence, it could be ascertained if the material models were capturing realistic material behaviour. A S2 glass/epoxy micro scale unit cell was tested in transverse tension, longitudinal tension and longitudinal shear. All tests were at a strain rate of 10000 /s for speed of analysis, the material models were not altered in any way so strain rate effects were still included. Each test was conducted with a low interfacial shear strength (-10% normal strength), the normal interfacial shear strength and a high interfacial shear strength (+10% normal strength). In terms of stress strain response there was no change in transverse tension and longitudinal tension loading responses. In longitudinal shear, as expected, the strength of the unit cell increased with increasing interfacial shear strength as shown in Figure 4-8.

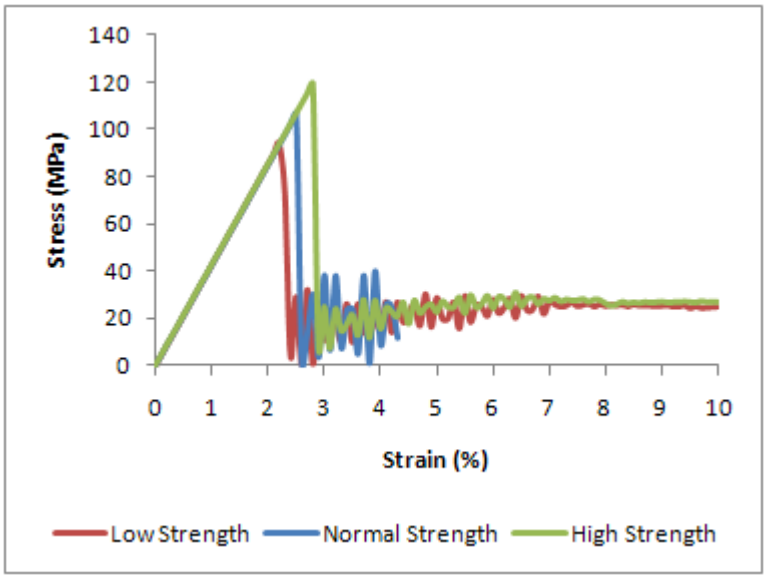

Figure 4-8. Stress strain curves of S2 glass epoxy micro unit cell in longitudinal shear at 10000 /s with low, normal and high interfacial shear strength

4.3.5 Interface Thickness Study

This study was conducted to gain confidence in the material models, described in 3.4. Changes were made in the interface constituents geometry where the resulting unit cell response would be predictable, hence, it could be ascertained if the material models were capturing realistic material behaviour. A S2 glass/epoxy micro scale unit cell was tested in transverse tension, longitudinal tension and longitudinal shear, see Figure 4-9. All tests were at a strain rate of 10000 /s for speed of analysis, the material models were not altered in any way so strain rate effects were still included. Each test was conducted with an interface thickness equal to the fibre radius (r) divided by 20 (thin), 10 (normal) and 5 (thick). In all three loading conditions the stiffness is increased as the interface becomes thinner, this is due to there being more stiff fibre material present in the unit cell. The fibre volume fractions for the thin (r/20), normal (r/10) and thick (r/5) interfaces are 57%, 54% and 48% respectively. In transverse tension and longitudinal shear the strength and shape of the stress strain curves are similar for all three interface thicknesses. In longitudinal tension the strength and shape of the stress strain curve is similar for the thin (r/20) and normal (r/10) interface thickness. However, in longitudinal tension with a thick interface (r/5) the failure mechanism changes, instead of all fibres and interfaces failing at the same time (as for thin and normal interface thicknesses) the central fibre

and interface fails first followed by the corner fibres and interfaces. This generates a two-step failure process seen in the stress strain response.

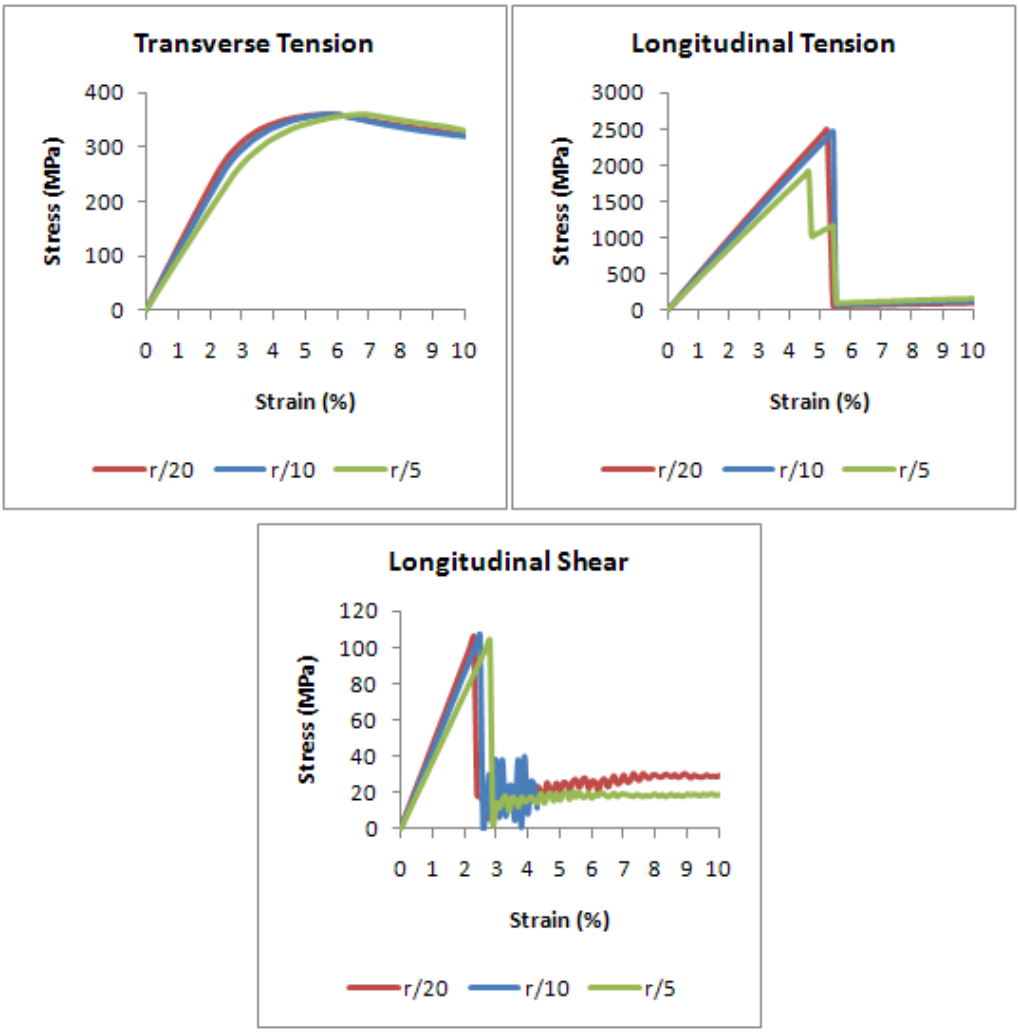

Figure 4-9. Stress strain curves of S2 glass epoxy micro unit cell in three loading conditions with a thin, normal and thick interface layer

4.3.6 Damage Evolution Study

This study was conducted to gain confidence in the material models, described in 3.4. Changes were made in the matrix constituent material properties where the resulting unit cell response would be predictable, hence, it could be ascertained if the material models were capturing realistic material behaviour. A S2 glass/epoxy micro scale unit cell was tested in transverse tension, longitudinal tension and transverse shear. All tests were at a strain rate of 10000 /s for speed of analysis, the material models were not altered in any way so strain rate effects were still included. Each test was conducted with a matrix strain softening

parameter, m, of 0.1, 1 and 10. The strain softening parameter controls how the epoxy resin matrix behaves post damage initiation. A value of 0.1 gives a very slow rate of stiffness reduction (ductile) after damage initiation, whereas, a value of 10 gives a very high rate of stiffness reduction (brittle).

In terms of the unit cell stress strain response there was no change in longitudinal tension loading as this is a fibre dominated response and damage evolution occurs in the matrix constituent only. Transverse tension and transverse shear loading demonstrated a similar change in stress strain response with a change in the value of m; due to both loading modes being matrix dominated. This change is discussed for transverse tension with reference to Figure 4-10.

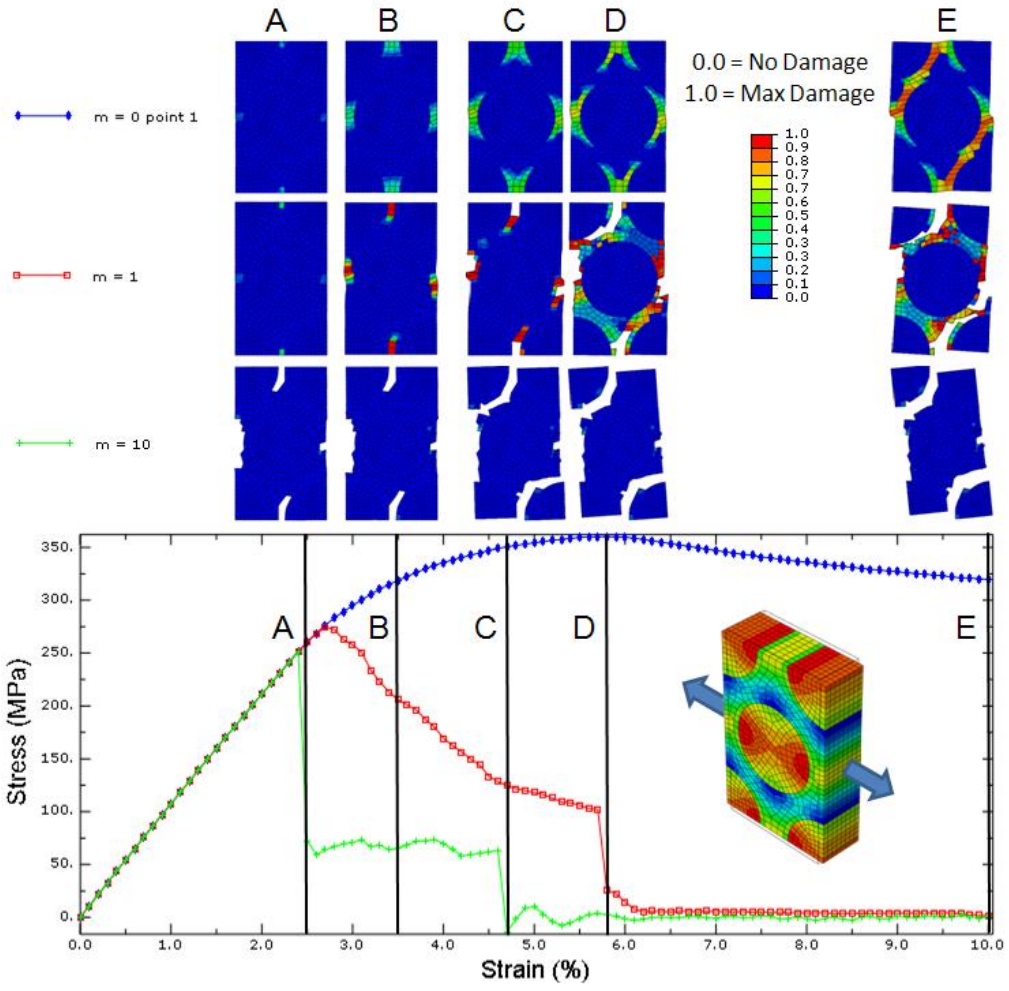

Figure 4-10. Stress strain curves for S2 glass epoxy micro unit cell in transverse tension at 10000 /s with different values for the strain softening parameter (m). The state of damage in the physical model is also shown at five different levels of strain (A, B, C, D and E). Red indicates maximum damage and blue indicates no damage.

Damage initiation occurs at the same location, horizontally between the fibres, in the micro unit cell in all three transverse tension simulations. This damage initiation also occurs at the same stress value, point A in Figure 4-10, due to the maximum stress criterion.

The damage evolution that occurs after damage initiation then differs in all three transverse tension simulations due to the different values for the strain softening parameter, m. With an m value of 10 the stiffness is rapidly degraded to such a point that some elements are at maximum damage. At this point the elements are deleted from the analysis, causing a physical crack path. This creates the large drop off in stress. The damage at this point has not had chance to create a crack path through the entire unit cell so it still has some ability to carry load, hence the step in the curve. As the loading continues the crack eventually bridges the entirety of the unit cell and the stress drops off to zero as the unit cell can no longer carry any load. With an m value of 0.1 the stiffness is degraded at a very slow rate, so much in fact that the stress continues to rise until it eventually plateaus off as more and more elements become damaged. No elements reach maximum damage and hence none are deleted from the analysis so there is no abrupt drop in stress. The rate of stiffness degradation for an m value of 1 is between the other two simulations. The stress gradually reduces after damage initiation and then drops off abruptly to zero. This abrupt drop off occurs for the same reason as in the simulation with an m value of 10, some elements having reached maximum damage are, therefore, deleted from the analysis. The explanations given here also apply to transverse shear loading as mentioned previously at the start of this section. It is clear that from this study that in matrix dominated loading modes the matrix strain softening parameter has a significant effect on the shape of the post elastic stress strain curve of the micro unit cell.

4.3.7 Transverse Tension Study

A S2 glass/epoxy micro scale unit cell was tested in tension in the two transverse directions (X and Y) to ascertain if there would be any differences in the mechanical response. Tests were conducted at 1, 1000 and 10000 /s. The results in terms of the stress strain responses are shown in Figure 4-11. The stiffness values in X and Y transverse tension

are the same, however, the strength in Y transverse tension is typically 30% greater than in X transverse tension at all three strain rates tested.

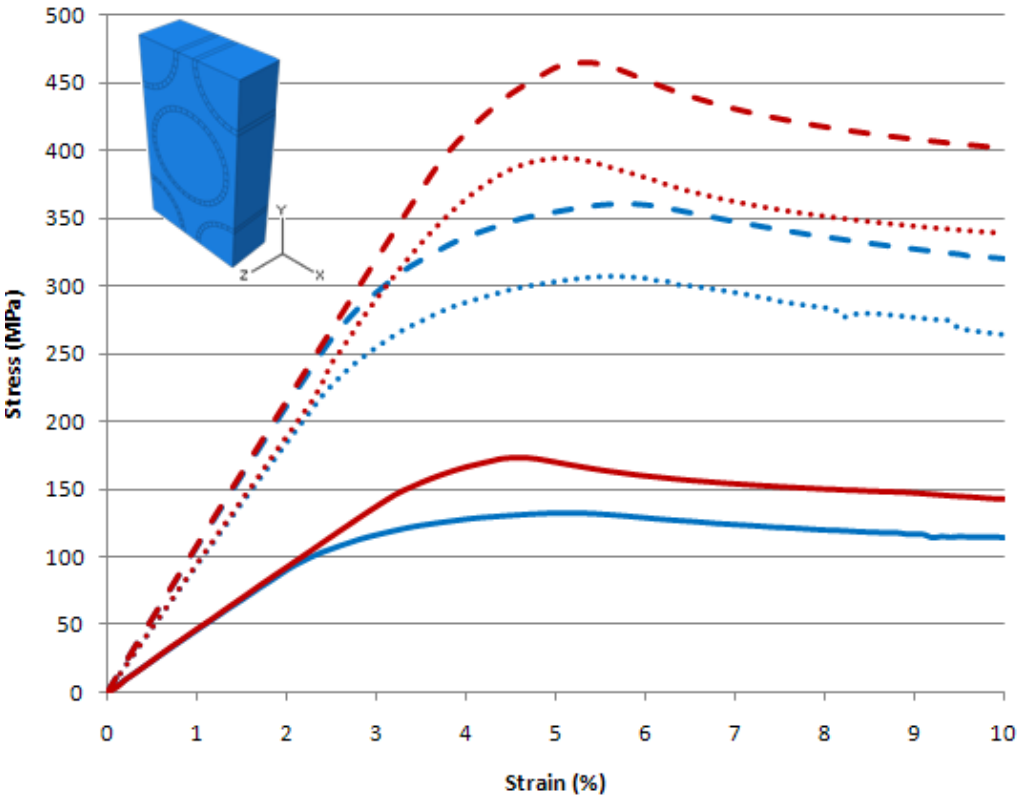

Figure 4-11. Stress strain curves for S2 glass/epoxy micro unit cells in X (blue) and Y (red) transverse tension. The strain rates tested were 1/s (solid line), 1000/s (dotted line) and 10000/s (dashed line).

The other difference between X and Y transvere tension is that damage initiates in different locations in the unit cell as shown in Figure 4-12. In X transverse tension, the damage initiates horizontally between the fibres, whereas, in Y transverse tension the damage intiates diagonally between the fibres. The damage then also propagates in a different manner, with X tension damage moving vertically through the unit cell and Y tension damage moving horizonally through the unit cell.

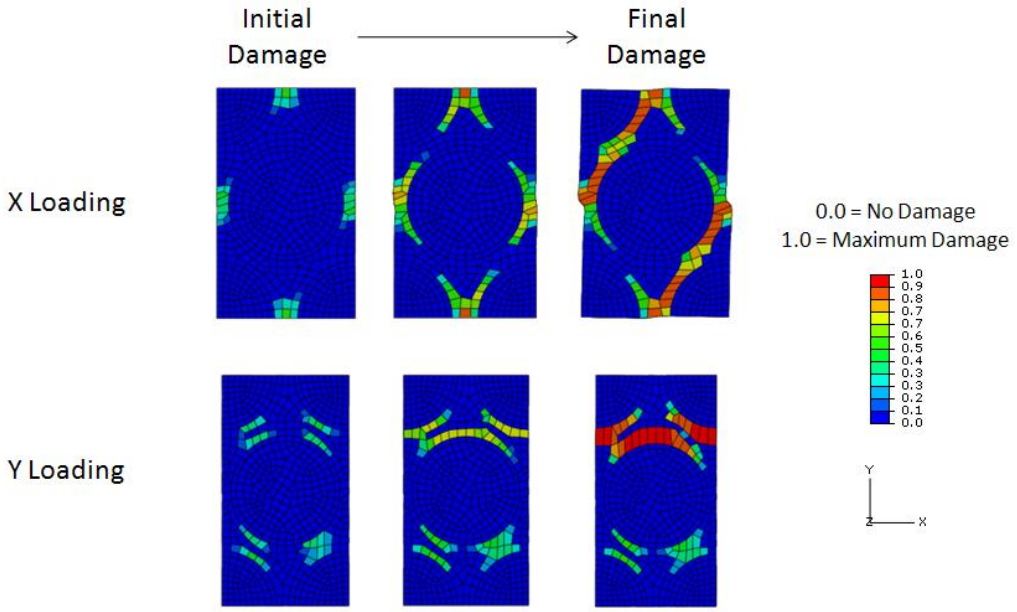

Figure 4-12. Damage in X and Y transverse tension loading at 10000/s. Red indicates maximum damage and blue indicates no damage.

Figure 4-13 helps to explain the initial location of damage in the two transverse tension loading conditions. In X loading the largest stress in the matrix is horizontally in between the fibres, whereas, in Y loading it is diagonally in between the fibres. This confirms the location of the damage as observed in Figure 4-12.

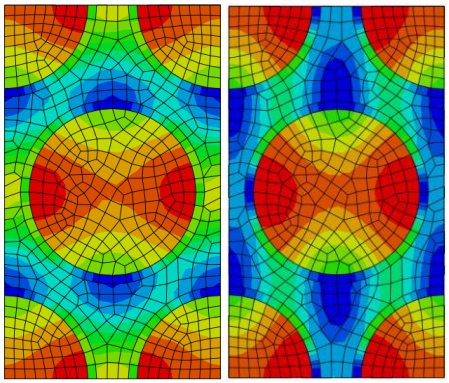

Figure 4-13. Initial von Mises stress state of the micro unit cell subjected to X transverse tension (left) and Y transverse tension (right). Red indicates high stress and blue indicates low stress.

These results are also reported elsewhere in the literature. A good comparison is seen with work done by Maligno [78]. Unit cells were tested in both X and Y transverse tension under quasi-static loading, with damage initiation and damage evolution also being modelled. The results showed the following comparable points with the work presented above; (a) a

higher strength, by around 30%, in Y transverse tension than X transverse tension, (b) identical stiffness values in X and Y transverse tension, (c) damage initiation horizontally between the fibres in X transverse tension and diagonally between the fibres in Y transverse tension and finally (d) damage evolution vertically through the unit cell in X transverse tension and horizontally through the unit cell in Y transverse tension.

The results on location of damage initiation and the direction of damage evolution presented by Maligno [78] are shown in Figure 4-14. The results in Figure 4-14 compare well to those in Figure 4-12. It is important to note that the results in Figure 4-14 are for quarter hexagonally packed unit cells, so some visualization (translations and rotations) is required to compare directly with Figure 4-12.

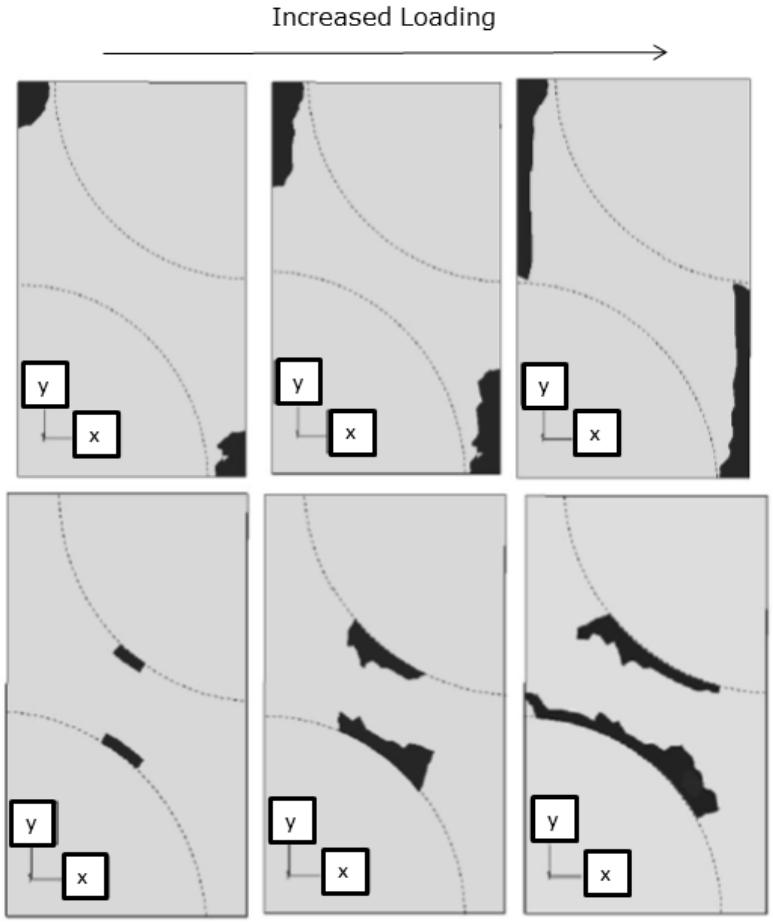

Figure 4-14. Damage initiation and evolution under uniaxial transverse tensile loading in X direction (top) and Y direction (bottom). Reproduced from [78]

For square fibre packing the stiffness's and strengths in the X and Y transverse directional would be identical, unlike the hexagonal packing where the stiffness's are the same and the strengths are different. Hexagonal packing has been used in this thesis due to the larger theoretical maximum fibre volume fraction that can be obtained; 90.7% for hexagonal compared to 78.5% for square.

In this thesis the properties resulting from micro x and y transverse loading are averaged for use as transverse meso scale yarn properties as detailed in Figure 4-36.

4.4 Micro Scale Modelling Results

This section presents the results of the carbon/epoxy and S2 glass/epoxy micro scale modelling. The unit cells for both materials have been tested in several loading conditions, which are demonstrated in Figure 4-15, and at strain rates of 1, 1000 and 10000 /s.

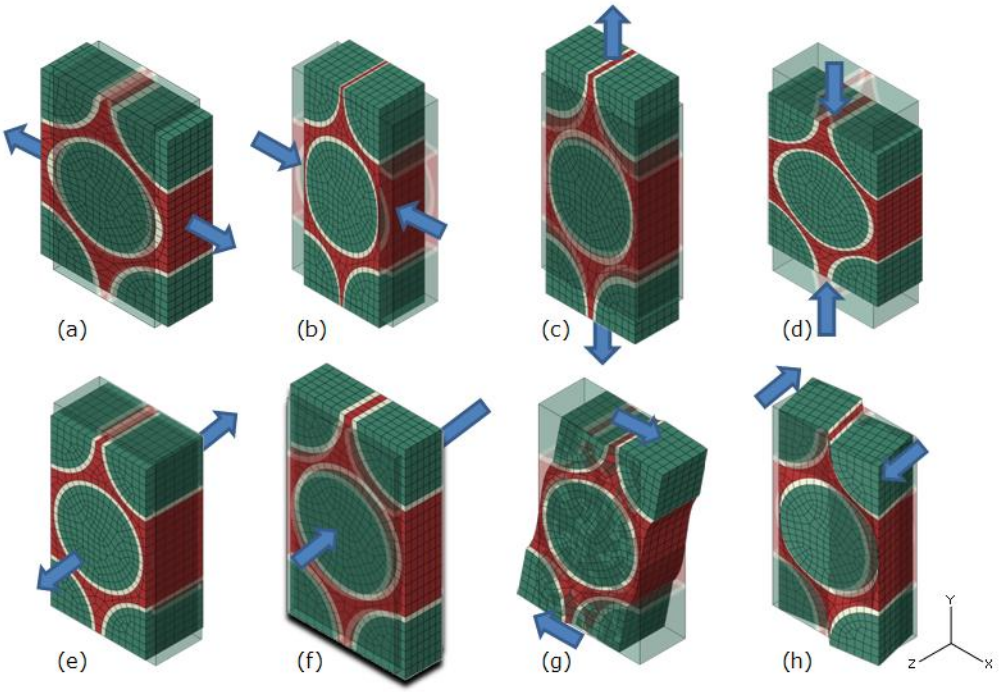

Figure 4-15. Micro scale unit cell loading conditions. (a) transverse x tension, (b) transverse x compression, (c) transverse y tension, (d) transverse y compression, (e) longitudinal z tension, (f) longitudinal z compression, (g) transverse xy shear and (h) longitudinal xz shear. The example unit cells are carbon micro scale unit cells with a deformation scale factors applied.

4.4.1 Carbon/Epoxy

The stress strain responses for the carbon/epoxy micro scale unit cell are presented in Figure 4-16 for transverse loading in the x direction, Figure 4-17 for transverse loading in the y direction, Figure 4-18 for longitudinal loading and Figure 4-19 for shear loading. For each loading condition the von Mises stress contour plots are shown in Figure 4-20 and the damage variable contour plots are shown in Figure 4-21. These results are discussed in sections 4.5 and 4.5.2 along with the S2 glass/epoxy results from section 4.4.2.

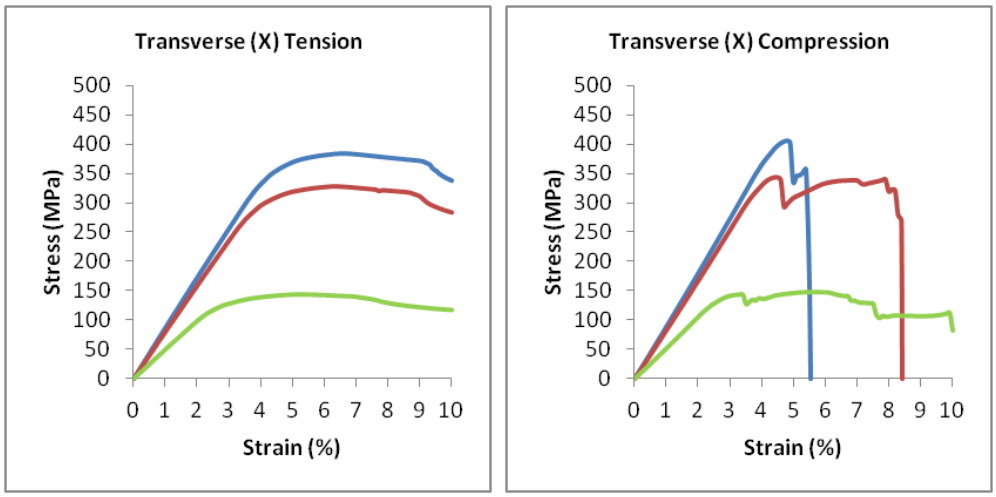

Figure 4-16. Stress strain curves for carbon/epoxy micro scale unit cell in transverse tension and transverse compression, in the X direction, at strain rates of 1 (green), 1000 (red) and 10000 (blue) /s

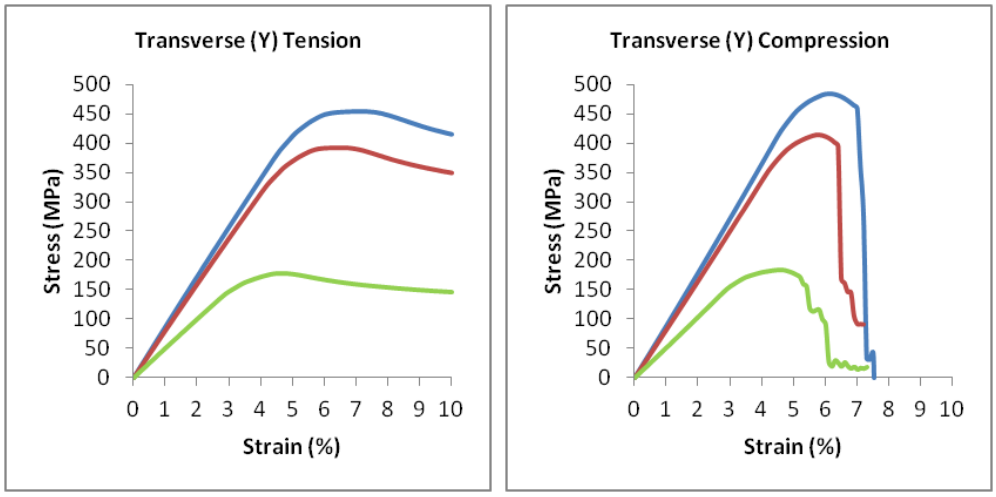

Figure 4-17. Stress strain curves for carbon/epoxy micro scale unit cell in transverse tension and transverse compression, in the Y direction, at strain rates of 1 (green), 1000 (red) and 10000 (blue) /s

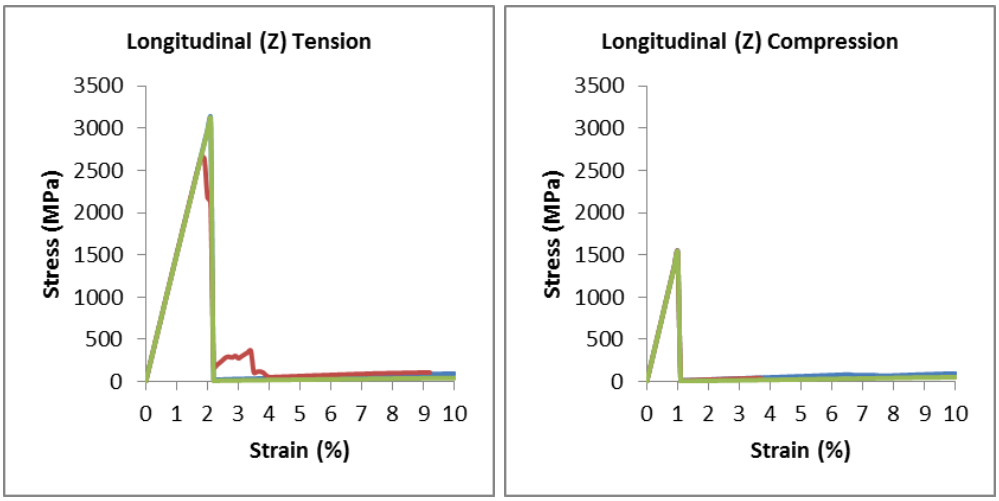

Figure 4-18. Stress strain curves for carbon/epoxy micro scale unit cell in longitudinal tension and longitudinal compression, in the Z direction, at strain rates of 1 (green), 1000 (red) and 10000 (blue) /s

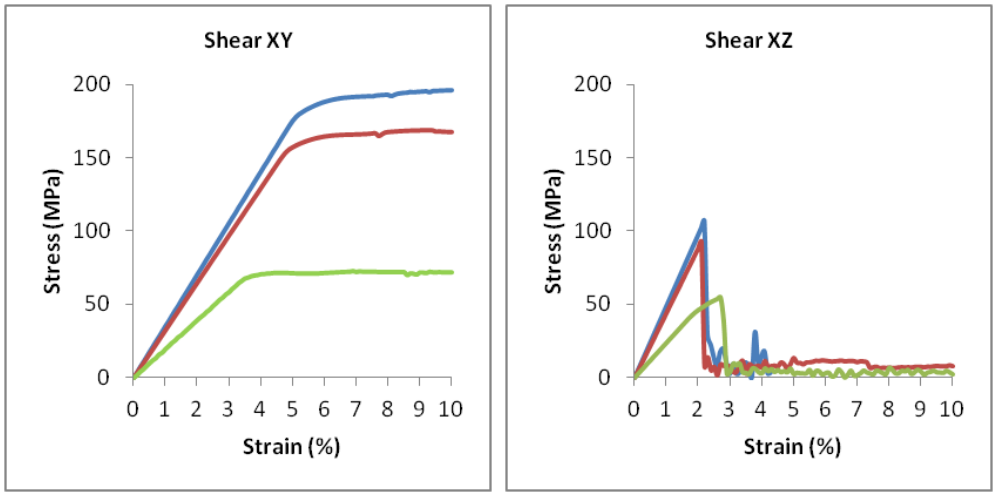

Figure 4-19. Stress strain curves for carbon/epoxy micro scale unit cell in transverse XY and longitudinal XZ shear at strain rates of 1 (green), 1000 (red) and 10000 (blue) /s

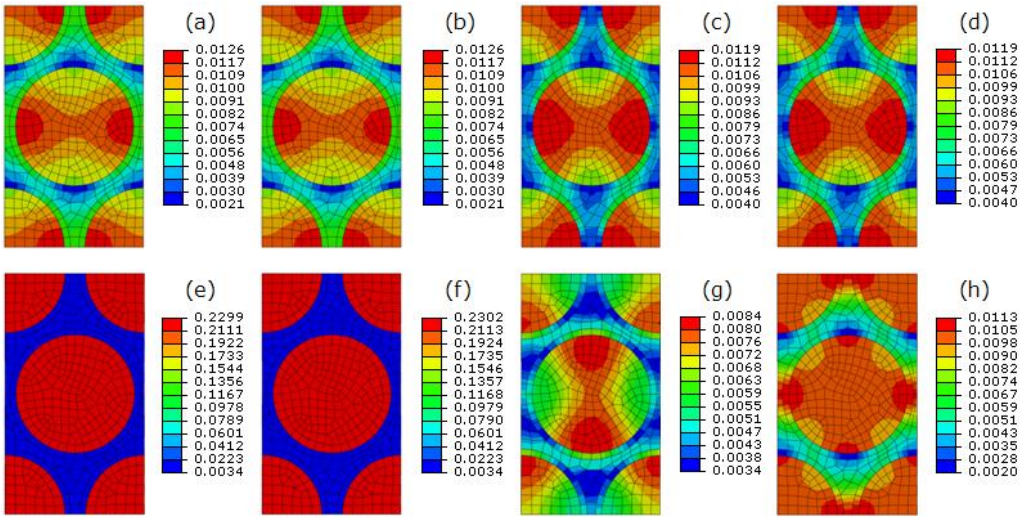

Figure 4-20. Carbon/epoxy micro scale unit cell von Mises stress contours for first step of analysis (reflecting the stress distribution throughout the elastic region) at 10000/s in (a) transverse x tension, (b) transverse x compression, (c) transverse y tension, (d) transverse y compression, (e) longitudinal z tension, (f) longitudinal z compression, (g) transverse xy shear and (h) longitudinal xz shear. Units are given in GPa

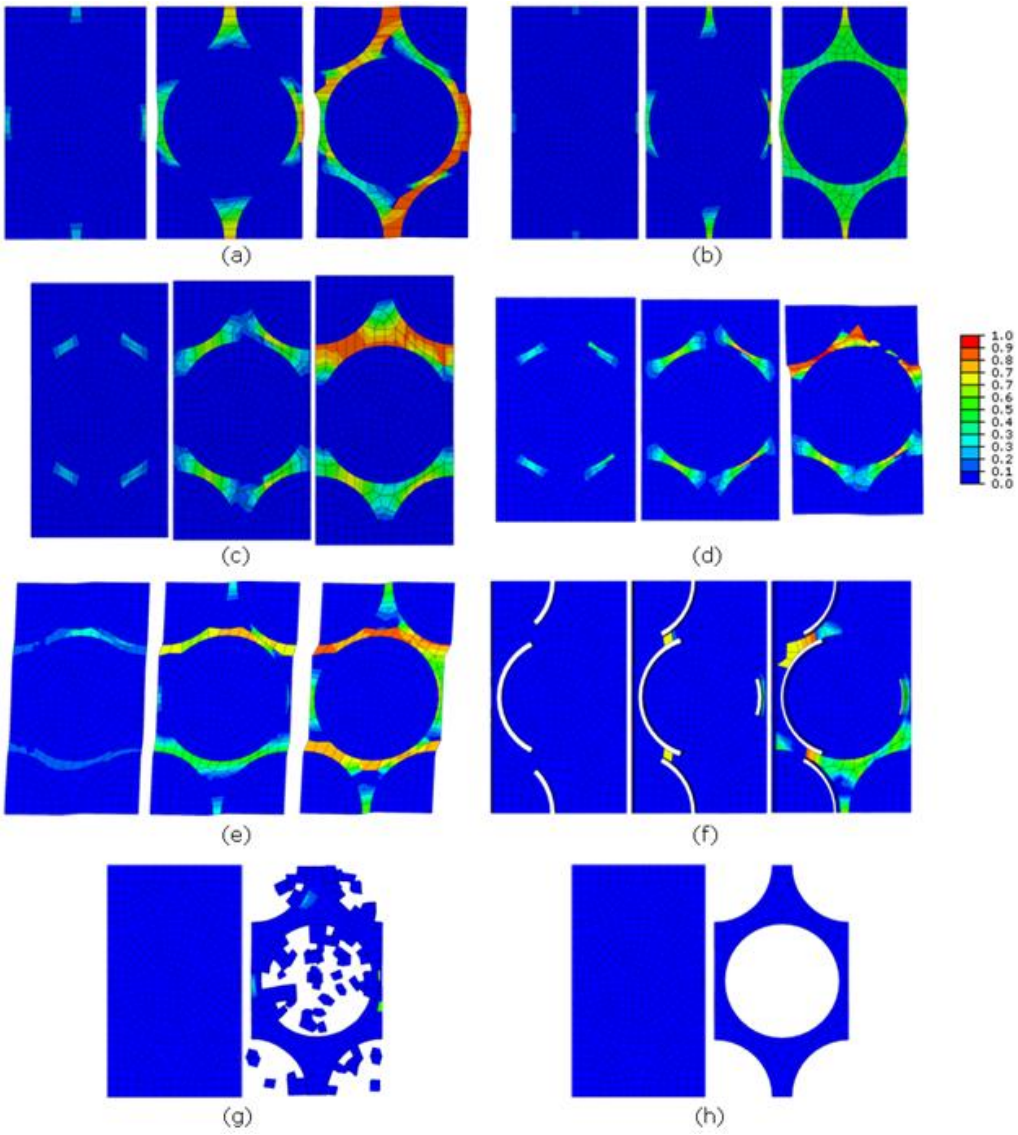

Figure 4-21. Carbon/epoxy micro scale unit cell damage variable contours. Damage varies from zero (blue) which indicates no damage to one (red) which indicates maximum damage. Unit cells are shown in (a) transverse x tension, (b) transverse x compression, (c) transverse y tension, (d) transverse y compression, (e) transverse xy shear, (f) longitudinal xz shear, (g) longitudinal z tension and (h) longitudinal z compression. Each loading condition has three stages of damage shown; initial, intermediate and final except for longitudinal loading where only two stages of damage are shown. Each loading condition is shown at a strain rate of 10000/s which is representative of damage at all strain rates.

4.4.2 S2 Glass/Epoxy

The stress strain responses for the S2 glass/epoxy micro scale unit cell are presented in Figure 4-22 for transverse loading in the x direction, Figure 4-23 for transverse loading in the y direction, Figure 4-24 for longitudinal loading, and Figure 4-25 for shear loading. For each loading condition the von Mises stress contour plots are shown in Figure 4-26 and the damage variable contour plots are shown in Figure 4-27. These results are discussed in sections 4.5 and 4.5.2 along with the carbon/epoxy results from section 4.4.1.

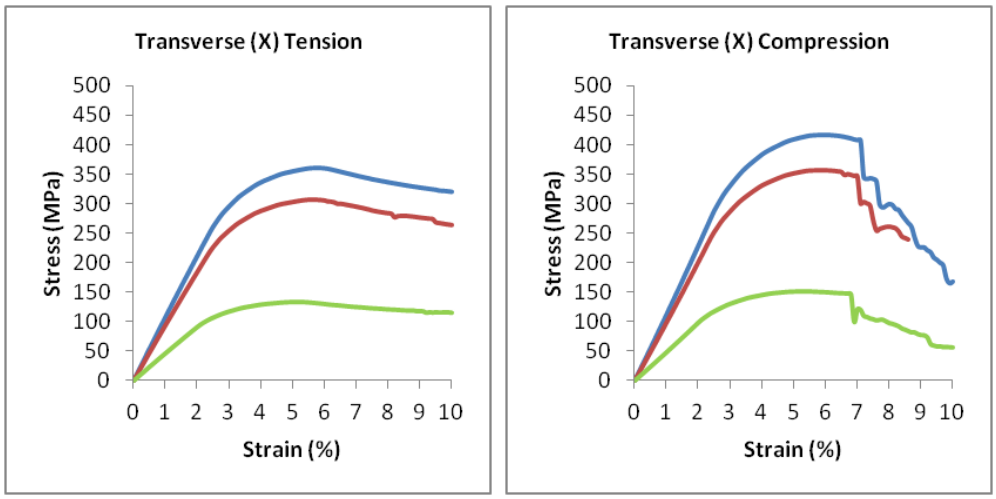

Figure 4-22. Stress strain curves for S2 glass/epoxy micro scale unit cell in transverse tension and transverse compression, in the X direction, at strain rates of 1 (green), 1000 (red) and 10000 (blue) /s

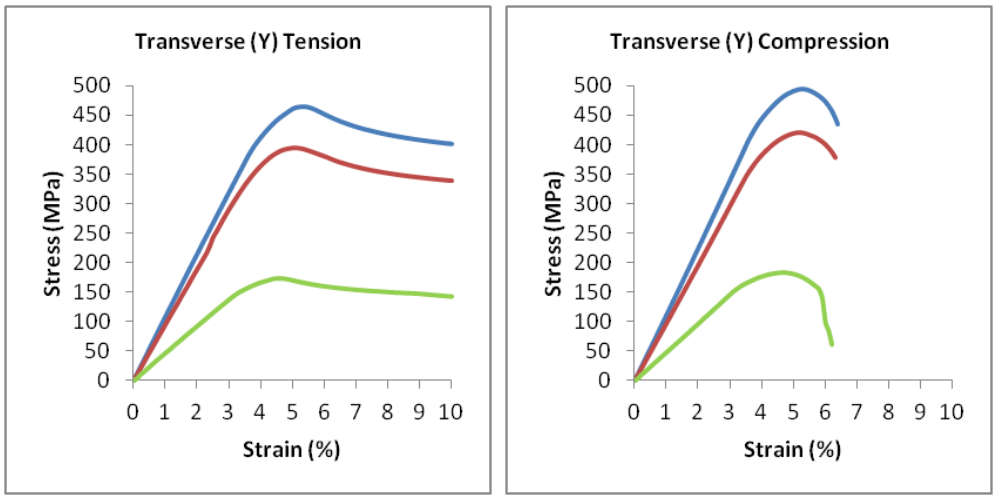

Figure 4-23. Stress strain curves for S2 glass/epoxy micro scale unit cell in transverse tension and transverse compression, in the Y direction, at strain rates of 1 (green), 1000 (red) and 10000 (blue) /s

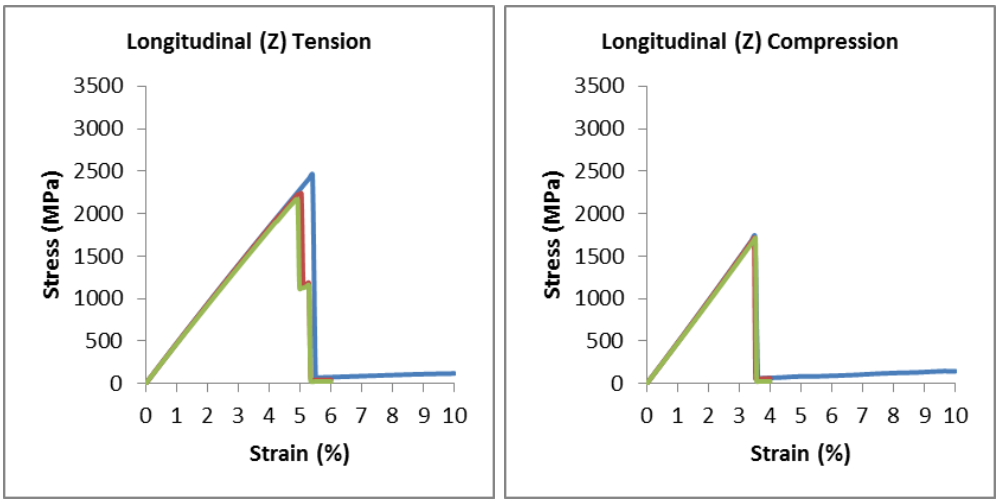

Figure 4-24. Stress strain curves for S2 glass/epoxy micro scale unit cell in longitudinal tension and longitudinal compression, in the Z direction, at strain rates of 1 (green), 1000 (red) and 10000 (blue) /s

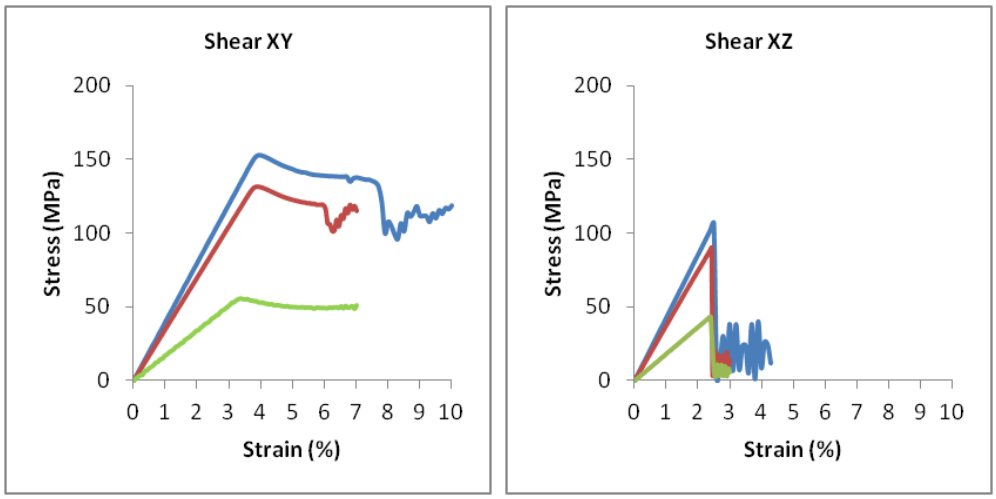

Figure 4-25. Stress strain curves for S2 glass/epoxy micro scale unit cell in transverse XY and longitudinal XZ shear at strain rates of 1 (green), 1000 (red) and 10000 (blue) /s

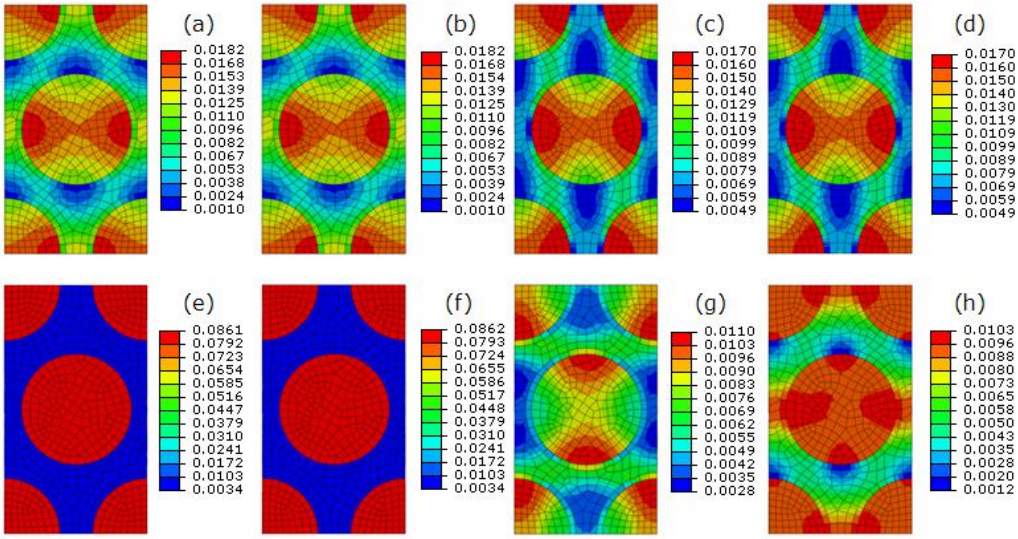

Figure 4-26. S2 glass/epoxy micro scale unit cell von Mises stress contours for first step of analysis (reflecting the stress distribution throughout the elastic region) at 10000/s in (a) transverse x tension, (b) transverse x compression, (c) transverse y tension, (d) transverse y compression, (e) longitudinal z tension, (f) longitudinal z compression, (g) transverse xy shear and (h) longitudinal xz shear. Units are given in GPa

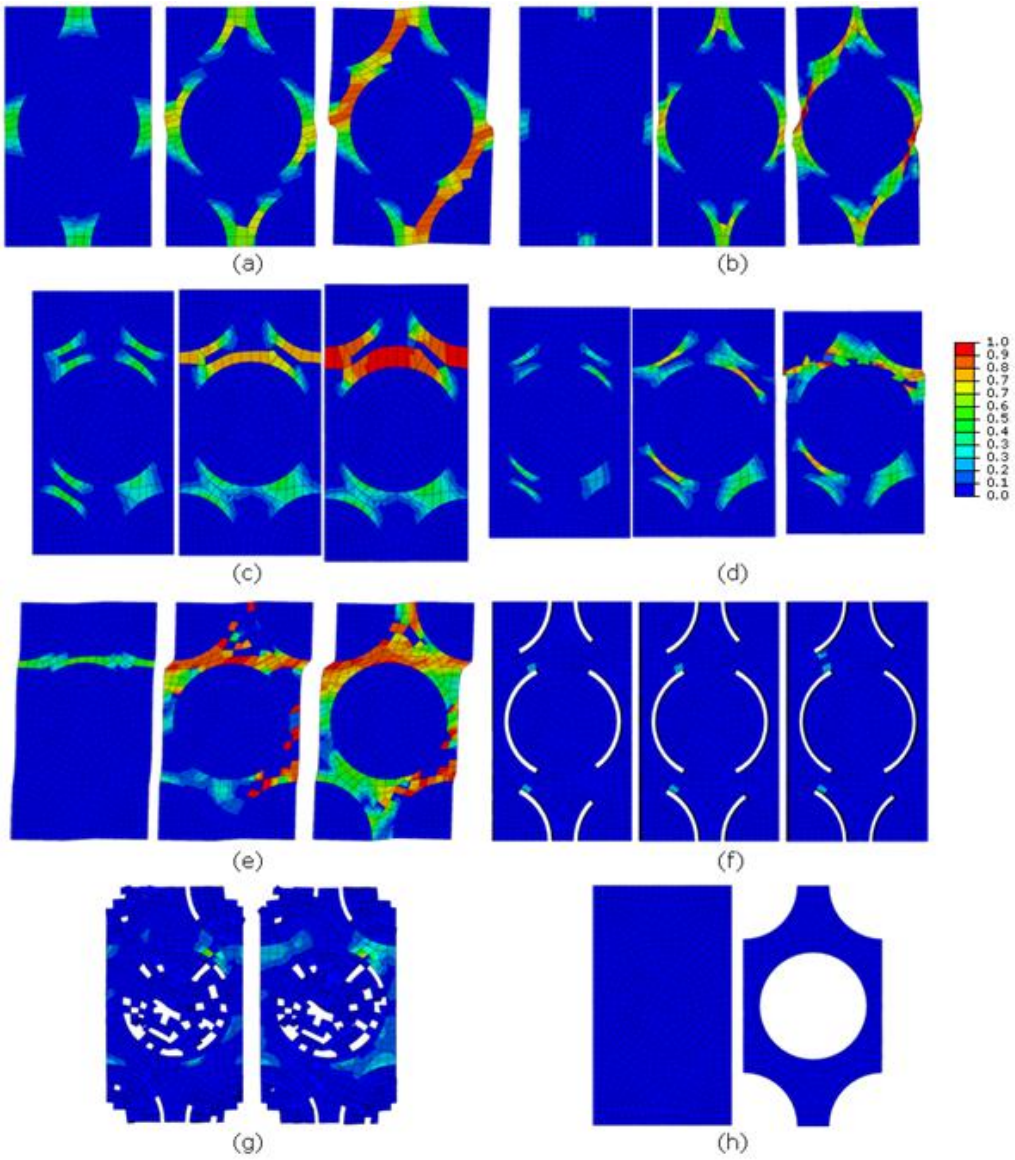

Figure 4-27. S2 glass/epoxy micro scale unit cell damage variable contours. Damage varies from zero (blue) which indicates no damage to one (red) which indicates maximum damage. Unit cells are shown in (a) transverse x tension, (b) transverse x compression, (c) transverse y tension, (d) transverse y compression, (e) transverse xy shear, (f) longitudinal xz shear, (g) longitudinal z tension and (h) longitudinal z compression. Each loading condition has three stages of damage shown; initial, intermediate and final except for longitudinal loading where only two stages of damage are shown. Each loading condition is shown at a strain rate of 10000/s which is representative of damage at all strain rates.

4.5 Micro Scale Modelling Discussion

4.5.1 Elastic and Damage Response

For both S2 glass/epoxy and carbon/epoxy micro scale unit cells in all loading conditions at all strain rates the stress strain response initially shows linear elastic behaviour.

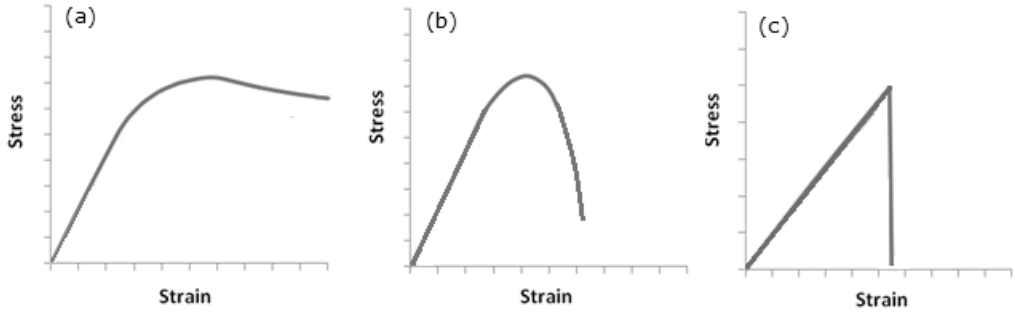

Figure 4-28. Shapes of stress strain curves seen in micro scale modelling results.

Matrix Dominated Loading Modes

For both S2 glass/epoxy and carbon/epoxy micro scale unit cells in transverse X tension, transverse Y tension and transverse XY shear, i.e. matrix dominated loading modes, the stress strain responses at all strain rates shows elastic behaviour followed by a section of gradual decreasing gradient with the shape shown in Figure 4-28 (a). This is ductile failure. This is shown in the stress strain curves for carbon/epoxy in Figure 4-16, Figure 4-17 and Figure 4-19 and for S2 glass/epoxy in Figure 4-22, Figure 4-23 and Figure 4-25. The section of gradual decreasing gradient, or strain softening, is a result of matrix damage accumulation seen physically in the damage contour plots for carbon/epoxy in Figure 4-21 (a), (c) and (e) and for S2 glass/epoxy in Figure 4-27 (a), (c) and (e). The amount and severity of damaged elements increases as the unit cell is subjected to larger strains and, as detailed in section 3.4.1, the matrix elements are damaged by gradually reducing their stiffness which results in a gradual reduction of stiffness in the unit cell stress strain response. In transverse X tension, Figure 4-21 (a) for carbon/epoxy and Figure 4-27 (a) for S2 glass/epoxy, the damage initiates horizontally between the fibres and proceeds to grow vertically eventually causing a 'crack' across the entire height of the unit cell at larger values of strain. In transverse Y tension, Figure 4-21 (c) for carbon/epoxy and Figure 4-27 (c) for S2 glass/epoxy, the damage initiates diagonally between the fibres and proceeds to grow horizontally eventually causing a 'crack' across the entire width of the unit

cell at larger values of strain. These results reflect the directional strength response discussed in section 4.3.7. In transverse XY shear, Figure 4-21 (e) for carbon/epoxy and Figure 4-27 (e) for S2 glass/epoxy, the damage initiates as horizontal lines, curving around the fibres, across the width of the unit cell and grows into all areas of the matrix at larger values of strain.

For S2 glass/epoxy and carbon/epoxy micro scale unit cells in transverse X compression and transverse Y compression the stress strain response at all strain rates is similar to that described for transverse X tension, transverse Y tension and transverse XY shear, however, the gradual decreasing gradient section is less gradual. The general shape of the stress strain curve is more like that shown in Figure 4-28 (b). The stress strain curves for transverse X and Y compression are shown in Figure 4-16 and Figure 4-17 for carbon/epoxy and Figure 4-22 and Figure 4-23 for S2 glass epoxy. As with transverse tension the transverse compression damage is a result of matrix damage accumulation. In transverse X and Y compression the damage initiates and evolves in a similar pattern to transverse X and Y tension respectively. The damage contour plots for transverse X compression can be seen in Figure 4-21 (b) for carbon/epoxy and Figure 4-27 (b) for S2 glass/epoxy. The damage contour plots for transverse Y compression can be seen in Figure 4-21 (d) for carbon/epoxy and Figure 4-27 (d) for S2 glass/epoxy.

It may initially seem strange that the stiffness degradation is less gradual in transverse compression than transverse tension as the strain softening parameter is the same for tension, compression and shear. However, in transverse compression, not transverse tension, after the maximum strength has been reached some matrix elements fail in shear. The shear strength (50MPa) is much lower than the compression strength (131MPa) so the elements reach maximum damage quickly and are deleted from the analysis. This gives some step drops in stress in the transverse compression stress strain curves. A good example of this is shown for the S2 glass/epoxy unit cell in Figure 4-22. The shape of the stress strain curves (at all strain rates) for transverse x compression is very similar to the transverse x tension stress strain curves for a few percent of strain after initial failure, where the elastic region finishes. There are then a few step drops in the stress in transverse compression due to the shear failure

discussed previously. This shear failure does not occur in transverse tension, the matrix elements just continue to be stretched for the full duration of the simulation.

Fibre and Interface Dominated Loading Modes

For S2 glass/epoxy and carbon/epoxy micro scale unit cells in longitudinal tension, longitudinal compression and longitudinal XZ shear the stress strain responses at all strain rates shows elastic behaviour followed by an abrupt, instant reduction in stiffness as in Figure 4-28 (c). This is brittle failure. The stress strain curves for longitudinal tension and compression are shown in Figure 4-18 for carbon/epoxy and Figure 4-24 for S2 glass/epoxy. The stress strain curves for longitudinal XZ shear are shown in Figure 4-19 for carbon/epoxy and Figure 4-25 for S2 glass/epoxy. The abrupt instant reduction in stiffness is due to failure in the fibres for longitudinal tension and compression as shown in the damage contour plots in Figure 4-21 (g) and (h) for carbon/epoxy and Figure 4-27 (g) and (h) for S2 glass/epoxy. By contrast, the abrupt instant reduction of stiffness is due to interface failure for longitudinal XZ shear as shown in the damage contour plots in Figure 4-21 (f) for carbon/epoxy Figure 4-27 (f) for S2 glass/epoxy. The failure in both cases is abrupt and instant as the fibre and interface material models perform element deletion as soon as damage is initiated; see sections 3.4.2 and 3.4.3 for information on the fibre and interface material models respectively.

For both carbon/epoxy and S2 glass/epoxy in longitudinal loading the tensile response has a higher strength than the compressive response, see Figure 4-18 and Figure 4-24. This is due to the higher tensile than compressive strength of carbon and S2 glass fibres in the input property data. It is important to consider how individual fibre properties are obtained. The testing of individual fibres can be problematic as they are very small, in the range of μm, making them difficult to handle. Micromechanics relations are often applied to tests on unidirectional laminae to extract individual fibre properties. These indirect methods are obviously not ideal but in some cases it is the only viable option in obtaining individual fibre properties [79].

General Observations

For S2 glass/epoxy and carbon/epoxy micro scale unit cells in all loading conditions at all strain rates initial failure occurs in an element where the maximum stress criterion reaches unity. For longitudinal loading this occurs in the fibres, for longitudinal XZ shear this occurs in the interfaces and for all other loading conditions this occurs in the matrix. The specific location of the failure within these constituents is in the highly stressed regions. These regions can be clearly identified by viewing the von Mises stress contour plots in Figure 4-20 for carbon/epoxy and Figure 4-26 for S2 glass/epoxy. In transverse X tension and compression the highest stress in the matrix is seen horizontally between the fibres. In transverse Y tension and compression the highest stress in the matrix is seen diagonally between the fibres. In longitudinal tension and compression the highest stress is equally spread over all fibres. In transverse XY shear the highest stress in the matrix is seen as a stress path horizontally across the width of the unit cell that curves between the fibres. In longitudinal XZ shear the highest stress in the interface is in the regions where the fibres are horizontally at their closest point. All these highest stressed regions correspond to the initial failure locations seen in the damage contour plots in Figure 4-21 for carbon/epoxy and Figure 4-27 for S2 glass/epoxy.

4.5.2 Strain Rate Dependent Response

For S2 glass/epoxy and carbon/epoxy micro scale unit cells the elastic and damage phases are both clearly strain rate sensitive and the increase in stiffness and strength with increasing strain rate can be seen under all loading conditions except longitudinal tension and compression, Figure 4-18 for carbon/epoxy and Figure 4-24 for S2 glass/epoxy. In longitudinal tension and compression the mode of failure is fibre dominated. The fibre material model has no strain rate dependence, shown in section 3.4.2, and hence the strain rate has little effect on the stress strain response in these loading modes. However, in longitudinal tension for both S2 glass/epoxy and carbon/epoxy a small increase in the strength with increasing strength is noticeable. This effect is due to the matrix and interface constituents strain rate dependence which has a small effect on the stress strain response of a fibre dominated loading mode. The quantification of this strain rate dependence, for both stiffness and strength, is discussed in section 4.6, where numerical constants describing micro scale strain rate

dependence are determined for passing micro scale behaviour to the meso scale.

4.5.3 Carbon and S2 Glass Comparison

In sections 4.5 and 4.5.2 general trends were pointed out that were applicable to both testing of carbon/epoxy and S2 glass/epoxy micro scale unit cells. There are obviously differences in the results due to the different input properties for the carbon and S2 glass fibres which will be discussed in this section. The difference in the stress strain responses can be seen in Figure 4-29.

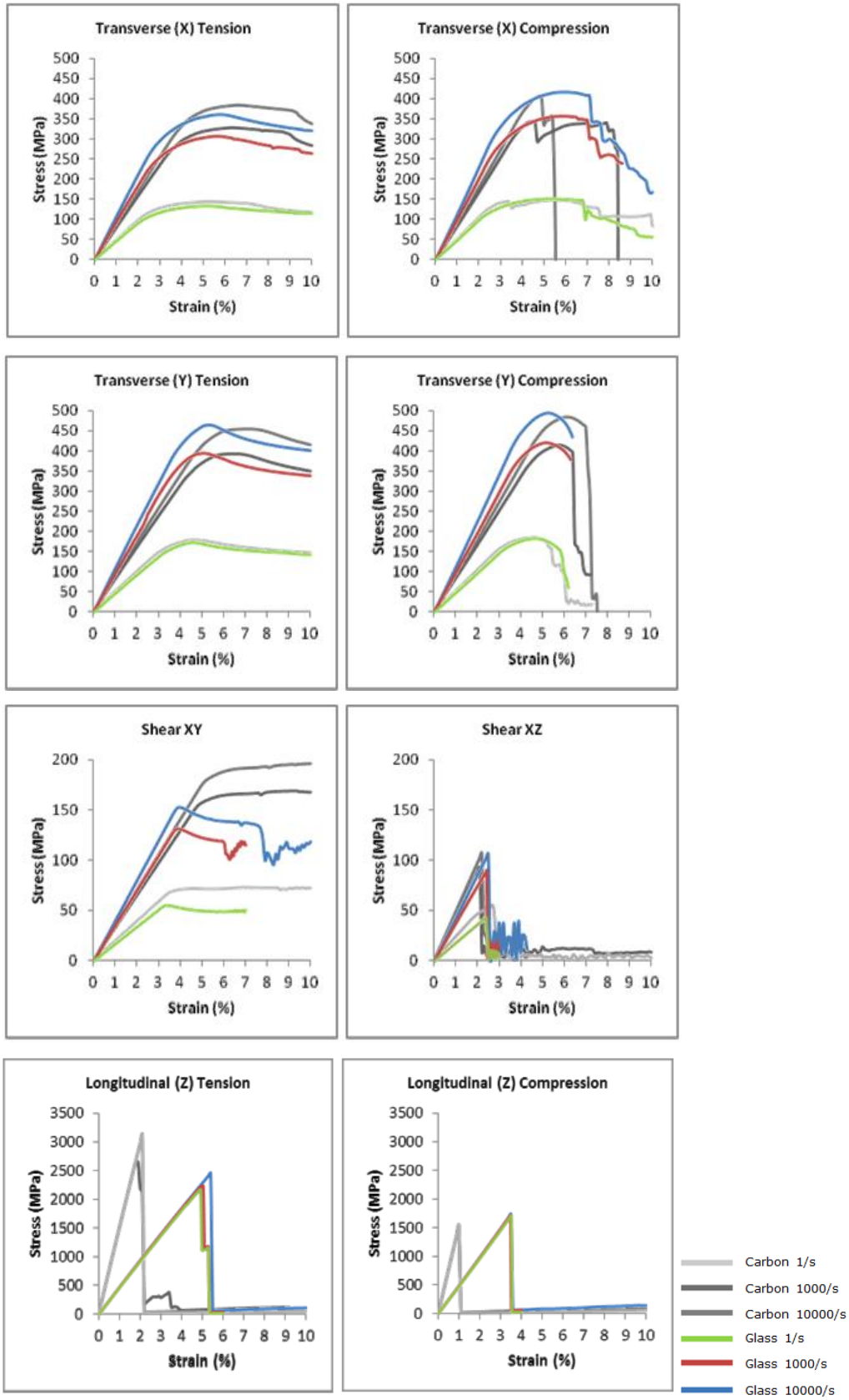

Figure 4-29. Comparison of carbon/epoxy (1/s-light grey, 1000/s-black, 10000/s-dark grey) and S2 glass/epoxy (1/s-green, 1000/s-red, 10000/s-blue) stress strain curves for all loading conditions.

Unit Cell Stiffness Properties

The Rule of Mixtures (ROM) was used to calculate longitudinal stiffness, transverse stiffness, longitudinal shear stiffness (XZ) and transverse shear stiffness (XY). These values were calculated using carbon material properties at the volume fraction of 66.28% and S2 glass material properties at the volume fraction of 54.32%. The results, shown in Figure 4-33 and Figure 4-34, suggest that the transverse stiffness and both shear stiffness's should be slightly larger for carbon/epoxy than S2 glass/epoxy and the longitudinal stiffness should be significantly larger for carbon/epoxy than S2 glass/epoxy. This is the case in the modelling results for longitudinal tension, longitudinal compression and longitudinal XZ shear at all rates of strain tested, see Figure 4-29 and Figure 4-30. For all other loading conditions (transverse (X and Y) tension and compression and transverse XY shear) this is only true for the modelling results at a strain rate of 1 /s, see Figure 4-29 and Figure 4-30. For the two higher rates of strain (1000 /s and 10000 /s) the modelling results show that the S2 glass/epoxy unit cell is slightly stiffer than the carbon/epoxy unit cell, see Figure 4-29 and Figure 4-30. The one anomaly in this trend is that in XY shear the stiffness values at 1/s are the same for both S2 glass/epoxy and carbon/epoxy unit cells.

	Strain Rate (/s)	S2 Glass / Epoxy Stiffness (GPa)	Carbon / Epoxy Stiffness (GPa)
Transverse X Tension	1	4.36	5.16
	1000	9.59	8.13
	10000	10.92	8.79
Transverse X Compression	1	4.38	5.17
	1000	9.63	8.15
	10000	10.96	8.81
Transverse Y Tension	1	4.70	4.99
	1000	9.61	8.13
	10000	11.18	8.69
Transverse Y Compression	1	4.80	4.99
	1000	9.62	8.14
	10000	11.20	8.71
Longitudinal Z Tension	1	47.01	151.23
	1000	47.73	151.78
	10000	47.97	151.97
Longitudinal Z Compression	1	46.88	151.54
	1000	47.78	152.09
	10000	48.06	152.28
Shear XY	1	1.67	1.67
	1000	3.54	3.25
	10000	4.13	3.44
Shear XZ	1	1.93	2.36
	1000	3.75	4.40
	10000	4.25	4.88

Figure 4-30. Table showing the values of unit cell stiffness from micro scale modelling results for both S2 glass/epoxy and carbon/epoxy in all loading modes and at all strain rates. Highlighted sections show which is unit cell has a larger stiffness value, S2 glass/epoxy or carbon/epoxy

The three loading conditions where carbon/epoxy unit cells are stiffer than S2 glass/epoxy unit cells at all strain rates (longitudinal tension, longitudinal compression and longitudinal XZ shear) all experience non matrix dominated failure i.e. longitudinal failure is fibre dominated and longitudinal shear failure is interface dominated. All other loading conditions experience matrix dominated failure and it is these modelling results which show a change in stiffness trend from carbon/epoxy unit cells being stiffer at 1/s to S2 glass/epoxy unit cells being stiffer at 1000/s and 10000/s. The matrix is the largest strain rate sensitive constituent, the fibre constituent is strain rate insensitive and the interface constituent is strain rate sensitive but a very small portion of the unit cell. It appears that the matrix is causing this effect of making S2 glass/epoxy unit cells stiffer than carbon/epoxy unit cells at high strain rates in transverse (X and

Y) tension and compression and transverse XY shear. The fibre volume fraction in the carbon/epoxy and S2 glass/epoxy unit cell is 66.28% and 54.32% respectively. The S2 glass/epoxy unit cell has a larger ratio of matrix material than the carbon/epoxy unit cell; hence, there is a larger ratio of strain rate sensitive material. When testing at high strain rates this larger ratio of strain rate sensitive material is assigned a larger stiffness value through the material model making the S2 glass/epoxy unit cell stiffer than the carbon/epoxy unit cell in transverse (X and Y) tension and compression and transverse XY shear.

Using the ROM equations with transverse fibre stiffness and fibre volume fraction values of 15GPa and 0.6628 for carbon respectively and 86GPa and 0.5432 for S2 glass respectively, one can calculate the transverse unit cell stiffness with matrix stiffness values varying from the quasi static value of 1.423GPa. Following this using the transverse unit cell stiffness values and Poisson's ratio values of 0.2 and 0.23 for carbon and S2 glass respectively one can calculate, using ROM, the unit cell transverse shear stiffness. The results, shown in Figure 4-31, further emphasise the previous point that when the matrix stiffness is strain rate scaled past a critical value, the S2 glass unit cell becomes stiffer than the carbon unit cell in transverse and transverse shear loading. Thus the ROM calculations agree with the strain rate dependence comparisons on condition appropriate resin properties are used for the particular rate of loading.

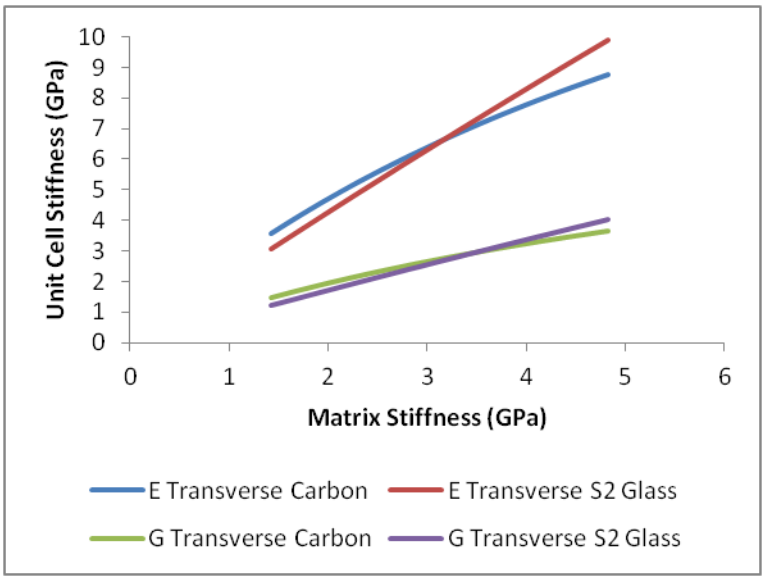

Figure 4-31. Unit cell transverse and transverse shear stiffness values at increasing matrix stiffness values using ROM equations.

Unit Cell Strength Properties

The failure strengths for carbon/epoxy and S2 glass/epoxy unit cells are similar for transverse, X and Y, tension and compression, see Figure 4-29 and Figure 4-32, as this is matrix dominated failure and both unit cells have identical matrix properties. The same reasoning exists for longitudinal XZ shear where failure strengths are similar, see Figure 4-29 and Figure 4-32, as this is interface dominated failure and both unit cells have identical interface properties. However, in longitudinal tension the carbon/epoxy unit cell has a higher strength than the S2 glass/epoxy unit cell, see Figure 4-29 and Figure 4-32. This is because the longitudinal tensile strength of carbon fibre, 4900MPa, is greater than that of S2 glass fibre, 4590MPa. In longitudinal compression the carbon/epoxy unit cell has a lower strength that the S2 glass/epoxy unit cell, see Figure 4-29 and Figure 4-32. This is because the longitudinal compressive strength of S2 glass fibre, 3100MPa, is greater than that of carbon fibre, 2500MPa. In transverse XY shear the failure strength is greater in the carbon/epoxy unit cell than the S2 glass/epoxy unit cell, see Figure 4-29 and Figure 4-32.

	Strain Rate (/s)	S2 Glass / Epoxy Strength (MPa)	Carbon / Epoxy Strength (MPa)
Transverse X Tension	1	133	144
	1000	308	329
	10000	360	384
Transverse X Compression	1	152	148
	1000	356	343
	10000	417	407
Transverse Y Tension	1	174	178
	1000	395	392
	10000	465	455
Transverse Y Compression	1	183	184
	1000	420	415
	10000	494	484
Longitudinal Z Tension	1	2166	3114
	1000	2240	2665
	10000	2463	3128
Longitudinal Z Compression	1	1714	1529
	1000	1718	1535
	10000	1739	1537
Shear XY	1	55	73
	1000	132	169
	10000	153	196
Shear XZ	1	43	54
	1000	90	92
	10000	107	107

Figure 4-32. Table showing the values of unit cell strength from micro scale modelling results for both S2 glass/epoxy and carbon/epoxy in all loading modes and at all strain rates.

4.5.4 Analytical Results Comparison

The graphs in Figure 4-33 and Figure 4-34 compare the longitudinal, transverse, longitudinal shear and transverse shear quasi-static stiffness's predicted from the micro scale modelling and an analytical method, namely the Rule of Mixtures, which is well documented in [9]. The longitudinal stiffness values compare extremely well with less than a 1% change between analytical and micro modelling results. For transverse, longitudinal shear and transverse shear stiffness the micro modelling results are always larger than the analytical predictions. The difference is small (around 10%) for S2 glass and carbon longitudinal shear and carbon transverse shear stiffness values but much larger (40 to 50%) for S2 glass and carbon transverse stiffness and S2 glass transverse shear stiffness values. It is important to note here that the micro scale modelling results

are being compared to an analytical method that is based on certain simplifications. It has been stated in the literature, [9], that the Rule of Mixtures is a poor approximation of transverse stiffness. This also leads to a poor approximation of the transverse shear stiffness as this value is calculated using the transverse stiffness. It is these values, transverse stiffness and transverse shear stiffness, where analytical results do not compare well to micro scale modelling results. The Rule of Mixtures gives a poor prediction of transverse stiffness due to the slab model approximation and equal stress assumption during transverse loading. It is more accurate to take into account the actual distribution of stress and strain during transverse loading, as with the micro modelling work in this thesis, with fibre geometry rather than the slab geometry approximation.

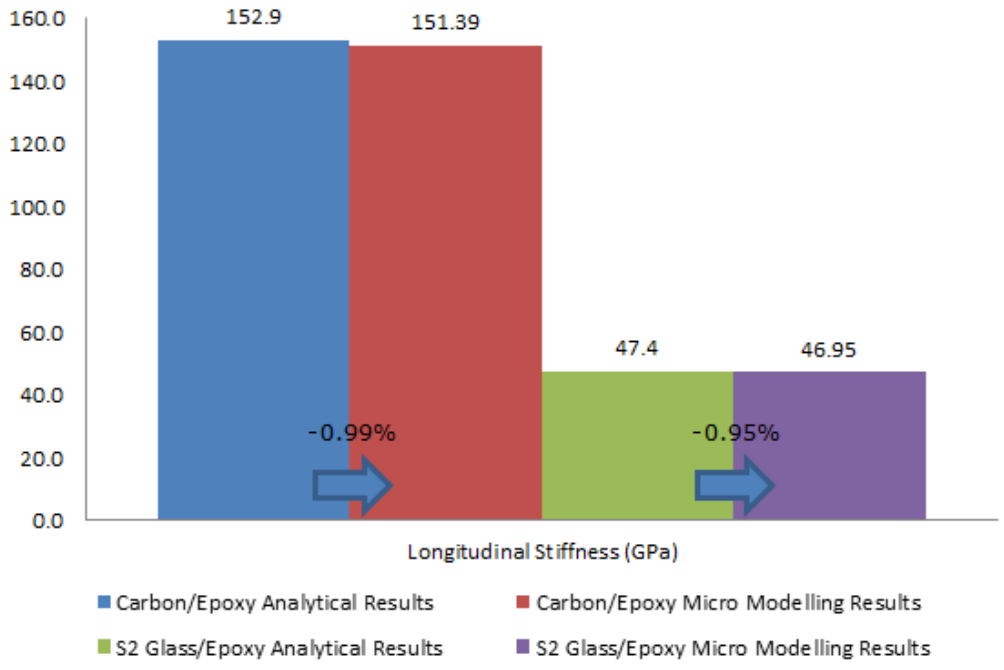

Figure 4-33. Longitudinal quasi-static stiffness comparison between analytical and micro scale modelling results

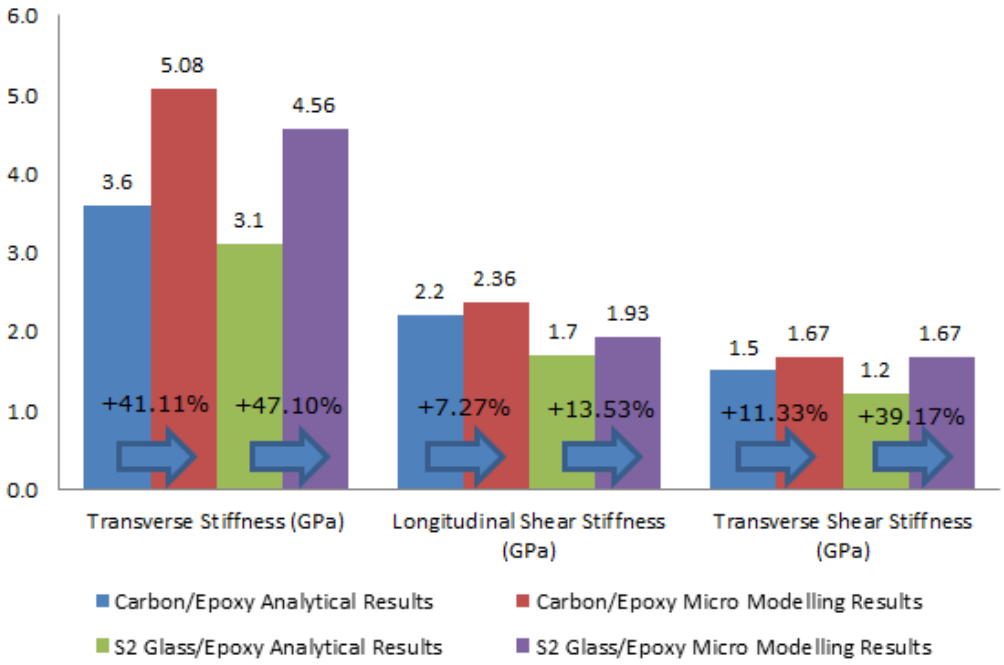

Figure 4-34. Transverse, longitudinal shear and transverse shear quasi-static stiffness comparison between analytical and micro scale modelling results

4.6 Micro to Meso Scale

All the micro scale modelling results for carbon/epoxy and S2 glass/epoxy unit cells are homogenised into properties that are carried forward for use as meso scale S2 glass and carbon yarn properties respectively. The following parameters are obtained from the stress strain curves: stiffness values, Poisson's ratio values, strengths, strain softening parameters and strain rate scaling constants for stiffness and strength. The stiffness, strength and Poisson's ratio values are simple to obtain. The strain softening parameters and strain rate scaling parameters require further analysis of the stress strain results.

The strain softening parameter controls the rate of stiffness degradation after damage initiation. The value is obtained through a curve fitting exercise where Equation 3-9, 3-10 and 3-11 are implemented in a spreadsheet with the appropriate stiffness and maximum stress criteria (calculated using stiffness, strain and strength). The resulting data is plotted against the micro modelling results stress strain curve and the strain softening parameter is altered so that the shape of the post elastic stress strain curve is the same. Twenty four strain softening parameters are obtained, for each material, from the twenty four stress strain curves (eight loading conditions tested at three strain rates). There is a significant

variation in these strain softening parameters as they represent everything from the abrupt stiffness degradation, such as in longitudinal tensile loading, to the gradual stiffness degradation, such as in transverse tensile loading. Values range from positive values less than one for gradual stiffness degradation to values of 100 for abrupt stiffness degradation.

A strain rate scaling constant is obtained by plotting a parameter (stiffness or strength) in a particular loading condition against the natural log of the strain rate. As each loading condition has been tested at three strain rates there will be three coordinates on the plot. The gradient of a linear trend line through these three coordinates divided by the value of the parameter (stiffness or strength) at the intersection with the y axis gives the strain rate scaling constant for the parameter in that particular loading condition. As there are eight loading conditions there will be eight strain rate scaling constants for stiffness and eight for strength. An example of one the plots described is shown in Figure 4-35 where the strain rate scaling constant would be the gradient of the trend line (0.40317) divided by the value of the parameter at the intersection with the y axis (5.19439) which equals 0.0776. The stiffness and strength against the natural log of strain rate plots for S2 glass/epoxy and carbon/epoxy micro scale unit cells in all loading conditions can be found in Appendix C.

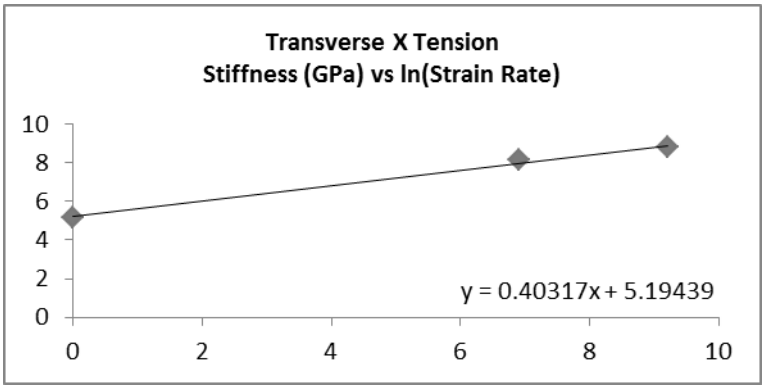

Figure 4-35. Stiffness against the natural log of strain rate for a carbon/epoxy micro scale unit cell subjected to transverse x tension.

The micro scale modelling results in a vast amount of material parameters that have to be reduced into homogenised material properties of the meso scale yarns. For example, the micro scale output properties produce eight strength strain rate scaling constants and the meso scale yarn input properties require one strength strain rate scaling constant. Figure 4-36

details how each of the meso scale yarn input properties are obtained from the large amount of micro scale output properties.

	Carbon/Epoxy	S2 Glass/Epoxy	
Longitudinal Stiffness (GPa)	151.3852	46.9465	Average of longitudinal tensile and longitudinal compressive stiffness values at 1/s strain rate
Transverse Stiffness (GPa)	5.0768	4.5627	Average of transverse X and Y tensile and compressive stiffness values at 1/s strain rate
Poisson's Ratio 12	0.3865	0.4420	Average of V12 from transverse X tension and compression and V21 from transverse Y tension and compression at 1/s strain rate
Poisson's Ratio 23	0.0091	0.0258	Average of V13 from transverse X tension and compression and V23 from transverse Y tension and compression at 1/s strain rate
In Plane Shear Stiffness 12 (GPa)	1.6722	1.6725	Shear XY stiffness value at 1/s strain rate
Longitudinal Shear Stiffness 13 (GPa)	2.3572	1.9316	Shear XZ stiffness value at 1/s strain rate
Longitudinal Tensile Strength (GPa)	3.1138	2.1661	Longitudinal tensile strength at 1/s strain rate
Longitudinal Compressive Strength (GPa)	1.5294	1.7139	Longitudinal compressive strength at 1/s strain rate
Transverse Tensile Strength (GPa)	0.1613	0.1533	Average of transverse X and Y tensile strengths at 1/s strain rate
Transverse Compressive Strength (GPa)	0.1662	0.1677	Average of transverse X and Y compressive strengths at 1/s strain rate
In Plane Shear Strength (GPa)	0.0728	0.0553	Shear XY strength value at 1/s strain rate
Longitudinal Shear Strength (GPa)	0.0544	0.0432	Shear XZ strength value at 1/s strain rate
Longitudinal Tensile Strain Softening Parameter	100	100	Assumed due to abrupt nature of failure
Longitudinal Compressive Strain Softening Parameter	100	100	Assumed due to abrupt nature of failure
Transverse Tensile Strain Softening Parameter	0.2750	0.2750	Average of transverse X and Y tensile strain softening parameters at 1, 1000 and 10000 /s strain rates
Transverse Compressive Strain Softening Parameter	1.1667	1.1667	Average of transverse X and Y compressive strain softening parameters at 1, 1000 and 10000 /s strain rates
In Plane Shear Strain Softening Parameter	0.1	0.6667	Average of shear XY strain softening parameters at 1, 1000 and 10000 /s strain rates
Longitudinal Shear Strain Softening Parameter	100	100	Assumed due to abrupt nature of failure
Longitudinal Stiffness Strain Rate Scaling Constant	0.0005	0.0025	Average of longitudinal tensile and compressive stiffness strain rate scaling constants
Transverse Stiffness Strain Rate Scaling Constant	0.0799	0.1564	Average of transverse X and Y tensile and compressive stiffness strain rate scaling constants
Shear Stiffness Strain Rate Scaling Constant	0.1170	0.1456	Average of shear XY and shear XZ stiffness strain rate scaling constants
Strength Strain Rate Scaling Constant	0.1250	0.1445	Average of all loading conditions strength strain rate scaling constants

Figure 4-36. Micro scale output properties / Meso scale yarn input properties for S2 glass/epoxy and carbon/epoxy with details of how the values were obtained

For some meso scale yarn input properties the choice of which micro scale output properties to average does not have a significant effect on the resulting value as the values are similar e.g. the meso scale yarn input property for longitudinal stiffness is the average of the longitudinal tensile and longitudinal compressive stiffness values from micro scale modelling, which are very similar. However, for some meso scale yarn input properties the choice of which micro scale output properties to average does have a significant effect on the resulting value as the values are not

similar. This is the case for the meso scale yarn input property called the strength strain rate scaling constant. This is an average of the strength strain rate scaling constant for all loading conditions from micro scale modelling i.e. eight values. These eight values for carbon/epoxy are 0.1802, 0.1898, 0.1690, 0.1763, -0.0045, 0.0005, 0.1842 and 0.1044 and for S2 glass/epoxy are 0.1867, 0.1902, 0.1827, 0.1848, 0.0126, 0.0013, 0.1935 and 0.1593 for transverse x tension, transverse x compression, transverse y tension, transverse y compression, longitudinal z tension, longitudinal z compression, transverse xy shear and longitudinal xz shear respectively. The values with the graphs they were obtained from are given in Appendix C. The average of the eight values gives 0.1250 for carbon/epoxy and 0.1445 for S2 glass/epoxy. These values are comparable to most values for the individual loading modes strain rate scaling constants, however, there is a significant difference between the longitudinal z tension and longitudinal z compression values and the average value. This is an important point to consider and the effect it has on the meso scale modelling results is discussed later in 5.5.2.

5 Meso Scale Modelling

5.1 Introduction

This chapter involves the numerical simulation and prediction of high strain rate material properties of composite lamina. The modelling takes place at the meso scale where fibre bundles / yarns are arranged in a desired architecture, e.g. 0°/90° NCF, and embedded in a matrix material. Finite element analysis of carbon/epoxy and S2 glass/epoxy meso scale unit cells provides the high strain rate properties of carbon/epoxy and S2 glass/epoxy composite lamina subsequently to be used in macro scale analyses. The key feature of this analysis is that the majority of input material properties have been generated by the micro scale modelling in Chapter 4.

The chapter first details some micrograph work to establish yarn geometries followed by some modelling studies that have been conducted to obtain certain modelling parameters and to gain confidence in the user defined material models. Meso scale modelling results are then presented for both carbon/epoxy and S2 glass/epoxy unit cells; see section 3.2 for unit cell definitions. The unit cells have been tested in in-plane tension, in-plane compression, through-thickness tension, through-thickness compression, in-plane shear and through-thickness shear loading. Each loading condition has been tested over a range of strain rates from 1 /s to 10000 /s. The analysis of the data is then presented including detailed assessment of the damage evolution and high strain rate material properties for use in macro scale modelling. The chapter is concluded with a detailed discussion of the results.

5.2 Meso Scale Micrograph Analysis

5.2.1 Yarn Dimension Study

This section presents the results of the meso scale micrograph analysis to determine yarn width and yarn height of carbon and S2 glass yarns described in section 3.2.2. The length of the carbon and S2 glass yarns were found to be 3235μm (standard deviation of 306μm) and 3611μm (standard deviation of 366μm) respectively. The height of the carbon and

S2 glass yarns were found to be 465μm (standard deviation of 35μm) and 424μm (standard deviation of 23μm) respectively. Examples of the optical micrographs used to make these measurements are shown in Figure 5-1. The shape of yarns can vary from elliptical to rectangular, as seen in Figure 5-1. This variability is investigated further in section 5.3.4.

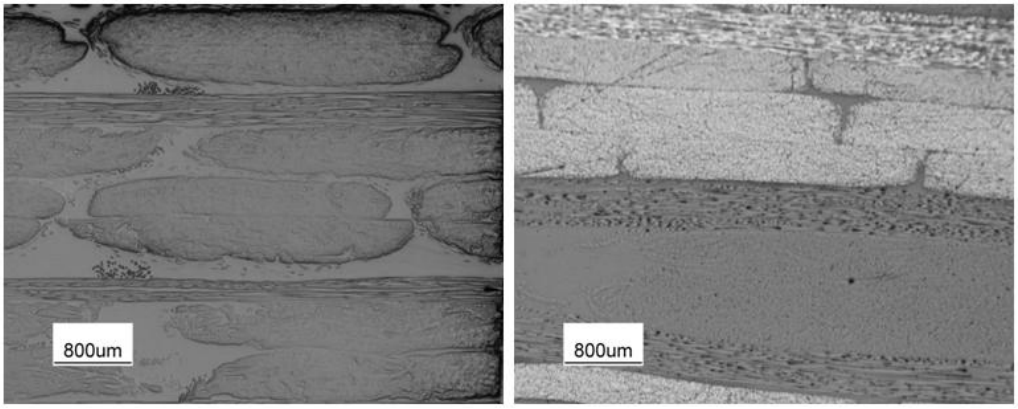

Figure 5-1. Optical micrographs of laminate cross sections of S2 glass/epoxy laminate (left) and hybrid carbon S2 glass/epoxy laminate (right)

5.3 Meso Scale Modelling Studies

5.3.1 Mesh Sensitivity Study

A mesh sensitivity study was conducted on a carbon/epoxy meso scale unit cell to establish the optimum mesh density giving accuracy of solution and convergence of results. The unit cell was tested at three different mesh densities in in-plane tension at 1000/s, the rate being selected for speed of analysis. The effect of mesh density on the stress strain response is presented in Figure 5-2 where it can be seen all responses were identical. To go to coarser meshes would introduce high aspect ratio elements in the small through thickness gaps; hence, the choice was made to run with the mesh with 28680 elements. The unit cell meshed at this density is shown in Figure 5-2.

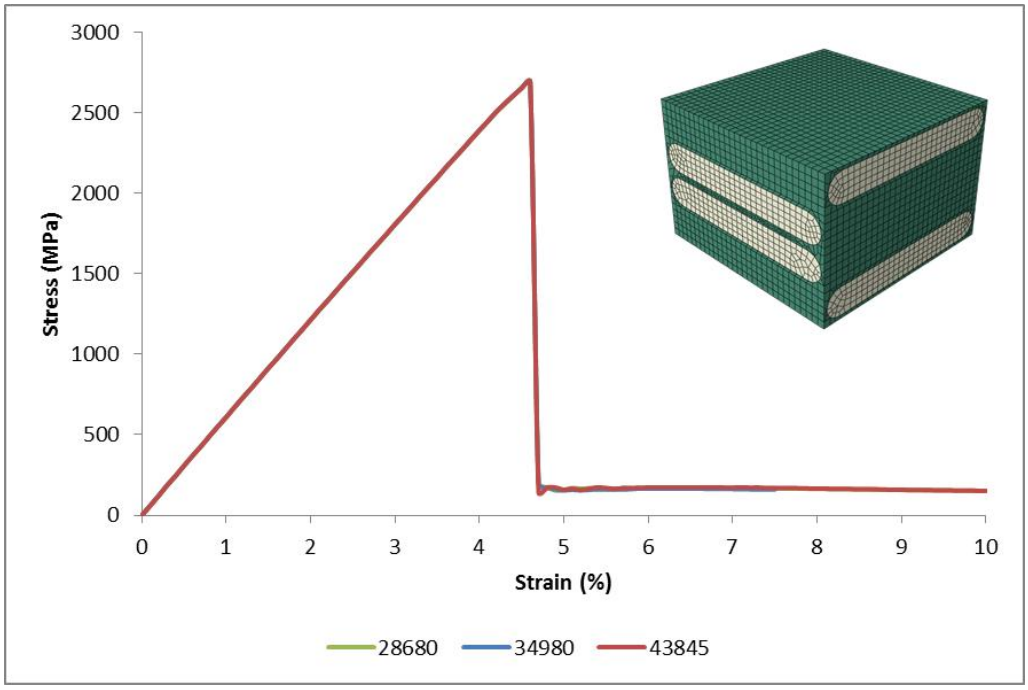

Figure 5-2. Stress strain response of carbon/epoxy meso scale unit cell with three different mesh densities subjected to in-plane tension at 1000 /s. The unit cell is shown with a mesh containing 28680 elements.

5.3.2 Mass Scaling Study

Mass scaling involves adding nonphysical mass to the model in order to achieve a larger stable time step and, therefore, reduced simulation run times. The technique should only be used when the addition of the nonphysical mass does not significantly affect the overall results. A carbon/epoxy meso scale unit cell was tested in in-plane tension with increasing density values from the original value. Simulations were run where the original density value was multiplied by 1e3, 1e6 and 1e9. This testing resulted in identical stress strain responses when density was multiplied by 1e3 and 1e6 but deviation from the original response with an oscillatory pattern occurred with a multiplier of 1e9. An appropriate level of mass scaling, a multiplier of 1e6, was chosen to be used for the meso simulations at the lowest strain rate where long simulations run times were expected. This speeded up the analyses significantly.

5.3.3 Strain Time Loading Study

The loading of the meso scale unit cells at the highest strain rate results in oscillatory unstable stress strain responses. The way in which unit cells are loaded in this study is by applying a direct strain to the unit cell in a defined time, where this time is varied to give the desired strain rate. The strain is applied in such a way to give a constant strain rate test i.e. by increasing the strain from zero strain at zero time to maximum strain at maximum time. This is shown in Figure 5-3 as the tabular amplitude and results in the unit cell begin subjected to an instantaneous strain rate which causes the oscillatory unstable stress strain responses. It is possible that these oscillations are due to stress wave propagation that was not seen in micro modelling due to the smaller length scale. The period of the oscillations could be due to the stress wave travelling through the unit cell and being reflected from unit cell boundaries. Further investigation into stress wave propagation, which is outside the scope of this thesis, would be required to verify this hypothesis.

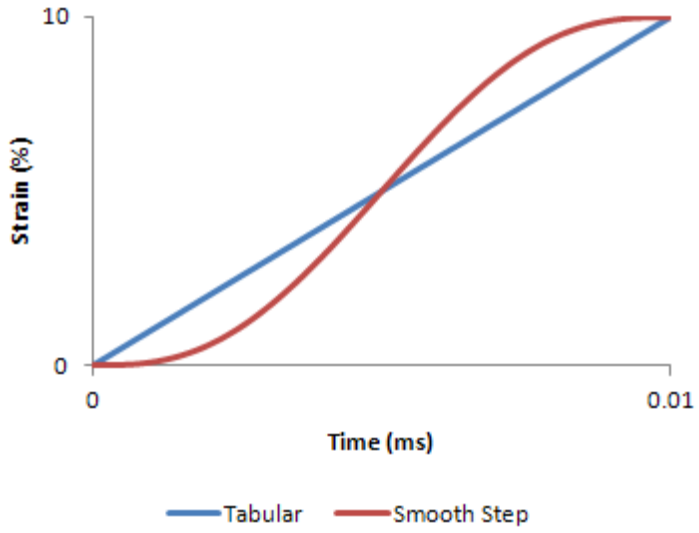

Figure 5-3. Strain vs Time plot showing tabular and smooth step loading amplitudes

In an attempt to resolve this issue, all loading conditions were tested at the highest strain rate with the tabular amplitude and also using a smooth step amplitude as shown in Figure 5-3. The smooth step amplitude allows a more gradual increase in the strain rate rather than a large instantaneous strain rate. The results in through thickness compression, which gives a good representation of the results in other loading conditions, is shown in Figure 5-4. The smooth step amplitude resolves the issue of an unstable response and does not appear to affect the stress strain response in a

significant way i.e. the general trend seen in the tabular stress strain response is very similar to the smooth step stress strain response if the oscillations were filtered out. The smooth step loading was subsequently used in all high strain rate simulations.

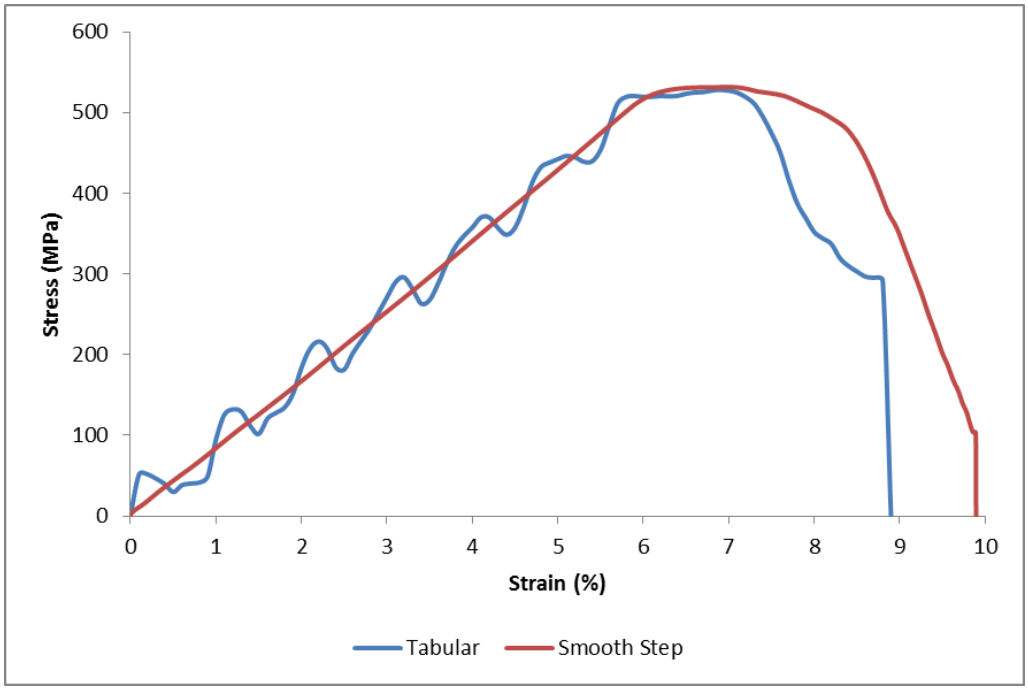

Figure 5-4. Stress strain response of carbon meso scale unit cell subjected to through thickness compression at 10000/s with two different loading amplitudes

5.3.4 Yarn Shape Sensitivity Study

Elliptical and rounded brick yarns demonstrate the two extremes of yarn shapes.

An elliptical yarn is defined by specifying three points; (1) a centre point, (2) an axis endpoint and (3) an arbitrary point whose distance from the first axis determines the length of the second axis. This is demonstrated in Figure 5-5.

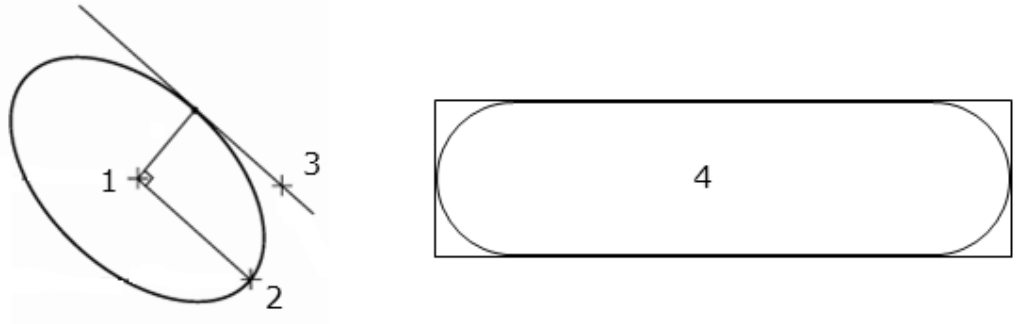

Figure 5-5. Ellipse generation: 1-centre point, 2-axis endpoint and 3-arbitrary point whose distance from the first axis determines the length of the second axis. 4-Rounded brick generation

A rounded brick yarn is defined by applying full rounds to each end of a rectangle as seen in Figure 5-5. In other words each corner of the rectangle has a filleted radius equal to half the height of the rectangle.

A NCF S2 glass/epoxy meso scale unit cell was tested in in-plane tension, in-plane compression, through-thickness tension, through-thickness compression, in-plane shear and through-thickness shear. The unit cell was tested at a strain rate of 1000/s for speed of analysis. This test procedure was performed twice, once with elliptical shaped yarns and once with rounded brick shape yarns. The dimensions of the elliptical shaped yarns were measured from micrographs i.e. yarn height and yarn width. The rounded brick shape yarn dimensions were adjusted to give the same volume fraction of yarns in the meso scale unit cell as for the elliptical yarn model.

An almost identical stress strain response for elliptical and rounded brick yarn models was obtained for all loading conditions. The only difference was in the through thickness tension where the post elastic response differed with the elliptical yarn model having a more ductile, less aggressive degradation of stiffness, response than the rounded brick yarn model, see Figure 5-6.

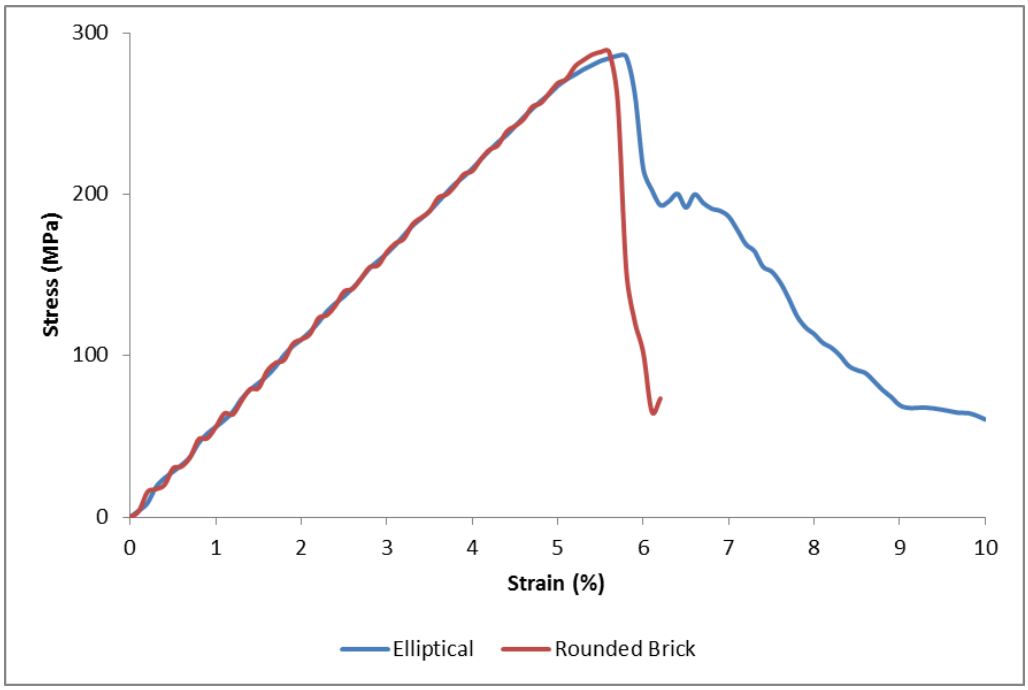

Figure 5-6. S2 glass/epoxy meso scale unit cell in through thickness tension at 1000 /s with elliptical and rounded brick yarn shapes.

Kari *et al* [80] investigated the effect of yarn cross sectional shape on the mechanical properties of 3D woven carbon/epoxy composites through finite element analysis. Five different weft yarn cross sections were considered ranging from sharp edged ellipses to rectangles to rectangles with semi-circular ends. The cross sections of the warp and binder yarns were the same in all five models by having a rectangular cross sectional shape. The maximum stress criterion was used for the initiation of stiffness degradation. All models were subjected to quasi static tensile loads in different directions to obtain key material properties. It was found that there was very little change in stiffness with different yarn cross sectional shapes as all yarns still had the same volume fraction which is the dominant factor in determining stiffness. There was a maximum change in strength of 2%, 15% and 30% in the weft, through-thickness and warp directions. The lowest strengths were often seen with sharp edged elliptical yarn cross sections which generated stress concentrations. The highest strengths were seen with rectangular or rectangular with semi-circular ends yarn cross sections as stress concentrations were reduced. The results of this investigation in terms of the effect of yarn cross sectional shape on stiffness compares well to the results in this thesis, however, there is some discrepancy between the effect of yarn cross sectional shape on strength. The results in this thesis show no change in

strength with change in yarn cross sectional shape and in the work by Kari *et al* [80] a maximum 2%, 15% and 30% change in strength is seen in the weft, through-thickness a warp directions respectively. This discrepancy could be due to the different models being tested, NCF compared to 3D woven composite materials.

Rounded brick yarn shapes will be used for all simulations, carbon/epoxy and S2 glass/epoxy. They are representative of the geometry seen in micrographs obtained and the choice of shape does not appear to affect the results as seen in the study conducted in this section. Rounded brick shaped yarns will also allow a higher maximum volume fraction of yarns within the meso scale unit cell.

5.3.5 In-Plane Loading Study

A NCF S2 glass/epoxy meso scale unit cell was tested in both in-plane tension directions, x and z. This study was conducted to ascertain if simulations needed to be conducted in both in-plane directions; in a similar fashion to the transverse loading study at the micro scale where results in the transverse x direction differed from the results in the transverse y direction, see section 4.3.7. The meso scale unit cell was tested at a strain rate of 1000/s for speed of analysis. The results, in terms of the stress strain response, were identical; hence, in-plane meso scale simulations in the proceeding results section were conducted in the x direction only.

5.4 Meso Scale Modelling Results

This section presents the results of the carbon/epoxy and S2 glass/epoxy meso scale modelling. The unit cells for both materials have been tested in multiple loading conditions, as shown in Figure 5-7, and at multiple strain rates (1, 1000 and 10000 /s).

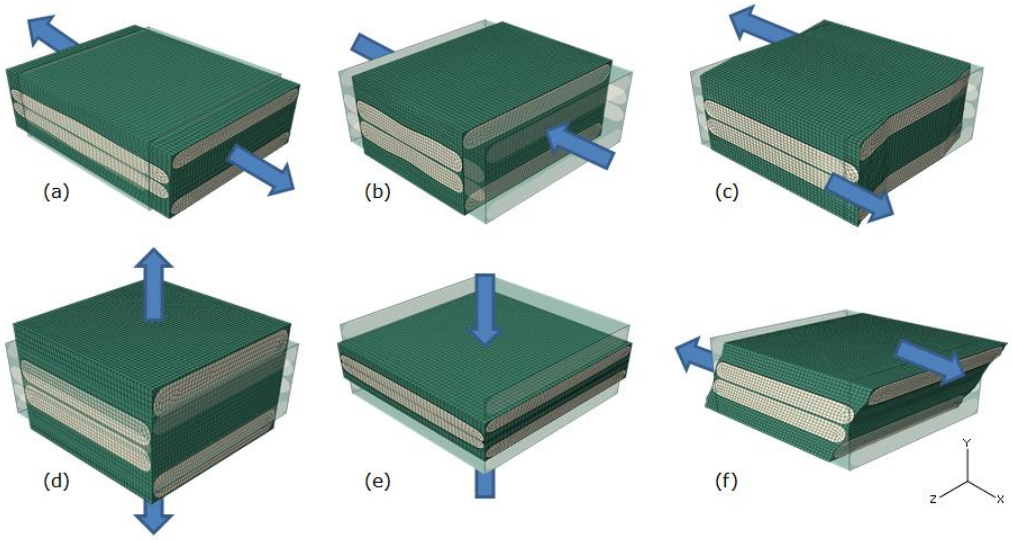

Figure 5-7. Meso scale unit cell loading conditions. (a) in-plane x tension, (b) in-plane x compression, (c) in-plane xz shear, (d) through thickness y tension, (e) through thickness y compression and (f) through thickness xy shear. The example unit cells are S2 glass/epoxy meso scale unit cells with deformation scale factors applied.

5.4.1 Carbon/Epoxy

The stress strain responses for the carbon/epoxy meso scale unit cell are presented in Figure 5-8 for in-plane loading (x direction), Figure 5-9 for through thickness loading (y direction) and Figure 5-10 for shear loading. For each loading condition the von Mises stress contour plots are shown in Figure 5-11. Damage variable contour plots are shown in Figure 5-13, Figure 5-14, Figure 5-15, Figure 5-16, Figure 5-17 and Figure 5-18 for in-plane tension, in-plane compression, through thickness tension, through thickness compression, through thickness shear and in-plane shear respectively. A description of how the damage variable contour plots are displayed is given in Figure 5-12. These results are discussed in detail in sections 5.5 and 5.5.2.

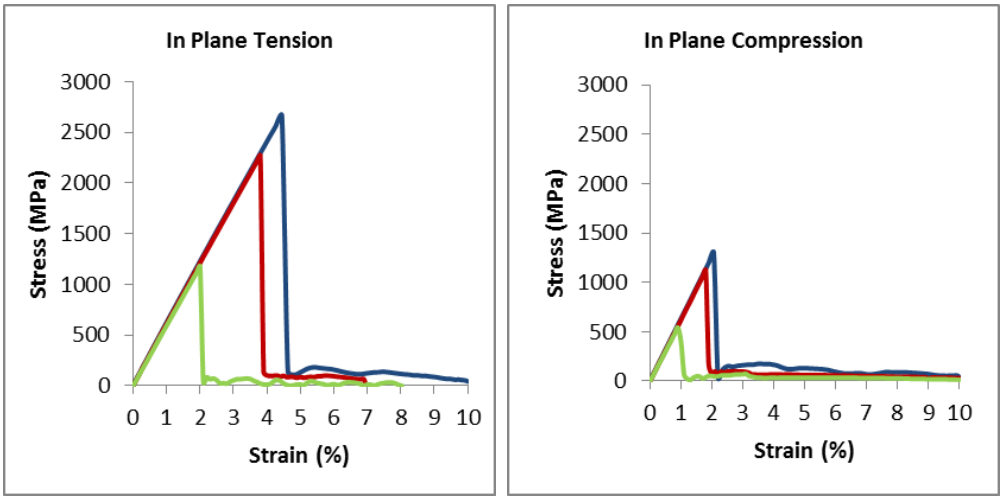

Figure 5-8. Stress strain curves for carbon/epoxy meso scale unit cell in in-plane tension and in-plane compression at strain rates of 1 (green), 1000 (red) and 10000 (blue) /s

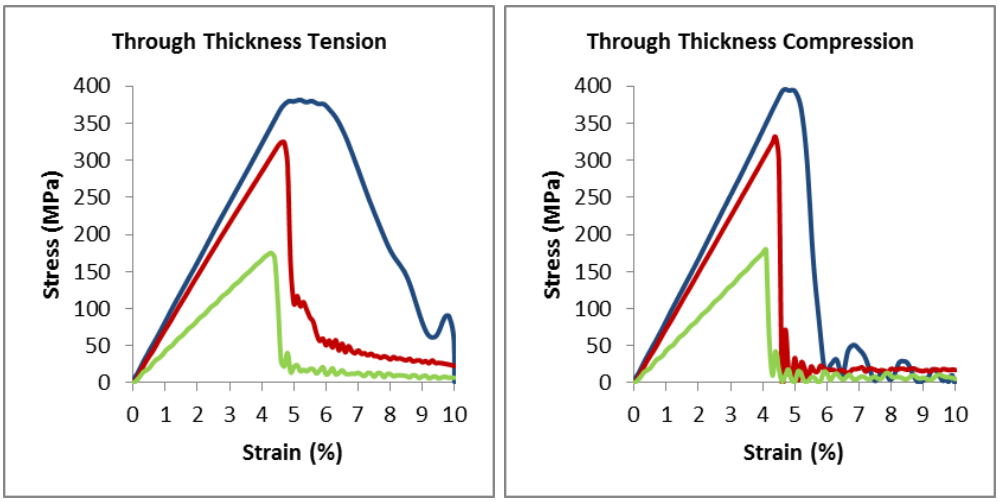

Figure 5-9. Stress strain curves for carbon/epoxy meso scale unit cell in through thickness tension and through thickness compression at strain rates of 1 (green), 1000 (red) and 10000 (blue) /s

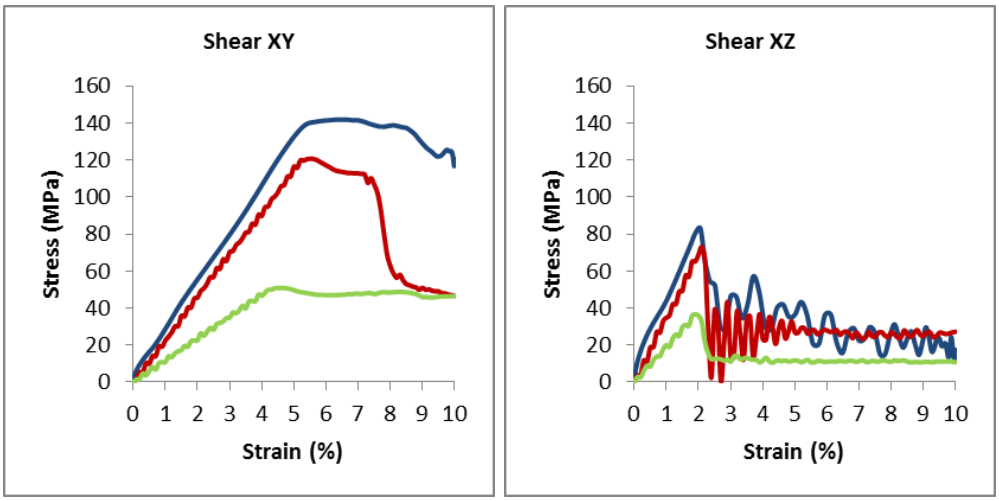

Figure 5-10. Stress strain curves for carbon/epoxy meso scale unit cell in through thickness XY shear and in-plane XZ shear at strain rates of 1 (green), 1000 (red) and 10000 (blue) /s

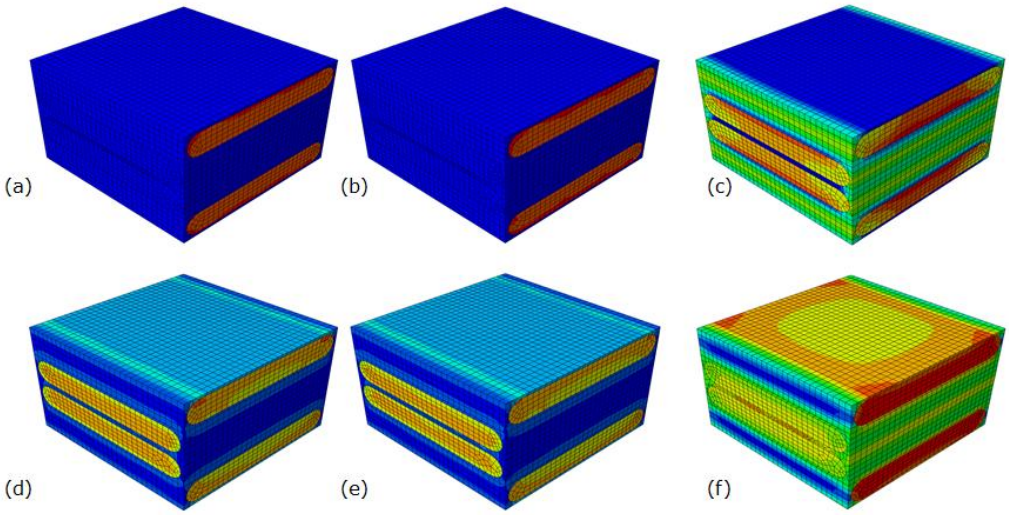

Figure 5-11. Carbon/epoxy meso scale unit cell von Mises stress contours before damage has initiated (reflecting the stress distributions throughout the elastic region) at 1/s in (a) in-plane x tension, (b) in-plane x compression, (c) in-plane xz shear, (d) through thickness y tension, (e) through thickness y compression and (f) through thickness xy shear. Red indicates high stress and blue indicates low stress.

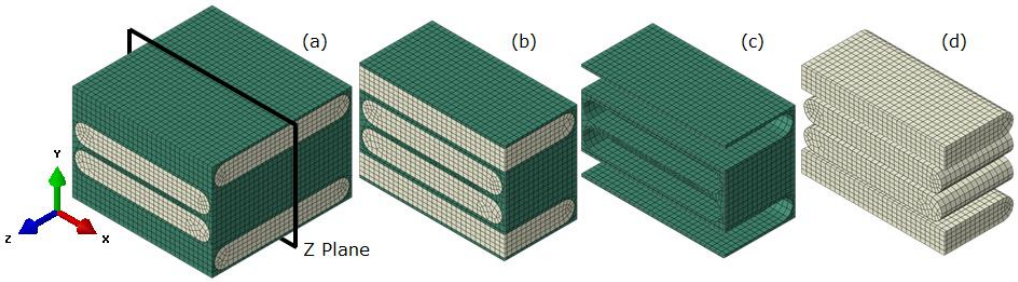

Figure 5-12. Diagram of how the damage variable contour plots are displayed in Figure 5-13 to Figure 5-18 for carbon/epoxy and Figure 5-23 to Figure 5-28 for S2 glass/epoxy. (a) full sized meso scale unit cell, (b) meso scale unit cell cut in half on the Z Plane, (c) as (b) but with yarn constituent removed, (d) as (b) but with matrix constituent removed. (c) and (d) are shown in the damage contour plots at different stages of damage (initial, intermediate and final) and at different strain rates (1/s, 1000/s and 10000/s). Initial / intermediate / final damage at 1/s is not necessarily at the same value of strain as 1000/s and 10000/s. The images are shown at values of strain that are representative of the stages of damage.

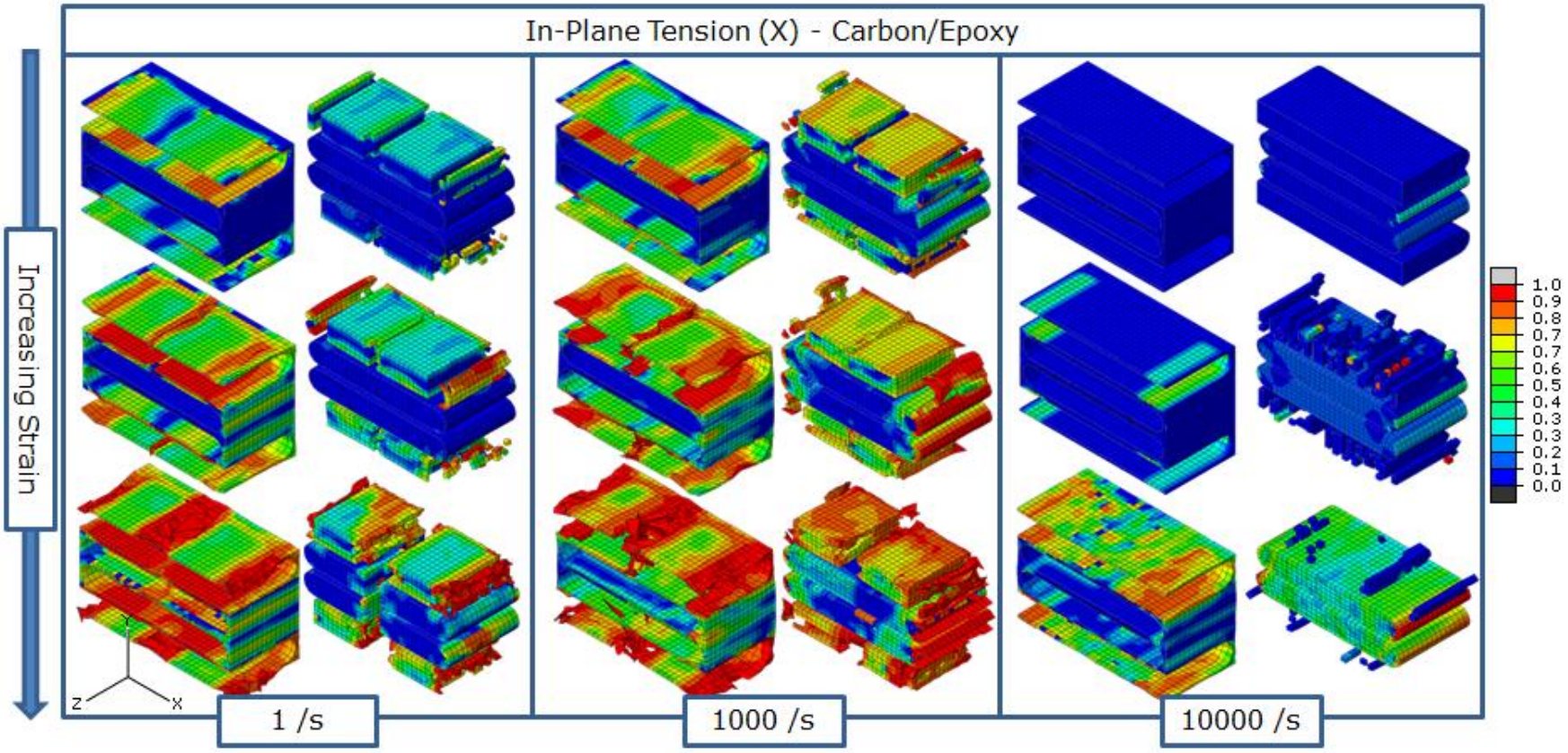

Figure 5-13. Carbon/epoxy meso scale unit cell damage variable contours. Damage varies from zero (blue) which indicates no damage to one (red) which indicates maximum damage. Unit cells are shown in in-plane tension at 1/s (left), 1000/s (centre) and 10000/s (right). Each loading condition has three stages of damage shown; initial (top), intermediate (middle) and final (bottom). The matrix and yarn regions of the unit cell are shown separately and have been cut in half along the z plane to show internal damage.

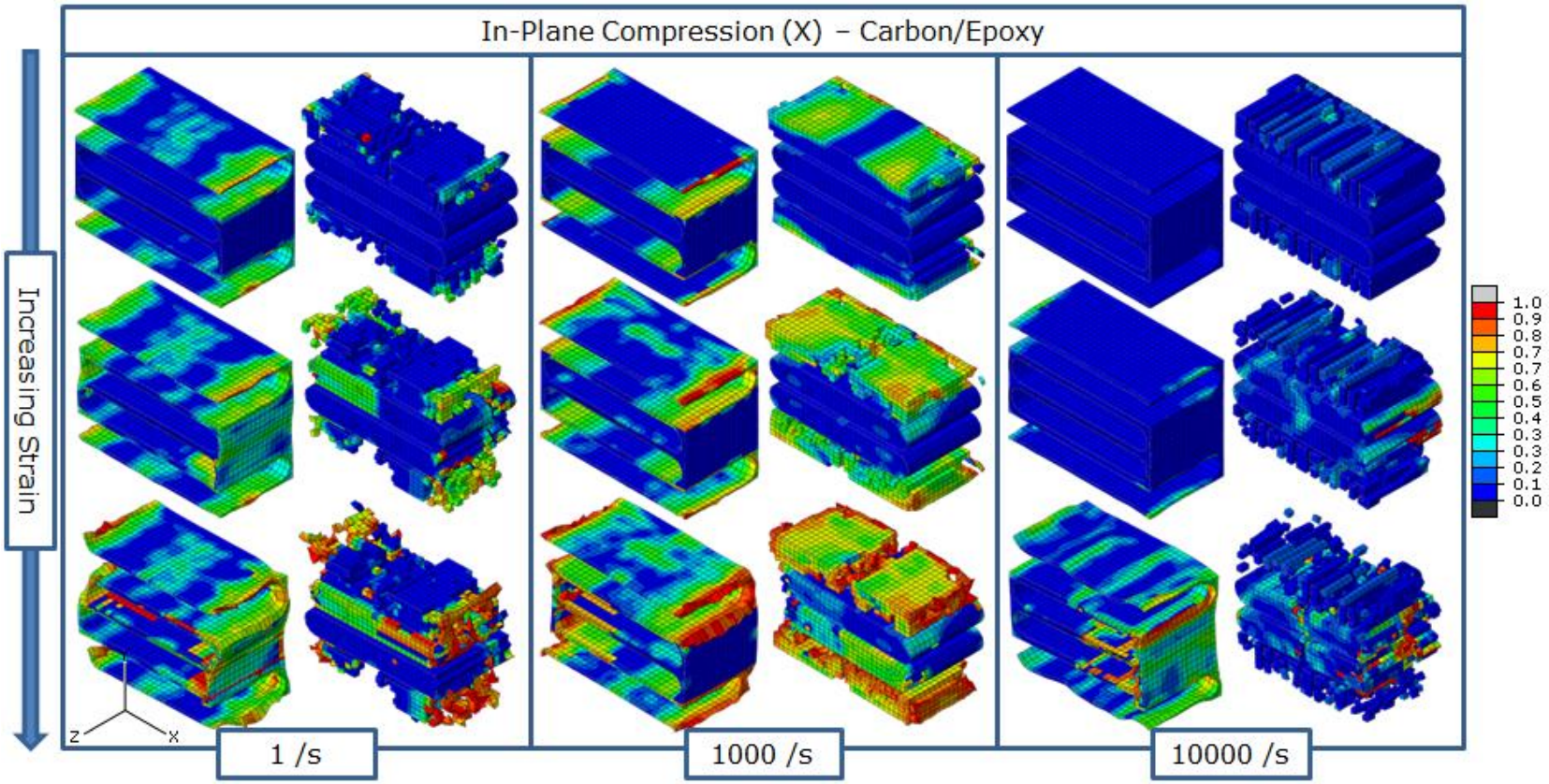

Figure 5-14. Carbon/epoxy meso scale unit cell damage variable contours. Damage varies from zero (blue) which indicates no damage to one (red) which indicates maximum damage. Unit cells are shown in in-plane compression at 1/s (left), 1000/s (centre) and 10000/s (right). Each loading condition has three stages of damage shown; initial (top), intermediate (middle) and final (bottom). The matrix and yarn regions of the unit cell are shown separately and have been cut in half along the z plane to show internal damage.

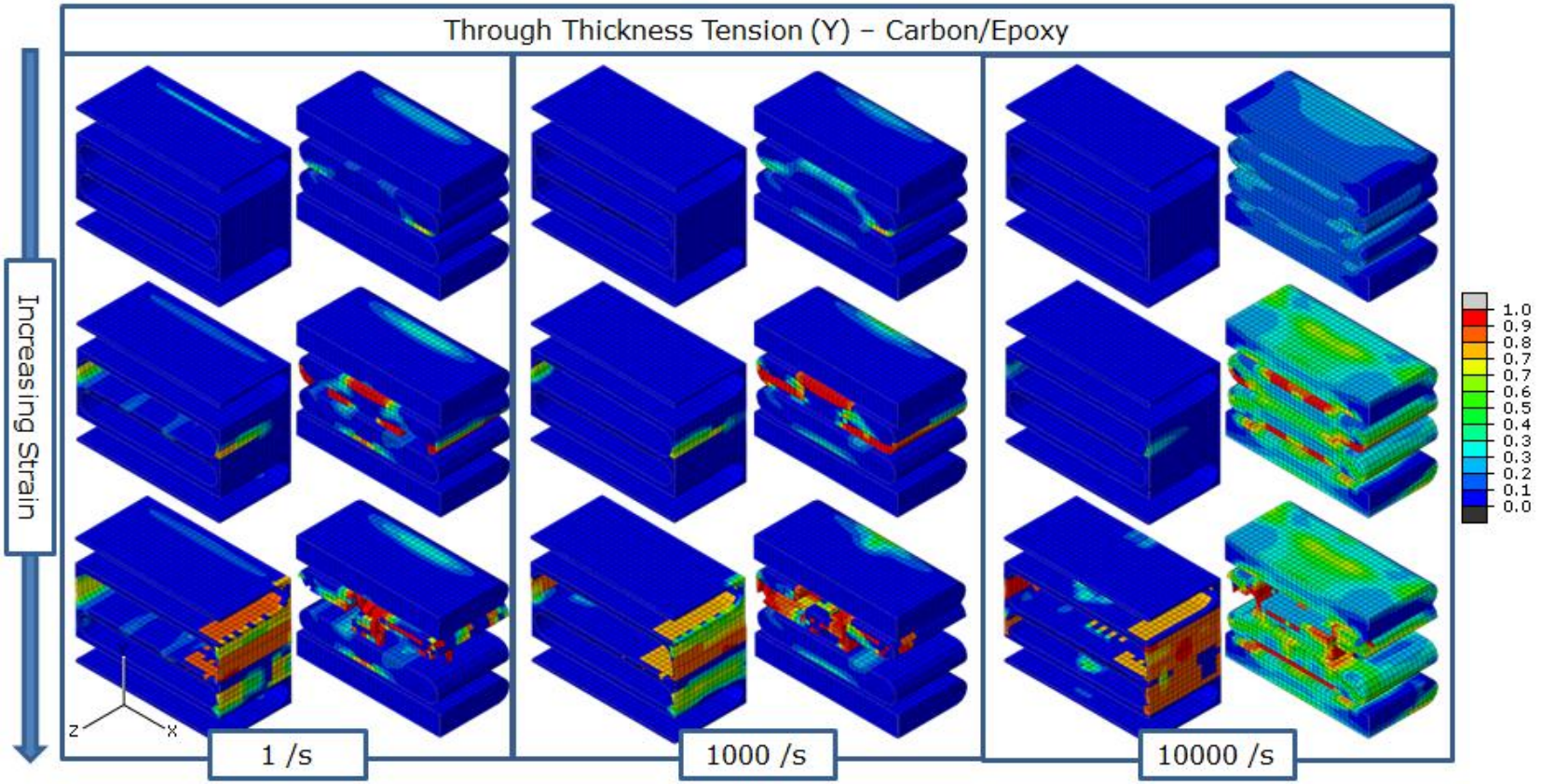

Figure 5-15. Carbon/epoxy meso scale unit cell damage variable contours. Damage varies from zero (blue) which indicates no damage to one (red) which indicates maximum damage. Unit cells are shown in through thickness tension at 1/s (left), 1000/s (centre) and 10000/s (right). Each loading condition has three stages of damage shown; initial (top), intermediate (middle) and final (bottom). The matrix and yarn regions of the unit cell are shown separately and have been cut in half along the z plane to show internal damage.

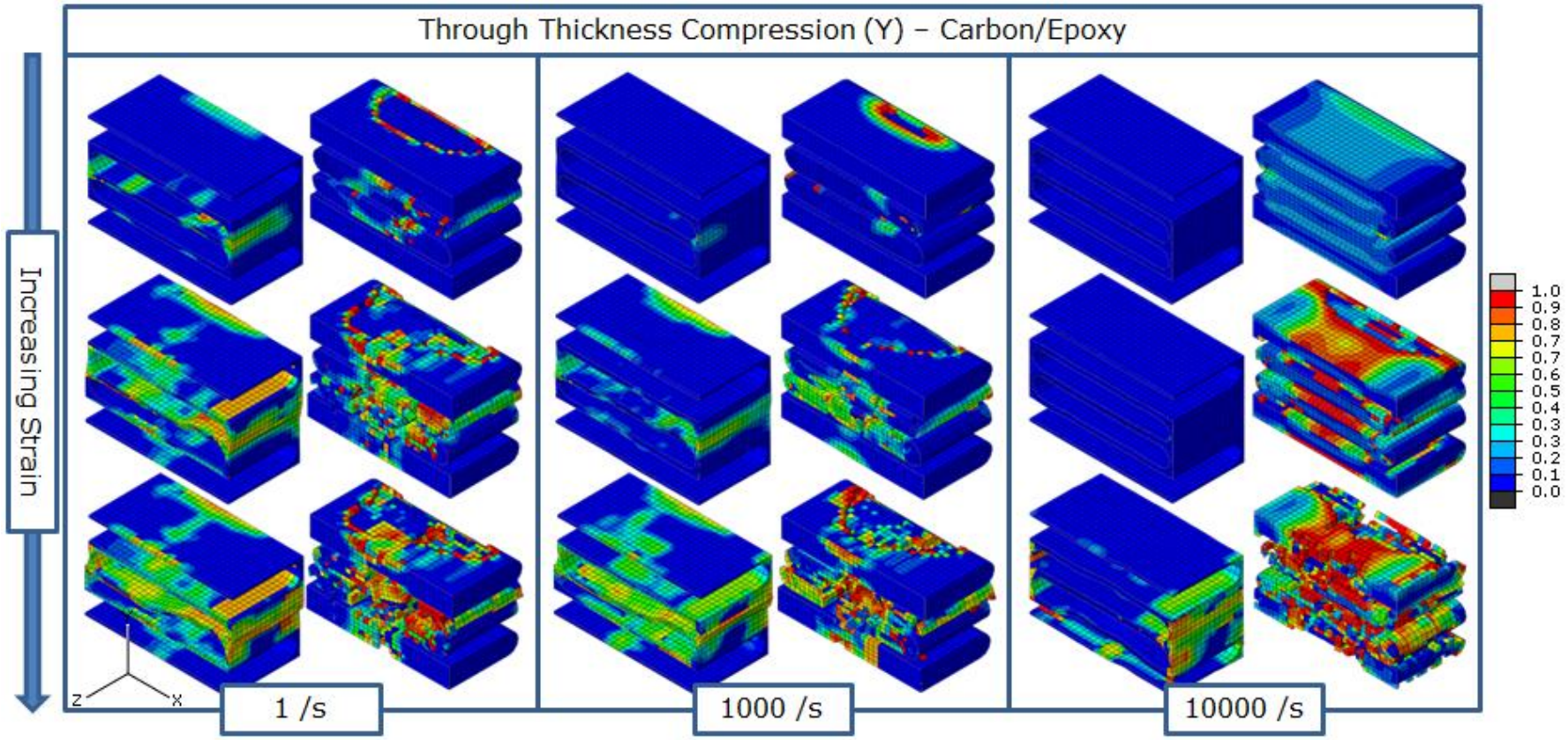

Figure 5-16. Carbon/epoxy meso scale unit cell damage variable contours. Damage varies from zero (blue) which indicates no damage to one (red) which indicates maximum damage. Unit cells are shown in through thickness compression at 1/s (left), 1000/s (centre) and 10000/s (right). Each loading condition has three stages of damage shown; initial (top), intermediate (middle) and final (bottom). The matrix and yarn regions of the unit cell are shown separately and have been cut in half along the z plane to show internal damage.

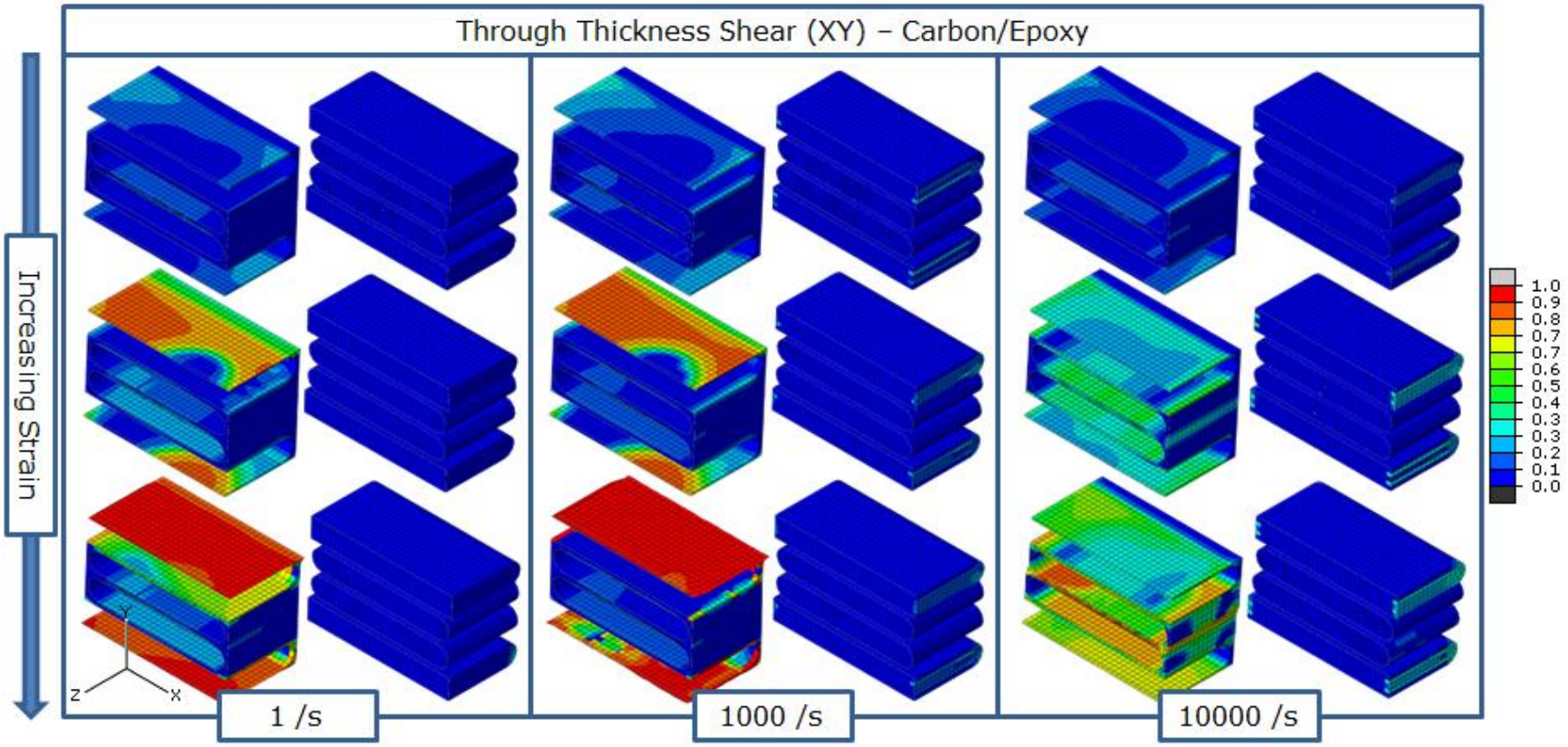

Figure 5-17. Carbon/epoxy meso scale unit cell damage variable contours. Damage varies from zero (blue) which indicates no damage to one (red) which indicates maximum damage. Unit cells are shown in through thickness shear at 1/s (left), 1000/s (centre) and 10000/s (right). Each loading condition has three stages of damage shown; initial (top), intermediate (middle) and final (bottom). The matrix and yarn regions of the unit cell are shown separately and have been cut in half along the z plane to show internal damage.

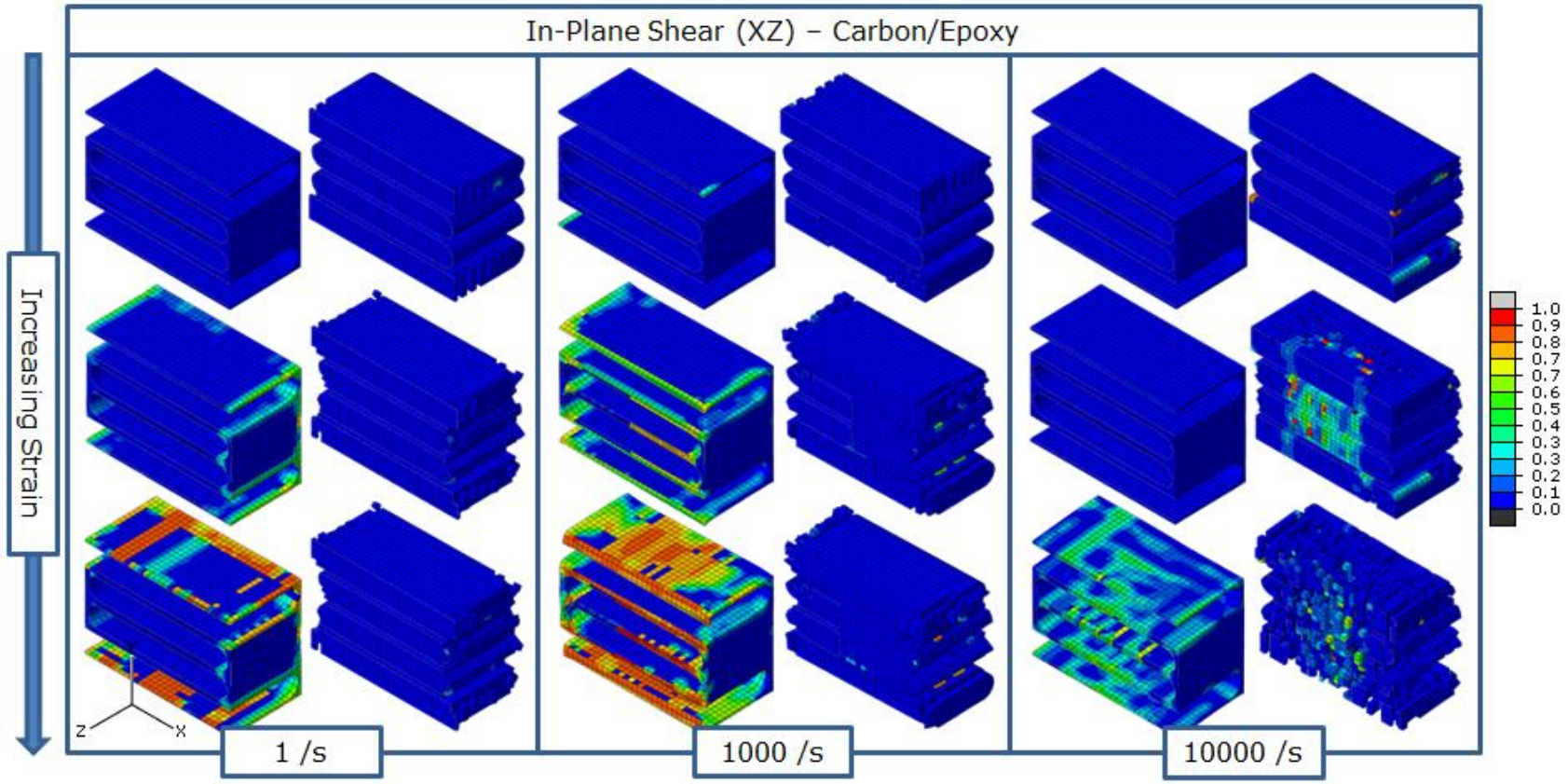

Figure 5-18. Carbon/epoxy meso scale unit cell damage variable contours. Damage varies from zero (blue) which indicates no damage to one (red) which indicates maximum damage. Unit cells are shown in in-plane shear at 1/s (left), 1000/s (centre) and 10000/s (right). Each loading condition has three stages of damage shown; initial (top), intermediate (middle) and final (bottom). The matrix and yarn regions of the unit cell are shown separately and have been cut in half along the z plane to show internal damage

5.4.2 S2 Glass/Epoxy

The stress strain responses for the S2 glass/epoxy meso scale unit cell are presented in Figure 5-19 for in-plane loading (x direction), Figure 5-20 for through thickness loading (y direction) and Figure 5-21 for shear loading. For each loading condition the von Mises stress contour plots are shown in Figure 5-22. Damage variables contour plots are shown in Figure 5-23, Figure 5-24, Figure 5-25, Figure 5-26, Figure 5-27 and Figure 5-28 for in-plane tension, in-plane compression, through thickness tension, through thickness compression, through thickness shear and in-plane shear respectively. A description of how the damage variable contour plots are displayed is given in Figure 5-12. These results are discussed in detail in sections 5.5 and 5.5.2.

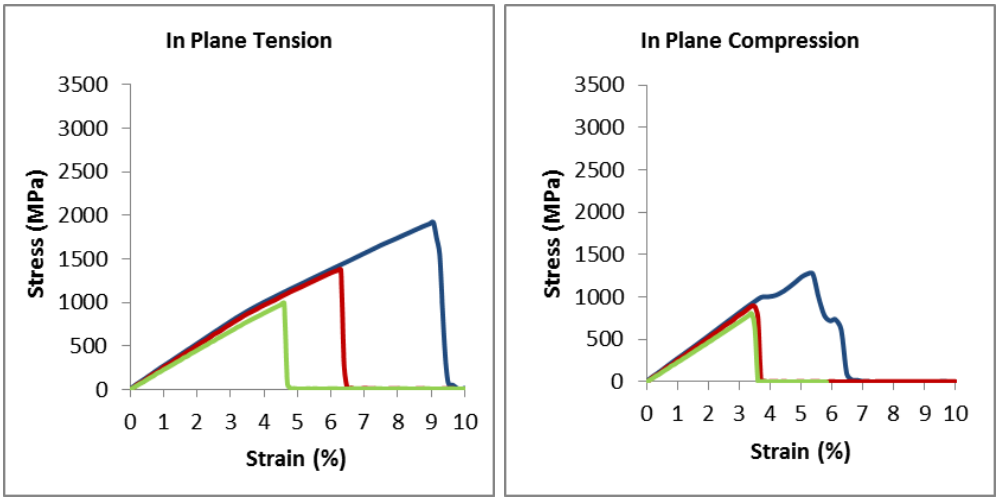

Figure 5-19. Stress strain curves for S2 glass/epoxy meso scale unit cell in in-plane tension and in-plane compression at strain rates of 1 (green), 1000 (red) and 10000 (blue) /s

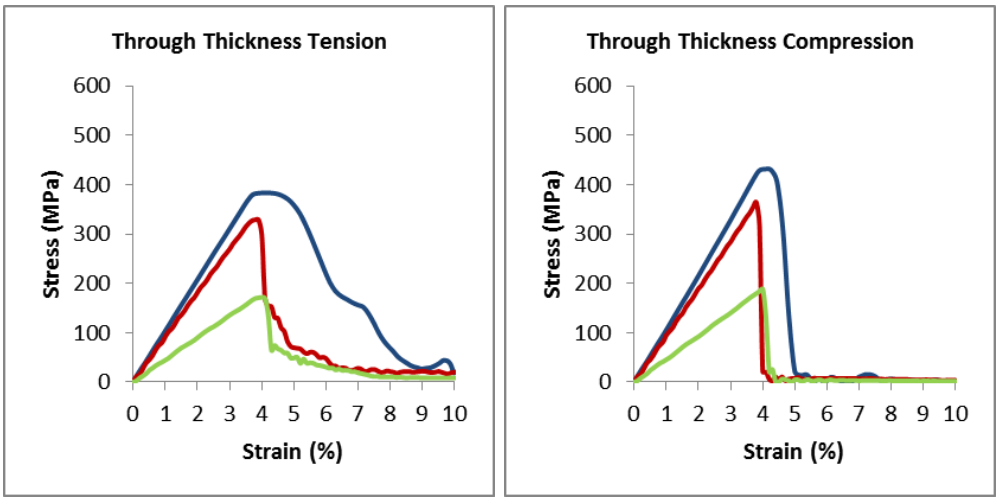

Figure 5-20. Stress strain curves for S2 glass/epoxy meso scale unit cell in through thickness tension and through thickness compression at strain rates of 1 (green), 1000 (red) and 10000 (blue) /s

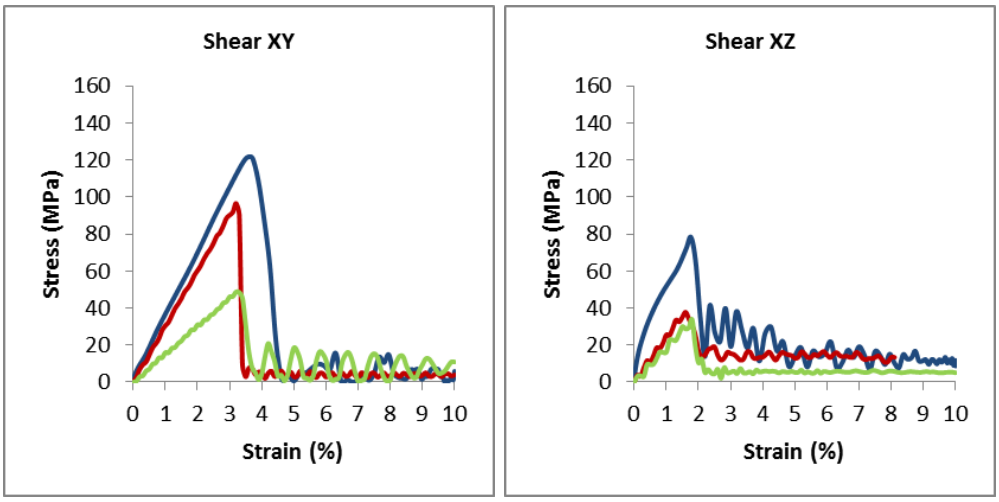

Figure 5-21. Stress strain curves for S2 glass/epoxy meso scale unit cell in through thickness XY shear and in-plane XZ shear at strain rates of 1 (green), 1000 (red) and 10000 (blue) /s

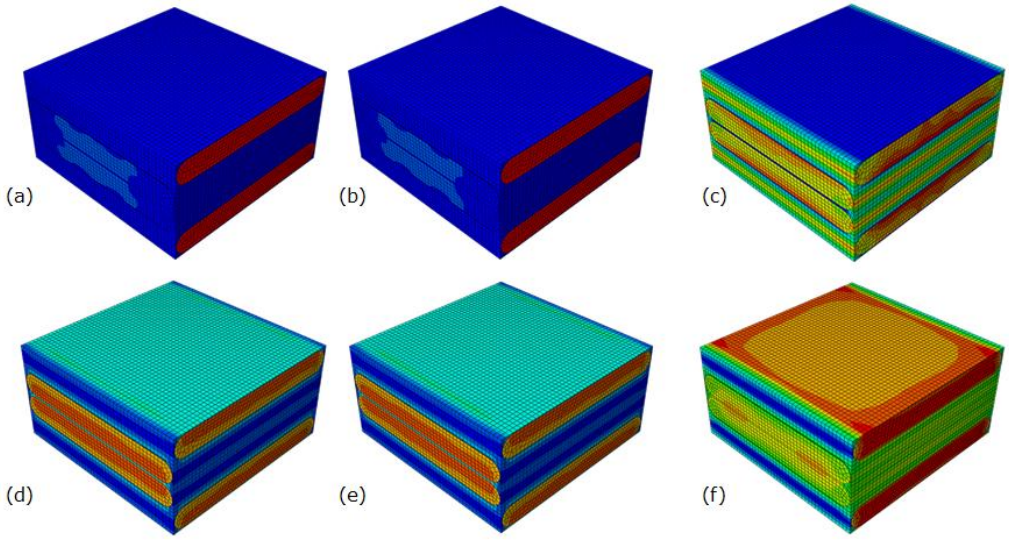

Figure 5-22. S2 glass/epoxy meso scale unit cell von Mises stress contours before damage has initiated (reflecting the stress distributions throughout the elastic region) at 1/s in (a) in-plane x tension, (b) in-plane x compression, (c) in-plane xz shear, (d) through thickness y tension, (e) through thickness y compression and (f) through thickness xy shear. Red indicates high stress and blue indicates low stress.

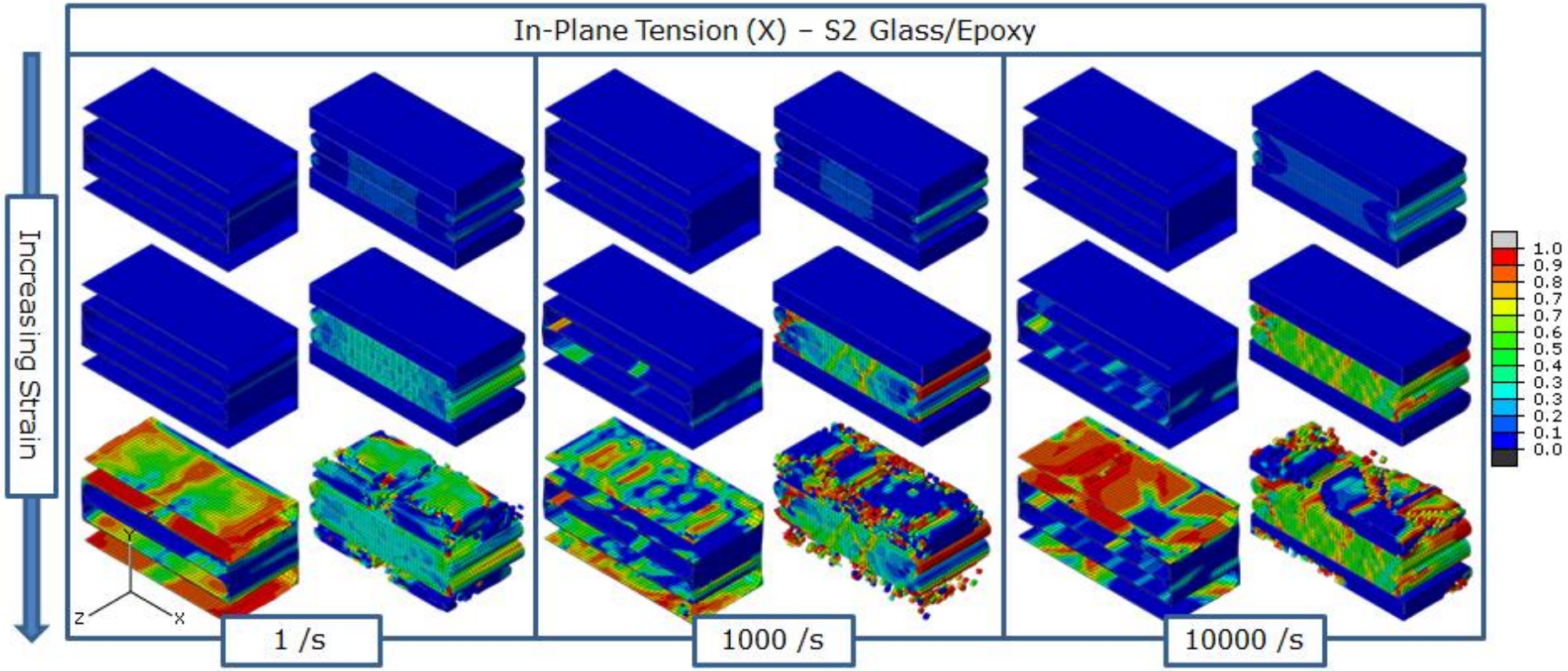

Figure 5-23. S2 glass/epoxy meso scale unit cell damage variable contours. Damage varies from zero (blue) which indicates no damage to one (red) which indicates maximum damage. Unit cells are shown in in-plane tension at 1/s (left), 1000/s (centre) and 10000/s (right). Each loading condition has three stages of damage shown; initial (top), intermediate (middle) and final (bottom). The matrix and yarn regions of the unit cell are shown separately and have been cut in half along the z plane to show internal damage.

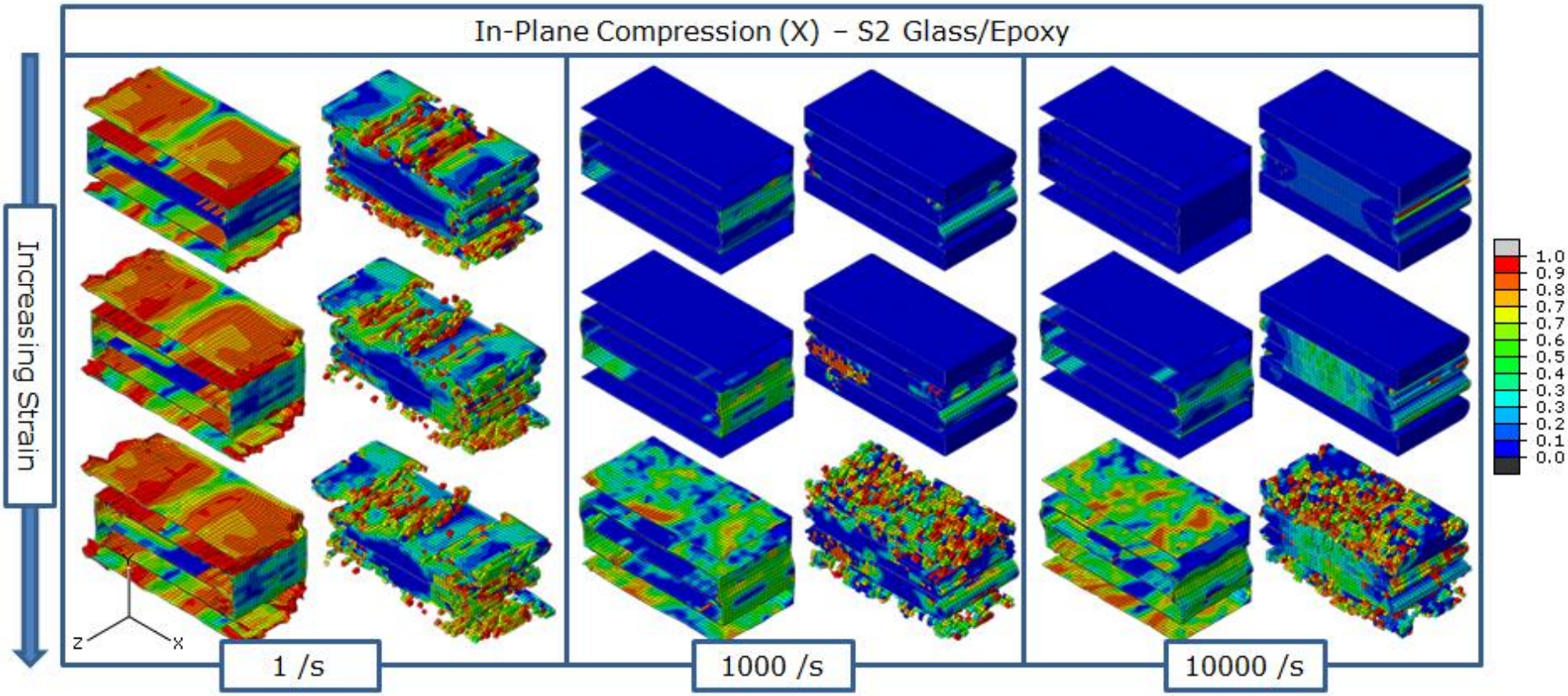

Figure 5-24. S2 glass/epoxy meso scale unit cell damage variable contours. Damage varies from zero (blue) which indicates no damage to one (red) which indicates maximum damage. Unit cells are shown in in-plane compression at 1/s (left), 1000/s (centre) and 10000/s (right). Each loading condition has three stages of damage shown; initial (top), intermediate (middle) and final (bottom). The matrix and yarn regions of the unit cell are shown separately and have been cut in half along the z plane to show internal damage.

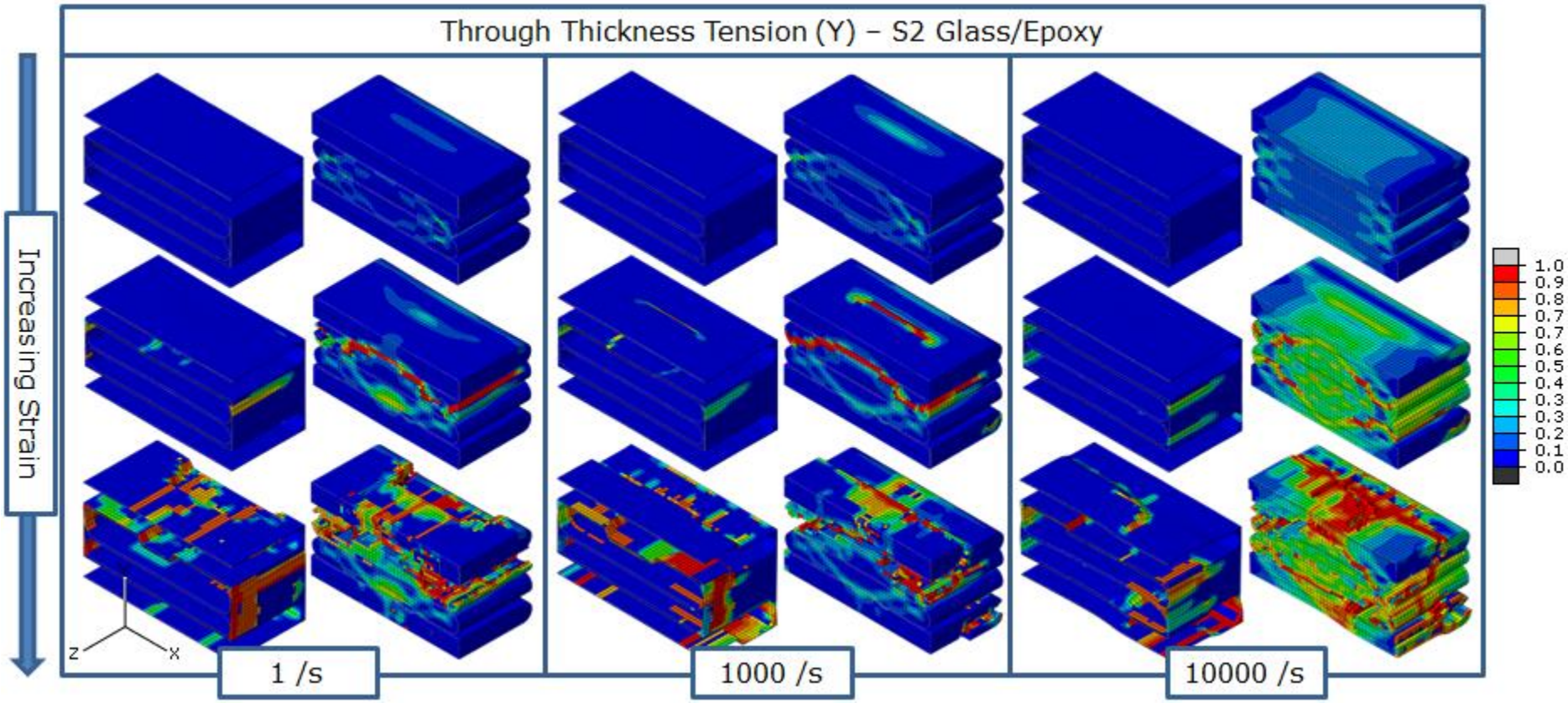

Figure 5-25. S2 glass/epoxy meso scale unit cell damage variable contours. Damage varies from zero (blue) which indicates no damage to one (red) which indicates maximum damage. Unit cells are shown in through thickness tension at 1/s (left), 1000/s (centre) and 10000/s (right). Each loading condition has three stages of damage shown; initial (top), intermediate (middle) and final (bottom). The matrix and yarn regions of the unit cell are shown separately and have been cut in half along the z plane to show internal damage.

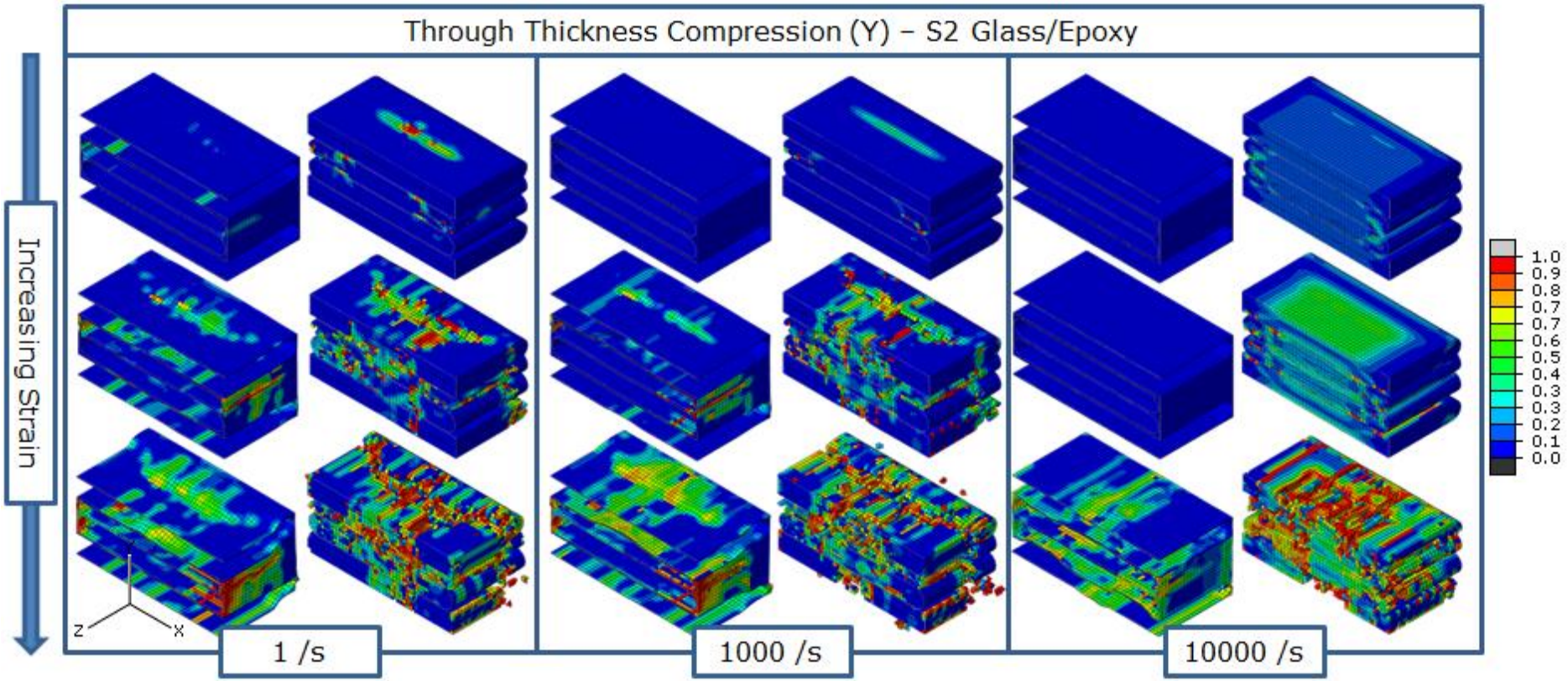

Figure 5-26. S2 glass/epoxy meso scale unit cell damage variable contours. Damage varies from zero (blue) which indicates no damage to one (red) which indicates maximum damage. Unit cells are shown in through thickness compression at 1/s (left), 1000/s (centre) and 10000/s (right). Each loading condition has three stages of damage shown; initial (top), intermediate (middle) and final (bottom). The matrix and yarn regions of the unit cell are shown separately and have been cut in half along the z plane to show internal damage.

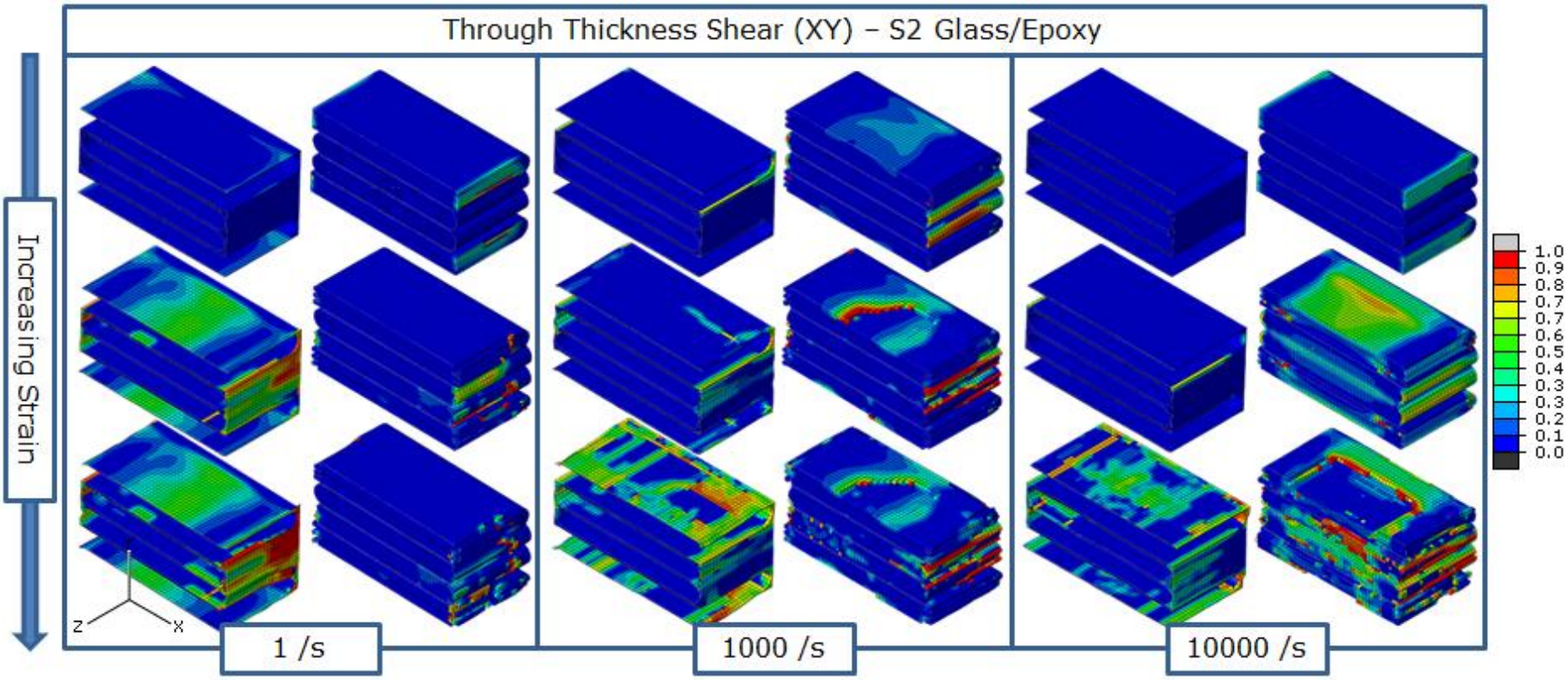

Figure 5-27. S2 glass/epoxy meso scale unit cell damage variable contours. Damage varies from zero (blue) which indicates no damage to one (red) which indicates maximum damage. Unit cells are shown in through thickness shear at 1/s (left), 1000/s (centre) and 10000/s (right). Each loading condition has three stages of damage shown; initial (top), intermediate (middle) and final (bottom). The matrix and yarn regions of the unit cell are shown separately and have been cut in half along the z plane to show internal damage.

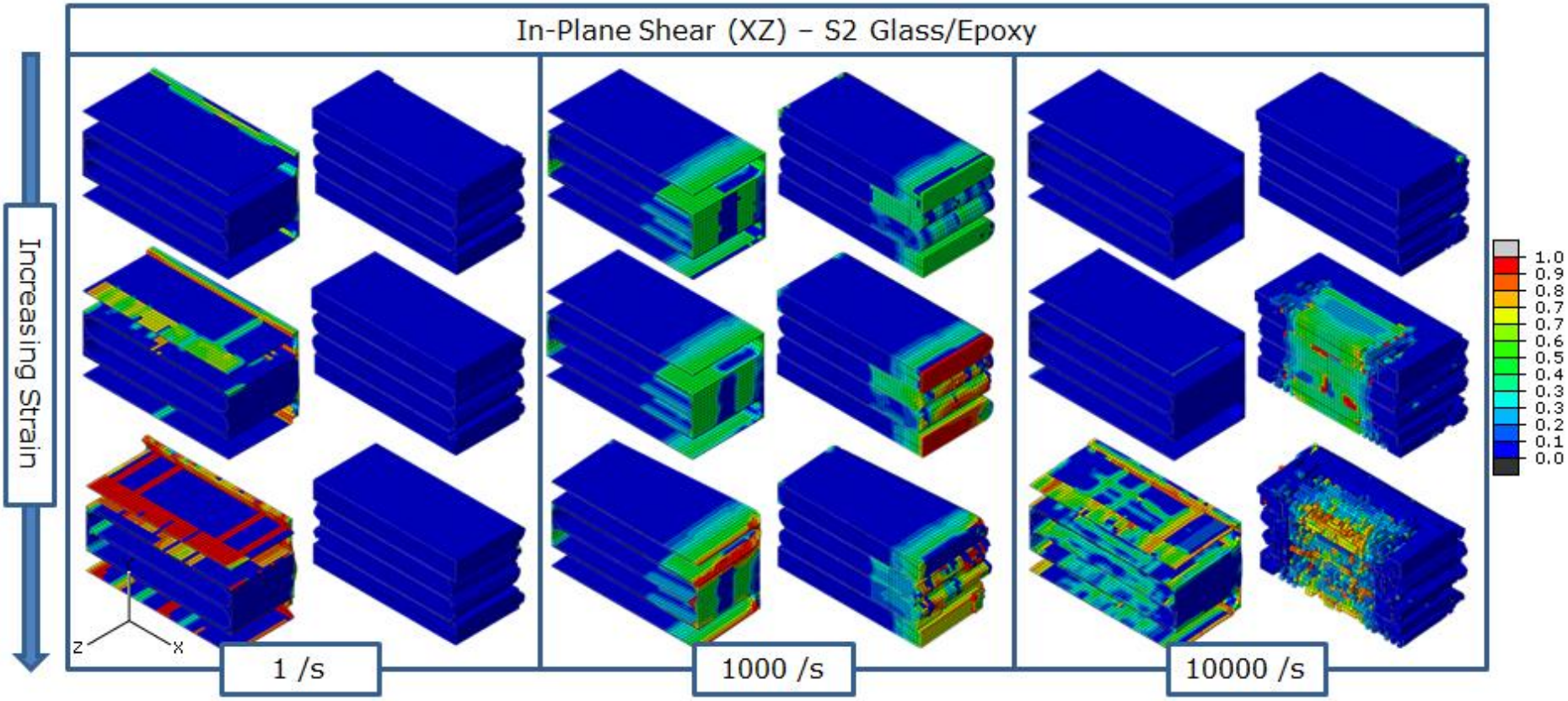

Figure 5-28. S2 glass/epoxy meso scale unit cell damage variable contours. Damage varies from zero (blue) which indicates no damage to one (red) which indicates maximum damage. Unit cells are shown in in-plane shear at 1/s (left), 1000/s (centre) and 10000/s (right). Each loading condition has three stages of damage shown; initial (top), intermediate (middle) and final (bottom). The matrix and yarn regions of the unit cell are shown separately and have been cut in half along the z plane to show internal damage.

5.5 Meso Scale Modelling Discussion

5.5.1 Elastic and Damage Response

For both S2 glass/epoxy and carbon/epoxy meso scale unit cells in all loading conditions at all strain rates the stress strain response initially shows linear elastic behaviour.

For both S2 glass/epoxy and carbon/epoxy meso scale unit cells in in-plane X tension, in-plane X compression, through thickness Y compression, in-plane XZ shear and through thickness XY shear (for S2 glass/epoxy only) the stress strain responses at all strain rates shows elastic behaviour followed by an abrupt, instant / almost instant reduction in stiffness i.e. brittle failure as shown schematically in Figure 4-28 (c). The stress strain responses are shown in Figure 5-8, Figure 5-9 and Figure 5-10 for carbon/epoxy and Figure 5-19, Figure 5-20 and Figure 5-21 for S2 glass/epoxy.

In-Plane Tension and Compression

For both S2 glass/epoxy and carbon/epoxy meso scale unit cells in in-plane tension and compression the abrupt reduction in stiffness occurs due to failure of the yarns parallel to the loading direction, seen clearly in the damage contour plots in Figure 5-13 and Figure 5-14 for carbon/epoxy and Figure 5-23 and Figure 5-24 for S2 glass/epoxy. If one considers what is happening to the yarns parallel to the loading direction at the micro scale it is apparent that the micro unit cell would be subjected to longitudinal tension (for meso scale in-plane tension) or longitudinal compression (for meso scale in-plane compression). These micro scale loading conditions result in a strain softening parameter of 100, Figure 4-36, as the strain softening parameter for a particular yarn element is selected based on the largest maximum stress criterion, explained in 3.4.4. This causes the abrupt failure seen in both S2 glass/epoxy and carbon/epoxy meso scale unit cells in in-plane tension and compression.

Damage also occurs in the yarns transverse to the loading direction. This damage does not appear to affect the integrity of the unit cell as the stress strain response is still dominated by the failure of the yarns parallel to the loading direction. It is well understood that loading of a cross-ply laminate parallel to one of the fibre directions results in through thickness cracking

of transverse plies even when the overall final failure is dominated by transverse to the fibre direction cracking of axial plies, see Figure 2-6. It can also be seen in the damage contour plots that the matrix is damaging without affecting the overall stress strain response, a process that happens in reality known as micro matrix cracking. The damage in the matrix and yarns transverse to the loading direction becomes more prominent after the yarns parallel to the loading direction have failed, as this is where the remaining load is transferred.

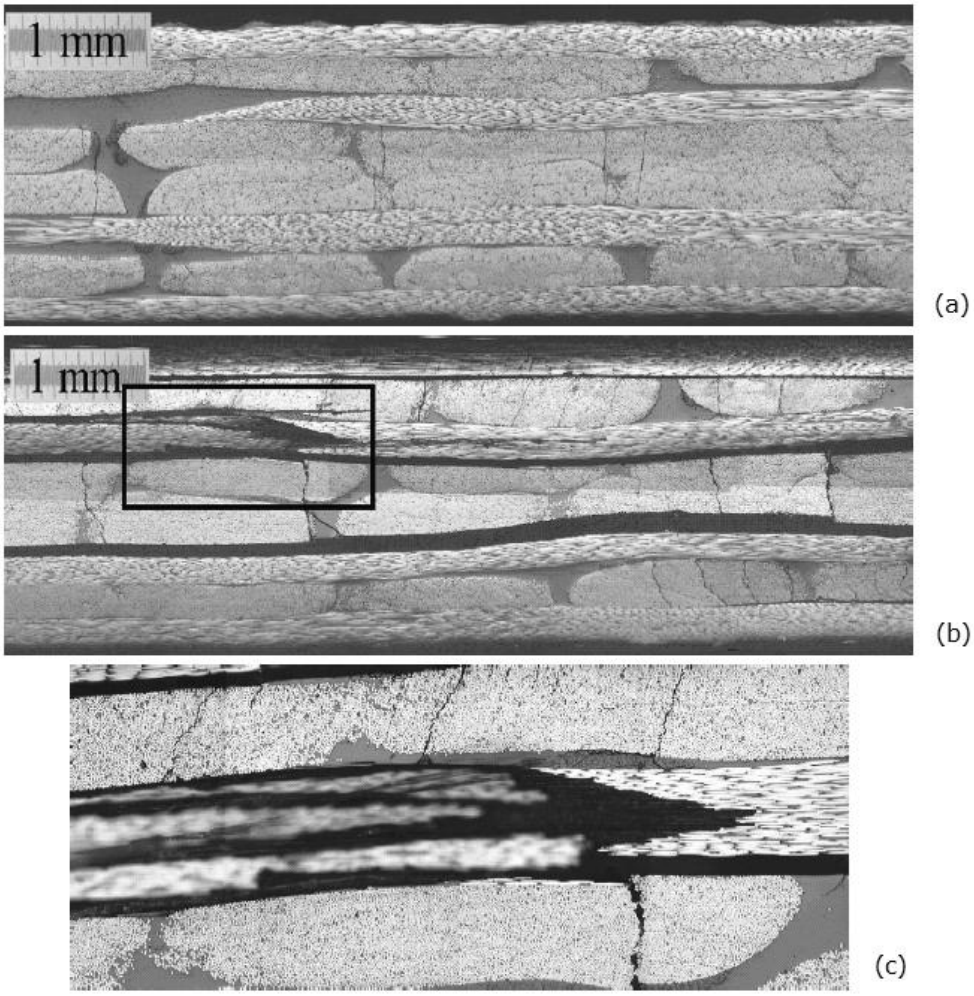

Figure 5-29. Carbon/epoxy NCF cross-ply laminate $[0/90/0/90]_S$ subjected to in-plane tension to (a) 0.66% and (b) 0.87%. Image (c) shows a magnified image of the blue box in image (b). Reproduced from [11].

Mattsson *et al* [11] took micrographs of a carbon/epoxy NCF cross-ply laminate $[0/90/0/90]_S$ after in-plane tensile loading to different levels of strain (0.66% and 0.87%). At 0.66% strain, see Figure 5-29 (a), some 90° yarns (those transverse to the loading direction) had developed cracks across their width. These cracks were more frequently located in the

middle 90° layer which had double thickness where the crack propagated across both 90° layers and sometimes into a 0° layer. At 0.87% strain, see Figure 5-29 (b) and (c), extensive damage is seen in the form of multiple traverse cracks in the 90° layers, delaminations between 0° and 90° layers and fracture of the 0° bundles. The researchers stress how it is difficult to detail the actual sequence of events. The in-plane tension damage contour plots for S2 glass/epoxy in Figure 5-23 shows the behaviour described above with the 90° yarn damage occurring across the middle 90° layer with double thickness before the damage propagates across the through thickness matrix regions and into the 0° layer causing extensive damage in the form of a high level of 90° yarn damage, delaminations (extensive through thickness matrix damage) and fracture of the 0° yarns.

Hosur *et al*[25] tested 32 ply cross-ply carbon/epoxy laminates in in-plane compression at 82, 163 and 817 /s rates of strain on a split Hopkinson bar. The in-plane compression samples failed with the laminate splitting into several sub-laminates. At higher strain rates the samples tended to split into less sub-laminates. It is hard to compare these results to the modelling results in this thesis, as the detailed mechanisms of failure were not the key focus of the research paper. However, the description of 'splitting' failure for in-plane compression implies a large amount of widespread damage which is seen in the damage contour plots in Figure 5-14 and Figure 5-24 for carbon/epoxy and S2 glass/epoxy results respectively.

Through Thickness Compression

For both S2 glass/epoxy and carbon/epoxy meso scale unit cells in through thickness compression the abrupt reduction in stiffness occurs due to failure of all yarns seen in the damage contour plots in Figure 5-16 for carbon/epoxy and Figure 5-26 for S2 glass/epoxy. If one considers what is happening to the yarns at the micro scale it is apparent that the micro unit cell would be subjected to transverse compression resulting in a transverse compressive strain softening parameter of 1.667, seen in Figure 4-36. This causes the abrupt failure, however, this value of 1.667 is much less than the value of 100 discussed previously which also gave abrupt failure. This lower value of strain softening parameter should produce a less abrupt failure resulting in a more gradual reduction in stiffness. This is seen in the through thickness compression stress strain curves at the higher rates of

strain with a gradual curve reduction in stiffness followed by abrupt failure. The abrupt failure at the lower strain rate tests is attributed to the complexity of loading conditions that are occurring within the yarns during the simulations. This results in certain elements being attributed a strain softening parameter, from micro modelling results, that is not the transverse compressive strain softening parameter of 1.667; it can be a shear strain softening parameter which generates a more abrupt reduction in stiffness.

Hosur *et al*[25] tested 32 ply cross-ply carbon/epoxy laminates in through thickness compression at 82, 163 and 817 /s rates of strain on a split Hopkinson bar. The through thickness compression samples did not fail at 82/s, failed through splitting and crushing at 163/s and failed through crushing and shear fracture at 817/s. It is hard to compare these results to the modelling results in this thesis, as the detailed mechanisms of failure were not the key focus of the research paper. However, the description 'crushing' failure for through-thickness compression implies a large amount of widespread damage which is seen in the damage contour plots in Figure 5-16 and Figure 5-26 for carbon/epoxy and S2 glass/epoxy results respectively.

In-Plane Shear

For both S2 glass/epoxy and carbon/epoxy meso scale unit cells in in-plane shear the abrupt reduction in stiffness occurs due to damage in elements in the yarn to such an extent that at maximum damage they are deleted from the analysis. During this damage process there is also a significant amount of damage occurring in the matrix. The damage contour plots for carbon/epoxy and S2 glass/epoxy are shown in Figure 5-18 and Figure 5-28 respectively.

Through Thickness Shear

For the carbon/epoxy, not S2 glass/epoxy, meso scale unit cell in through thickness XY shear the stress strain response at all strain rates shows elastic behaviour followed by a section of gradual decreasing gradient similar to the shape shown schematically in Figure 4-28 (a) i.e. ductile. The stress strain responses are shown in Figure 5-10. The reason for this type of damage occurring in just the carbon/epoxy meso scale unit cell and not the S2 glass/epoxy meso scale unit cell is that there are larger gaps of matrix material between the yarns in the carbon/epoxy meso scale unit

cell. This leads to matrix dominated through thickness shear failure in the carbon/epoxy unit cell, shown in Figure 5-17. The matrix has a strain softening parameter of 0.1 for tension, compression and shear; which gives a stress strain response exhibiting a gradual reduction in stiffness. For the S2 glass/epoxy meso scale unit cell, damage is not matrix dominated, it occurs in both the matrix and the yarns, shown in the damage contour plots in Figure 5-27. The yarns have multiple strain softening parameters for different loading conditions. These yarn strain softening parameters are derived from the micro scale modelling work and are given in Figure 4-36 and range from 0.1 to 100. The yarn strain softening parameters of interest in meso scale through thickness shear loading is the micro scale longitudinal shear strain softening parameter, 100, for the yarns parallel to the loading direction and the micro scale transverse shear strain softening parameter, 0.6667, for the yarns transverse to the loading direction. This is clearly seen in Figure 5-30. The final failure in the S2 glass/epoxy meso scale unit cell subjected to through thickness shear is due to failure in the yarns parallel to the loading direction. These are the yarns that are subjected to longitudinal shear at the micro scale which corresponds to a strain softening parameter of 100 giving abrupt failure.

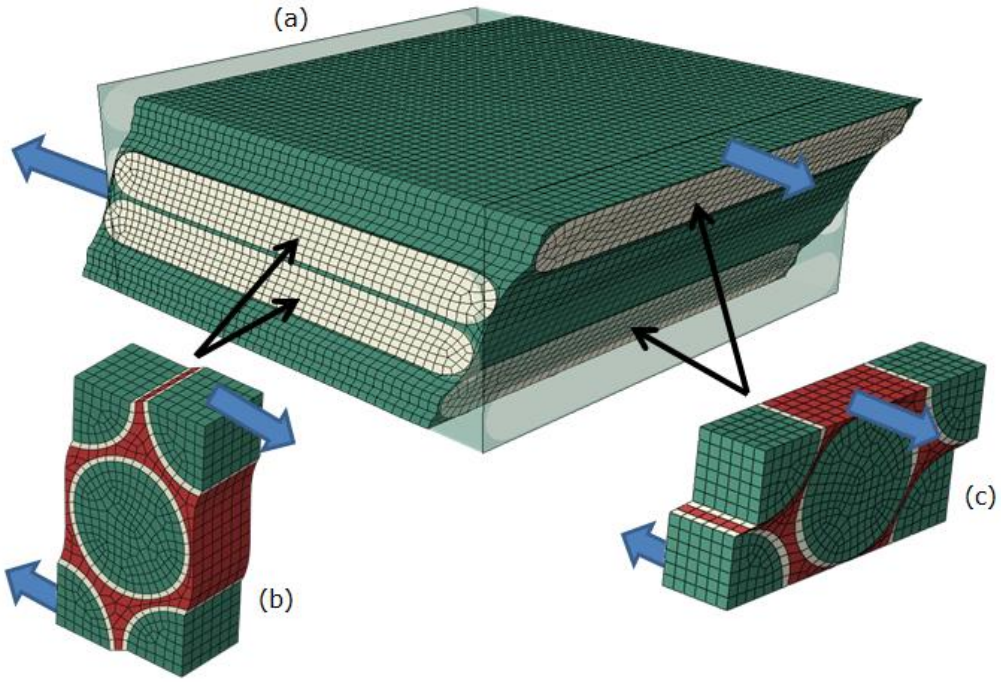

Figure 5-30. (a) Meso scale unit cell loaded in through thickness shear, (b) Micro scale unit cell loaded in transverse shear and (c) Micro scale unit cell loaded longitudinal shear. The yarns parallel to the meso scale loading direction are subjected to longitudinal shear at the micro scale, whereas, the yarns transverse to the meso scale loading direction are subjected to transverse shear at the micro scale.

Through Thickness Tension

For S2 glass/epoxy and carbon/epoxy meso scale unit cells in through thickness Y tension, the stress strain response at the strain rates of 1/s and 1000/s show elastic behaviour followed by an abrupt, instant reduction in stiffness as schematically shown in Figure 4-28 (c) i.e. brittle failure. As the strain rate is increased to 10000/s the stress strain response changes and shows elastic behaviour followed by a section of gradual decreasing gradient with the shape shown schematically in Figure 4-28 (b) i.e. a more ductile failure. The stress strain responses are shown in Figure 5-9 for carbon/epoxy and Figure 5-20 for S2 glass/epoxy. The abrupt reduction in stiffness at 1/s and 1000/s occurs due to yarn failure, seen in Figure 5-15 and Figure 5-25 for carbon/epoxy and S2 glass/epoxy respectively. The more gradual reduction in stiffness seen at 10000/s is seen due to the increased spread of low level damage throughout the entirety of the yarns, again seen in Figure 5-15 and Figure 5-25. The results effectively show a change in the strain softening parameter (for through thickness tension, which will be used for macro input properties) with strain rate as this controls the amount of stiffness degradation in the post elastic region. In through thickness tension one would expect to see a large amount of matrix damage in the through thickness spacing between yarns. This type of damage leads to delamination followed by yarn failure. In both the carbon/epoxy and S2 glass/epoxy damage contour plots there is limited damage in the matrix in the through thickness spacing between the yarns and this is not the cause of ultimate failure. The reason why the model is not replicating this type of damage could be due to a number of reasons; the through thickness spacing (and in-plane spacing) are not measured values as they are adjusted proportionally to give the required volume fractions (see 3.2.2) and in reality the through thickness spacing would vary from yarn to yarn with the large spaces creating a greater chance of a delamination zone.

General Observations

For S2 glass/epoxy and carbon/epoxy micro scale unit cells in all loading conditions at all strain rates initial failure occurs in an element where the maximum stress criterion reaches unity. The specific location of the failure, yarn or matrix constituent, is in the highly stressed regions. These regions can be clearly identified by viewing the von Mises stress contour plots in Figure 5-11 for carbon/epoxy and Figure 5-22 for S2 glass/epoxy.

5.5.2 Strain Rate Dependent Response

For S2 glass/epoxy and carbon/epoxy meso scale unit cells the elastic and damage phases are both clearly strain rate sensitive and the increase in stiffness and strength with increasing strain rate can be seen under all loading conditions except in-plane tension and compression. In in-plane tension and compression, stress strain curves shown in Figure 5-8 for carbon/epoxy and Figure 5-19 for S2 glass/epoxy, there is little or no change in stiffness with increasing strain rate, however, there is an increase in strength observed with increasing strain rate.

In the meso scale simulations there are multiple factors that affect the resulting strain rate dependence. The matrix material model scales stiffness with the same values in tension, compression and shear. The yarn material model scales stiffness with three different strain rate scaling constants; one for longitudinal stiffness, one for transverse stiffness and one for shear stiffness. The latter three parameters are derived from the micro scale modelling and result in the values in Figure 4-36. The value for the longitudinal stiffness strain rate scaling constant is much lower (practically zero) than the transverse and shear stiffness strain rate scaling constants. In in-plane tension and compression testing the longitudinal stiffness of the yarn plays a large role in determining the overall stiffness of the meso scale unit cell, as the yarn transverse stiffness (for carbon/epoxy) and matrix stiffness are small in comparison. The longitudinal stiffness of the yarn will have been strain rate scaled by an insignificant amount at all strain rates resulting in little or no change in stiffness of the carbon/epoxy and S2 glass/epoxy meso scale unit cell in in-plane tension and compression.

It can, however, be seen that the strength in in-plane tension and compression testing does change significantly with increasing strain rate in both carbon/epoxy and S2 glass/epoxy meso scale unit cells. For the yarn material model there is only one strain rate scaling constant for strength which is the average of all strength strain rate scaling constants at the micro scale from all loading conditions. Therefore, even though in Figure 4-18 and Figure 4-24 there is no change in strength with increasing strain rate in micro scale longitudinal tension and compression, the longitudinal tensile/compressive strength value of the yarn is scaled in the same manner as all other yarn strength parameters. The result is a large change

in strength with increasing strain rate for carbon/epoxy and S2 glass/epoxy meso scale unit cells in in-plane tension and compression. It is also important to consider that the transverse yarns and matrix material will have some effect on the material response and, hence, how much the strength changes in in-plane tension and compression with increasing strain rate. Only one value was used for the yarn strength strain rate scaling constant at the meso scale for simplification and also to have consistency with the MAT162 material model in LS-DYNA, where resulting data is transferred for macro scale analyses (see section 5.6).

In the S2 glass/epoxy meso scale unit cell in in-plane compression there is little change in the response between 1/s and 1000/s. This is due to a change in the damage modes. With increasing strain rate there appears to be an increasing amount of damage in the yarns transverse to the loading direction before the failure of the yarns parallel to the loading direction. This can be seen in the damage contour plots in Figure 5-24.

5.6 Meso to Macro Scale

All the meso scale modelling results for carbon/epoxy and S2 glass/epoxy unit cells are homogenised into properties that are carried forward for use as macro scale S2 glass/epoxy and carbon/epoxy lamina properties respectively. The following parameters are obtained from the stress strain curves: stiffness values, Poisson's ratio values, strengths, strain softening parameters and strain rate scaling constants for stiffness and strength. The material properties used in the macro scale modelling studies are not given in this thesis for confidentiality reasons; however, the values are obtained in the same manner as described in Section 4.6.

The stiffness and strength against the natural log of strain rate plots for S2 glass/epoxy and carbon/epoxy meso scale unit cells in all loading conditions can be found in Appendix D.

5.7 Macro Scale Modelling Case Studies

The macro scale modelling work, which utilises the multi-scale modelling results in this thesis, was conducted by two industrial partners involved in the project. BAE Systems conducted blast impact modelling and QinetiQ conducted ballistic impact modelling. This section presents two case

studies of the macro scale modelling work edited from a joint publication with The University of Nottingham, BAE Systems and QinetiQ [32].

5.7.1 Blast Panel Case Study

Simulation of a preliminary armour design concept has been undertaken to assess the response to blast load and to compare results with tests undertaken in the early phases of the LiMBS project.

The configuration of the test is shown in Figure 5-31. The 800mm x 800mm test panel is clamped by through-bolts to a rigid steel framework. Blast loading is applied to the upper surface from a 2 kg pancake charge of PE4, offset from the upper surface by 150mm. The panel is comprised of two materials; a toughened steel front face (Armox 340) and an S2 glass/carbon composite laminate behind. The two layers of material are held together by the clamping force imposed by the rig.

Figure 5-31. Blast panel experimental test setup

Numerical simulations were performed using LS-DYNA. The extent of the finite element model is shown in Figure 5-32 (quarter symmetry employed). The use of a quarter symmetry model is a simplification that needs to be carefully considered, especially if ±45 layers are being explicitly modelled. Single point integration hexahedral elements were employed throughout the model, each ply of the carbon/S2-glass laminate being represented as a single layer of elements. MAT_COMPOSITE_MSC (MAT162) was used to describe the rate dependent behaviour of the carbon and S2 glass materials. These material models were populated with data supplied from micro/meso-scale modelling. Tiebreak interfaces were defined between the adjacent laminate layers with failure parameters

specified to represent delamination. The panel was loaded directly with pressure histories derived from a preliminary 2-D axisymmetric Euler analysis of the detonation of the 2kg pancake charge.

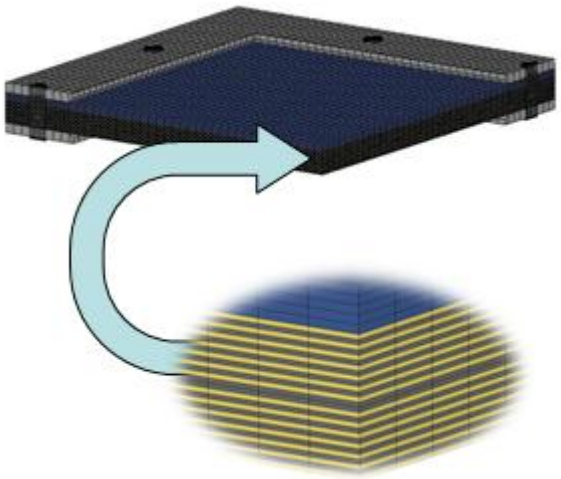

Figure 5-32. Model setup with detail of blast panel cross section

The level of predicted damage to the panel is shown in Figure 5-33, alongside the post-experimental test panel. Post-test damage in the laminate is characterized by significant intra-lamina failure and gross delamination, with bulging deformation, but no penetration, of the steel front face. The model predicts a similar pattern of failure in the composite, combining fibre and matrix in-plane failure with delamination across the majority of the panel. The model also shows good agreement with data from timing pins positioned behind the test panel (recording the time at specific levels of panel displacement). In addition, the overall deformation level of the front steel face is closely aligned to the deformation measured in test.

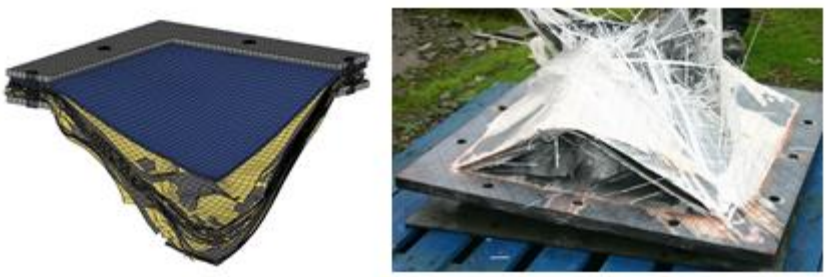

Figure 5-33. Blast panel damage. Model (left) and experimental test (right)

The overall results provide confidence in the modelling approach and material data employed to simulate this blast event. The techniques

established have provided the means to move forward with the assessment of alternative blast configurations to support the development of lightweight, multi-material armour concepts.

5.7.2 Ballistic Panel Case Study

Building upon work undertaken in support of the Europa CAFV (Carbon Fibre for Armoured Fighting Vehicles) project [81], QinetiQ are currently investigating the use of multi-scale modelling as a means of predicting the ballistic and spall liner performance of structural composites. The resistance of 24mm thick hybrid S2 glass / Carbon laminates to perforation by 12.7mm fragment simulating projectiles (FSP) was initially assessed experimentally to determine the V_{50} ballistic limit, which defines the impact speed at which 50% of projectiles would be expected to perforate the target. For the baseline 24mm thick S2 glass / carbon hybrid considered under the LiMBS project, a ballistic limit velocity of 646m/s was obtained.

Numerical modelling of the fragment impact tests was undertaken in LS-DYNA using MAT_COMPOSITE_SOLID_FAILURE (MAT59) to represent the hybrid composite target. Using the micro/meso-scale modelling data, the 24mm thick quasi-isotropic laminate was divided into 28 layers of elements, with each layer representing two plies of the physical laminate and with fibres running in the 0 and 90 or +45 and -45 directions. Given the strain rate dependent nature of the material properties derived from the micro and meso scale models, and in the absence of strain rate dependency within MAT59, initial simulations have used quasi-static material property data to represent the glass and carbon reinforced layers of the hybrid composite laminate.

The 12.7mm FSP was represented as a right circular AISI 4340 steel cylinder using MAT_JOHNSON_COOK (MAT15) and EOS_GRUNIESEN. Contact between the projectile and target was achieved using an eroding contact algorithm, with erosion added to the composite material model to delete severely distorted elements from the simulation.

The ballistic impact model was run for a series of increasing impact velocities to determine the predicted performance limit of the hybrid composite target. Figure 5-34 illustrates the model for a fragment impact

velocity of 600 m/s, while the projectile's velocity history is shown in Figure 5-35.

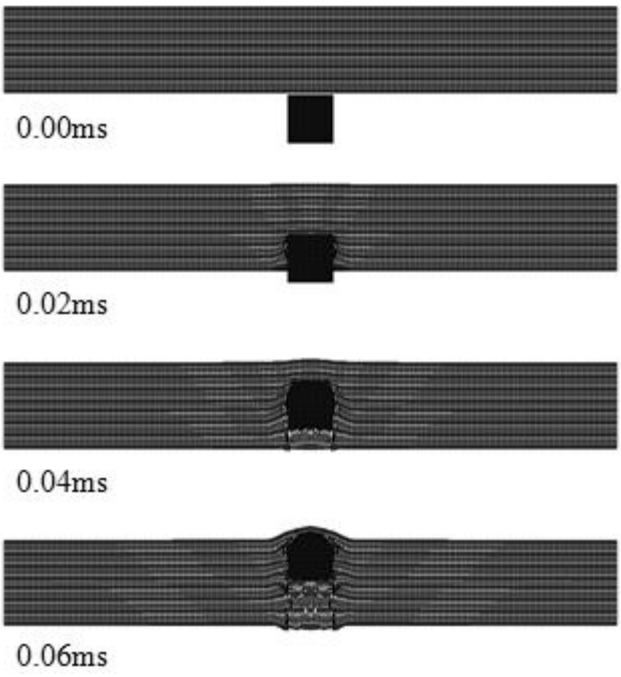

Figure 5-34. Ballistic impact model representing impact of 12.7mm FSP on 24mm thick hybrid glass/carbon target at 600m/s

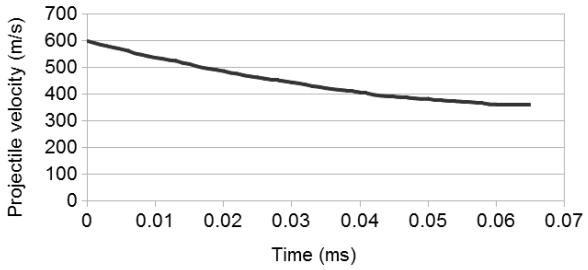

Figure 5-35. Predicted velocity history for 12.7mm FSP impacting 24mm thick hybrid glass/carbon target at 600m/s

The results obtained from the initial ballistic impact models indicate that, using quasi-static material property data, the model under-predicts the resistance of the hybrid composite target to fragment perforation. To a large extent, this is to be expected, with both the S2 glass and carbon meso-scale models reporting an appreciable level of strain rate sensitivity.

Future work under the LiMBS project will investigate the use of high strain rate property data as a means of improving the predictive capability of the ballistic impact model, the effect of through thickness reinforcement on the

development of damage within the target, and the ability of numerical modelling to predict the spall liner performance of structural composites in terms of the behind armour cone angle resulting from overmatching threats.

6 Experimental Testing

6.1 Introduction

This chapter details the experimental testing conducted to validate the meso scale modelling in Chapter 5 and give confidence in the micro scale modelling in Chapter 4.

S2 glass/epoxy and carbon/epoxy NCF composite laminates were tested in in-plane tension (0°/90° layup), in-plane compression (0°/90° layup) and in-plane shear (± 45° layup) at quasi-static (all loading conditions) and intermediate rates of strain (compression only). Quasi-static (≈ 1/s) and intermediate (≈ 100/s) strain rate testing was conducted on an electromechanical universal static test machine and an instrumented falling weight drop tower respectively.

This chapter firstly details the experimental methodology, followed by the results in graphical and tabular format and finally a discussion of the results with a comparison to the modelling work is presented.

6.2 Methodology

6.2.1 Manufacturing Process

All composite panels were manufactured by Permali Gloucester Limited [82] using a resin infusion method known as vacuum bagging. The carbon fabric used was 1010 gsm / 0 90 / 34 700 24K / 1270 and the S2 glass fabric used was 1010 gsm / 0 90 / S2 463-AA-250 / 1270, both supplied by Sigmatex [83]. The epoxy resin used was SICOMIN SR1710 / SD7820, supplied by Matrix Composite Materials Company [84]. Two 600mm x 600mm composite panels were manufactured, one 4 ply S2 glass/epoxy and one 4 ply carbon/epoxy. All panels were symmetric about the mid-plane and had a 0°/90° layup sequences with 4 plies where a single ply comprises one 0° and one 90° layer. The thickness was chosen to ensure buckling did not occur in in-plane compression testing at both quasi-static and intermediate strain rates.

Quasi-static and intermediate strain rate test specimens were cut from the panels using a band saw and circular blade cutting saw. In-plane shear specimens were cut from the 0°/90° panels at a 45° angle.

6.2.2 Quasi-Static Testing

The quasi-static testing procedures presented in this section are based on the work by Brown *et al* [6]. All quasi-static testing was conducted on an Instron 5581 (shear) and 5985 (tension and compression) electromechanical universal test machine with data (time, load, longitudinal and transverse extension and strain) being recorded using the Instron and an Imetrum non-contact video extensometer [85]. The extension and strain data was obtained by setting up a four point bi-axial virtual gauge in the Imetrum software package. Quasi-static test specimen dimensions are shown in Figure 6-1. The specimens were tested at a crosshead speed of 2 mm/min, giving strain rates of 0.0002/s for tension and shear specimens and 0.001/s for compression specimens based on the gauge lengths in Figure 6-1.

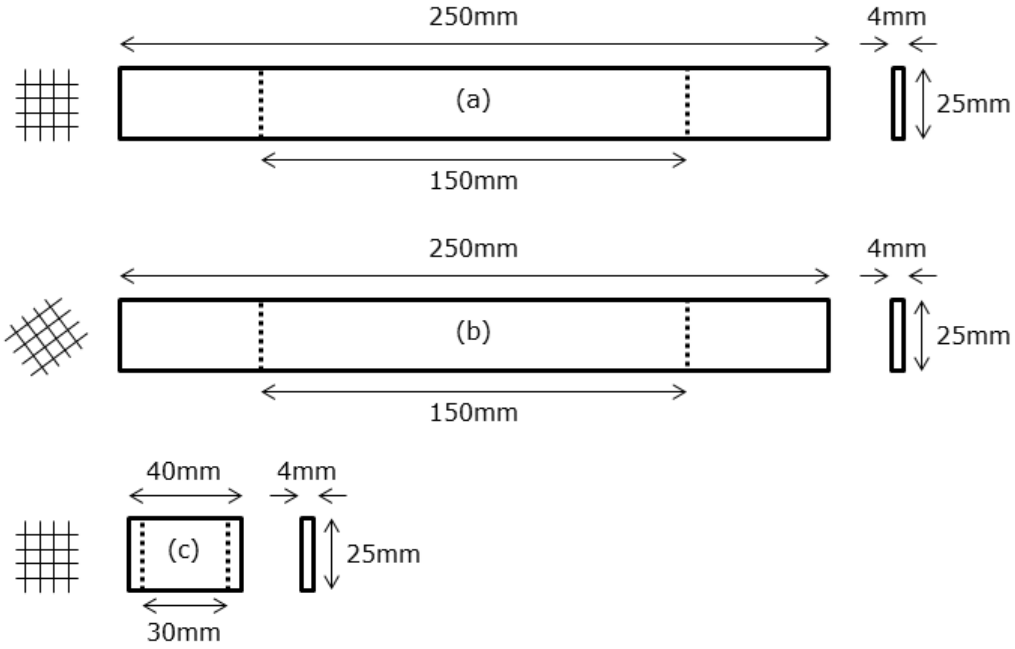

Figure 6-1. Quasi-static (a) tension, (b) shear and (c) compression test specimen dimensions. The dotted lines on the specimens indicate the gauge length. The grids to the left of the specimen indicate 0°/90° or ± 45° layup sequence.

In-Plane Tensile Testing

Quasi-static tensile testing was performed according to the ASTM standard D3039 [86]. The quasi-static tensile specimens were straight sided specimens 25mm wide and 250mm in length (150mm gauge length). All specimens consisted of 4 plies in a 0°/90° layup sequence, giving a thickness of 4mm. The electromechanical universal test machine was fitted with rotationally self-aligning wedge grips.

In-Plane Shear Testing

Quasi-static shear testing was performed according to the ASTM standard D3518 [87]. The quasi-static shear specimens were straight sided specimens 25mm wide and 250mm in length (150mm gauge length). All specimens consisted of 4 plies in a ± 45° layup sequence, giving a thickness of 4mm. The quasi-static shear testing was performed in the same manner as the quasi-static tensile testing. The shear strain was calculated as the longitudinal strain minus the transverse strain and the shear stress was calculated as the longitudinal load divided by two times the area as detailed in the ASTM standard D3518 [87].

In-Plane Compression Testing

The quasi-static compression specimens were straight sided specimens 25mm wide and 40mm in length (30mm gauge length). All specimens consisted of 4 plies in a 0°/90° layup sequence, giving a thickness of 4mm. A compression fixture was installed in the electromechanical universal test machine that consisted of a T-shaped impactor that is guided by two vertical channels in a steel supporting block. The specimen was clamped between two steel end caps and placed directly under the impactor. Please consult the paper by Brown *et al* [6] for further information on the compression fixture.

6.2.3 Intermediate Strain Rate Testing

The intermediate strain rate testing procedures presented in this section are based on the work by Brown *et al* [6]. All intermediate strain rate testing was conducted on an instrumented falling weight drop tower test machine. Intermediate strain rate test compression specimen dimensions are shown in Figure 6-1 (c), i.e. they are the same as quasi-static specimens.

In-Plane Compression Testing

The intermediate strain rate compression specimens were straight sided specimens 25mm wide and 40mm in length (30mm gauge length). All specimens consisted of 4 plies in a 0°/90° layup sequence, giving a thickness of 4mm. The compression fixture used for quasi static compression testing, described in 6.2.2, was installed in the instrumented falling weight drop tower where the impactor of the drop tower contacted the T-shaped impactor of the compression fixture. Load was measured with a piezoelectric load cell and a Kistler [88] Charge Meter (Type 5015A) and the specimen strain response was measured with 5mm gauge length strain gauges (KFG-5-120-C1-11L3M3R) and a FLYDE [89] Transducer Amplifier (Type FE-579-TA). The single axial strain gauge was bonded symmetrically mid-width and mid-length of each specimen. Load cell and strain gauge readings (quarter bridge circuit) were recorded at a sample rate of 200 kHz on to computer using a Data Translation [90] high speed simultaneous USB data acquisition module (Type DT 9836) and the Measure Foundry [90] software. A crosshead mass of 85kg was used which impacted the specimens at 3 m/s giving an initial strain rate of 100/s based on the gauge length in Figure 6-1 (c).

6.3 Experimental Results

This section presents the results of the quasi static and intermediate strain rate testing detailed in the methodology in section 6.2.

6.3.1 Quasi Static Results

This section presents the results of the quasi static experimental testing detailed in the methodology in section 6.2.2. The stress strain responses for carbon/epoxy and S2 glass/epoxy samples are shown in Figure 6-3, Figure 6-4 and Figure 6-5 for in-plane tension, compression and shear respectively. Images of the tested samples are shown for in-plane tension in Figure 6-6 and Figure 6-7 for carbon/epoxy and S2 glass/epoxy samples respectively. The images of the in-plane compression and in-plane shear tested samples are shown in Figure 6-8 and Figure 6-9 respectively for both carbon/epoxy and S2 glass/epoxy. The numbers in the legend of the stress strain curve match the numbers in the images of the tested samples. Some numbers are missing from the stress strain curves; this is due to being unable to generate the stress strain curve due to invalid data from the video extensometer. Figure 6-2 summarises the mean and standard

deviation of the moduli and ultimate stresses for the quasi-static tests in tension, compression and shear.

	Carbon Stiffness (GPa)		Glass Stiffness (GPa)	
Quasi Static In-Plane Tension	55.5	± 9.6	22.2	± 1.9
Quasi Static In-Plane Compression	42.3	± 6.2	24.6	± 1.0
Quasi Static In-Plane Shear	3.5	± 0.4	3.6	± 0.4

	Carbon Strength (MPa)		Glass Strength (MPa)	
Quasi Static In-Plane Tension	576.8	± 48.8	461.3	± 57.8
Quasi Static In-Plane Compression	358.2	± 59.8	383.9	± 26.8
Quasi Static In-Plane Shear	57.5	± 2.3	51.5	± 5.1

Figure 6-2. Quasi static experimental results. The top and bottom table show results for stiffness and strength respectively. Results are shown in in-plane tension, compression and shear for carbon/epoxy and S2 glass/epoxy

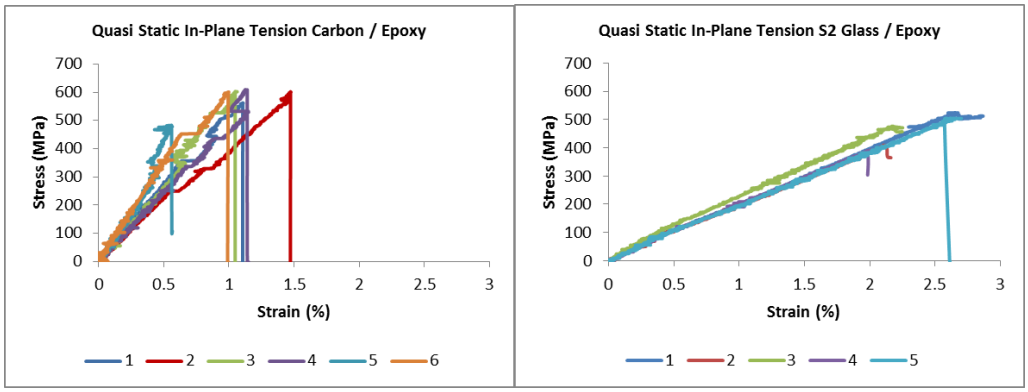

Figure 6-3. Quasi static in-plane tension stress strain responses for carbon/epoxy and S2 glass/epoxy samples

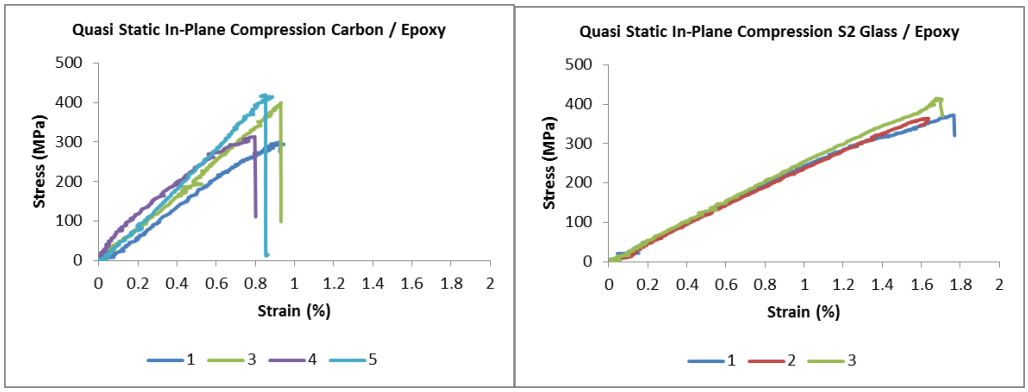

Figure 6-4. Quasi static in-plane compression stress strain responses for carbon/epoxy and S2 glass/epoxy samples

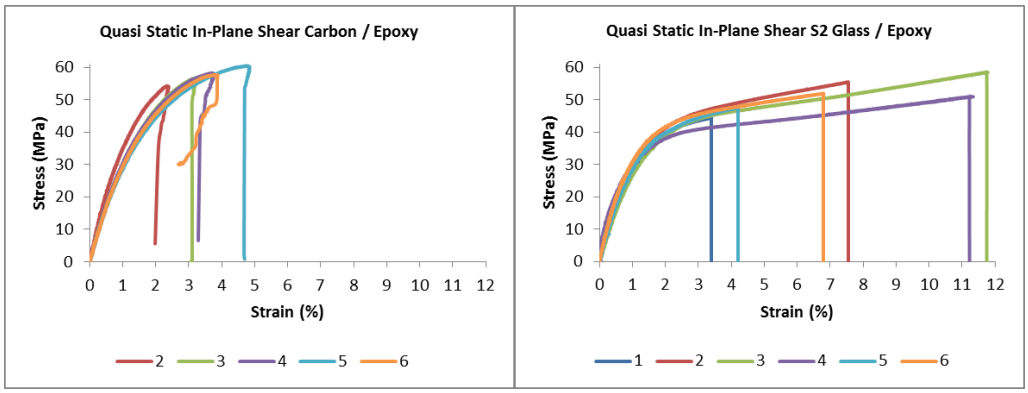

Figure 6-5. Quasi static in-plane shear stress strain responses for carbon/epoxy and S2 glass/epoxy samples

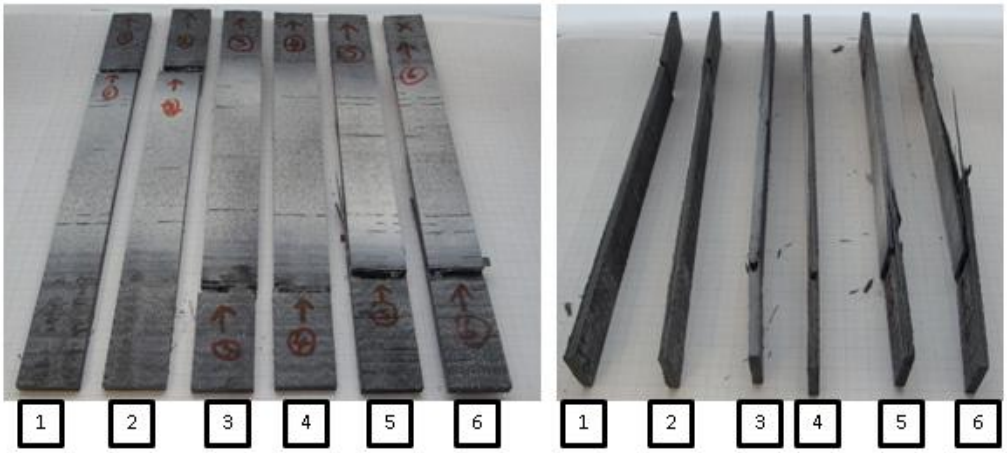

Figure 6-6. Quasi static in-plane tension carbon/epoxy tested samples, front and side view. Samples 1-6 left to right.

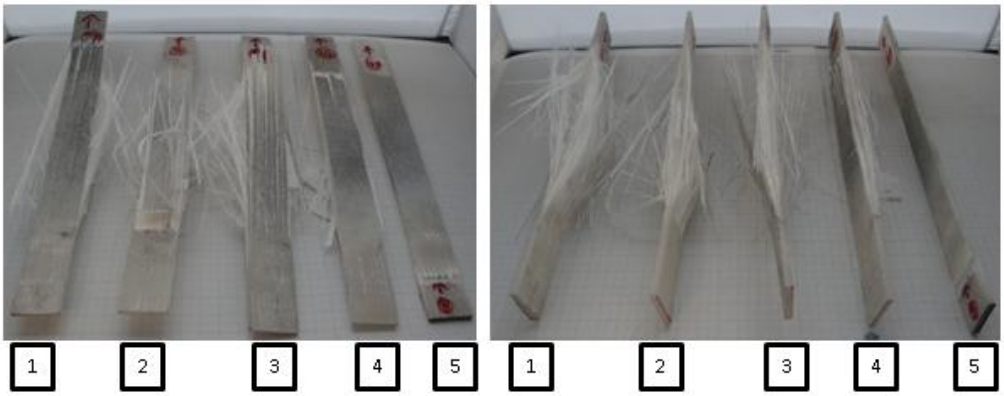

Figure 6-7. Quasi static in-plane tension S2 glass/epoxy tested samples, front and side view. Samples 1-5 left to right.

Figure 6-8. Quasi static in-plane compression carbon/epoxy (top row samples 1-5 left to right) and S2 glass/epoxy (bottom row samples 1-5 left to right) tested samples, front and side view

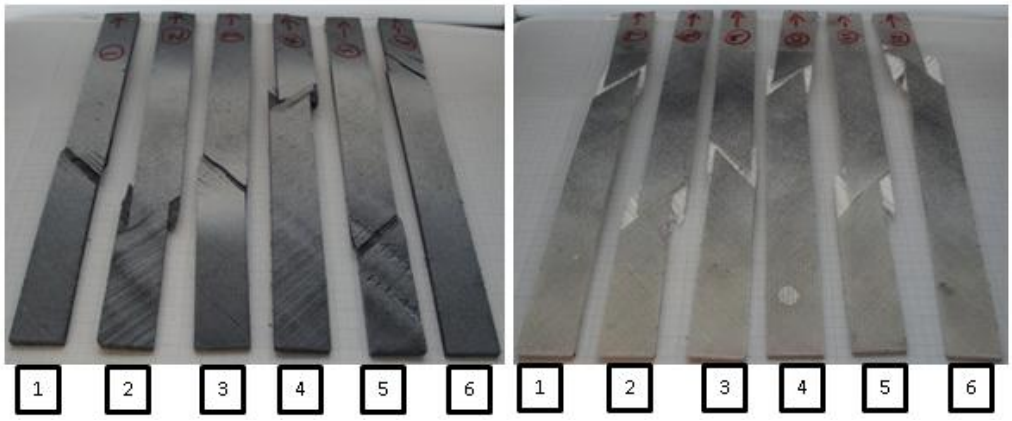

Figure 6-9. Quasi static in-plane shear carbon/epoxy (left) and S2 glass/epoxy (right) tested samples, front view. Samples 1-6 left to right.

6.3.2 Intermediate Strain Rate Results

This section presents the results of the intermediate strain rate experimental testing detailed in the methodology in section 6.2.3. The in-plane compression stress strain responses for carbon/epoxy and S2 glass/epoxy samples are shown in Figure 6-11 and Figure 6-12 respectively. Images of the tested samples are shown in Figure 6-13. The numbers in the legend of the stress strain curves match the numbers in the images of the tested samples. There is no stress strain curve for carbon/epoxy test 1 (C1); this is due to being unable to generate the stress strain curve due to invalid data from the strain gauges. Figure 6-10 summarises the mean and standard deviation of the moduli and ultimate stresses for the intermediate strain rate tests in compression.

	Carbon Stiffness (GPa)		Glass Stiffness (GPa)	
In-Plane Compression	81.4	± 2.3	53.9	± 3.3

	Carbon Strength (MPa)		Glass Strength (MPa)	
In-Plane Compression	531.9	± 38.9	453.2	± 10.7

Figure 6-10. Intermediate strain rate experimental results. The top and bottom table show results for stiffness and strength respectively. Results are shown in in-plane compression for carbon/epoxy and S2 glass/epoxy

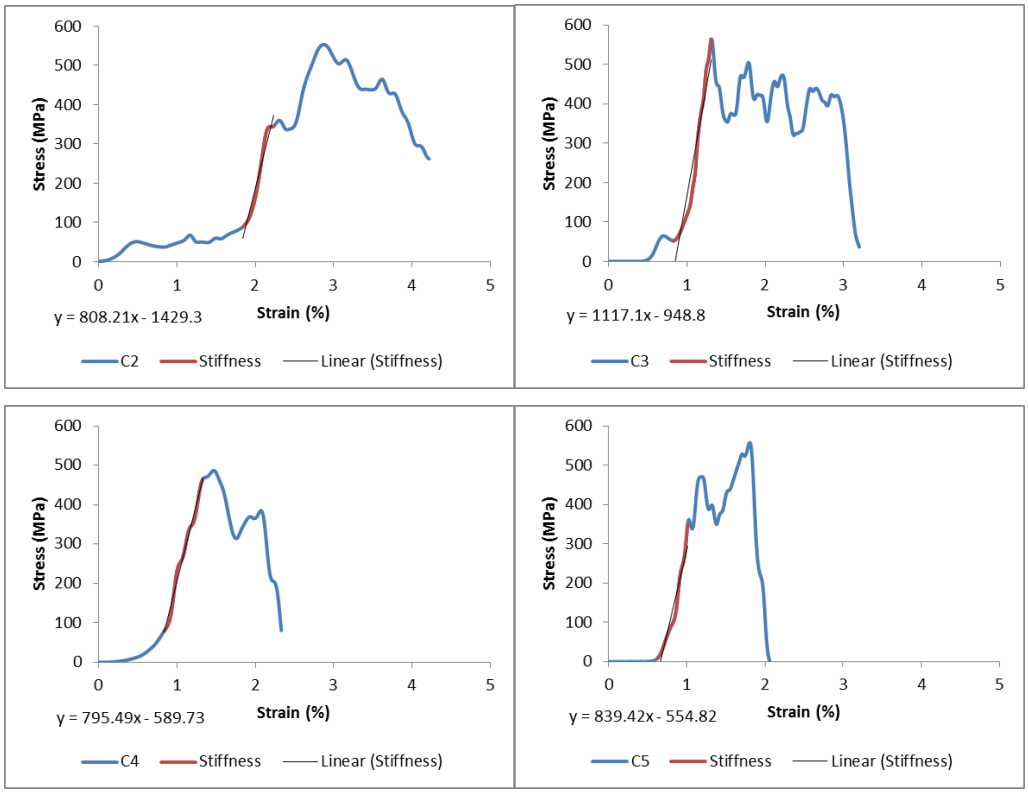

Figure 6-11. Intermediate strain rate in-plane compression stress strain responses for carbon/epoxy samples.

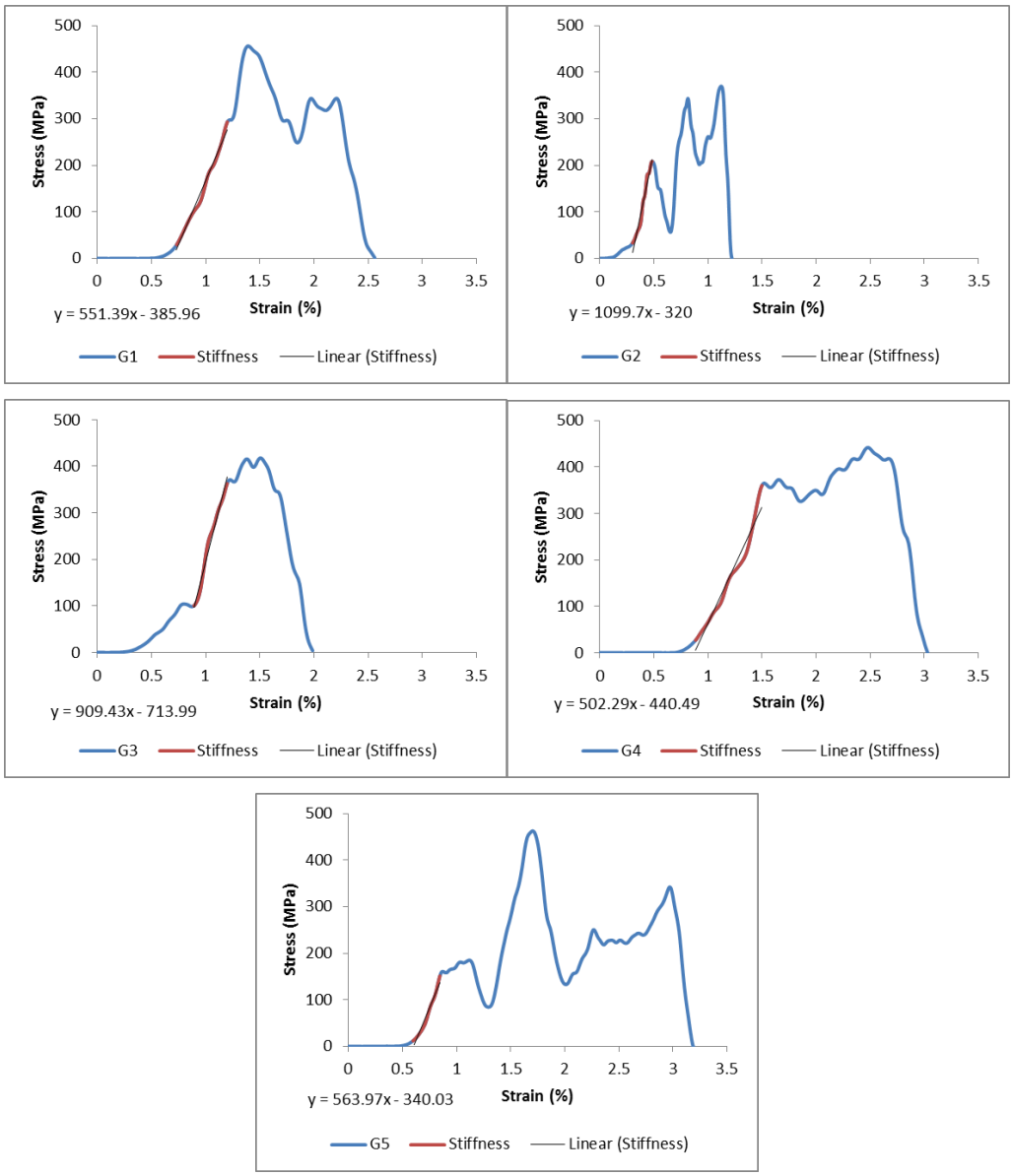

Figure 6-12. Intermediate strain rate in-plane compression stress strain responses for S2 glass/epoxy samples.

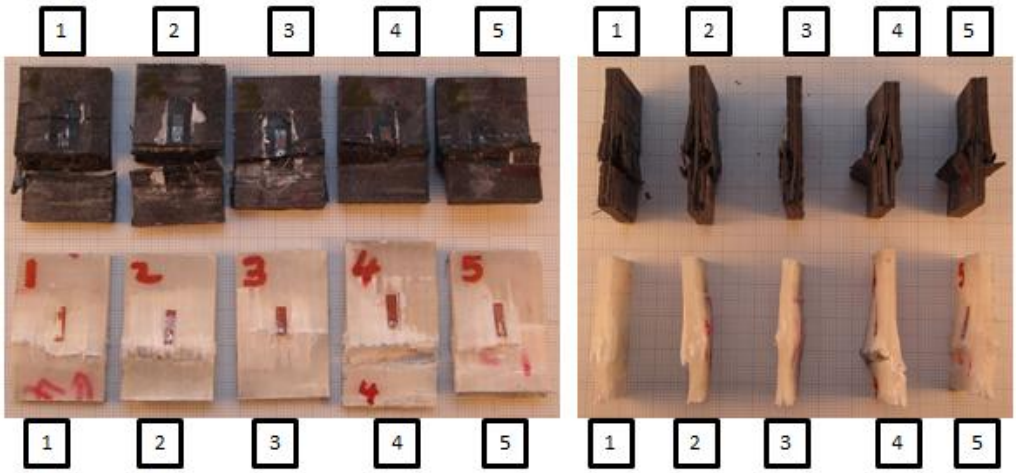

Figure 6-13. Intermediate strain rate in-plane compression carbon/epoxy (top row samples 1-5 left to right) and S2 glass/epoxy (bottom row samples 1-5 left to right) tested samples, front and side view

6.4 Discussion

6.4.1 Quasi Static Results

Stress Strain Responses

The quasi static stress strain response for both carbon/epoxy and S2 glass/epoxy in in-plane tension and in-plane compression, see Figure 6-3 and Figure 6-4, is approximately linear elastic up to a maximum value of stress. The quasi static stress strain response for both carbon/epoxy and S2 glass/epoxy in in-plane shear, see Figure 6-5, shows an initial linear elastic region followed by a gradual reduction in stiffness up to a maximum value of stress.

After reaching the maximum values of stress for carbon/epoxy in in-plane tension and for both carbon/epoxy and S2 glass/epoxy in in-plane shear there is an abrupt reduction in stress to practically zero. This abrupt reduction in stress to practically zero also occurs for the S2 glass/epoxy sample 5 in in-plane tension and for the carbon/epoxy samples 3, 4 and 5 in in-plane compression.

S2 glass/epoxy samples 1, 2, 3 and 4 in in-plane tension, carbon/epoxy sample 1 in in-plane compression and S2 glass/epoxy samples 1, 2 and 3 in in-plane compression show a gradual step by step reduction in stress after reaching the maximum value of stress. This is not shown in the stress strain curves in Figure 6-3 and Figure 6-4 as the video extensometer does not perform well with a cycle of large reductions in stress then large increases of stress so the data is only valid up to the maximum value of stress, which has been plotted in the stress strain curves. The force time curves recorded on the Instron test machine gives information of the gradual step by step reduction in stress for the samples discussed in this paragraph and are shown in Figure 6-14. To summarise; one S2 glass/epoxy sample in in-plane tension has an abrupt failure whilst all other are gradual and one carbon/epoxy sample in in-plane compression has a gradual failure whilst all others are abrupt. All S2 glass/epoxy samples in in-plane compression have a gradual failure.

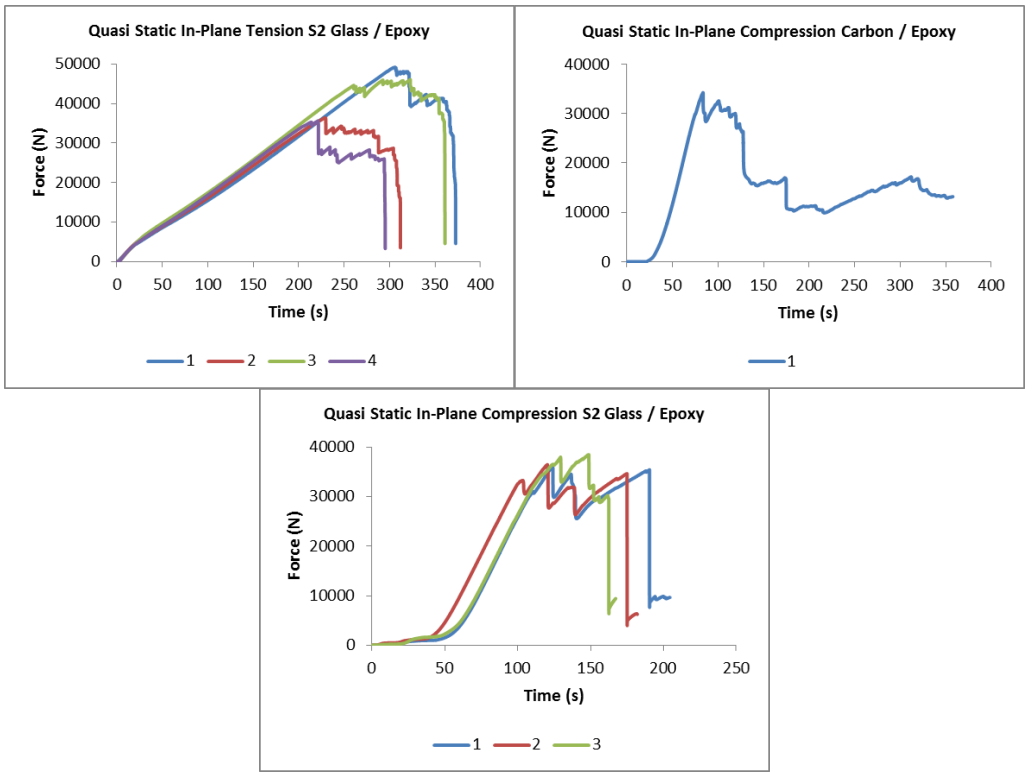

Figure 6-14. Force Time responses for those responses that show gradual step reductions in force / stress after the maximum value.

Damage Mechanisms

Carbon/epoxy in-plane tension samples failed through cracking across the width of the samples, perpendicular to the loading direction, see Figure 6-6. These cracks occurred due to matrix cracking, transverse yarn pull out and longitudinal yarn fracture generating the abrupt reduction in stiffness seen in Figure 6-3. In samples 1-4 the damage is very localised to the crack across the width of the samples, however, in samples 5 and 6, although there is a clear crack across the width of the sample, the damage spreads further along the length of the samples with extensive delamination and pull out of lamina layers. The stress strain responses for samples 5 and 6 in Figure 6-3 are the stiffest of all responses. It is however difficult to attribute this completely to the final state of failure.

S2 glass/epoxy in-plane tension samples fail through a gradual process of longitudinal fibres splitting and splaying away from the sample, see Figure 6-7. This damage works its way inwards (through the thickness) from the front and back face of the samples until there is only a small amount of load bearing material left mid-thickness of the samples. This section then splits causing final failure. This gradual failure mechanism gives the step reductions in force shown in the force time curves in Figure 6-14. The

reason for S2 glass/epoxy sample 5 failing abruptly rather than gradually, see Figure 6-3, is due to the difference in failure mechanism seen in Figure 6-7. Sample 5 fails with a crack across the width, perpendicular to the loading direction, at the bottom of the sample. This failure most likely occurred due to manufacturing defects such as a resin rich region or the presence of voids leading to stress concentrations in that particular region.

Carbon/epoxy and S2 glass/epoxy in-plane compression samples failed through delamination, fibre kinking and through thickness shear as shown in Figure 6-8 and Figure 6-15. The carbon/epoxy samples sustain much more damage than the S2 glass/epoxy samples. The reason for carbon/epoxy sample 1 failing gradually rather than abruptly as all the other samples did is due to the difference in failure mechanism seen in Figure 6-8. Looking at the side view it is clear to see sample 1 has sustained a significant larger amount of damage than the other samples.

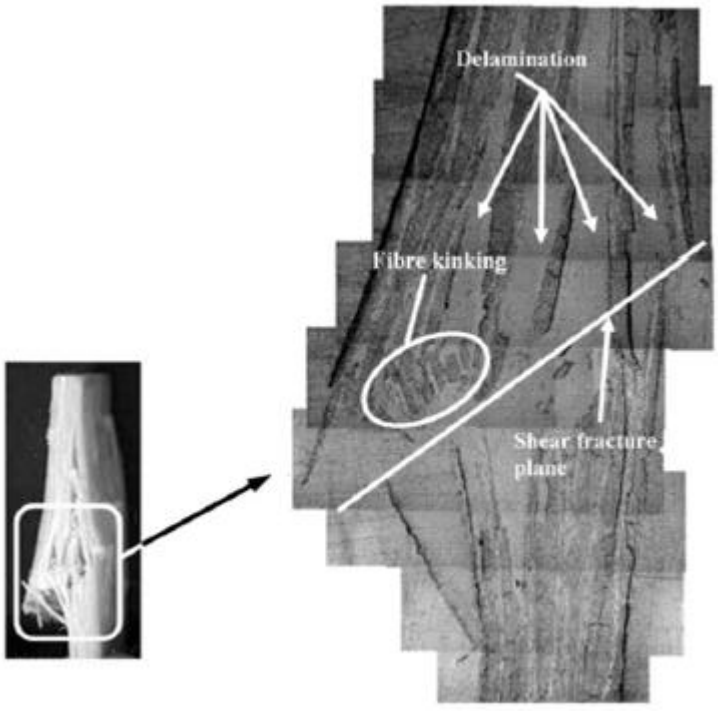

Figure 6-15. Optical micrograph of in-plane compression specimen edited from [6]

Carbon/epoxy and S2 glass/epoxy in-plane shear samples failed through delamination and sliding of lamina layers. This generates the cracks seen in Figure 6-9 which are at a 45º angle to the specimen sides i.e. in the ±45º layup direction. The S2 glass/epoxy samples experience more damage with a greater amount of sliding of layers over one another. This

produces the larger strain to failure for S2 glass/epoxy samples than carbon/epoxy samples seen in the stress strain responses in Figure 6-5. It can also be seen that there is a large variation in the strain to failure between different samples tested. This variation occurs due to the difference in samples from manufacturing causing a different amount of delamination and layer sliding.

Modelling and Experimental Comparison

This section compares the experimental results with the results obtained by the multi-scale modelling procedures presented in this thesis. These multi-scale modelling results have been derived from a long process of both micro and meso scale modelling where the results of micro scale modelling provided the input properties for meso scale modelling. The properties for quasi-static stiffness and strength for both carbon/epoxy and S2 glass/epoxy in in-plane tension, compression and shear are shown in Figure 6-16 for both experimental and modelling results.

	EXPERIMENTAL Carbon Stiffness (GPa)	MODELLING Carbon Stiffness (GPa)	EXPERIMENTAL Glass Stiffness (GPa)	MODELLING Glass Stiffness (GPa)
Quasi Static In-Plane Tension	55.5 ± 9.6	58.8	22.2 ± 1.9	21.5
Quasi Static In-Plane Compression	42.3 ± 6.2	60.3	24.6 ± 1.0	23.7
Quasi Static In-Plane Shear	3.5 ± 0.4	1.9	3.6 ± 0.4	1.9

	EXPERIMENTAL Carbon Strength (MPa)	MODELLING Carbon Strength (MPa)	EXPERIMENTAL Glass Strength (MPa)	MODELLING Glass Strength (MPa)
Quasi Static In-Plane Tension	576.8 ± 48.8	1176.5	461.3 ± 57.8	991.1
Quasi Static In-Plane Compression	358.2 ± 59.8	542.4	383.9 ± 26.8	805.4
Quasi Static In-Plane Shear	57.5 ± 2.3	36.7	51.5 ± 5.1	33.8

Figure 6-16. Comparison of quasi static experimental results and modelling results at a strain rate of 1/s. The top and bottom table show results for stiffness and strength respectively. Results are shown in in-plane tension, compression and shear for carbon/epoxy and S2 glass/epoxy.

The experimental and modelling values for stiffness for both materials in in-plane tension and in-plane compression compare very well. However, the modelling results slightly under-predict the in-plane shear stiffness.

The experimental and modelling values for strength for both materials in all loading conditions do not compare well. The modelling results significantly over-predict the strength in in-plane tension and in-plane compression and slightly under-predict the strength in in-plane shear.

Although the strength prediction is not accurate the modelling framework is picking up key features such as how the in-plane tensile strength is greater

than the in-plane compressive strength for both materials. Experimentally the in-plane tensile strength is 61% and 20% greater than the in-plane compressive strength for carbon/epoxy and S2 glass/epoxy respectively. Numerically the in-plane tensile strength is 117% and 23% greater than the in-plane compressive strength for carbon/epoxy and S2 glass/epoxy respectively.

The reason for the differences between experimental and modelling results is likely to be a result of the input material properties chosen for the micro scale modelling. These input properties were from literature and were not for the exact type of carbon, glass and epoxy used to manufacture the experimental samples. The results from the micro modelling are used in meso scale modelling; hence, the error will be carried through the multi-scale modelling process. Another reason could be that the micro and meso scale modelling was conducted on idealised structures. The experimental samples do not have uniform hexagonal packing of fibres within the yarns at the micro scale or a perfect $0^0/90^0$ or $\pm 45^0$ yarn architecture at the meso scale. This would usually lead to the modelling over-predicting strength values; which is the case for in-plane tension and in-plane compression testing which are fibre dependent modes of testing. Another consideration is that, in reality, not all fibres have the same value of strength; this is often taken into account in modelling work with random values of strength being assigned within a defined range to each fibre modelled. Zhao and Takeda [91] investigated the effect of interfacial adhesion and statistical fibre strength on the tensile strength of UD glass/epoxy composites. The researchers investigated the effect of five different fibre surface treatments. For each fibre surface treatment around forty tensile tests of single filaments were conducted on 24mm long specimens at 0.3 mm/min on a mini tester with a 4.9N load cell. For all surface treatments there was a large standard deviation from the average fibre strength. For example, water sized surface treatment resulted in an average fibre strength of 2.24 GPa with a standard deviation of 0.97. The maximum and minimum fibre strength was 4.73 GPa and 0.89 GPa respectively. It is clear to see form these results that fibres within a composite will not all have the same strength and the range of values can be large. Failure of the weakest fibre in a composite material can cause the onset of further damage mechanisms which can lead to ultimate failure of the component.

Ultimately the composite may only be as strong as the weakest fibre, as the failure of this fibre could lead to the initiation of further damage mechanisms.

A simple ROM calculation to determine the axial tensile strength of a UD lamina with the tensile fibre strength, tensile matrix strength and fibre volume properties given in Appendix B gives values of 3289 MPa and 2549 MPa for carbon/epoxy and S2 glass/epoxy respectively. Making the assumption that in a cross-ply laminate the transverse layers contribute nothing to the strength then the cross-ply laminate strength would reduce to 50% of the values above giving 1644.5 MPa and 1274.5 MPa for carbon/epoxy and S2 glass/epoxy respectively. These values are clearly greater (by at least a factor of 2) than the experimentally measured values obtained. It is believed that by using manufacturer's values for fibre strength we are significantly overestimating the actual fibre strength and in turn the yarn strength and cross-ply laminate strength.

Until now, all reasons for the differences between experimental and modelling results have been explained due to issues with the modelling; however, defects within the samples due to manufacturing issues are also likely to account for some of the discrepancy. Some tested samples had localised variations in thickness leading to cross sections of smaller areas which could lead to increased areas of stress. The thickness of the tested samples was taken to be an average of measurements at three points along the samples length. Resin rich regions and voids will also create stress concentrations and possibly lead to premature failure of the samples. There is evidence in the literature for this. For example, short beam shear and three-point flexure testing performed on $[0^o/90^o]_{4S}$ carbon/epoxy laminates by Ghiorse [92] showed that for every 1% increase in void volume fraction, the inter-laminar shear strength reduced by 5%-15%. Figure 6-17 shows an example of the cross sections of the carbon and glass laminates tested in the previous sections of this chapter. It is clear to see inter-yarn (in between the different yarns) and intra-yarn (within yarns) voids which could have generated premature failure due to the stress concentrations they develop. The average void volume fractions within the laminates are 2.4% and 1.5% for the carbon/epoxy and S2 glass/epoxy laminates respectively. Measurements were made by calculating the area fraction of the images in Figure 6-17 after they had

been cropped, to remove non-laminate sections, and a threshold applied to only show void regions utilising the ImageJ [73] software package. The samples measured were spare experimental test specimens that were cut from the same laminates as the actual test specimens. It is not just the void volume fraction which could cause premature failure but also the size of the voids, in some cases they are as large as a lamina layer, see Figure 6-17. In addition, Figure 6-17 shows the variety of yarn shapes and the change in the yarn paths across the laminate, clearly different to the idealised meso scale unit cell geometry. An extreme case of change in yarn path is seen for the carbon/epoxy samples in Figure 6-17 where at the bottom of the micrograph the yarn (with a left to right longitudinal direction) disappears out of the plane of the micrograph for a small section. The effect of fibre orientation variation like this was studied by Vallons *et al* [93] for the tensile strength of biaxial carbon/epoxy NCF composites. The researchers manufactured NCF chain stitched biaxial ±45º carbon/epoxy fully symmetric 2.1mm thick composite plates with a fibre volume fraction of around 57%. The samples were cut with different orientations relative to one of fibre directions and tested in quasi static tension. For 25mm wide test samples, cut with a 5^0 orientation, the stiffness and strength decreased by 10% and 50% respectively when compared to the 0^0 orientation samples. This demonstrates a significant potential reduction in strength. For the tested samples in this thesis, Figure 6-17 indicates that the orientation of the fibres can vary significantly from the 0º orientation. The manufacture of the laminates and the cutting of the laminates into samples can both contribute to this variation.

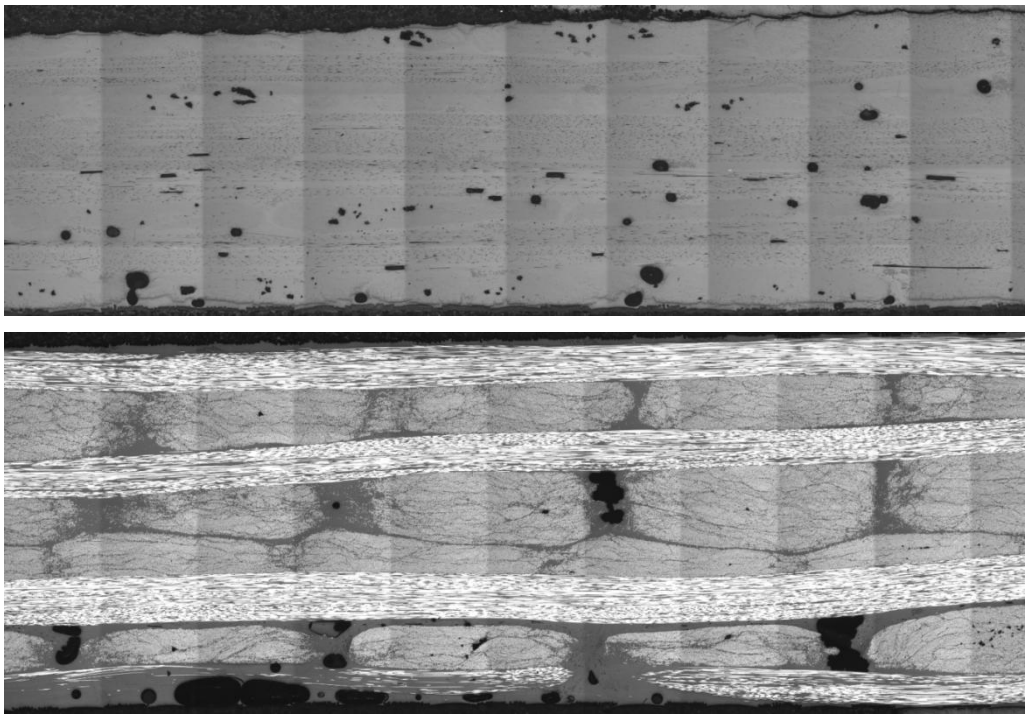

Figure 6-17. Example optical micrographs of the cross sections of 0°/90° NCF cross-ply S2 glass/epoxy (top) and carbon/epoxy (bottom) laminates tested in this chapter.

6.4.2 Intermediate Strain Rate Results

Stress Strain Responses

The stress strain responses for carbon/epoxy and S2 glass/epoxy samples tested at intermediate strain rates in in-plane compression are given in Figure 6-11 and Figure 6-12 respectively. These dynamic stress strain curves exhibit an initial non-linear region followed by linear elastic deformation. The initial non-linear region does not represent the material response; it is instead due to the slack and alignment of the specimen in the compression test fixture. The dynamic elastic modulus is not measured from this non-linear region, it is measured from the linear elastic region indicated in the stress strain curves in Figure 6-11 and Figure 6-12 by the red region with a linear 'least squares' trend line.

The linear elastic region is followed by yielding at a maximum value of stress, plastic deformation and finally failure which is indicated by a large reduction in stress. In some responses there are multiple yield points of the stress strain curve where there is a large drop in stress followed by a large increase in stress to a higher value than the previous yield point. This is seen in response number 5 for carbon/epoxy (C5) in Figure 6-11

and response number 2 and 5 for S2 glass/epoxy (G2 and G5) in Figure 6-12.

Damage Mechanisms

The carbon/epoxy and S2 glass/epoxy intermediate strain rate samples tested in in-plane compression fail in a similar manner to the quasi static strain rate samples described in section 6.4.1. The failure is due to delamination, fibre kinking and through thickness shear. The tested dynamic samples are shown in Figure 6-13.

Strain Rate Dependence

The average stiffness and strength values for quasi static and intermediate strain rate tested specimens are given in Figure 6-18 for both carbon/epoxy and S2 glass/epoxy in in-plane compression loading. It is important to note that values of stiffness and strength from intermediate strain rate responses 3 for carbon/epoxy (C3) and 2 and 3 for S2 glass/epoxy (G2 and G3) were removed from the averaging calculations. It was decided that the responses were significantly different to the other responses i.e. in some cases the stiffness was more than double some of the other responses which all fell within a narrow range of values indicated by the low standard deviation values. The reason for these untypical results was most likely a result of noisy strain gauge data which made it difficult to process the stress strain curves.

	Quasi Static Stifness (GPa)		Intermediate Strain Rate Stiffness (GPa)		Quasi Static Strength (MPa)		Intermediate Strain Rate Strength (MPa)	
Carbon/Epoxy	42.3	± 6.2	81.4	± 2.3	358.2	± 59.8	531.9	± 38.9
S2 Glass/Epoxy	24.6	± 1.0	53.9	± 3.3	383.9	± 26.8	453.2	± 10.7

Figure 6-18. Experimental values of stiffness and strength for carbon/epoxy and S2 glass/epoxy samples at quasi static (0.001/s) and intermediate (100/s) rates of strain in in-plane compression.

Experimentally the stiffness and strength both increase with increasing strain rate for both carbon/epoxy and S2 glass/epoxy samples. The stiffness increases by 92% and 119% for carbon/epoxy and S2 glass/epoxy samples respectively. The strength increases by 48% and 18% for carbon/epoxy and S2 glass/epoxy samples respectively.

Hosur *et al* [25] experimentally tested cross ply carbon epoxy laminates in in-plane compression over a range of strain rates. The dynamic stiffness

and strength values were larger than the static stiffness and strength values. For cross ply in-plane compression loading, the stiffness and peak stress increased by 114% and 17% respectively when comparing quasi static loading to loading at 82 /s (compared to 100/s strain rate experimentally tested in this thesis). This compares with the increased values of 92% and 48% in this work for stiffness and strength respectively. The similarities between the test results in this paper and those in Hosur's work are: the stiffness experiences a larger increase than strength with increasing strain rate and the stiffness increases by around a factor of two when comparing quasi static to intermediate strain rates.

Modelling and Experimental Comparison

The stiffness and strength values for quasi static (1/s) and intermediate strain rate testing (100/s) on carbon/epoxy and S2 glass/epoxy meso scale unit cells in in-plane compression are given in Figure 6-19. The values are obtained from the stiffness and strength against the natural log of the strain rate plots from the in-plane compression meso scale modelling results given in Appendix D and supplied here in Figure 6-20. Substituting values of ln(1) and ln(100), i.e. 0 and 4.6, into the 'least squares' linear trend line equation gives the values of stiffness and strength at 1/s and 100/s strain rates. These calculations are required as simulations were conducted at 1, 1000 and 10000/s only; not 100/s.

	Quasi Static Stifness (GPa)	Intermediate Strain Rate Stiffness (GPa)	Quasi Static Strength (MPa)	Intermediate Strain Rate Strength (MPa)
Carbon/Epoxy	60.2	61.7	544.1	925.9
S2 Glass/Epoxy	24.1	24.5	765.0	959.0

Figure 6-19. Modelling values of stiffness and strength for carbon/epoxy and S2 glass/epoxy meso scale unit cells at quasi static (1/s) and intermediate (100/s) rates of strain

Carbon/Epoxy

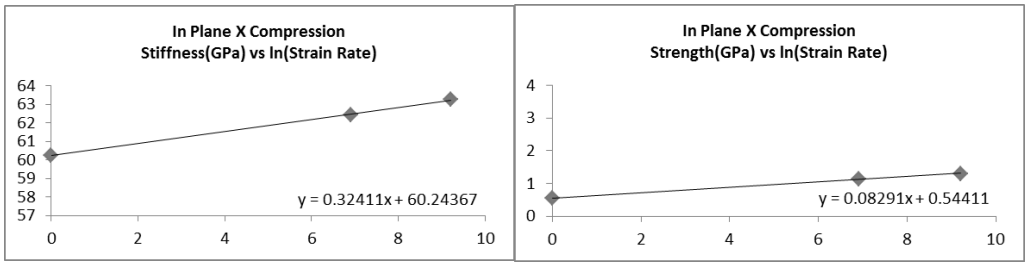

S2 Glass/Epoxy

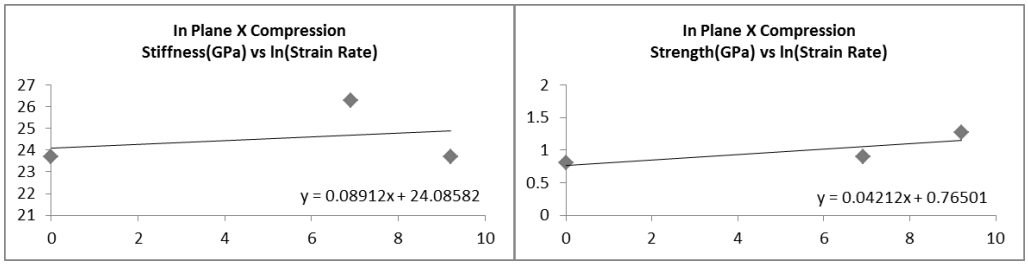

Figure 6-20. Stiffness and Strength against the natural log of the strain rate plots for in-plane compression loading of carbon/epoxy (top) and S2 glass/epoxy (bottom) meso scale unit cells. The blue dots are results at 1/s, 1000/s and 10000/s.

From the modelling results the stiffness and strength both increase with increasing strain rate in in-plane compression for both carbon/epoxy and S2 glass/epoxy meso scale unit cells. The stiffness increases by 2.5% and 1.7% for carbon/epoxy and S2 glass/epoxy meso scale unit cells respectively. The strength increases by 70.2% and 25.4% for carbon/epoxy and S2 glass/epoxy meso scale unit cells respectively. Comparing this to the experimental increases in stiffness and strength from quasi static to 100/s strain rates the strength increases compare reasonably well; 48% compared to 70.2% for carbon/epoxy and 18% compared to 25.4% for S2 glass/epoxy. The stiffness increases, however, do not compare well with the experimental results showing a increase of roughly a factor of two and the modelling results showing little change at all.

The differences between experimental and modelling results in terms of the percentage change in stiffness and strength with strain rate are likely to be due to, from a modelling perspective, the fact that fibre strain rate dependence was not included at the micro scale. The fibre strain rate depdendece was not included due to the limited literatue data availiable. The papers that were found, and referenced in the literature review of this thesis in section 2.2.4, indicated that carbon fibres were regarded as

strain rate insensitive and that glass fibres were strain rate dependent over a low strain rate range. High strain rate testing of single glass fibres was not found in the literature, presumably due to the difficulty of this type of experimental testing. It is also important to mention that there are difficulties in establishing the elastic regions of the intermediate strain rate experimental results and hence the straight line fits to establish the elastic moduli may not be truly representative of the material response, see the stress strain responses in Figure 6-11 and Figure 6-12.

7 Conclusions and Recommendations

7.1 Introduction

This chapter begins with a general discussion of the work and the main conclusions from the work conducted. This will then be followed by an outline of recommendations for future work.

7.2 Discussion

Multi-Scale Modelling

A hierarchical multi-scale modelling approach has been demonstrated with finite element modelling occurring at the micro, meso and macro scale of analysis. Information has been transferred between the scales in the form of material properties. The key and novel feature of this work is that the effect of strain rate on stiffness and strength has been captured at each scale and this information transferred to the proceeding larger scale. Some key issues became apparent in the homogenisation of material properties due to the vast amount of data from one scale of analysis that had to be condensed for the higher scale of analysis. For example, how does one utilise the results from eight loading modes tested at three strain rates at the micro scale in the meso scale modelling. Choices made in the information transfer process can have a dramatic effect at the higher scale of analysis. For example, the micro scale modelling produces eight strain rate scaling constants for strength i.e. the strength scales differently in each micro scale loading mode. These eight constants are averaged into one strain rate scaling constant for strength for use in the meso scale yarn material model. The average value is comparable to most of the individual micro values except the longitudinal values which are smaller. The effect is that yarn longitudinal strength at the meso scale is over scaled with increasing strain rate. Although it is clear that further work is required to improve the multi-scale modelling process an excellent framework has been set out to enable virtual material characterisation to progress in the field of composite materials. The entire multi-scale virtual material characterisation procedure has already been demonstrated with the micro and meso scale modelling in this thesis being used in blast and ballistic modelling on macro scale composite laminates. For such complex multi-

scale modelling to progress it is believed that automation is of paramount importance and this has been advanced through the use of Python programming within Abaqus. Python was utilised to fully set up simulations at both the micro and meso scale. The programming was particularly useful in performing repetitive tasks such as applying linear constraint equations on a node by node basis to implement periodic boundary conditions based on translational symmetry. Python programming was further utilised to operate on simulation output files and produce stress strain data as well as calculate key parameters such as stiffness and strength.

Composite Material Models

This work has created and developed advanced material models in the form of user subroutines, coded in Fortran, in the Abaqus explicit finite element code. Material models have been created for fibre and interface at the micro scale, yarn at the meso scale and matrix at the micro and meso scales. The material models control the initial linear elastic response, damage initiation, damage evolution and strain rate dependence. The section of the material models that deals with damage incorporates damage initiation, based on the maximum stress criterion, and damage evolution, based on a damage mechanics approach or element deletion, depending on the material constituent. It was deemed that the maximum stress criterion would be appropriate for this type of modelling, however, current commercial material models use more advanced and often interactive criteria. This is something that would have to be investigated in a multi-scale modelling process in future work. It could well be discovered that the extra complexity of the more advanced failure criteria would be lost in the information transfer process of material properties. The damage mechanics approach used for certain constituents to control post elastic behaviour produced excellent results in terms of gradual reductions in stress with increasing strain. The use of element deletion in certain constituents gave obviously very little control over the failure process but was used in constituents where it was deemed failure would most likely be brittle e.g. fibres. Strain rate dependence is incorporated in certain constituents through logarithmic equations which scale the stiffness and strength. The input properties for this at the micro scale were from experimental testing and the results demonstrated clear increases of stiffness and strength with increasing strain rate. The clear weakness of

such an advanced composite material model is the large amount of development time in writing and testing the code within the desired finite element package. It is important to consider the failure mechanisms that were not captured in this work, such as fibre kinking. The micro scale model was not longitudinally thick enough to see the kinking / buckling of fibres and there was no attempt to represent this failure mechanism at the meso and macro scale. One, however, could argue that the use of a lower value for compressive strength than tensile strength of the fibres at the micro scale went some way to address this failure mechanism.

Micro Scale Modelling

The micro scale finite element modelling conducted in this doctoral thesis involved the testing of carbon/epoxy and S2 glass/epoxy unidirectional composites. Idealised hexagonally packed unit cells were tested in longitudinal tension, longitudinal compression, transverse tension (two directions), transverse compression (two directions), longitudinal shear and transverse shear. All loading conditions were tested at 1/s, 1000/s and 10000/s rates of strain. The micro scale modelling predicted the linear elastic response, damage initiation and its evolution with increasing strain and the strain rate dependence of stiffness and strength. The resulting micro unit cell stiffness values compared well to the Rule of Mixtures predictions, especially in longitudinal loading for which the analytical predications are most reliable and accurate. It is however believed that the strength values were over predicted due to the fibre input properties and a statistical fibre strength approach would have yielded better comparisons to analytical methods and experimental testing. The micro unit cell modelling captured gradual, in transverse tension, compression and shear loading, and abrupt, in longitudinal tension, compression and shear loading, reductions in stiffness in the post elastic response. This was achieved through the material models with matrix dominated responses being based on maximum stress criterion and continuum damage mechanics theory and fibre/interface dominated responses being based on maximum stress criterion and element deletion. Micro unit cell stiffness and strength was shown to increase with strain rate in all loading modes except longitudinal loading. The location of damage initiation and its progression through the micro scale unit cell with increasing strain was physically captured on a 3D meshed model. The key damage mechanics simulated were matrix cracking, fibre fracture and interfacial damage.

Meso Scale Modelling

The meso scale finite element modelling conducted in this doctoral thesis involved the testing of carbon/epoxy and S2 glass/epoxy 0°/90° NCF composite laminates. Meso scale unit cells were tested in in-plane tension, in-plane compression, through thickness tension, through thickness-compression, in-plane shear and through thickness shear. All loading conditions were tested at 1/s, 1000/s and 10000/s rates of strain. The meso scale modelling predicted the linear elastic response, damage initiation and its evolution with increasing strain and the strain rate dependence of stiffness and strength. As with the micro modelling the meso modelling also captured the physical locations of damage and its progression in yarn or matrix material. The majority of stress strain responses for the meso scale unit cell produced abrupt reductions in stiffness in the post elastic response. Gradual reductions in stiffness in the post elastic response occurred when the material response was matrix dominated, e.g. carbon/epoxy in through thickness shear, with significant damage occurring in the through thickness matrix regions. Meso unit cell stiffness and strength was shown to increase with strain rate in all loading conditions, except in-plane loading where only strength increased. It was not expected that in-plane meso scale loading would show a significant increase in strength with increasing strain rate as in-plane loading is a longitudinal yarn dominated response and micro scale longitudinal loading gave little rate dependence. The reduction and averaging of micro scale modelling data caused this issue for strength as the strain rate scaling constants for strength from all micro loading modes were averaged into one yarn strength strain rate scaling constant for use at the meso scale. The same issue was not apparent for stiffness as three strain rate scaling constants for stiffness were used for the meso scale yarn material model; one for longitudinal, transverse and shear stiffness. The longitudinal strain rate scaling constant for stiffness was much lower than the transverse and shear value allowing strain rate dependence of stiffness in through thickness and shear loading and not in-plane loading. This work has indicated the shortcomings of some current strain rate dependent material models where only one strength strain rate scaling constant is utilised.

Experimental Testing

To validated the meso scale modelling, and in turn the overall multi-scale modelling framework, 0°/90° NCF carbon/epoxy and S2 glass/epoxy meso scale samples were tested in in-plane tension, compression and shear at low (all loading modes) and intermediate (compression only) strain rates. The testing was conducted on; an electromechanical universal static test machine and an instrumented falling weight drop tower. The quasi static experimental and modelling values for stiffness for both materials in in-plane tension and in-plane compression compared very well. However, the modelling results slightly under-predict the quasi static in-plane shear stiffness. The quasi static experimental and modelling values for strength for both materials in all loading conditions did not compare well. The modelling results significantly over-predicted the quasi static strength in in-plane tension and in-plane compression and slightly under-predicted the quasi static strength in in-plane shear. From the modelling results the stiffness and strength both increased with increasing strain rate (from quasi static to 100 /s) in in-plane compression for both carbon/epoxy and S2 glass/epoxy meso scale unit cells. The stiffness increased by 2.5% and 1.7% for carbon/epoxy and S2 glass/epoxy meso scale unit cells respectively. The strength increased by 70.2% and 25.4% for carbon/epoxy and S2 glass/epoxy meso scale unit cells respectively. Comparing this to the experimental increases in stiffness and strength from quasi static to 100/s strain rates the strength increases compare reasonably well; 48% compared to 70.2% for carbon/epoxy and 18% compared to 25.4% for S2 glass/epoxy. The stiffness increases, however, do not compare well with the experimental results showing an increase of roughly a factor of two and the modelling results showing little change at all. The reasons for the differences for modelling and experimental results have been discussed with the main reasons likely to be idealised micro/meso geometries and manufactuers fibre strength data, rather than statistical fibre strengths, giving large modelling strength predictions and voids, resin rich regions, local variations in thickness and variations in yarn shapes and paths giving low experimental strength values.

7.3 Conclusions

In this section the major conclusions of this doctoral investigation are presented.

- Multi-scale modelling has shown promise to be a viable alternative to experimental testing in the future in predicting component level material properties.
- The material models implemented in the multi-scale modelling process have predicted the linear elastic response, damage initiation and its evolution with increasing strain and the strain rate dependence of stiffness and strength at both the micro and meso scale of analysis.
- Finite element modelling on micro scale unit cells enabled the prediction of meso scale yarn properties that compared well to analytical methods.
- Finite element modelling on meso scale unit cells enabled the prediction of macro scale properties. The properties were validated against experimental testing on 0°/90° NCF laminates. Quasi static stiffness values compared well and the modelling picked up some key strain rate dependent features that were apparent in the experimental results.
- Discrepancies between modelling and experimental results, primarily for strength, were attributed to non-representative modelling due to using idealised micro/meso geometries and manufacturer's fibre strength data, rather than implementing statistical fibre strengths. The effect of defects, voids and fibre orientation issues, within the experimental samples was also deemed account for some of the discrepancy.

7.4 Recommendations for Future Work

The work conducted in this thesis has generated numerous areas of possible future work that, if conducted, would be beneficial to the continued development of high strain rate multi scale modelling of polymer composite materials. The recommendations for future work are summarised below.

Micro Scale Experimental Testing:

- The strain rate dependence of the fibres at the micro scale is not considered in this study. It is widely accepted that carbon fibres are strain rate insensitive in the sense that strain rate has a negligible effect on stiffness, ultimate strength and failure strain [19, 20]. However, it has been shown by Yazici [21] that S2 glass fibres can demonstrate strain rate sensitivity. Yazici only tested the fibres over a range of strain rates below 1/s; hence, experimental testing of S2 glass fibres from quasi static to high rates of strain would yield valuable information which could be included in the micro scale fibre material model in this thesis.
- It is recommended that an experimental test program be conducted on an epoxy matrix material in tension, compression and shear over the full range of strain rates from quasi static to thousands per second. This would show how stiffness and strength scale with increasing strain rate in all three loading conditions. The matrix material model in this thesis used strain rate scaling constants from compression testing for all three loading condition values. There is a distinct lack of data in the literature on the high strain rate testing of epoxy matrix material in tension and shear due to the added complexity of modifying high strain rate test equipment such as the split Hopkinson bar.
- An experimental program to test micro scale samples in all loading conditions over a range of strain rates would help to verify the modelling results obtained.

Meso Scale Experimental Testing:

- An experimental program to test meso scale samples in all loading conditions over a range of strain rates would help to verify the modelling results obtained.

Micro Scale Modelling:

- Micro scale testing of representative volume elements with randomly dispersed fibres would give an insight into the difference in material properties when compared to an idealised packing, such as hexagonal as in this thesis. Figure 7-1 shows some early work that the thesis author has already conducted in this area, where an RVE with randomly placed fibres is tested in transverse tension.

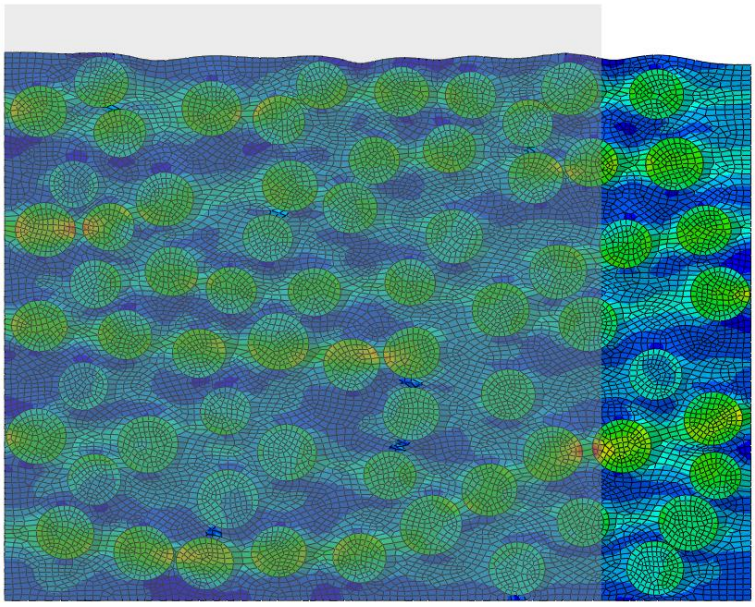

Figure 7-1. Representative volume element (RVE) containing 40% randomly placed fibres with randomly assigned fibre radii within a defined range. Shaded area shows original RVE and deformed shape occurs due to transverse tension. 25% strain applied to right edge in an implicit analysis, left and bottom edges have zero normal displacement. Contours show von Mises stress where red indicates high stress and blue indicates low stress.

Meso Scale Modelling:

- When converting micro scale results into meso scale properties some of the detail is lost in the homogenisation process. The meso scale yarn material model only has four strain rate scaling constants (longitudinal stiffness, transverse stiffness, shear stiffness and strength) whereas the micro scale modelling results could have provided a lot more e.g. strain rate scaling constants for strengths in all loading conditions. A re-run of the meso scale simulations with more detailed material properties would provide interesting results for comparison.
- The modelling methodology in this thesis has focused on NCF. It would be an interesting study to extend the type of meso scale unit cells tested to woven fabrics and other more complex fabric architectures.
- Meso scale variability such as the change of yarn shape along the yarn path would be a new interesting area of study.

General Modelling:

- A comparison of damage contour plots for two different types of failure criteria would be an interesting piece of work. One could use

maximum principal stress, amongst a multitude of others, instead of the maximum stress criterion used in this thesis.

- This work in this thesis has been limited to epoxy matrix materials and carbon and S2 glass fibres. The methodology can, and should, be applied to other types of composite materials such as those with polyester, vinyl ester and thermoplastic matrix materials with possible aramid fibre inclusions. However, for success, constituent material data would be needed for these materials.
- The influence of voids and material defects in the material properties is a large area of research. The effect of this on the high strain rate properties of polymer composite materials is unknown and is recommended for future work.
- The boundary conditions used in this thesis allow for easy application of multi axial loading in micro and meso scale modelling e.g. bi-axial compression. It was considered outside the scope of this thesis but would be an obvious area for future development. Figure 7-2 shows some early work that the thesis author has already conducted in this area, where a micro scale unit cell is subjected to multi axial loading.

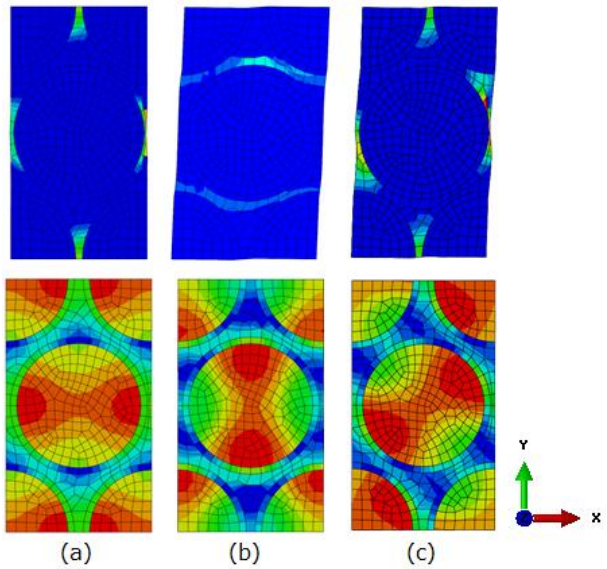

Figure 7-2. Carbon/epoxy micro scale unit cell damage contour plots showing initial damage locations at various steps of the analysis (top row) and von Mises stress contours (bottom row) for first step of analysis at 10000/s in (a) transverse x compression, (b) transverse xy shear and (c) multi axial loading combining transverse x compression and transverse xy shear. For top row blue indicates no damage and red indicates maximum damage. For bottom row red indicates high stress and blue indicates low stress.

References

1. *AGY Product Information S2 Glass Fibers. [cited 09/07/12]; Availiable from: http://www.agy.com*.
2. *Joint Improvised Explosive Device Defeat Organization (JIEDDO): Annual Report 2010. Availiable from: www.jieddo.dod.mil/.*
3. *BBC News Website: Q&A Snatch Land Rovers. [cited 31/05/11]; Availiable from: http://news.bbc.co.uk/1/hi/uk/7703703.stm*.
4. *BBC News Website: MoD signs deal to replace Snatch vehicle with Foxhound. [cited 31/05/11]; Availiable from: http://www.bbc.co.uk/news/uk-11877801*.
5. French, M. and A. Wright, *'Developing mine blast resistance for composite based military vehicles', in N Uddin (ed.), Blast protection of civil infrastructures and vehicles using composites*, 2010, Woodhead Publishing Limited, Cambridge. p. 244-268.
6. Brown, K.A., R. Brooks, and N.A. Warrior, *The static and high strain rate behaviour of a commingled E-glass/polypropylene woven fabric composite.* Composites Science and Technology, 2010. **70**(2): p. 272-283.
7. *Encyclopedia Britannica Website. [cited 25/11/11]; Availiable from: http://www.britannica.com*.
8. Edgren, F., et al., *Formation of damage and its effects on non-crimp fabric reinforced composites loaded in tension.* Composites Science and Technology, 2004. **64**(5): p. 675-692.
9. Hull, D. and T.W. Clyne, *An Introduction to Composite Materials*1996: Cambridge University Press.
10. *Plymouth University Website. [cited 29/09/11]; Availiable from: http://www.tech.plym.ac.uk/sme/MATS324/MATS324A4%20fracture.htm*.
11. Mattsson, D., R. Joffe, and J. Varna, *Damage in NCF composites under tension: Effect of layer stacking sequence.* Engineering Fracture Mechanics, 2008. **75**(9): p. 2666-2682.
12. Littell, J.D., et al., *Measurement of epoxy resin tension, compression, and shear stress-strain curves over a wide range of strain rates using small test specimens.* Journal of Aerospace Engineering, 2008. **21**(3): p. 162-173.
13. Gilat, A., R.K. Goldberg, and G.D. Roberts, *Strain rate sensitivity of epoxy resin in tensile and shear loading.* Journal of Aerospace Engineering, 2007. **20**(2): p. 75-89.
14. Jordan, J.L., J.R. Foley, and C.R. Siviour, *Mechanical properties of Epon 826/DEA epoxy.* Mechanics of Time-Dependent Materials, 2008. **12**(3): p. 249-272.
15. Hou, J.P., C. Ruiz, and A. Trojanowski, *Torsion tests of thermosetting resins at impact strain rate and under quasi-static loading.* Materials Science and Engineering a-Structural Materials Properties Microstructure and Processing, 2000. **283**(1-2): p. 181-188.
16. Miwa, M., et al., *Strain-Rate and Temperature-Dependence of Shear Properties of Epoxy-Resin.* Journal of Materials Science, 1995. **30**(7): p. 1760-1765.
17. Gerlach, R., et al., *Experimental characterisation and constitutive modelling of RTM-6 resin under impact loading.* Polymer, 2008. **49**(11): p. 2728-2737.
18. Hogg, P.J., *Perspectives - Composites in armor.* Science, 2006. **314**(5802): p. 1100-1101.
19. Zhou, Y.X., D.Z. Jiang, and Y.M. Xia, *Tensile mechanical behavior of T300 and M40J fiber bundles at different strain rate.* Journal of Materials Science, 2001. **36**(4): p. 919-922.

20. Zhou, Y.X., et al., *Tensile behavior of carbon fiber bundles at different strain rates.* Materials Letters, 2010. **64**(3): p. 246-248.
21. Yazici, M., *Loading Rate Sensitivity of High Strength Fibers and Fiber/Matrix Interfaces.* Journal of Reinforced Plastics and Composites, 2009. **28**(15): p. 1869-1880.
22. Tanoglu, M., et al., *A new technique to characterize the fiber/matrix interphase properties under high strain rates.* Composites Part a-Applied Science and Manufacturing, 2000. **31**(10): p. 1127-1138.
23. Fishpool, D.T., et al., *Preferential Energy Absorbing Interfaces for Ballistic and Structural Applications*, in *The 18th International Conference On Composite Materials*2011: Jeju, South Korea.
24. Vural, M. and G. Ravichandran, *Transverse failure in thick S2-glass/epoxy fiber-reinforced composites.* Journal Of Composite Materials, 2004. **38**(7): p. 609-623.
25. Hosur, M.V., et al., *High strain rate compression response of carbon/epoxy laminate composites.* Composite Structures, 2001. **52**(3-4): p. 405-417.
26. Okoli, O.I. and G.F. Smith, *Failure modes of fibre reinforced composites: The effects of strain rate and fibre content.* Journal of Materials Science, 1998. **33**(22): p. 5415-5422.
27. Jacob, G.C., et al., *Strain rate effects on the mechanical properties of polymer composite materials.* Journal of Applied Polymer Science, 2004. **94**(1): p. 296-301.
28. Sierakowski, R.L., *Strain Rate Effects in Composites.* Applied Mechanics Review, 1997. **50**(12): p. 741-762.
29. Zukas, J.A., et al., *Impact Dynamics*1982: John Wiley & Sons.
30. Hamouda, A.M.S. and M.S.J. Hashmi, *Testing of composite materials at high rates of strain: advances and challenges.* Journal of Materials Processing Technology, 1998. **77**(1-3): p. 327-336.
31. Field, J.E., et al., *Review of experimental techniques for high rate deformation and shock studies.* International Journal of Impact Engineering, 2004. **30**(7): p. 725-775.
32. Lidgett, M., et al., *Multi-Scale Modelling Of Polymer Composite Materials Under Blast and Ballistic Loading*, in *The 18th International Conference On Composite Materials*2011: Jeju, South Korea.
33. Cox, B. and Q.D. Yang, *In quest of virtual tests for structural composites.* Science, 2006. **314**(5802): p. 1102-1107.
34. Li, S.G., *On the unit cell for micromechanical analysis of fibre-reinforced composites.* Proceedings of the Royal Society of London Series a-Mathematical Physical and Engineering Sciences, 1999. **455**(1983): p. 815-838.
35. Li, S.G., *Boundary conditions for unit cells from periodic microstructures and their implications.* Composites Science and Technology, 2008. **68**(9): p. 1962-1974.
36. Nye, J.F., *Physical Properties of Crystals - Their Representation by Tensors and Matrices*1957: Oxford University Press.
37. Garnich, M.R. and V.M.K. Akula, *Review of Degradation Models for Progressive Failure Analysis of Fiber Reinforced Polymer Composites.* Applied Mechanics Reviews, 2009. **62**(1).
38. Zhao, L.G., N.A. Warrior, and A.C. Long, *Finite element modelling of damage progression in non-crimp fabric reinforced composites.* Composites Science and Technology, 2006. **66**(1): p. 36-50.

39. Orifici, A.C., I. Herszberg, and R.S. Thomson, *Review of methodologies for composite material modelling incorporating failure.* Composite Structures, 2008. **86**(1-3): p. 194-210.
40. Knight Jr, N.F., *User-Defined Material Model for Progressive Failure Analysis.* NASA STI Report Series, 2006.
41. Schweizerhof, K., et al., *Crashworthiness Analysis with Enhanced Composite Material Models in LS-DYNA - Merits and Limits*, in *LS-DYNA World Conference*1998: Detroit, Michigan, USA.
42. Matzenmiller, A., J. Lubliner, and R.L. Taylor, *A Constitutive Model for Anisotropic Damage in Fiber-Composites.* Mechanics of Materials, 1995. **20**(2): p. 125-152.
43. *Abaqus 6.9 Documentation, DS Simula*, 2009.
44. Yen, C., *Ballistic impact modelling of composite materials*, in *7th International LS-DYNA Users Conference*2002: Dearborn, Michigan.
45. Zheng, X.H. and W.K. Binienda, *Rate-dependent shell element composite material model implementation in LS-DYNA.* Journal of Aerospace Engineering, 2008. **21**(3): p. 140-151.
46. Goldberg, R.K., G.D. Roberts, and A. Gilat, *Incorporation of mean stress effects into the micromechanical analysis of the high strain rate response of polymer matrix composites.* Composites Part B-Engineering, 2003. **34**(2): p. 151-165.
47. Daniel, I.M., B.T. Werner, and J.S. Fenner, *Strain-rate-dependent failure criteria for composites.* Composites Science and Technology, 2011. **71**(3): p. 357-364.
48. Meyer, L.W. and M. Mayer, *'New Strain Rate Dependent Material Model for Fiber Reinforced Composites', in Tom Proulx (ed.), Time Dependent Constitutive Behavior and Fracture/Failure Processes, Vol. 3: Proceedings of the 2010 Annual Conference on Experimental and Applied Mechanics*, 2011, Springer. p. 149-158.
49. Cuntze, R.G., *The FAILURE MODE CONCEPT - a new comprehensive 3D-strength analysis concept for any brittle and ductile behaving material.* European Conference on Spacecraft Structures, Materials and Mechanical Testing, Proceedings, 1999. **428**: p. 269-287.
50. Heimbs, S., et al., *Crash Simulation of an F1 Racing Car Front Impact Structure*, in *7th European LS-DYNA Conference*2009: Salzburg, Austria.
51. Ernst, G., et al., *Multiscale progressive failure analysis of textile composites.* Composites Science and Technology, 2010. **70**(1): p. 61-72.
52. Sun, C.T. and R.S. Vaidya, *Prediction of composite properties, from a representative volume element.* Composites Science and Technology, 1996. **56**(2): p. 171-179.
53. Fiedler, B., et al., *Failure behavior of an epoxy matrix under different kinds of static loading.* Composites Science and Technology, 2001. **61**(11): p. 1615-1624.
54. Lemaitre, J. and J.L. Chaboche, *Mécanique des matériaux solides*1988.
55. Hillerborg, A., M. Modeer, and P.E. Petersson, *Analysis of crack formation and crack growth in concrete by means of fracture mechanics and finite elements.* Cement and Concrete Research, 1976. **6**: p. 773-782.
56. Vogler, M., G. Ernst, and R. Rolfes, *Invariant Based Transversely-Isotropic Material and Failure Model for Fiber-Reinforced Polymers.* Cmc-Computers Materials & Continua, 2010. **16**(1): p. 25-49.

57. Juhasz, J., R. Rolfes, and K. Rohwer, *A new strength model for application of a physically based failure criterion to orthogonal 3D fiber reinforced plastics.* Composites Science and Technology, 2001. **61**(13): p. 1821-1832.
58. Puck, A. and H. Schurmann, *Failure analysis of FRP laminates by means of physically based phenomenological models.* Composites Science and Technology, 2002. **62**(12-13): p. 1633-1662.
59. Wang, X.F., et al., *Multi-scale analyses of 3D woven composite based on periodicity boundary conditions.* Journal Of Composite Materials, 2007. **41**(14): p. 1773-1788.
60. Van Den Broucke, B., et al., *Modelling of Damage in Textile Reinforced Composites: Micro-Meso Approach*, in *Symposium on Finite Element Modeling of Textiles and Textile Composites*2007: St Petersburg, Russia.
61. *Katholieke Universiteit Leuven Website - WiseTex Suite Section. [cited 25/11/11]; Availiable from: http://www.mtm.kuleuven.be/Onderzoek/Composites/software/wisetex*.
62. Okereke, M., et al., *Virtual Testbed for Numerical Homogenization of Elastic Behaviour and Damage Initiation in Bidirectional Composites*, in *5th European Congress on Computational Methods in Applied Sciences and Engineering*2008: Venice, Italy.
63. Zhang, B.M., et al., *Hierarchical multiscale modeling of failure in unidirectional fiber-reinforced plastic matrix composite.* Materials & Design, 2010. **31**(5): p. 2312-2318.
64. Foreman, J.P., et al., *Rate dependent multiscale modelling of fibre reinforced composites.* Plastics Rubber and Composites, 2009. **38**(2-4): p. 67-71.
65. Grujicic, M., et al., *Multi-scale ballistic material modeling of cross-plied compliant composites.* Composites Part B-Engineering, 2009. **40**(6): p. 468-482.
66. Iremonger, M.J., *Polyethylene composites for protection against high velocity small arms bullets*, in *International Symposium on Ballistics*1999: San Antonio. p. 946-953.
67. Lua, J., W. Gregory, and J. Sankar, *Multi-scale dynamic failure prediction tool for marine composite structures.* Journal of Materials Science, 2006. **41**(20): p. 6673-6692.
68. Daniel, I.M., et al., *Mechanical Behaviour and Failure Criteria of Composite Materials under Static and Dynamic Loading*, in *The 17th International Conference on Composite Materials*2009: Edinburgh, UK.
69. Fujita, Y., T. Kurashiki, and M. Zako, *Study on the Transverse Strength of Unidirectional Composite*, in *The 14th European Conference on Composite Materials*2010: Budapest, Hungary.
70. Aminjikarai, S.B. and A. Tabiei, *A strain-rate dependent 3-D micromechanical model for finite element simulations of plain weave composite structures.* Composite Structures, 2007. **81**(3): p. 407-418.
71. Mishnaevsky, L. and P. Brondsted, *Three-dimensional numerical modelling of damage initiation in unidirectional fiber-reinforced composites with ductile matrix.* Materials Science and Engineering a-Structural Materials Properties Microstructure and Processing, 2008. **498**(1-2): p. 81-86.
72. Tursun, G., et al., *The influence of transition phases on the damage behaviour of an Al/10vol.%SiC composite.* Computational Materials Science, 2006. **37**(1-2): p. 119-133.
73. *ImageJ. Image Processing and Analysis in Java. [cited 05/10/11]; Availiable from: http://rsb.info.nih.gov/ij/*.

74. Gommer, F., A. Endruweit, and A.C. Long, *Non-Uniformity Of The Filament Distribution In Fibre Bundles And Its Effect On Defect Formation In Liquid Composite Moulding*, in *The 18th International Conference on Composite Materials*2011: Jeju, South Korea.
75. Li, S.G. and A. Wongsto, *Unit cells for micromechanical analyses of particle-reinforced composites.* Mechanics of Materials, 2004. **36**(7): p. 543-572.
76. Lidgett, M., et al., *Virtual modelling of microscopic damage in polymer composite materials at high rates of strain.* Plastics Rubber and Composites, 2011. **40**(6-7): p. 324-332.
77. Gutkin, R. and S.T. Pinho, *Practical Application Of Failure Models To Predict The Response Of Composite Structures*, in *The 18th International Conference On Composite Materials*2011: Jeju, South Korea.
78. Maligno, A.R., *Finite Element Investigations on the Microstructure of Composite Materials*, in *School of Mechanical, Materials and Manufacturing Engineering*2007, The University of Nottingham: Nottingham.
79. Soden, P.D., M.J. Hinton, and A.S. Kaddour, *Lamina properties, lay-up configurations and loading conditions for a range of fibre-reinforced composite laminates.* Composites Science and Technology, 1998. **58**(7): p. 1011-1022.
80. Kari, S., et al., *Effect Of Yarn Cross-Sectional Shapes And Crimp On The Mechanical Properties Of 3D Woven Composites*, in *The 17th International Conference On Composite Materials*2009: Edinburgh, UK.
81. Wright, A. and M. French, *The response of carbon fibre composites to blast loading via the Europa CAFV programme.* Journal of Materials Science, 2008. **43**(20): p. 6619-6629.
82. *Permali Gloucester Limited Website. [cited 06/03/12]; Availiable from: http://www.permali.co.uk/*.
83. *Sigmatex Company Website. [cited 24/04/12]; Availiable from: http://www.sigmatex.com/Home*.
84. *Matrix Composite Materials Company Website. [cited 24/04/12]; Availiable from: http://www.sicomin.co.uk/*.
85. *Imetrum Company Website. [cited 24/04/12]; Availiable from: http://www.imetrum.com/*.
86. *ASTM-D3039, Standard Test Method for Tensile Properties of Polymer Matrix Composite Materials. ASTM International, 1995.*
87. *ASTM-D3518, Standard Test Method for In-Plane Shear Response of Polymer Matrix Composite Materials by Tensile Test of a ±45° Laminate. ASTM International, 1995.*
88. *Kistler Company Website. [cited 24/04/12]; Availiable from: http://www.kistler.com*.
89. *FLYDE Company Website. [cited 24/04/12]; Availiable from: http://www.fylde.com/*.
90. *Data Translation Company Website. [cited 24/04/12]; Availiable from: http://www.datatranslation.com/*.
91. Zhao, F.M. and N. Takeda, *Effect of interfacial adhesion and statistical fiber strength on tensile strength of unidirectional glass fiber/epoxy composites. Part I: experiment results.* Composites Part a-Applied Science and Manufacturing, 2000. **31**(11): p. 1203-1214.
92. Ghiorse, S.R., *Effect of Void Content on the Mechanical-Properties of Carbon Epoxy Laminates.* Sampe Quarterly-Society for the Advancement of Material and Process Engineering, 1993. **24**(2): p. 54-59.

93. Vallons, K., et al., *Fibre Orientation Effects On The Tensile Properties Of Biaxial Carbon/Epoxy NCF Composites*, in *The 17th International Conference on Composite Materials*2009: Edinburgh, UK.

Appendix A Publications

Lidgett, M., Brooks, R., Warrior, N.A., Brown, K. Virtual Modelling of Microscopic Damage in Polymer Composite Materials at High Rates of Strain. Proceedings of the 14th European Conference on Composite Materials (ECCM). 2010. Budapest, Hungary.

Brooks, R., **Lidgett, M.**, Warrior, N.A., Brown, K. Multi-Scale Modelling of Damage in Textile Composite Materials at High Rates of Strain. Proceedings of the 10th International Conference on Textile Composites (TEXCOMP). 2010. Lille, France.

Lidgett, M., Brooks, R., Warrior, N.A., Brown, K. Virtual Modelling of Microscopic Damage in Polymer Composite Materials at High Rates of Strain. Plastics, Rubber and Composites. 2011. 40. p. 324-332.

Lidgett, M., Brooks, R., Warrior, N.A., Brown, K., Martindale, N., Wright, A., French, M. Multi-Scale Modelling of Polymer Composite Materials under Blast and Ballistic Loading. Proceedings of the 18th International Conference on Composite Materials (ICCM). 2011. Jeju, South Korea.

Wright, A., French, M., **Lidgett, M.,** Brooks, R. Foxhound: the UK's latest composite armoured vehicle. Proceedings of the SAMPE EUROPE 33rd International Technical Conference. 2012. Paris, France.

Appendix B Material Properties

	Matrix Value
Stiffness (GPa)	1.423
Poisson's Ratio	0.34
Shear Stiffness (GPa)	0.53
Tensile Strength (GPa)	0.121
Compressive Strength (GPa)	0.131
Shear Strength (GPa)	0.05
Strain Softening Parameter	0.1
Density (kg/mm^3)	1.3E-06
Strain Rate Scaling Constant for Stiffness at Low Rates	0.0401
Strain Rate Scaling Constant for Stiffness at High Rates	0.1571
Stiffness Low Rate / High Rate Threshold (/s)	199.35
Strain Rate Scaling Constant for Strength at Low Rates	0.0329
Strain Rate Scaling Constant for Strength at High Rates	0.1788
Strength Low Rate / High Rate Threshold (/s)	88.58

	Carbon Fibre Value	S2 Glass Fibre Value
Longitudinal Young's Modulus (GPa)	230	86
Transverse Young's Modulus (GPa)	15	86
Poisson's Ratio 12	0.25	0.23
Poisson's Ratio 23	0.016	0.23
Poisson's Ratio 31	0.2	0.23
Shear Modulus 13 (GPa)	7	34.96
Shear Modulus 13 (GPa)	15	34.96
Shear Modulus 23 (GPa)	15	34.96
Longitudinal Tensile Strength (GPa)	4.9	4.59
Longitudinal Compressive Strength (GPa)	2.5	3.1
Radius (mm)	0.004470	0.00605
Fibre Volume Fraction	0.6628	0.5432
Density (kg/mm^3)	1.8E-06	2.4E-06

	Interface Value
Stiffness (GPa)	1.423
Poisson's Ratio	0.34
Shear Stiffness (GPa)	0.53
Shear Failure Stress (GPa)	0.03703
Strain Rate Scaling Constant for Shear Failure Stress	0.2647
Density (kg/mm^3)	1.3E-06
Interface Thickness (mm)	0.000605

Appendix C Micro Scale Strain Rate Scaling Plots

Carbon/Epoxy

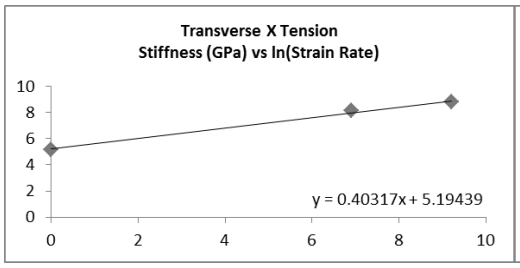

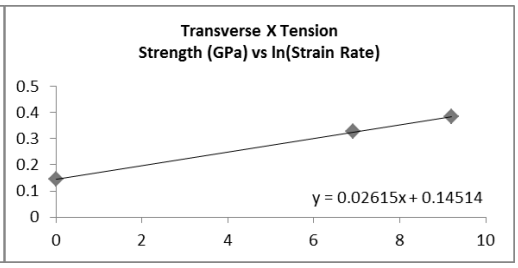

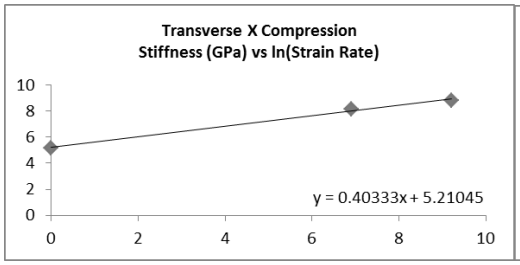

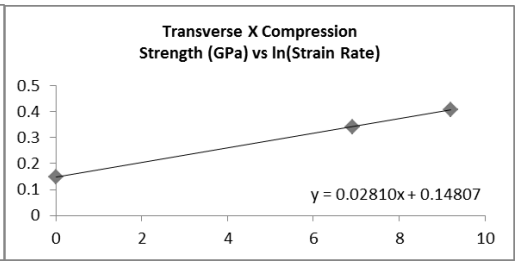

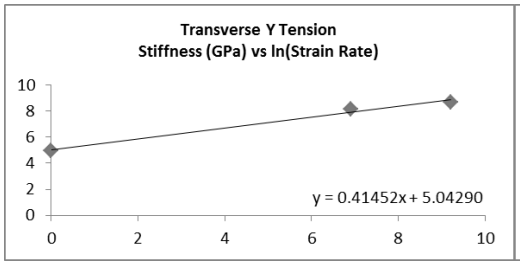

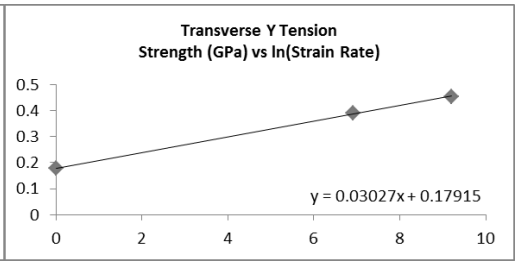

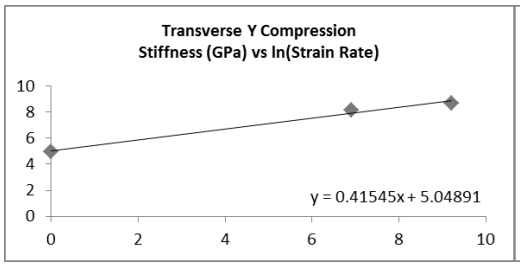

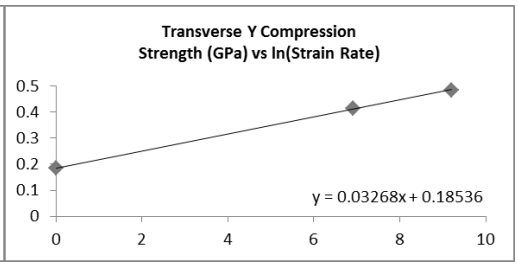

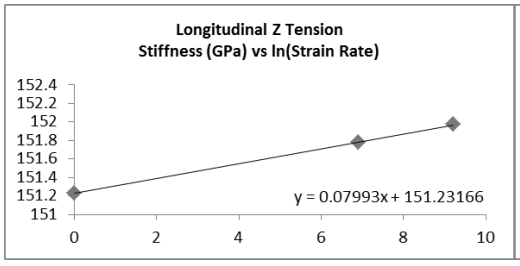

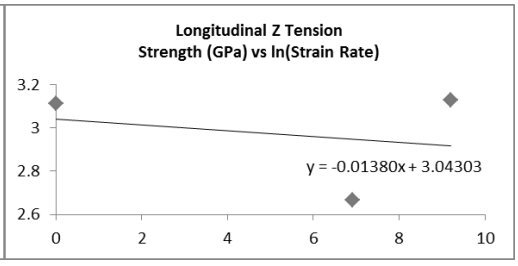

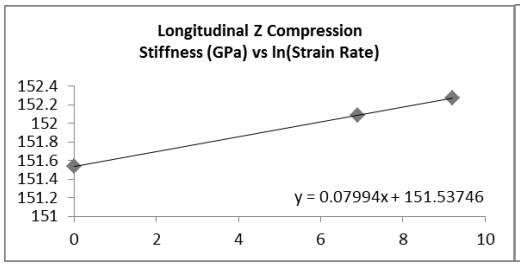

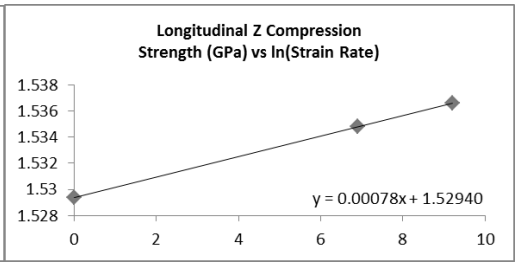

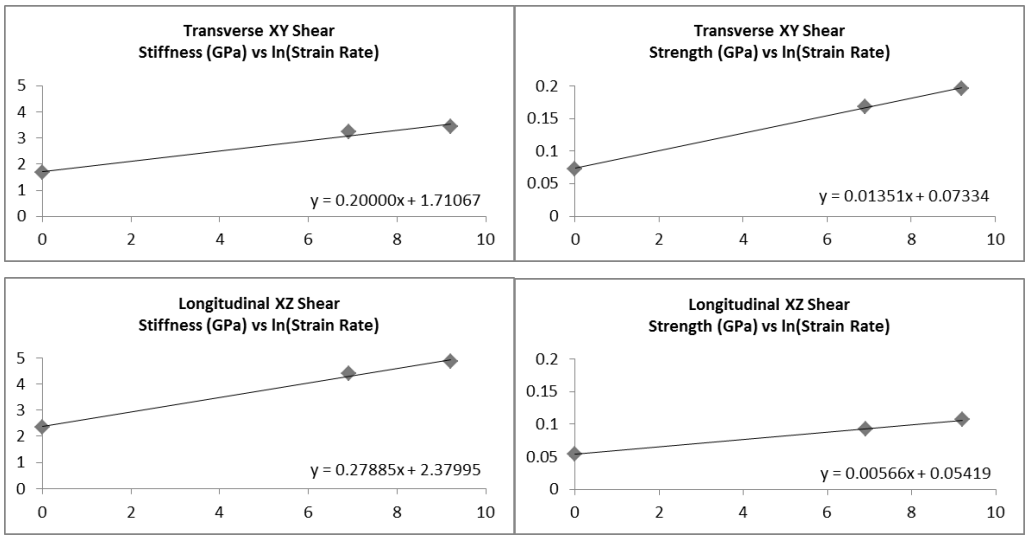

	Stiffness Strain Rate Scaling Constant	Strength Strain Rate Scaling Constant
Transverse X Tension	0.0776	0.1802
Transverse X Compression	0.0774	0.1898
Transverse Y Tension	0.0822	0.1690
Transverse Y Compression	0.0823	0.1763
Longitudinal Z Tension	0.0005	-0.0045
Longitudinal Z Compression	0.0005	0.0005
Transverse XY Shear	0.1169	0.1842
Longitudinal XZ Shear	0.1172	0.1044

S2 Glass/Epoxy

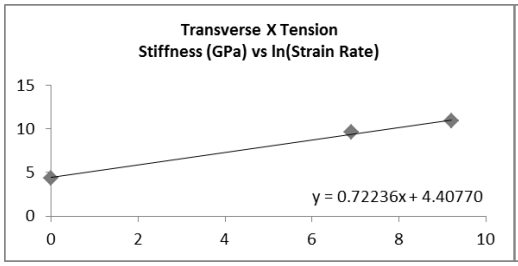

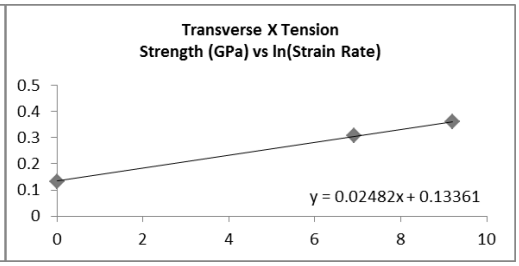

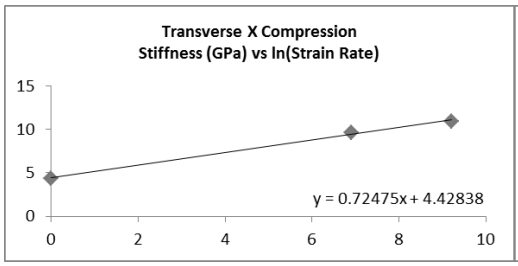

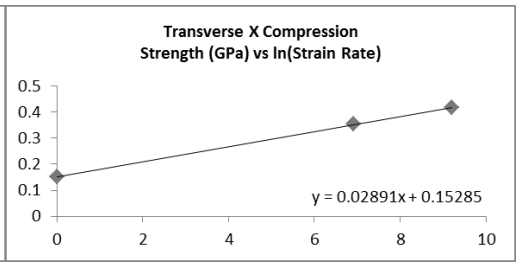

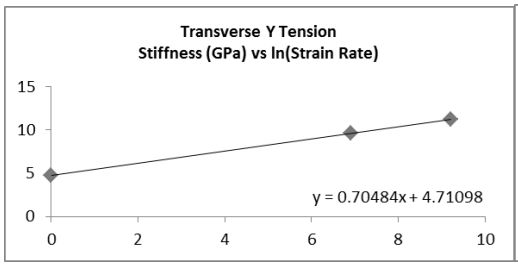

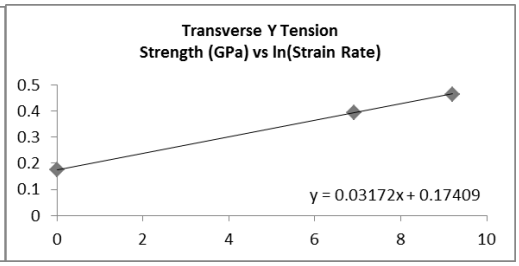

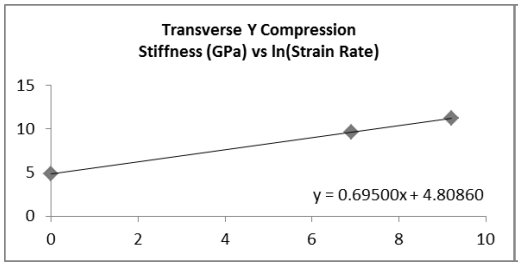

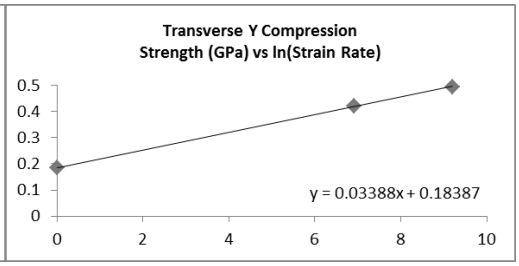

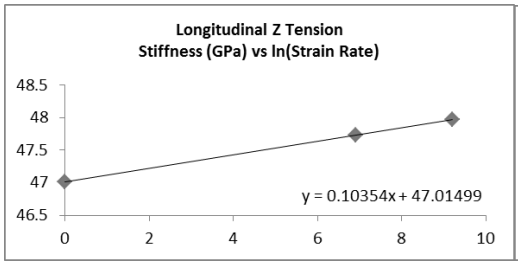

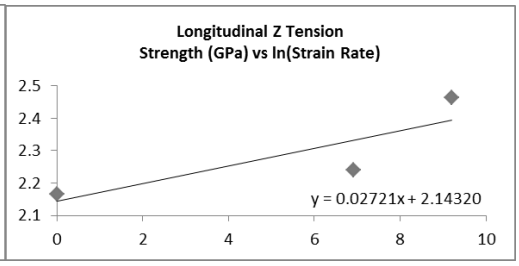

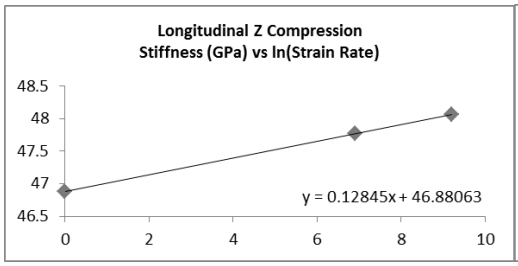

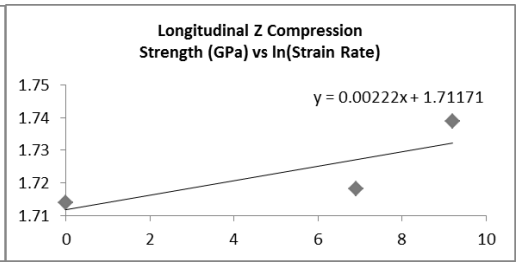

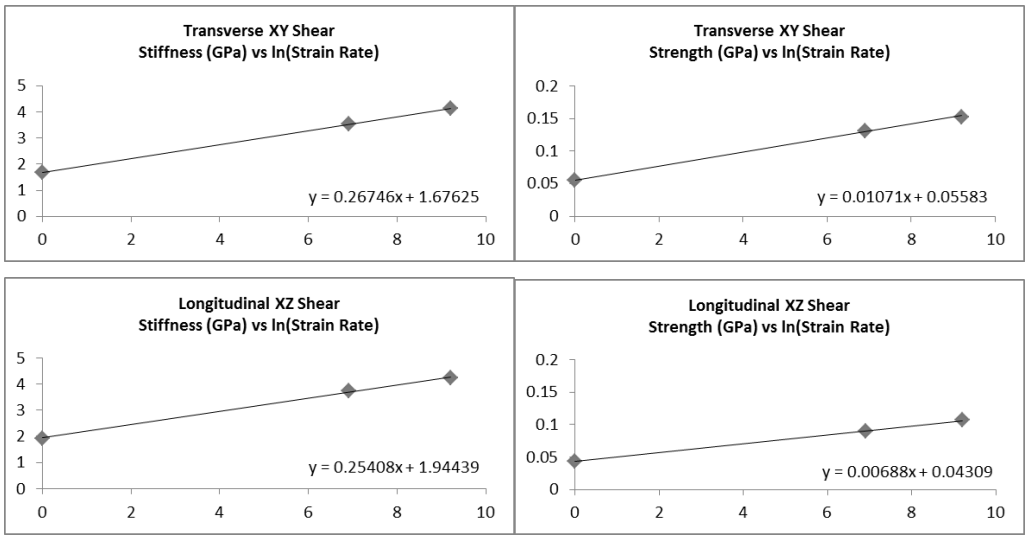

	Stiffness Strain Rate Scaling Constant	Strength Strain Rate Scaling Constant
Transverse X Tension	0.1657	0.1867
Transverse X Compression	0.1654	0.1902
Transverse Y Tension	0.1498	0.1827
Transverse Y Compression	0.1446	0.1848
Longitudinal Z Tension	0.0022	0.0126
Longitudinal Z Compression	0.0027	0.0013
Transverse XY Shear	0.1599	0.1935
Longitudinal XZ Shear	0.1315	0.1593

Appendix D Meso Scale Strain Rate Scaling Plots

Carbon/Epoxy

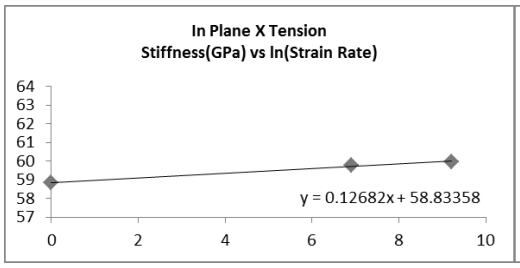

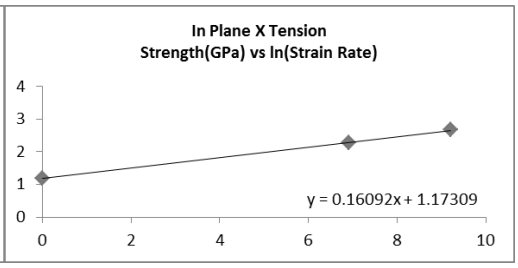

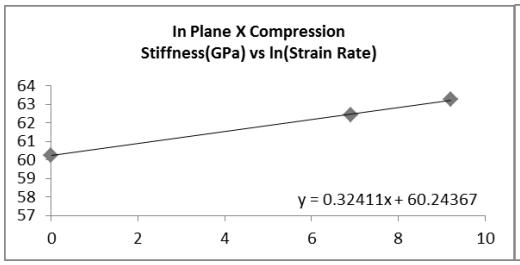

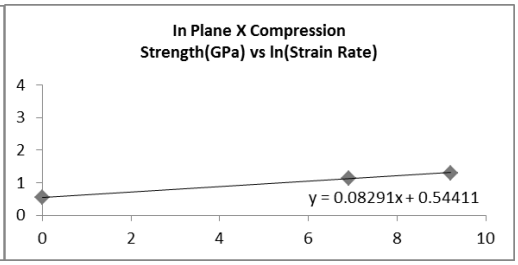

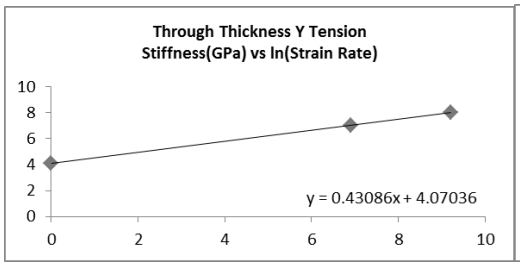

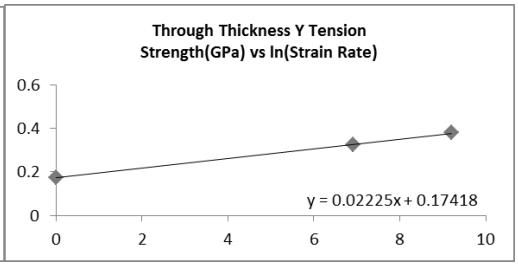

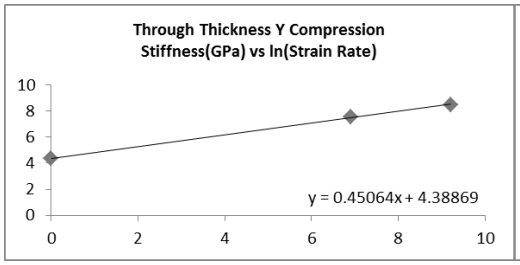

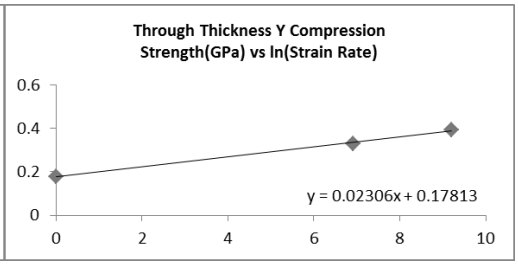

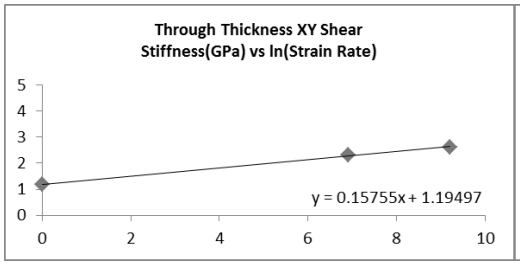

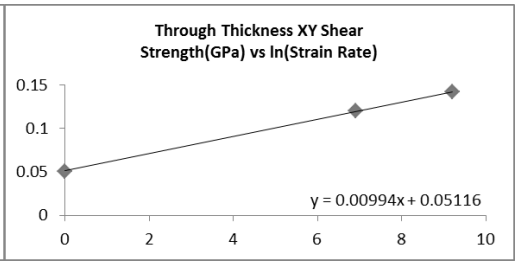

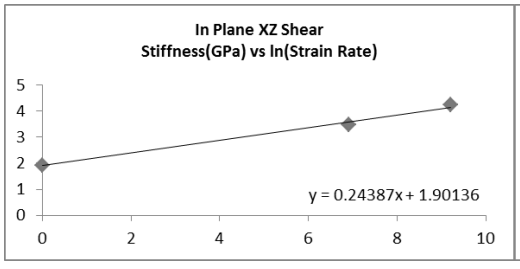

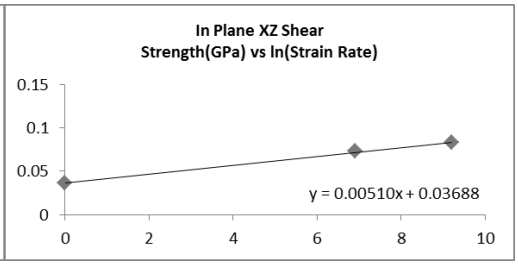

	Stiffness Strain Rate Scaling Constant	Strength Strain Rate Scaling Constant
In-Plane X Tension	0.0022	0.1372
In-Plane X Compression	0.0054	0.1524
Through Thickness Y Tension	0.1059	0.1277
Through Thickness Y Compression	0.1027	0.1295
Through Thickness XY Shear	0.1318	0.1943
In-Plane XZ Shear	0.1283	0.1383

S2 Glass/Epoxy

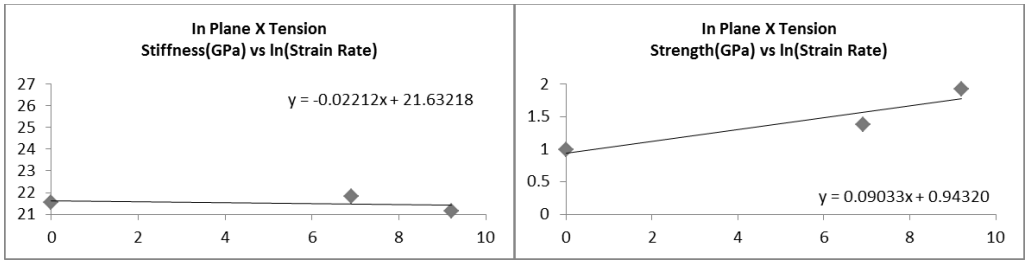

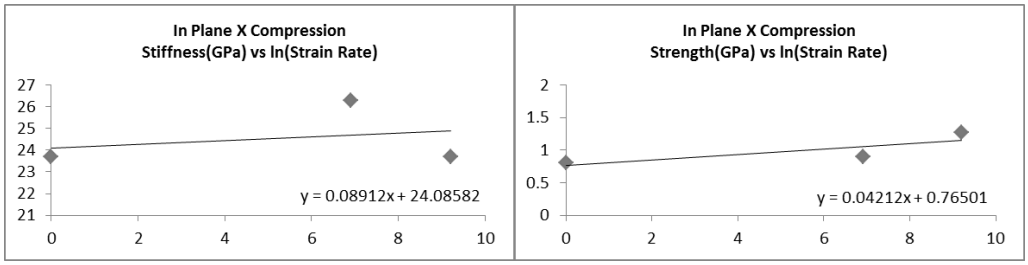

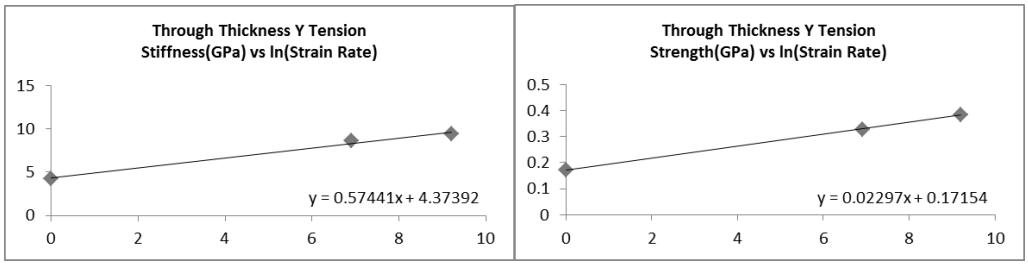

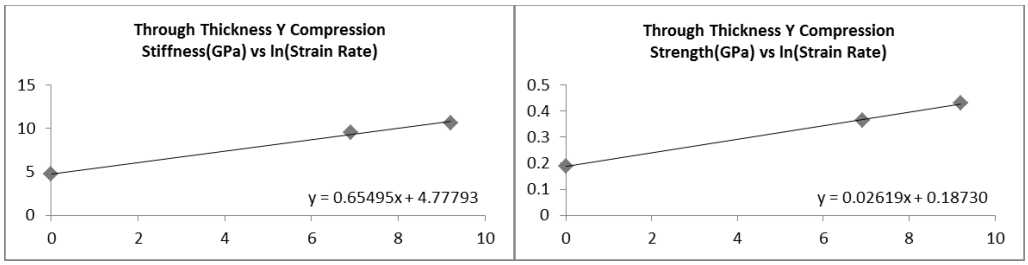

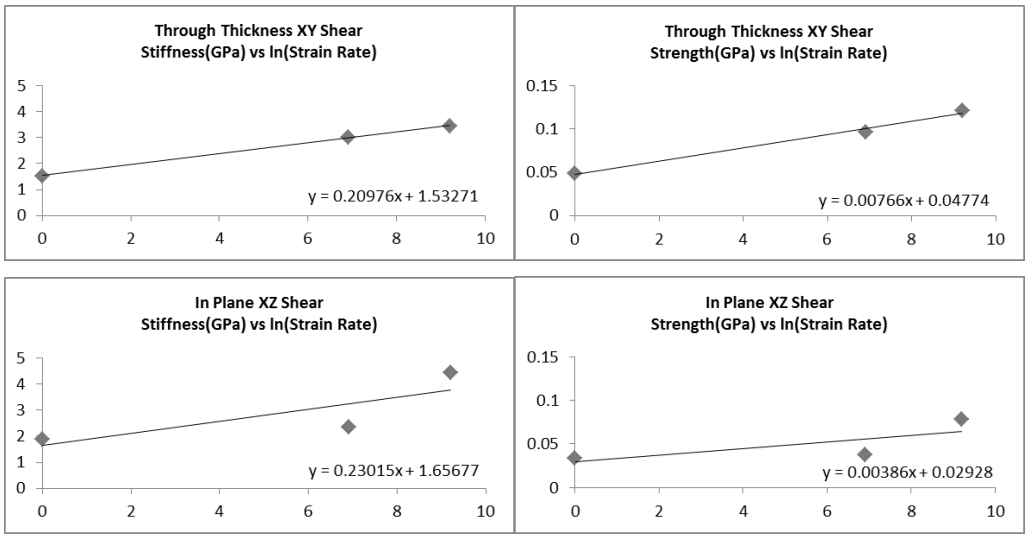

	Stiffness Strain Rate Scaling Constant	Strength Strain Rate Scaling Constant
In-Plane X Tension	-0.0010	0.0958
In-Plane X Compression	0.0037	0.0551
Through Thickness Y Tension	0.1313	0.1339
Through Thickness Y Compression	0.1371	0.1398
Through Thickness XY Shear	0.1369	0.1605
In-Plane XZ Shear	0.1389	0.1318